ROMANIAN ACADEMY

Speech and Image Processing and Analysis Models Applied to Biometrics and Computer Vision

Habilitation Thesis

TUDOR BARBU

Senior Researcher I

Institute of Computer Science of the Romanian Academy
Iaşi, Romania

February, 2015

Familiei mele,

CONTENTS

(a) Summary

This abilitation thesis presents the most significant scientific accomplishments I have achieved since I received the PhD degree in January 2005, and also my future professional, scientific and academic career development and evolvement plans. Besides this summary, it is composed of a main part *b*, containing three subparts.

The major subpart *b*(*i*), entitled ***Scientific and professional achievements***, describes in three chapters the most important results obtained in the period 2005-2014. In these almost ten years my research activity has lied at the intersection of computer science, digital signal processing, and applied mathematics. I have essentially followed four main research directions in this period: image pre-processing, machine learning, biometrics and computer vision. Mathematical models, mostly based on partial differential equations (PDEs), have been introduced in all these domains. Since the most important of these domains, which are biometrics and computer vision, are mainly based on image and voice signal analysis, many speech and image analysis techniques for biometrics and computer vision have been developed by us. The other two approached domains have the role to facilitate the tasks related to biometrics and computer vision. The proposed image pre-processing techniques are based on PDE models and enhance the images, thus facilitating the potential image analysis tasks. The machine learning algorithms are widely used in both biometrics and computer vision. Our machine learning solutions represent novel media feature vector classification algorithms using some specially created metrics. Each chapter is composed of several sections, each section being related to a subdomain and composed of subsections corresponding to various techniques, ending with a conclusion section.

First chapter, entitled *Mathematical models for image processing and machine learning*, is related to my first two directions. In the first section there are described our proposed image filtering methods using hyperbolic second-order equations. The developed image noise reduction approaches based on nonlinear diffusion are presented in the second section. The third section describes the proposed variational PDE image denoising and restoration techniques. Some special metrics for media (audio, image and video) feature vectors and several automatic feature vector clustering techniques modeled by us are explained in the fourth section.

Second chapter, entitled *Biometric authentication techniques*, describes our main results achieved in the biometrics domain. The developed voice recognition techniques based on mel-cepstral speech analysis are discussed in the first section. The second section presents the proposed facial recognition models, while the third section presents our fingerprint authentication approaches. The investigated multi-modal biometric technologies are described in the fourth section.

The third chapter is entitled *Image analysis based computer vision models* and presents my accomplishments in computer vision area. Its first section describes the proposed image segmentation techniques, while our temporal video segmentation approaches are described in the second section. The third section presents the variational PDE-based image reconstruction models introduced by us. The considered image and video recognition solutions are discussed in the fourth section. In the fifth section there are described content-based image indexing and retrieval systems. The developed image and video object detection and tracking technologies are outlined in the sixth section.

All research results described in these chapters have been soft-implemented, and disseminated in numerous publications. Since January 2005, I have authored over 66 published

works disseminating the major achievements in the mentioned domains, including 2 books, 1 book chapter, 33 articles published in recognized international journals (18 ISI journals and 15 journals indexed by international databases) and 30 papers published in volumes of international scientific events (including 2 conferences ranked as A, 5 ranked as B, 3 ranked as C, by ARC). Besides these works, the research results have been disseminated in 20 scientific reports elaborated at our institute, under my coordination. The scientific impact of my works is also proven by the 160 citations (no self-citations) received by them, according to Google-Academic.

The second subpart *b*(*ii*), entitled ***Professional, scientific and academic career evolvement and development plans,*** disscuses the future research results, first. In the future I will continue to follow the mentioned research directions, improving the proposed techniques, developing new methods and approaching new subdomains. In *b*(*ii*) I suggest how our existing approaches can be further improved, and how new image restoration, biometric authentication and computer vision solutions would look like. Several new PDE models for denoising and inpainting are mainly discussed. New subdomains of the major domains will also be considered. In *b*(*ii*) I explain how new biometrics subdomains, such as iris recognition and text-independent voice recognition, or new computer vision areas, like image registration and optical flow, will be approached as part of my future research.

Then, my academic career evolvement and development plans are outlined. I consider and explain in detail the following major objectives of the career development plan: forming a new generation of well-prepared researchers in my domains of interest; building and coordinating effective research collectives capable to conduct important projects; establishing more scientific collaborations with well-known researchers and institutes from Romania or abroad; performing teaching activities.

My abilitation thesis ends with the bibliography *b*(*iii*), where references of top 10 **selected papers** are marked in bold.

(a) Rezumat

Această teză de abilitare prezintă cele mai importante dintre realizările mele ştiinţifice obţinute de la primirea titlului de doctor, în ianuarie 2005, până în prezent, şi de asemenea planurile de dezvoltare şi evoluţie a carierei mele profesionale, ştiinţifice şi academice. Pe lângă acest rezumat, teza este compusă dintr-o parte principală *b*, conţinând trei subpărţi.

Subpartea principală *b*(*i*), intitulată ***Realizări ştiinţifice şi profesionale***, descrie în cele trei capitole ale sale cele mai importante rezultate obţinute în perioada 2005-2014. În aceşti aproape zece ani, activitatea mea de cercetare s-a situat la intersecţia dintre informatică, procesarea semnalelor digitale şi matematica aplicată. În respectiva perioadă am urmat în principal următoarele patru direcţii de cercetare: pre-procesarea imaginilor, învăţare automată, biometrie şi vizune computerizată. Modele matematice, în majoritate bazate pe ecuaţii cu derivate parţiale, au fost introduse în toate aceste domenii. Deoarece cele mai importante dintre aceste domenii, şi anume biometria şi viziunea computerizată, sunt bazate mai ales pe analiza semnalului de imagine şi voce, numeroase tehnici de analiză a vorbirii şi imaginilor, utilizabile în biometrie şi viziunea computerizată, au fost dezvoltate de către noi. Celelalte două domenii abordate au rolul de a facilita procesele biometrice sau ale viziunii computerizate. Tehnicile de pre-procesare a imaginilor pe care le-am propus sunt bazate pe modele PDE şi prin îmbunătăţirea imaginilor facilitează potenţialele procese de analiză imagistică. Algoritmii de învăţare automată sunt des utilizaţi atât în biometrie, cât şi în viziunea computerizată. Soluţiile noastre de învăţare automată reprezintă noi algoritmi de clasificare a vectorilor de trăsături media, care utilizează metrici special construite. Fiecare capitol este compus din câteva secţiuni, fiecare secţiune abordând un anumit subdomeniu şi compusă la rândul său din subsecţiuni corespunzând unor diverse tehnici, şi se încheie cu concluzii.

Primul capitol, intitulat *Modele matematice de procesare a imaginilor şi învăţare automată*, se referă la primele două direcţii. În prima secţiune sunt descrise metodele propuse pentru filtrarea imaginilor utilizând ecuaţii hiperbolice de ordinul II. Tehnicile de reducere a zgomotului din imagine bazate pe difuzia neliniară, dezvoltate de noi, sunt prezentate în secţiunea a doua. Cea de-a treia secţiune prezintă tehnicile PDE variaţionale propuse pentru curăţirea de zgomot şi restaurarea imaginilor. Metricile speciale pentru vectorii de trăsături media (audio, imagistici și video) şi tehnicile automate de clusterizare automată a vectorilor de trăsături, pe care le-am modelat, sunt explicate în secţiunea a patra.

Al doilea capitol, intitulat *Tehnici de autentificare biometrică*, descrie cele mai importante rezultate pe care le-am obţinut în domeniul biometric. Tehnicile dezvoltate pentru recunoaşterea vocii, bazate pe analiza mel-cepstrală a vorbirii, sunt discutate în prima secţiune. Cea de a doua descrie modelele de recunoaştere facială propuse, iar a treia secţiune prezintă metodele noastre de autentificare a amprentelor digitale. Tehnologiile biometrice multi-modale investigate sunt descrise în cea de-a patra secţiune.

Capitolul trei este intitulat *Modele de viziune computerizată bazate pe analiza imagistică* şi prezintă rezultatele obţinute în domeniul viziunii computerizate. Prima secţiune descrie tehnicile de segmentare a imaginii propuse, în timp ce metodele noastre de segmentare temporală video sunt descrise în a doua secţiune. A treia secţiune prezintă modelele variaţionale de tip PDE pentru reconstrucţia imaginilor, pe care le-am introdus. Soluţiile considerate pentru recunoaştere a imaginilor şi secvenţelor video sunt discutate în a patra secţiune. În secţiunea cinci sunt descrise sisteme informatice de indexare și regăsire de imagini pe baza de conţinut. Tehnologiile

construite pentru detectarea şi urmărirea obiectelor imagistice şi video sunt prezentate în secţiunea a şasea.

Rezultatele cercetării descrise în aceste capitole au fost implementate soft, și diseminate în numeroase publicaţii. Începând cu ianuarie 2005, am publicat peste 66 de lucrări diseminând principalele realizări în domeniile menţionate, incluzând 2 cărţi, 1 capitol de carte, 33 articole publicate în jurnale internaţionale recunoscute (18 jurnale ISI şi 15 jurnale indexate de bazele de date internaţionale) şi 30 articole publicate în volume ale evenimentelor ştiinţifice internaţionale (incluzând 2 conferinţe tip A, 5 de tip B, 3 de tip C, conform ARC). Înafara acestor lucrări, rezultatele cercetării au fost diseminate în 20 de rapoarte ştiinţifice elaborate la institutul nostru, sub coordonarea mea. Impactul ştiinţific ridicat al acestor lucrări este demonstrat de cele 160 citări (excluzând auto-citările) primite, conform Google-Academic.

Cea de-a doua subparte *b*(*ii*), intitulată ***Planuri de dezvoltare şi evoluţie a carierei profesionale, ştiinţifice şi academice,*** ia mai întâi în discuţie viitoarele rezultate în cercetare. În viitor voi continua să urmez direcţiile de cercetare menţionate, îmbunătăţind technicile propuse, dezvoltând noi metode şi abordând noi subdomenii. În *b*(*ii*) sunt sugerate modalităţile prin care metodele noastre existente pot fi îmbunătățite, precum şi modul în care vor arăta noile soluţii de restaurare imagistică, autentificare biometrică şi viziune computerizată. Câteva modele noi de tip PDE pentru filtrare şi reconstrucţie sunt în principal abordate. Totodată, noi subdomenii ale domeniilor principale vor fi considerate. În *b*(*ii*) sunt apoi explicate modalităţile de abordare în cadrul cercetării viitoare ale subdomeniilor nou-introduse, precum recunoaşterea irisului ori recunoaşterea vocii independentă de text, în cazul biometriei, sau înregistrarea imaginilor şi fluxul optic, în cazul viziunii computerizate.

În continuare sunt prezentate planurile de evoluţie şi dezvoltare ale carierei academice. Am considerat şi explicat în detaliu următoarele obiective majore ale planului de dezvoltare a carierei: formarea unei noi generaţii de cercetători bine pregătiţi în domeniile mele de interes; organizarea şi coordonarea unor colective de cercetare eficiente, capabile să ducă la îndeplinire proiecte importante; stabilirea de noi colaborări ştiinţifice cu personalităţi şi instituţii de renume în cercetare; desfăşurarea unor activităţi didactice, de predare.

Teza de abilitare se încheie cu bibliografia *b*(*iii*), în care referințele **lucrărilor selectate** în top 10 sunt marcate in bold.

(b) Scientific achievements and career development plans

(i) Scientific and professional achievements

This main part of the abilitation thesis presents the most important scientific results accomplished in the last 10 years that is the period following my PhD award. It is composed of 3 chapters, each of them describing the major achievements in one of these main areas of interest: image enhancement, biometrics and computer vision. Besides the proposed PDE-based image denoising and restoration models, first chapter outlines also some machine learning algorithms. The most significant results achieved in the biometrics field are described in the second chapter, where both supervised and unsupervised biometric recognition models, based on voice, face, fingerprints and combinations of these identifiers, are presented. The third chapter illustrates the main computer vision achievements, representing original image and video segmentation, image reconstruction, image and object recognition, CBIR and object detection/tracking techniques. My major contributions to the approached domains, described in the next 3 chapters, are as follows:

- A linear PDE-based image denoising technique using hyperbolic second-order equations
- A nonlinear anisotropic diffusion model for image restoration
- Image noise removal approach based on diffusion porous media flow
- A 4th-order diffusion-based model for image noise reduction
- Two novel PDE variational models for image denoising
- A Hausdorff-Pompeiu derived metric for different-sized 2D feature vectors
- A novel similarity metric constructed for images characterized by *key points*
- Automatic unsupervised classification models using region-growing and validation indexes
- Text-dependent voice recognition system using a robust DDMFCC-based feature extraction
- An automatic unsupervised speaker recognition model
- An eigenimage-based facial recognition technique
- A 2D Gabor filtering-based face recognition approach
- A SIFT-based automatic unsupervised face recognition model
- Minutia-matching based fingerprint recognition solution
- Pattern-based fingerprint matching methods using 2D Gabor filters and DWT decomposition
- Multimodal biometric technologies combining voice, face and fingerprint recognition models
- Automatic moment-based image segmentation techniques
- A PDE level-set based contour tracking model
- An automatic temporal video segmentation technique
- A robust PDE variational image reconstruction approach
- Novel image and video recognition models using various content-based feature vectors
- Object recognition model using moment-based shape analysis and content-based recognition
- Automatic clustering-based image indexing and retrieval techniques
- Content-based image retrieval systems using SAM indexing and relevance-feedback schemes
- Automatic face detection technique based on skin filtering and cross-correlation procedures
- A SVM-based human cell detection technique using HOG-based feature vectors
- Object detection and tracking models using temporal-differencing and object matching
- Video tracking technique using a novel *N*-Step Search algorithm and HOG features.

The results described in these chapters have been disseminated in over 66 published works (books, chapters, articles in recognized international journals or conference volumes). My **selected most relevant 10 papers** contain the most accomplishments from the above list.

1. Mathematical models for image processing and machine learning

During the past three decades, the mathematical models have been increasingly used in some traditionally engineering domains like signal and image processing, analysis, and computer vision. This chapter describes several robust mathematical models for image pre-processing (processing images for future analysis tasks) and machine learning.

The most important image pre-processing tasks, namely the image denoising and restoration, are performed using some partial differential equation (PDE) based mathematical models. The partial differential equations have been successful for solving various image processing and computer vision tasks since 1980s [1]. The variational and PDE-based approaches have been widely used and studied in these domains in the last decades, mainly because of their modeling flexibility and some advantages of their numerical implementation [1].

Image noise reduction with feature preservation is still a focus in the image processing field and a serious challenge for the researchers. An efficient denoising technique has to not only substantially reduce the quantity of image noise but also preserve the image boundaries and other characteristics. The conventional smoothing models, such as the averaging, median, Wiener, or the classic 2D Gaussian filter succeed in noise reduction, but could also have undesired effects on edges or other image details and structures [2,3]. The PDE-based models provide efficient image filtering while preserving the features [4].

Some novel linear and nonlinear PDE-based image noise removal techniques are described in the next three sections. Thus, a modified Gaussian filter kernel provided by second-order hyperbolic diffusion equations is introduced in section 1.1. Several nonlinear diffusion equation based filtering techniques are discussed in the second section. The third section describes our PDE variational image restoration models.

Several mathematical models are introduced for the classification of various media feature vectors. Supervised and unsupervised classification models are described in the fourth section, related to machine learning. Some metrics specially created for complex feature vectors and used by these classifiers, are also modeled mathematically and presented in 1.4.

1.1. Image filtering methods using hyperbolic second-order equations

Gaussian noise, representing the statistical noise having the probability density function equal to that of the normal distribution is very often encountered in acquired digital images. So, the Gaussian noise reduction represents a very important image processing task that has been approached using both linear and nonlinear filtering algorithms [2,3].

Many classical image processing techniques can be reinterpreted as approximations of PDE-based models. Thus, the classic 2D Gaussian filtering model can be provided by the heat equation. This Gaussian filter, like other conventional linear filters such as the average filter [2], is efficient in smoothing the noise, but also has the disadvantage of blurring image edges. For this reason, I proposed a linear PDE-based denoising model using a modified Gaussian filter kernel in a 2012 paper [5].

The introduced mathematical model differs from the classic Gaussian model provided by heat equations, by a localization property. The classical filter has no localization property, the heat equation solution propagating with infinite speed, and this fact affects the edges. The classical Gaussian kernel, $G_t(x,y)=\frac{1}{4\pi t}e^{-\frac{x^2+y^2}{4t}}, (x,y)\in R^2, t>0$, is replaced with a modified kernel provided by some second-order hyperbolic equations [5]. The new improved kernel, $E(t,x,y):(0,\infty)\times R^2 \to R$, is obtained as the solution of the following PDE hyperbolic model:

$$\begin{cases} \varepsilon^2 \frac{\partial^2 E}{\partial t^2}+\gamma \frac{\partial E}{\partial t}-\Delta E=0 \\ E(0,x,y)=\delta,\ \frac{\partial E}{\partial t}(0,x,y)=0 \end{cases}, \ t\geq 0, (x,y)\in \Omega \subset R^2 \tag{1.1}$$

where $\varepsilon \geq 0$, $\gamma \geq 0$ and δ is the Dirac measure in R^2 concentrated in 0. Therefore, the Gaussian restoration process $u(t,x,y)=(G_t * u_0)(x,y)$ becomes:

$$u(t,x,y)=(E(t)*u_0)(x,y)=\int_{\Omega\subset R^2} E(t,x-\xi,y-\eta)u_0(\xi,\eta)d\xi d\eta \tag{1.2}$$

where $u_0=u_0(x,y), (x,y)\in\Omega\subset R^2$ is the image affected by noise, while *u* represents the restored image and is also the solution to the second-order linear differential equation:

$$\begin{cases} \varepsilon^2 \frac{\partial^2 u}{\partial t^2}+\gamma \frac{\partial u}{\partial t}-\Delta u=0, \text{in } (0,\infty)\times R^2 \\ u(0,x,y)=u_0(x,y), \frac{\partial u}{\partial t}(0,x,y)=0, \forall (x,y)\in R^2 \end{cases} \tag{1.3}$$

This equation, representing the *telegraphist's equation*, is used also as a non-Fourier model for heat propagation (the Cattaneo-Vernotte model). It is well known that the solution *u* to (1.3) propagates with finite speed [6], and so, taking (1.3) as a model for image denoising, it behaves better than the standard Gaussian model. A robust mathematical treatment of the proposed restoration model is also provided. We have demonstrated in [5] the existence and uniqueness of the hyperbolic equation's solution. The equation (1.3) has a unique weak solution *u* = *u* (*t*, *x*, *y*) which is continuous in *t* with values in $L^2(R^2)$.

The described PDE hyperbolic model is approximated in [5] using an implicit finite difference scheme. The following numerical approximation scheme has been provided in our paper:

$$(\varepsilon^2+\gamma h)u^{k+1}-(2\varepsilon^2+\gamma h)u^k+\varepsilon^2 u^{k-1}+h^2 A u^{k+1}=0 \tag{1.4}$$

where *h* > 0 and *A* is the elliptic operator $Au=-\Delta u$.

The convergence of the numerical scheme given by (1.4) is also demonstrated in [5]. For simplicity, the following explicit scheme can be used instead of it:

$$u^{k+1} = -\frac{h^2}{\varepsilon^2 + \gamma h} Au^k + \frac{2\varepsilon^2 + \gamma h}{\varepsilon^2 + \gamma h} u^k - \frac{\varepsilon^2}{\varepsilon^2 + \gamma h} Au^{k-1} = 0, k = 1,2,... \qquad (1.5)$$

This scheme converges to a solution representing the restored image *u* in a low number of iterations. Our iterative smoothing algorithm not only removes a great amount of Gaussian noise from the image, but also preserves the image edges very well. It has been tested on hundreds images corrupted with various levels of Gaussian noise, very good denoising results being obtained [5]. Also, our PDE restoration technique outperforms most classical image filtering algorithms, as resulting from the performed method comparisons. Such a method comparison is described in the next figure.

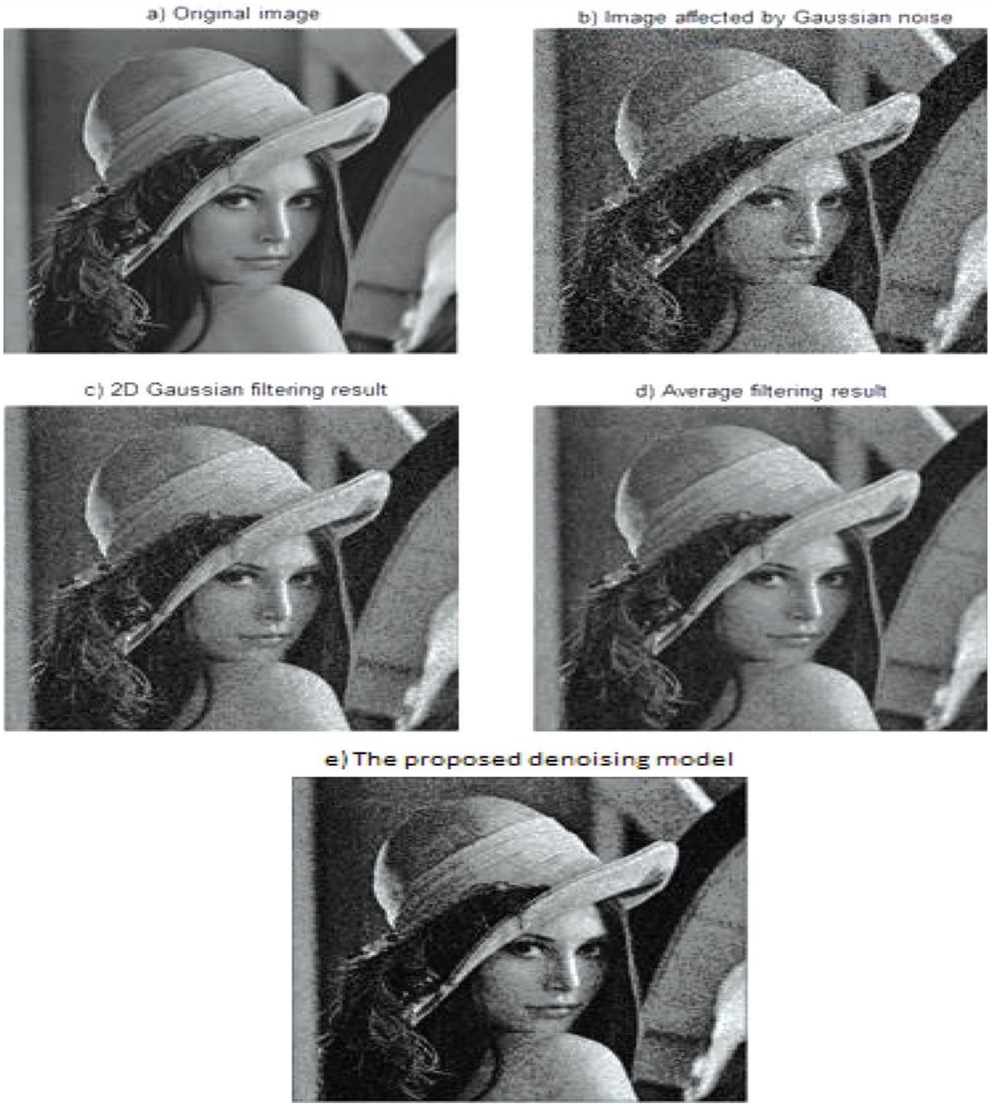

a) Original image

b) Image affected by Gaussian noise

c) 2D Gaussian filtering result

d) Average filtering result

e) The proposed denoising model

Fig. 1.1. The modified Gaussian filter compared with some conventional filters

One can see in Fig. 1.1 the original grayscale *Lena* image (a), the image affected by Gaussian noise characterized by a standard deviation value of 0.5 (b), the smoothing result obtained by a [3 × 3] 2D Gaussian filter kernel (c), the averaging filtering result produced by a [3 × 3] mean filter kernel (d) and, finally, the image filtered by our modified Gaussian model. The improved Gaussian filter substantially increases image quality. It not only removes a greater amount of noise than the classic Gaussian kernel and also provides a better image contrast. Also, this hyperbolic denoising procedure executes very fast, being characterized by a low complexity and computational time [5].

Also, the linear PDE-based model described here can be further transformed into more sophisticated nonlinear diffusion schemes [5]. Such a nonlinear hyperbolic filtering model, which makes the focus of our current research, has the following form:

$$\begin{cases} \alpha \frac{\partial^2 u}{\partial t^2} + \beta^2 \frac{\partial u}{\partial t} - div\left(\psi_u\left(\|\nabla u\|\right) \cdot \nabla u\right) + \lambda\left(u - u_0\right) = 0 \\ u(0, x, y) = u_0(x, y) \\ \frac{\partial u}{\partial t}(0, x, y) = u_1(x, y) \\ u(t, x, y) = 0, \quad \forall t \geq 0, \ (x, y) \in \partial\Omega \end{cases} \quad , \ (x, y) \in \Omega \quad (1.6)$$

Other nonlinear 2nd and 4th order hyperbolic diffusion models derived from (1.3) are also considered. It should be said also that PDE hyperbolic model (1.3) can be used as a filtering technique to extract the coherent and incoherent components of a forced turbulent flow and to identify coherent vortices as in [7]. We expect to give more details in a forthcoming article.

1.2. Nonlinear diffusion based image noise removal approaches

The diffusion equations have proved their usefulness in domains like physics and engineering sciences for a very long time. Since 1980s, these PDEs have played an important role in the image processing and analysis domains [1]. Diffusion equations offer numerous advantages for image denoising and restoration [8]. They are the mathematically best-founded approaches in image pre-processing. Also, they allow a reinterpretation of some classical filtering techniques under a new unifying framework. Thus, the idea of using the diffusion equations in image denoising and restoration arose from the use of the classic Gaussian filter in multiscale image analysis. The convolution of an image with a 2D Gaussian kernel amounts to solve the diffusion equation in two dimensions (*heat equation*).

A diffusion equation having the form $\frac{\partial u}{\partial t} = div\left(C(x, y, t) \cdot \nabla u\right)$ becomes linear if the diffusion tensor *C* does not depend on the evolving image *u* (*t, x, y*). The linear diffusion models are the simplest PDE–based image denoising techniques. The main drawback of the linear PDE denoising algorithms is the blurring effect that can affect image details. The linear diffusion has no localization property and may dislocate image boundaries when moving from finer to coarser scales. The nonlinear diffusion is characterized by a tensor that is a function of the image *u*: $C(x, y, t) = g\left(u(t, x, y)\right)$. The nonlinear diffusion based techniques overcome the blurring and localization problems faced by the linear approaches [8]. They perform the image smoothing along but not across the edges.

1.2.1. Related work

These nonlinear PDE models have been extensively studied since the early work of P. Perona and J. Malik in 1987 [9]. The influential Perona-Malik denoising scheme represents the most popular nonlinear anisotropic diffusion technique. If the diffusion tensor is constant over the entire image domain, one speaks of *isotropic* diffusion, while a space-dependent filtering is called *anisotropic*. The filter proposed by Perona and Malik reduces the diffusivity at those locations having a larger likelihood to represent image edges and is characterized by the following nonlinear diffusion equation:

$$u_t = \frac{\partial u}{\partial t} = div\left(g(\|\nabla u\|^2) \cdot \nabla u\right) \tag{1.7}$$

with the noisy image u_0 as the initial condition. Perona and Malik considered two variants of the monotonous decreasing diffusivity function that controls the blurring intensity, $g:[0,\infty]\rightarrow[0,\infty]$, which are:

$$g(s^2) = e^{-\frac{s^2}{k^2}};\ g(s^2) = \frac{1}{1+\left(\frac{s}{k}\right)^2} \tag{1.8}$$

where parameter $k > 0$ represents the diffusivity conductance [9]. They discretized the PDE model as following:

$$u^{t+1} = u^t + \lambda \cdot \left[c_N^t \cdot \nabla_N u^t + c_S^t \cdot \nabla_S u^t + c_E^t \cdot \nabla_E u^t + c_W^t \cdot \nabla_W u^t\right] \tag{1.9}$$

where

$$\nabla_N u^t = u^t{}_{x-1,y} - u^t{}_{x,y},\ \nabla_S u^t = u^t{}_{x+1,y} - u^t{}_{x,y},\ \nabla_E u^t = u^t{}_{x-1,y+1} - u^t{}_{x,y},\ \nabla_W u^t = u^t{}_{x-1,y} - u^t{}_{x,y} \tag{1.10}$$

and

$$c_N^t = g\left(\left|\nabla_N u^t\right|\right), c_S^t = g\left(\left|\nabla_S u^t\right|\right), c_E^t = g\left(\left|\nabla_E u^t\right|\right), c_W^t = g\left(\left|\nabla_W u^t\right|\right) \tag{1.11}$$

Perona-Malik scheme provides an efficient edge-preserving image smoothing that has been further improved in many nonlinear diffusion based techniques derived from it in the recent years. There are numerous papers that investigate the mathematical properties, the numerical implementations and the possible applications of this denoising framework. The stability of Perona-Malik model has been extensively studied in the last two decades [8,10]. The nonlinear PDE-based techniques inspired by the influential Perona-Malik scheme differ from each other through the diffusivity (edge-stopping) function. The function g has to satisfy some certain conditions, such as positivity, decreasing monotony, g (0) = 1 and convergence to 0.

The total variation (TV) diffusivity, given by $g(s^2) = \frac{1}{|s|}$, and its regularized version $g(s^2) = \frac{1}{\sqrt{s^2 + \varepsilon^2}}$ represent popular edge-stopping functions [11]. Charbonnier et al. proposed the Charbonnier diffusivity [12], that is $g(s^2)=\left(1+\frac{s^2}{k^2}\right)^{-1/2}$, and J. Weickert [8] proposed an anisotropic diffusion model based on edge-stopping function $g(s^2)=\begin{cases}1-e^{-\frac{C_m}{(s^2/k^2)^m}}, & \text{if } |s|>0\\ 1, & \text{if } s=0\end{cases}$, where $1=e^{-C_m}\cdot(1+2C_m\cdot m)$, $m\in\{2,3,4\}$, $C_2=2.3366$, $C_3=2.9183$ and $C_4=3.3148$. Black et al. developed the *robust anisotropic diffusion* (RAD) [13]. They used robust estimation theory to model the diffusivity function called Tukey's biweight: $g(s^2)=\begin{cases}\left(\left(1-\frac{s^2}{5k^2}\right)^2, & \text{if } \frac{s^2}{5}\le k^2\\ 0, & \text{if } \frac{s^2}{5}>k^2\end{cases}\right)^2$.

These nonlinear diffusion techniques may also differ through the way they choose the diffusivity conductance parameter. When the gradient magnitude exceeds the value of *k*, the corresponding boundary is enhanced. Some methods, including the Perona-Malik filter, use a fixed *k* value. Other approaches make this parameter a function of time, *k* (*t*). A high *k* (0) value is considered at the beginning, then *k* (*t*) is reduced gradually, as the image is smoothed. Other approaches detect automatically this parameter as a function of the current state of the evolving image. Various noise estimation methods can be used in the detection process [14]. A solution is to estimate the noise at each iteration as the difference between the averages of images processed by the morphological operations of opening and closing. In this case the conductance parameter is computed as $k=avg(u\circ S)\text{-}\,avg\,(u\bullet S)$, *S* being a structuring element. Another solution is to estimate the noise using the *p*-norm of the image: $k=\frac{\sigma\|u\|_p}{m}$, where *m* is the number of pixels and σ is proportional to the average intensity [14]. Other solutions determine the conductance diffusivity as the *robust scale* of the image, by using statistics like the median [13]: $k=\sigma_e=1.4826\cdot median(u)\|\|\nabla u\|-median(u)\|\nabla u\|\|$.

1.2.2. Novel anisotropic diffusion models for image restoration

We developed a nonlinear anisotropic diffusion-based restoration technique that improves the Perona-Malik denoising scheme and outperforms the other nonlinear PDE based smoothing algorithms [15,16]. It is based on the following PDE parabolic model:

$$\begin{cases}\frac{\partial u}{\partial t}=div\left(g_{K(u)}\left(|\nabla u|^2\right)\cdot\nabla u\right), & (x,y)\in\Omega\\ u(0,x,y)=u_0\end{cases}\qquad(1.12)$$

where u_0 is the initial (noised) state of the image and $\Omega\subset R^2$ represents its domain. The nonlinear diffusion equation provided by (1.12) uses a novel edge-stopping function $g_{K(u)}:[0,\infty)\to[0,\infty)$ that is modeled as following:

$$g_{K(u)}(s^2)=\begin{cases}\alpha\cdot\sqrt{\dfrac{K(u)}{\beta\cdot s^2+\gamma}}, & \text{if}\quad s>0\\ 1, & \text{if}\quad s=0\end{cases}\tag{1.13}$$

where the parameters $\alpha,\beta\in[0.5,0.8]$ and $\gamma\in[0.5,5)$. The function given by (1.13) is based on a conductance diffusivity parameter that depends on the current state of the image. We compute automatically this parameter in [15], on the basis of image noise estimation at each time *t*, as following:

$$K(u)=\frac{median(u)}{\varepsilon\cdot n(u)}\cdot\|u\|_F\quad ,\tag{1.14}$$

where $\varepsilon\in(0,1]$, $\|u\|_F$ is the Frobenius norm of image *u*, *median*(*u*) represents its median value and *n*(*u*) is the number of its pixels.

Then we demonstrate that the proposed diffusivity function is properly modeled, satisfying the conditions required by an edge-stopping function. We have $g_{K(u)}(0)=1$. Also, function $g_{K(u)}$ is always positive, because $\alpha\cdot\sqrt{\dfrac{K(u)}{\beta\cdot s^2+\gamma}}>0,\forall s\in R.$ It is also monotonically decreasing, because $g_{K(u)}(s_1^2)=\alpha\cdot\sqrt{\dfrac{K(u)}{\beta\cdot s_1^2+\gamma}}\le\alpha\cdot\sqrt{\dfrac{K(u)}{\beta\cdot s_2^2+\gamma}}=g_{K(u)}(s_2^2)$, $\forall s_1\ge s_2$, Also, we have $\lim_{s\to\infty}g_{K(u)}(s^2)=0$ [16].

The proposed edge-stopping function has also an important property related to the flux. If one considers the flux function defined as $\phi(s)=s\cdot g_{K(u)}(s^2)$, the image enhancement and edge sharpening process depends on the sign of its derivative, $\phi'(s)$ [17]. Thus, if the derivative of the flux function of a diffusion model is positive ($\phi'(s)>0$), then that model is a forward parabolic equation. Otherwise, for $\phi'(s)<0$, that nonlinear diffusion model represents a backward parabolic equation [15-17]. The derivative of the flux function of our PDE model is computed as following:

$$\phi'(s)=g_{K(u)}(s^2)+2s^2g_{K(u)}'(s^2)=\frac{\alpha\sqrt{K(u)}}{\sqrt{\beta s^2+\gamma}}-\frac{\alpha\sqrt{K(u)s^2}}{\beta s^2+\gamma}\cdot\frac{\beta}{\sqrt{\beta s^2+\gamma}}\tag{1.15}$$

which leads to

$$\phi'(s)=\frac{\alpha\sqrt{K(u)}}{\sqrt{\beta s^2+\gamma}}-\frac{\alpha\sqrt{K(u)s^2}}{\beta s^2+\gamma}\cdot\frac{\beta}{\sqrt{\beta s^2+\gamma}}=\phi'(s)=\frac{\alpha\sqrt{K(u)}}{(\beta s^2+\gamma)^{3/2}}\left[\beta s^2+\gamma-\beta s^2\right]=\frac{\alpha\gamma\sqrt{K(u)}}{(\beta s^2+\gamma)^{3/2}}\tag{1.16}$$

Since $\frac{\alpha\gamma\sqrt{K(u)}}{\left(\beta s^2+\gamma\right)^{3/2}} > 0, \forall s$ one obtains $\phi'(s) > 0$ for any *s*, which means our PDE denoising model is a forward parabolic equation that is stabile and quite likely to have a solution.

We investigated the existence of this solution **in the first selected paper** (see Barbu & Favini [16]), where we provide a rigorous mathematical treatment for our anisotropic diffusion-based model. While, in general, the problem (1.12) is ill-posed, we have proved the existence and uniqueness of a weak solution in a certain case that is related to some values of the model's parameters. We have demonstrated that our nonlinear PDE model converges if $\gamma = \alpha^2$. The following modification of the edge-stopping function has been considered:

$$g_{K(u)}(s^2) = \begin{cases} \alpha\sqrt{\frac{K(u)}{\beta s^2+\gamma}} & \text{if } 0 < s \le M \\ \frac{\alpha}{\sqrt{\gamma}} & \text{if } s = 0 \end{cases} \tag{1.17}$$

where $M > 0$ is arbitarily large but fixed. If the parabolic model (1.12) uses $g_{K(u)}$ given by (1.17) for each $u_0 \in L^2(\Omega)$ (the space of all Lebesgue square integrable functions on Ω) there is a unique weak solution *u* to the PDE problem (see [16]).

The proposed nonlinear anisotropic diffusion model was discretized using a 4-nearest-neighbours discretization of the Laplacian operator. So, from the equation (1.12) one obtains $\frac{\partial u}{\partial t} = div\left(g_{K(u)}\left(\|\nabla u\|^2\right)\nabla u\right) \Rightarrow u(x,y,t+1) - u(x,y,t) \cong g_{K(u)}\left(\|\nabla u\|^2\right)\Delta u + \nabla\left(g_{K(u)}\left(\|\nabla u\|\right)\right)\cdot\nabla u$, which leads to the next numerical approximating scheme:

$$u^{t+1} = u^t + \lambda\sum_{q\in N_p} g_{K(u)}\left(\left|\nabla u_{p,q}(t)\right|\right)^2 \cdot \nabla u_{p,q}(t) \tag{1.18}$$

where $\lambda \in (0,1)$, N_p is the set of pixels representing the 4-neighborhood of the pixel *p* (given by pair of coordinates *x, y*) and $\nabla u_{p,q}(t) = u(q,t) - u(p,t)$ is the image gradient magnitude in a particular direction at iteration *t*. The iterative procedure given by (1.18) is applied on the image for each $t \in \{0, 1, ..., N\}$. The smoothed image u^N is obtained from the noisy image $u^0 = u_0$ in a relatively low number of steps, *N* [16].

Many image enhancement experiments using the described anisotropic diffusion-based technique were performed by us. The proposed denoising technique have been tested on hundreds images corrupted with various levels of Gaussian noise, satisfactory restoration results being obtained. The following parameters of the PDE-based filtering model provided the best results: $\alpha = 0.7, \beta = 0.65, \gamma = 0.5, \varepsilon = 0.3, \lambda = 0.33$ and *N* = 15, respectively. Because we have $\alpha^2 \cong \gamma$, the denoising scheme has a unique solution for these parameters. The iterative scheme converges fast to that solution, the number of iterations, *N*, being quite low. The performance of our restoration method is assessed by using the *norm of the error image* measure, computed as $\sqrt{\sum_{x=1}^{X}\sum_{y=1}^{Y}(u^N(x,y)-u_0(x,y))^2}$ [16].

Method comparisons have been also performed, the performance of our technique being compared with those of the state of the art denoising methods. Our approach performs much better than conventional smoothing methods and linear PDE-based denoising algorithms. Also, the anisotropic diffusion restoration model proposed here outperforms many other nonlinear diffusion-based techniques [15]. It produces better noise filtering results and converges faster than Perona-Malik algorithm and other improved versions of it. Some compared image denoising results are displayed in Fig. 1.2. One can see in this figure the original $[512\times 512]$ *Lena* image, the image corrupted by a Gaussian noise characterized by $\mu = 0.21$ and *var* = 0.02, the image smoothed by our AD method, image denoised by the two versions (diffusivity functions) of the Perona-Malik framework, and the filtering results produced by the $[3\times 3]$ 2D Gaussian, average, median and Wiener kernels.

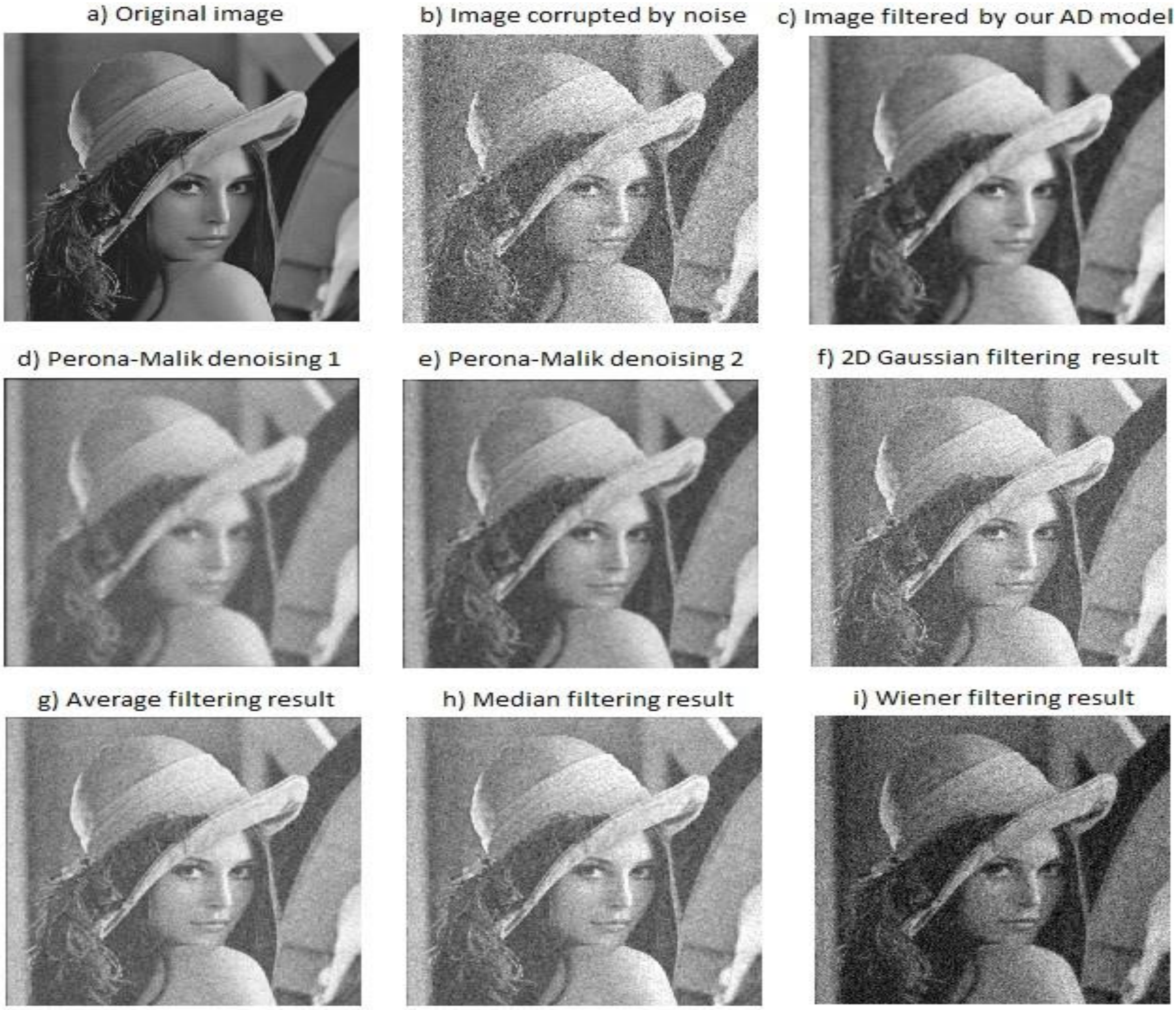
a) Original image
b) Image corrupted by noise
c) Image filtered by our AD model
d) Perona-Malik denoising 1
e) Perona-Malik denoising 2
f) 2D Gaussian filtering result
g) Average filtering result
h) Median filtering result
i) Wiener filtering result

Fig. 1.2. Noised image filtered with various denoising techniques

Table 1.1. Norm-of-the-error image values for several denoising algorithms

Our AD	P-M 1	P-M 2	Gaussian	Average	Median	Wiener
5.1×10^3	6.1×10^3	5.9×10^3	7.3×10^3	6.4×10^3	6×10^3	5.8×10^3

Obviously, the best denoising result was produced by our model (c). The corresponding norm of the error image values are registered in Table 1.1. The minimum NE value, representing the best smoothing, corresponds to the AD approach described here. Our nonlinear PDE-based restoration approach not only removes a high amount of image noise, but also preserves the boundaries very well. Its edge-preserving character is also obvious from the above figure.

We have also investigated other edge-stopping functions, besides (1.13) and (1.17), and achieved effective anisotropic diffusion schemes. A newly developed PDE restoration model is

$$\begin{cases} \frac{\partial u}{\partial t} = div\left(\psi_{K(u)}\left(\|\nabla u\|\right)\nabla u\right) - \lambda(u-u_0) \\ u(0,x,y) = u_0 \end{cases} \tag{1.19}$$

where $K(u) = \delta \cdot \mu\left(\|\nabla u\|\right) + r \cdot ord(u)$, *ord* () = order in evolving sequence, $\delta \in (2,3)$, $r \in (0,1)$ and

$$\psi_{K(u)}(s) = \begin{cases} \dfrac{\xi}{\left(s/K(u)\right)^2 + K(u)\left|\log_{10}\left(s/K(u)\right)\right|}, \forall\, s > 0 \\ 1, \qquad \text{for } s = 0 \end{cases}, \xi \in (1,8), \tag{1.20}$$

its image denoising results being disseminated in a paper under consideration (not yet published).

1.2.3. Image denoising approach based on diffusion porous media flow

We also designed a nonlinear filter for image noise removal based on the diffusion flow generated by the porous media equation [18]. The proposed nonlinear diffusion-based restoration model provides a robust edge-preserving smoothing, while also removing the staircasing effect. It has the following form:

$$\begin{cases} \frac{\partial u}{\partial t}(t,x) - \Delta\beta(u(t,x)) = 0, \text{in } (0,\infty)\times\Omega \\ \beta(u(t,x)) = 0, (0,\infty)\times\partial\Omega \end{cases} \tag{1.21}$$

where $u(0,x) = u_0$, $\mathbf{\Omega}$ represents a bounded domain of R^2 with a sufficiently smooth boundary $\partial\mathbf{\Omega}$ and $\beta : R \to R$ is monotonically increasing, $\beta(0) = 0$ and $\lim\limits_{r\to\pm\infty}\beta(r) = \pm\infty$.

We demonstrate in [18] that PDE model (1.21) has a unique strong solution $u:[0,\infty)\to H^{-1}(\Omega)$ that is given by the exponential formula $u(t) = \lim\left(I + \frac{t}{n}A\right)^{-n} u$, where the nonlinear operator $A\colon D(A) \subset H^{-1}(\Omega) \to H^{-1}(\Omega)$ is defined by the following equation:

$$Au = -\Delta\beta(u), \quad \forall u \in D(A) \tag{1.22}$$

with $D(A)=\left\{u\in L^1(\Omega);\beta(u)\in H_0^1(\Omega)\right\}$. In particular, (1.22) amounts to saying that the implicit finite difference scheme $u_{k+1}+hAu_{k+1}=u_k$, $u_0=g$, $k=0,1,...$, where $k=\left[\frac{t}{h}\right]$, is convergent to $u(t)$. A rigorous mathematical investigation of the existence, uniqueness and strength of this PDE model's solution is provided in our 2013 article (see [18]).

One then determines the explicit version of the implicit scheme. The next iterative finite-difference based explicit numerical approximation model is obtained:

$$\begin{cases} u_{i,j}^{k+1} = u_{i,j}^{k} + \lambda\cdot\left(\left(u_{i+1,j}^{k-1}\right)^{\frac{1}{\alpha}} + \left(u_{i-1,j}^{k-1}\right)^{\frac{1}{\alpha}} + \left(u_{i,j-1}^{k-1}\right)^{\frac{1}{\alpha}} + \left(u_{i,j+1}^{k-1}\right)^{\frac{1}{\alpha}} - 4\left(u_{i,j}^{k-1}\right)^{\frac{1}{\alpha}}\right) \\ u_{i,j}^{0} = u_0(i,j), \forall i,j \end{cases} \tag{1.23}$$

where k = 1,…,K. The initial degraded image is successfully filtered in K steps by using the iterative scheme (1.23) with some properly selected parameters, α and λ. The resulted u^K represents the final image denoising result.

A proper selection of the parameter values is quite important and cannot be a priori defined. The selection of K in our simulation was dictated by the many experiments performed in specific examples. It turns out the selection of a high number of iterations, for example $K > 40$ value, could produce a blurring effect on the processed image, while using a low K value, such as $K < 5$, may provide an unsatisfactory image smoothing result. Also, a great K value increases the computational complexity of this image filtering process, producing a much higher computation time. Also, using a large enough λ value, such as $\lambda > 5$, could increase the image degradation. A very small λ parameter, like $\lambda < 0.1$, produces no visible restoration results. The parameter α must satisfy the condition $\frac{1}{\alpha}\in(0,1)$, for an efficient noise removal.

Our diffusion porous media flow based denoising algorithm was compared with other well-known nonlinear diffusion schemes. In [18] we performed mathematically supported method comparisons with the Perona-Malik framework, the PDE denoising model developed by Kacur and Mikula [19], and the total variation model [11]. In order to perform these comparisons we transformed our nonlinear diffusion model into an equivalent variational model, given by this minimization problem:

$$u_\infty = \arg\min\left\{\int_\Omega \eta(u(x)dx + \frac{\lambda}{2}\left\|u-u_0\right\|_{H^{-1}(\Omega)}^2\right\} \tag{1.24}$$

where $u\in L^1(\Omega)\cap H^{-1}(\Omega)$ and η is the potential function corresponding to the nonlinear diffusivity function $\beta : R \rightarrow R$.

Thus, the function $u\rightarrow\left\|u-u_0\right\|_{H^{-1}(\Omega)}^2$ represents a penalty term that forces the restored image $u=u(x)$ to stay close to the initial image. The fact that the distance from u to u_0 is taken in the norm $\|\cdot\|_{H^{-1}(\Omega)}$ that is considerably weaker than the $L^2(\Omega)$- norm used by the Perona-Malik scheme, as well as the most diffusion techniques, has the advantage that it allows to work with very degraded initial images that practically are not represented by Lebesgue integrable functions but by distributions. However, it should be said that our model has a considerable better denoising effect than Perona & Malik algorithm. Also, it outperforms the Kacur-Mikula image restoration scheme that is based on a boundary value problem which converges to a weak solution (see [19]). The present PDE technique is also more convenient that the total variation model [11], that is constructed in a non-energetic space (the space of functions with bounded variation) and so difficult to treat from the computational point of view. As a matter of fact, by regularization necessary to construct a viable numerical scheme, the TV model loses most of the theoretical advantages regarding the sharp edge detection and elimination of the *staircasing* effect [20]. The staircasing effect, representing creation in the image of flat regions separated by artifact boundaries [20], is common in denoising procedures with high smoothing effect. Unlike other nonlinear diffusion based techniques, like Perona-Malik and its versions, this restoration approach succeeds in removing this staircase effect, this fact representing another important advantage of our PDE model.

The diffusion porous media flow based denoising method described here was tested on various image datasets, satisfactory filtering results being obtained. Hundreds of grayscale images affected by various levels of Gaussian noise were filtered by using the presented approach. The optimal noise reduction results were achieved using the following set of parameters of the diffusion model: $\alpha = 2$, corresponding to the physical model of diffusion in plasma, $\lambda = 1.5$ and N = 20. One can see the image smoothing example based on these parameter values that is displayed in Fig. 1.3. As we have already mentioned, numerous method comparisons were also performed, the denoising results of our technique being compared against the results obtained by other nonlinear diffusion based methods. Obviously, the proposed PDE model outperforms not only both versions of the Perona-Malik method, but also some well-known conventional filters, such as 2D Gaussian filter and the averaging filter.

So, the standard $[512 \times 512]$ image of *Lena* is displayed in the grayscale form in Fig. 1.3 (a). Its version corrupted by an amount of Gaussian noise characterized by parameters 0.2 (mean) and 0.02 (variance), is depicted in Fig. 1.3 (b). In Fig. 1.3 (c) there is displayed the image smoothing result produced by the classic $[3 \times 3]$ Gaussian 2D filter kernel, while the noise reduction obtained by the $[3 \times 3]$ averaging filter kernel is represented in Fig. 1.3 (d). The noise removal achieved by the Perona-Malik scheme is displayed in Fig. 1.3 (e), while the denoising result provided by our nonlinear PDE model is represented in Fig. 1.3 (f). One can observe in these figures the better smoothing effect of our approach, its edge-preservation character and the efficient removing of the staircasing effect.

The norm of the error image is also computed here, in order to assess the performance levels of each denoising approach. These NE values corresponding to all these image filtering techniques are registered in the next table. As one can see in Table 1.2, the porous media equation based smoothing technique developed by us outperforms all the other image filters, minimizing the respective error (see the lowest value, 5.15×10^3). Also, our denoising algoritm executes quite fast, given its low time complexity. The values of the *Peak Signal-to-Noise Ratio* (PSNR) measure [2,3] were also computed to asses the method performance and gave us the same conclusion.

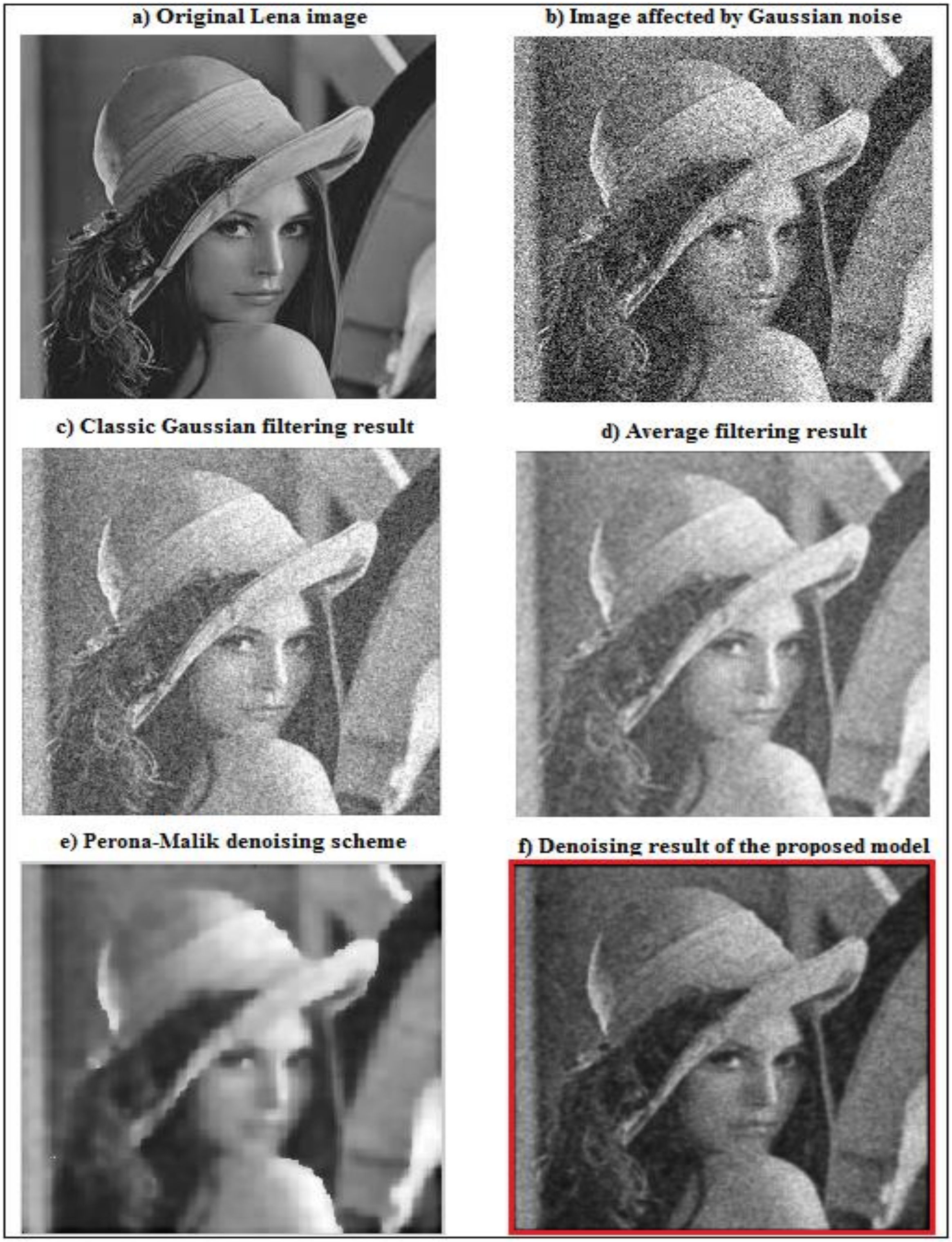
a) Original Lena image
b) Image affected by Gaussian noise
c) Classic Gaussian filtering result
d) Average filtering result
e) Perona-Malik denoising scheme
f) Denoising result of the proposed model

Fig. 1.3. Gaussian noise removal results of our model compared with those of other methods

Table 1.2. Values of norm of the error image parameter for several noise removal approaches

Denoising technique	Gaussian Filter	Average Filter	Perona-Malik filter	Proposed filter
Norm of the error	6.40×10^3	6.05×10^3	6.84×10^3	5.35×10^3

1.2.4. Fourth order diffusion models for image noise reduction

The fourth order PDE models are more effective at staircasing effect removing during the image smoothing process than the second-order PDEs. The most popular fourth-order PDE restoration scheme is the nonlinear isotropic diffusion method proposed by Y. L. You and M. Kaveh in 2000.

Also, the static and video images, especially those based on ultrasounds, are often affected by *speckle noise*, which represents a multiplicative noise that is locally correlated and prevents a proper feature extraction and analysis from the affected images. In recent years numerous speckle denoising techniques have been developed. The most important are the Frost filtering [21], that replaces the pixel of interest with the weighted sum of the values in a moving kernel, the Discrete Wavelet Transform based approaches, using complex DWT - 2D and DWT - 3D [22], and the fourth-order PDE based smoothing techniques derived from You-Kaveh [23].

We developed an effective nonlinear diffusion-based method for removing both the Gaussian and speckle noise from images and video sequences. This image denoising approach proposed in [24] is based on the following fourth-order PDE model:

$$\frac{\partial u}{\partial t} + \Delta(\psi(\Delta u)\Delta u) = 0 \tag{1.25}$$

where the Laplacian $\Delta u = \nabla^2 u$ and ψ represents a diffusivity function modelled as following:

$$\psi(s) = \frac{s}{s^2 + k} \tag{1.26}$$

where $k > 0$ represents a chosen constant. Obviously, this function ψ is monotone decreasing and converges to 0. Thus, it satisfies the main conditions of a noise filtering function [23]:

$$\begin{cases} \lim\limits_{s \to \infty} \psi(s) = 0 \\ \psi(0) = 0 \end{cases} \tag{1.27}$$

In our 2011 paper one demonstrates rigorously the well-posedness of the problem (1.25) [24]. Thus, we prove that this problem is indeed well posed if the function $u \to \psi(u)u \equiv g(u)$ is continuous and monotonically nondecreasing (see [24] for more).

Then we perform a robust discretization of the proposed PDE-based model [24]. We set $d_{k,j} = \psi(\Delta_{k,j}u)\Delta_{k,j}u$, where $\Delta_{k,j}u$ is a finite-difference based discretization of Δu , and obtain the following iterative approximation scheme for the differential model:

$$u_{k,j}^{i+1} = u_{k,j}^{i} + \left[d_{k+1,j}^{i} + d_{k-1,j}^{i} + d_{k,j+1}^{i} + d_{k,j-1}^{i} - 4d_{k,j}^{i}\right], \tag{1.28}$$

where $i = 1,2,...,n.$ We also impose some boundary value conditions of zero flux boundary type, which have the following form for an $[M \times N]$ image:

$$\begin{cases} u_{N+1,j} = u_{N,j}, u_{-1,j} = u_{0,j}, j = 0,...,M \\ u_{k,-1} = u_{k,0}, u_{k,M+1} = u_{k,M}, k = 0,...,N \end{cases} \tag{1.29}$$

A lot of noise removal experiments using the proposed PDE based technique have been conducted, satisfactory results being achieved. The iterative scheme (1.28) has been successfully applied on hundreds sonar images and video frames affected by noise. That image noise has been substantially reduced by our PDE filter, as one can see in the next example.

In Fig. 1.4 there is displayed a video frame from a radar movie, depicting a military vehicle moving on a battlefield, which is seriously affected by Gaussian and speckle noise. The denoising result is displayed in Fig. 1.5. The object of interest, that vehicle, can be more easily visualized and detected in the second figure.

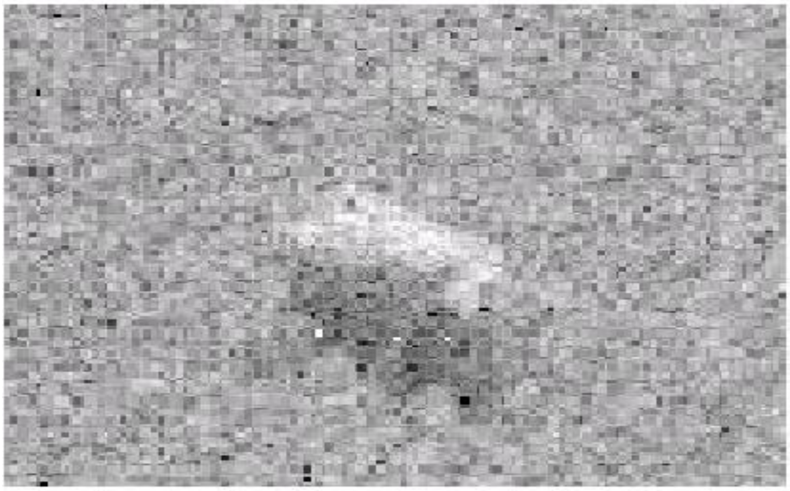

.

Fig. 1.4. Ultrasound frame affected by speckle noise

From the performed method comparison we have found that our PDE-based filtering model outperforms many other image denoising approaches. Our technique provides much better speckle noise reduction results than Frost filters [21] or 2D conventional filters. Also it performs better at staircase effect removal than 2nd-order PDE methods, although it still suffers from the blurring effect. So, we are trying to improve the class of 4th-order PDE models given by (1.25), by proposing new versions for function ψ that would lead to a better deblurring. We have achieved encouraging denoising results by modelling $\psi(s)$ as in (1.13), (1.17) or (1.20) and also by combining 2nd and 4th order diffusions, which are disseminated in some articles yet to appear.

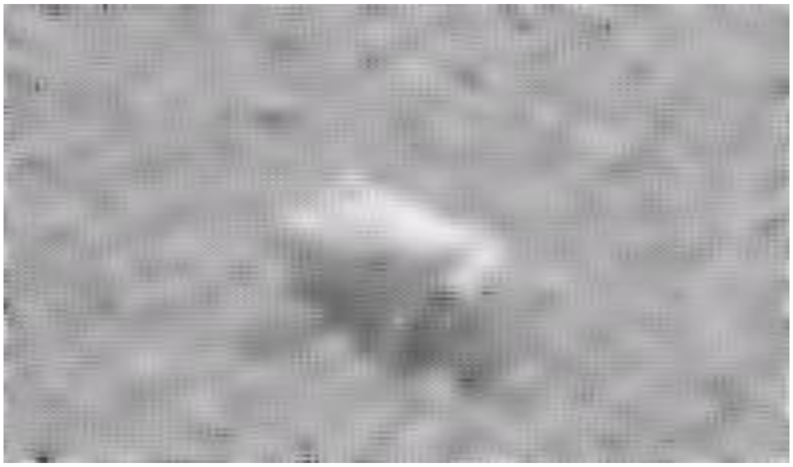

Fig. 1.5. The image denoising result

1.3. Variational PDE techniques for image denoising and restoration

The variational approaches have important advantages in both theory and computation, compared with other techniques. They can achieve high speed, accuracy and stability using the extensive results of the numerical PDE algorithms. Variational PDE methods represent useful tools for solving various image processing and analysis tasks, one of them being the image denoising.

Each variational denoising technique is based on a minimization of an energy functional composed of a data component and a smoothing term. The variational denoising and restoration approaches differ with regard to the modeling of these components.

An influential variational image smoothing model was developed by Rudin, Osher and Fetami in 1992 [25]. Their filtering technique, named Total Variation (TV) denoising, is based on the minimization of the TV norm. TV denoising is remarkably effective at simultaneously preserving image edges whilst smoothing away noise in flat regions, but it also suffers from the staircasing effect and its corresponding Euler-Lagrange equation is highly nonlinear and difficult to compute [25]. In the last two decades, numerous PDE techniques which improve this classical variational scheme have been proposed [26]. We developed two variational models that provide an efficient noise reduction while eliminating the staircasing effect [27,28]. The proposed techniques are described in the next subsections.

1.3.1. A robust variational PDE model for image denoising

The general variational framework used for image denoising and restoration is based on the following the energy functional:

$$E[u] = \int_{\Omega} (u-u_0)^2 + \alpha\psi\left(\|\nabla u\|^2\right), \quad \alpha > 0 \tag{1.30}$$

where the function ψ is the regularizer, or penalizer, of the smoothing term and α represents the regularization parameter or smoothness weight [29].

We modeled a robust smoothing component, based on a novel penalizer function and a proper value of the smoothness weight [27]. Thus, we consider in [27] the following regularizer, $\psi : [0,\infty) \to [0,\infty)$:

$$\psi(s) = \eta\sqrt{\frac{k}{\beta}}\ln\left(s + \sqrt{s^2 + \frac{\gamma}{\beta}}\right) + \nu \cdot s; \quad k > 0, \eta, \beta, \gamma, \nu \in (0,1) \tag{1.31}$$

We use some proper values for the penalizer's parameters. Then, we compute a minimizer for the energy functional given by (1.30), using the function provided by (1.31):

$$u_{\min} = \arg\min_{u \in U} E(u) = \arg\min_{u \in U} \int_{\Omega} (u-u_0)^2 + \alpha\psi\left(\|\nabla u\|^2\right) dxdy \tag{1.32}$$

The minimization result $u_{\min}$ represents the restored image. The minimization process is performed by solving the next Euler-Lagrange equation [26,29,30]:

$$u - u_0 - \alpha div\left(\psi'\left(\|\nabla u\|^2\right)\nabla u\right) = 0 \Leftrightarrow \frac{u - u_0}{\alpha} - div\left(\psi'\left(\|\nabla u\|^2\right)\nabla u\right) = 0 \qquad (1.33)$$

This leads to the following PDE equation:

$$\frac{\partial u}{\partial t} = div\left(\psi'\left(\|\nabla u\|^2\right)\nabla u\right) - \frac{u - u_0}{\alpha} \qquad (1.34)$$

where the positive function ψ' is obtained by computing the derivative of the function given by (1.31):

$$\psi'\left(s^2\right) = \frac{\nu\sqrt{\beta s^2 + \gamma} + \eta\sqrt{k}}{\sqrt{\beta s^2 + \gamma}} \qquad (1.35)$$

So, the partial differential equation (1.34) becomes

$$\begin{cases} \dfrac{\partial u}{\partial t} = div\left(\dfrac{\eta\sqrt{\beta\|\nabla u\|^2 + \gamma} + \alpha\sqrt{k}}{\sqrt{\beta\|\nabla u\|^2 + \gamma}} \cdot \nabla u\right) - \dfrac{u - u_0}{\alpha} \\ \\ u(0, x, y) = u_0 \end{cases} \qquad (1.36)$$

One can demonstrate the PDE model given by (1.36) converges to a unique strong solution, that is $u^* = u_{\min}$. In [27] we propose a robust discretization scheme for solving it. The numerical approximation of our PDE model uses a 4-NN discretization of the Laplacian operator [27]. So, from (1.34) we obtain:

$$u(x, y, t+1) \cong u(x, y, t) + div\left(\psi'\left(\|\nabla u\|^2\right)\nabla u\right) - \frac{u - u_0}{\alpha} \qquad (1.37)$$

that leads to

$$u^{t+1} = u^t + \lambda \sum_{q \in N(p)} \psi'\left(\|\nabla u_{p,q}(t)\|^2\right)\nabla u_{p,q}(t) - \frac{u - u_0}{\alpha} \qquad (1.38)$$

where $\lambda \in (0, 1)$, t =1, …,N, $N(p) = \{(x-1, y), (x+1, y), (x, y-1), (x, y+1)\}$, p = (x, y) and $\nabla u_{p,q}(t) = u(q, t) - u(p, t)$.

The variational PDE model developed by us converges fast to the solution $u^N \cong u_{\min}$, the parameter N taking quite low values. The effectiveness of the proposed denoising technique and its numerical approximation is proved by the satisfactory image smoothing results obtained from our experiments [27].

Other numerical approximation schemes can also be applied to the continuous model (1.36). We have tested successfully some discretization solutions based on finite-difference method, which provide a more mathematically correct approximation of the $div\left(\psi'\left(\|\nabla u\|^2\right)\nabla u\right)$ component, but also lead to somewhat weaker restoration results.

Thus, the described variational approach has been successfully applied on hundreds of images corrupted with various level of Gaussian noise (various mean and variance values). The algorithm is applied with some properly chosen parameters providing optimal results: $\alpha = 9, k = 25, \eta = 0.7, \beta = 0.66, \gamma = 0.5, \nu = 0.2, \lambda = 0.3, N = 15$.

From the performed method comparison we have found that our method outperforms many other noise reduction algorithms. Our approach achieves considerably better edge-preserving denoising results than non-PDE filters, such as the average, Gaussian, or median filters. It also obtains a better restoration and converges faster than other PDE variational schemes, like the quadratic variational model, characterized by a regularizer $\psi\left(s^2\right) = s^2$, or the Perona-Malik variational scheme, given by $\psi\left(s^2\right) = \lambda^2\left(\log\left(1 + \frac{s^2}{\lambda^2}\right)\right)$ [29]. The proposed model also outperforms the well-known TV denoising algorithm [25], because it removes the staircasing effect.

Some image denoising results and method comparison are described in the next figure and table. In Fig. 1.6, there are displayed: a) the original $[512 \times 512]$ *Baboon* image; b) the image corrupted with Gaussian noise given by $\mu = 0.211$ and *var* = 0.023; c) the image restored using the described variational model; d) the quadratic denoising; e) the Perona-Malik noise reduction; f) – i) the image denoising results achieved by the 2D Gaussian, average, median and Wiener 2D $[3 \times 3]$ filter kernels. Obviously, the image in c), corresponding to our variational approach, represents the best smoothing result [27].

The corresponding norm of the error values are displayed in Table 1.3. One can see in the following table that the minimum NE value, 5×10^3, corresponds also to our PDE variational scheme. More image denoising results obtained from our tests are provided in my 2013 paper (see [27]).

Table 1.3. Norm-of-the-error values for some noise removal techniques

Our algorithm	Quadratic	Perona-Malik	2D Gaussian	Average	Median	Wiener 2D
5×10^3	6×10^3	5.9×10^3	7.3×10^3	6.5×10^3	6.1×10^3	5.8×10^3

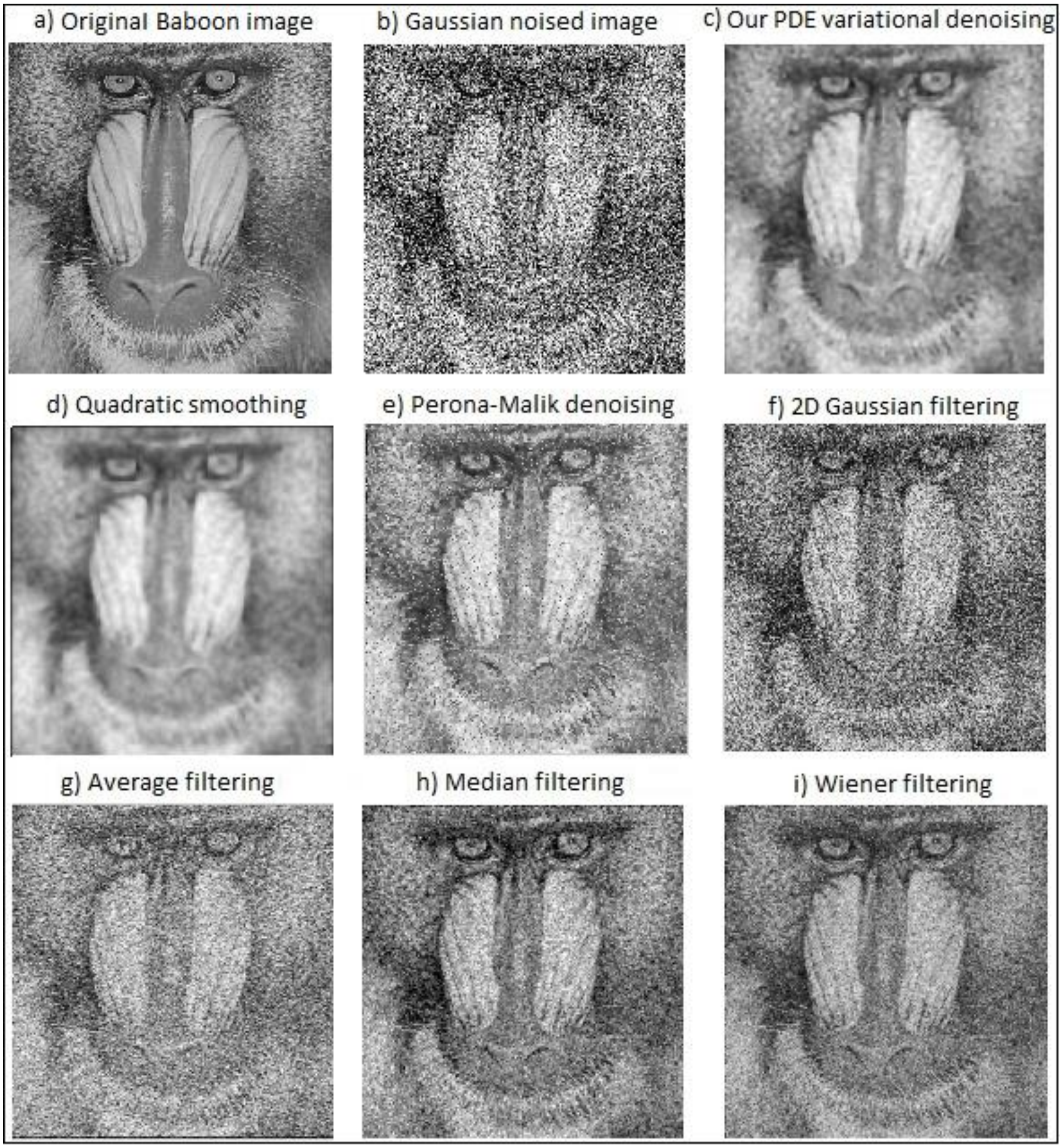

Fig. 1.6. The *Baboon* image smoothed using various denoising techniques

1.3.2. Variational image restoration approach

Another variational image denosing and restoration technique developed by us is described in [28]. It is based on the minimization of a convex energy functional of gradient under minimal growth conditions. This PDE-based approach is related to minimization in bounded variation norm and has a smoothing effect on the degraded image while preserving the edges and other features very well [28]. Thus, we considered there the following minimization problem to be solved:

$$u_{\min} = \underset{u \in X(\Omega)}{\arg\min} \left\{ \frac{1}{2} \int_{\Omega} (u(x) - u_0(x))^2 + \int_{\Omega} \psi\left(\left\| \nabla u(x) \right\|^2 \right) \right\} dx \tag{1.39}$$

where u_0 is the initial image, affected by noise. In order for the minimization problem to be well posed one assumes that ψ is convex and lower semicontinous and $X(\Omega)$ must be taken, in general, as a distribution space on Ω. The following regularizer function is considered for this PDE variational model: $\psi(s) = |s_1| \cdot \log(|s_1| + 1) + |s_2| \cdot \log(|s_2| + 1), s = (s_1, s_2)$. The minimization problem is then associated with a boundary value problem having the following form:

$$\begin{Bmatrix} u - div_x \beta = u_0, \text{in } \Omega \\ (\beta(\nabla u), \nu) = 0, \text{ on } \partial\Omega \end{Bmatrix} \tag{1.40}$$

where β represents the subdifferential of ψ. In [28] we demonstrate that the PDE variational problem (1.39) has a unique minimizer that represents the weak solution to the boundary value problem (1.40).

A numerical approximation based on the discretization of the variational PDE model is then provided (see [28] for more). Thus, we obtain the following explicit finite difference scheme:

$$u_{i,j}^{n+1} = kb_{ij}^n u_{i+1,j}^n + \left(1 - k - 2kb_{ij}^n - 2kd_{ij}^n\right) u_{i,j}^n + kb_{ij}^n u_{i-1,j}^n + kd_{ij}^n u_{i,j-1}^n + kd_{ij}^n u_{i,j+1}^n + ku_{ij}^0 \tag{1.41}$$

where

$$b_{i,j}^n = B(u_{i+1,j}^n - u_{i-1,j}^n), d_{i,j}^n = B(u_{i,j+1}^n - u_{i-1,j}^n) \tag{1.42}$$

with

$$B(u) = \frac{|u| + 2}{(|u| + 1)^2} \tag{1.43}$$

This explicit approximation scheme is stable and convergent for $k \le 0.5$ [28]. The iterative algorithm that applies the scheme on the evolving image for n = 1, 2, … , N, produces an efficient smoothing u^N of the initial noisy image $u^0 = u_0$ in a relatively low number of iterations, N.

The proposed variational approach has been tested on numerous images affected by Gaussian noise, these experiments proving its restoration effectiveness. Method comparisons have been also performed and we have found that our technique outperforms the most conventional denoising filters, such as Gaussian, Laplacian, Laplacian of Gaussian (LoG), Wiener adaptive filter, average, and median filter. Some color image denoising results are displayed in Fig. 1.7. One can see that our PDE approach provides a better noise reduction than average, median and Wiener filters and also corresponds to the minimum error (NE) value.

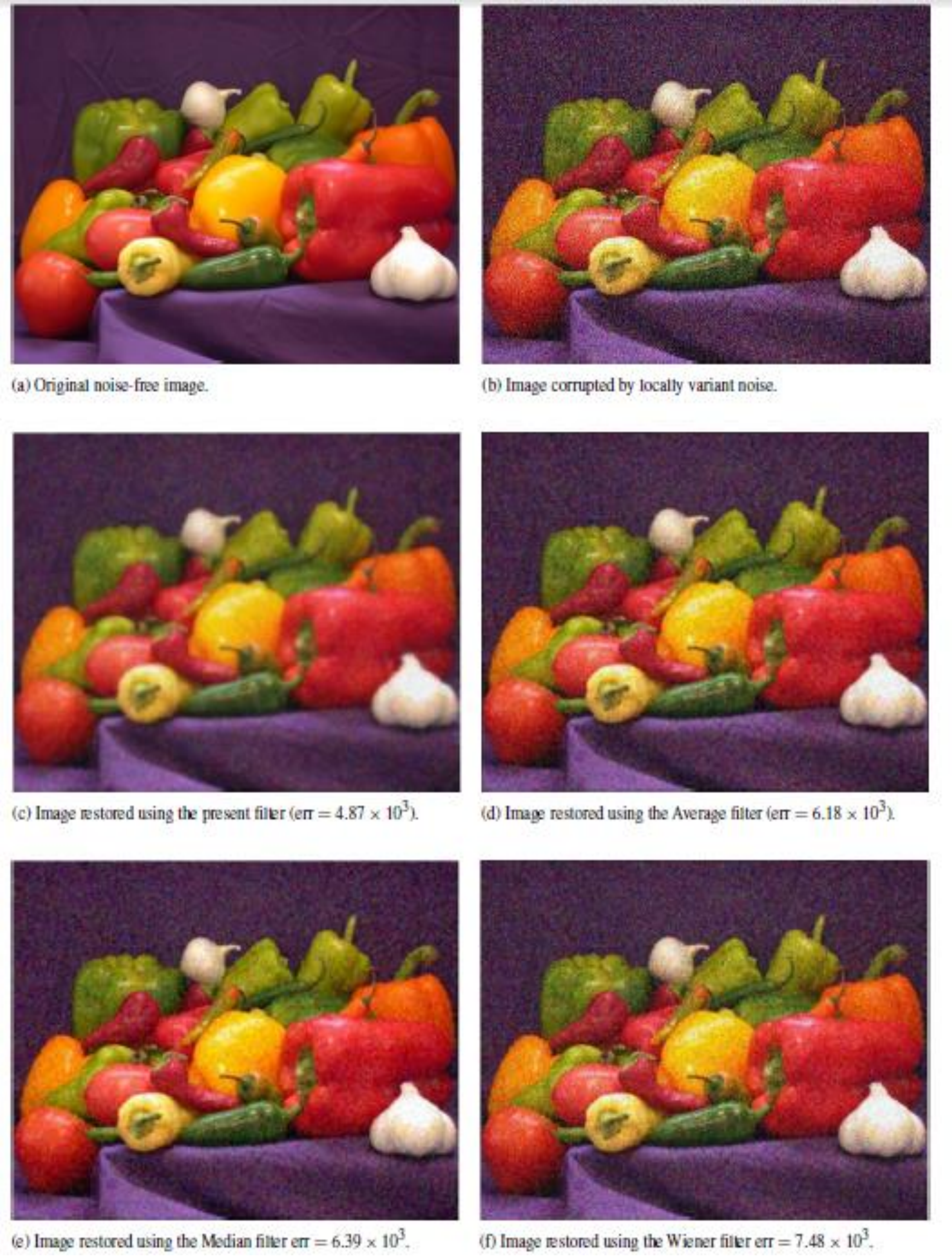

(a) Original noise-free image.

(b) Image corrupted by locally variant noise.

(c) Image restored using the present filter (err = 4.87×10^3).

(d) Image restored using the Average filter (err = 6.18×10^3).

(e) Image restored using the Median filter err = 6.39×10^3.

(f) Image restored using the Wiener filter err = 7.48×10^3.

Fig. 1.7. Method comparison: restoration results obtained by various image filters

1.4. Mathematical models for media feature vector classifiers and metrics

If in the previous sections we described several mathematical models related to image processing, herein we present some machine learning models related to image, and generally media, analysis. As one will see in future chapters, digital media analysis consists of the extraction of meaningful information from media objects, such as images, videos and sounds, and produces *feature vectors* that describe the content of these objects.

The feature vectors are very useful in some important media analysis processes like recognition, segmentation or tracking. These analysis procedures work with distance values, therefore they require proper metrics to measure the distances between these feature vectors. The conventional metrics, such as the well-known Euclidian distance, cannot always be used, because the media feature vectors can be computed in various forms, depending on the featured object and the intended analysis goal. These feature vectors could often represent complex structures and not common vectors or matrices. Even if they represent common vectors (1D, 2D, 3D), their dimensions may differ, therefore the distance between them cannot be computed using conventional metrics.

For this reason, we have introduced some special metrics for certain media feature vectors. Their mathematical models are described in the next two subsections. The proposed metrics were used by various classifiers modeled by us. Any media pattern recognition process consists of a feature extraction operation and a classification of the resulted media feature vectors. We developed both supervised and unsupervised media feature vector classifiers during our research activity. Some supervised recognition (classification) techniques will be presented in the next chapters. Several automatic unsupervised classification models are described in the last two subsections.

1.4.1. A Hausdorff-derived metric for different-sized 2D feature vectors

Some important media analysis tasks approached by us require computing distances between different-sized two-dimension feature vectors that have one equal dimension. As we will see in the next chapter, the vocal recognition techniques described there use 2D speech feature vectors of this type (see **selected paper 2** in [31]). We also developed a reputation system based on an automatic web community user recognition approach that models feature sets containing vectors having only one equal dimension [32].

To measure distances between such feature vectors, we proposed in [31] a special metric working properly for matrices having at least one equal size, that was further investigated in next papers [32,33]. It is derived from the Hausdorff-Pompeiu metric for sets [34]. If X and Y are two compact subsets of a metric space M, the Hausdorff-Pompeiu distance between them, $d_H(X,Y)$, is defined as the minimal number r such that the closed r-neighborhood of any x in X contains at least one point y of Y and vice versa. So, if $dist(x, y)$ denotes the distance in M, then the Hausdorff-Pompeiu metric is computed as follows:

$$d_H(X,Y) = \max\{\sup_{x \in X} \inf_{y \in Y} dist(x,y), \sup_{y \in Y} \inf_{x \in X} dist(x,y)\} \tag{1.44}$$

We have derived this metric, considering 2D feature vectors instead of sets [31-33]. Thus, we represent the two feature vectors to be compared as two matrices having the same number of rows: $A=(a_{ij})_{n\times m}$ and $B=(b_{ij})_{n\times p}$. Two more helping vectors are introduced: $y=(y_i)_{p\times 1}$ and $z=(z_i)_{m\times 1}$, then, $\|y\|_p=\max\limits_{0\le i\le p}|y_i|$ and $\|z\|_m=\max\limits_{0\le i\le m}|z_i|$ are computed. With these notations we created a new metric *d* having the following form:

$$d(A,B)=\max\left\{\sup_{\|y\|_p\le 1}\inf_{\|z\|_m\le 1}\|By-Az\|,\sup_{\|z\|_m\le 1}\inf_{\|y\|_p\le 1}\|By-Az\|\right\} \tag{1.45}$$

This restriction based metric represents the Hausdorff-Pompeiu distance between the sets $B(y:\|y\|_p\le 1)$ and $A(z:\|z\|_m\le 1)$ in the metric space *R*^{n}, so, it can be written as:

$$d(A,B)=d_H(B(y:\|y\|_p\le 1),A(z:\|z\|_m\le 1)) \tag{1.46}$$

From $By-Az=\sum_{k=1}^{p}b_{ik}y_k-\sum_{j=1}^{m}a_{ij}z_j$, one gets $\|By-Az\|_n=\max\limits_{1\le i\le n}\left|\sum_{k=1}^{p}b_{ik}y_k-\sum_{j=1}^{m}a_{ij}z_j\right|$, which leads to:

$$\sup_{\|y\|_p\le 1}\inf_{\|z\|_m\le 1}\|By-Az\|_n=\sup_{\|y\|_p\le 1}\inf_{\|z\|_m\le 1}\max_{1\le i\le n}\left|\sum_{k=1}^{p}b_{ik}y_k-\sum_{j=1}^{m}a_{ij}z_j\right| \tag{1.47}$$

This can be seen as a *max min* optimization problem and according to the classical J. von Neumann min max theorem [35] we have:

$$\sup_{\|y\|_p\le 1}\inf_{\|z\|_m\le 1}\|By-Az\|_n=\inf_{\|z\|_m\le 1}\sup_{\|y\|_p\le 1}\|By-Az\|_n \tag{1.48}$$

Moreover, the saddle point (y_0,z_0) of this problem could be computed by solving the next system:

$$\begin{cases}\nabla_z\left(\|By-Az\|_n\right)+\eta_1=0\\ \nabla_y\left(\|By-Az\|_n\right)+\eta_2=0\end{cases},\quad(\eta_1,\eta_2)\in N(y,z) \tag{1.49}$$

where $N(y,z)$ is the normal cone to the set $\{y;\|y\|_p\le 1\}\times\{z;\|z\|_m\le 1\}$ and which can be expressed in terms of the Lagrange multipliers. Finally, $\{\nabla_y,\nabla_z\}$ represent gradients taken in generalized sense of convex analysis (see [36]). However, since (1.48) is hard to compute for large dimensions of *A* and *B* we replace it by a simpler one. So, the set $\{y\mid\|y\|_p\le 1\}$ is replaced with $F = \left\{ \underbrace{\{1,0,...,0\},\{0,1,...,0\},...,\{0,0,...,1\}}_{p\text{ components}} \right\}$ and the set $\{z \mid \|z\|_m \leq 1\}$ with $G = \left\{ \underbrace{\{1,0,...,0\},\{0,1,...,0\},...,\{0,0,...,1\}}_{m\text{ components}} \right\}$ [36]. Thus, we may take:

$$\sup_{y\in F} \inf_{z\in G} \|By - Az\|_n = \sup_{1\leq k\leq p} \inf_{1\leq j\leq m} \sup_{1\leq i\leq n} \left| b_{ik} - a_{ij} \right| \tag{1.50}$$

While the above formula is not identical with (1.48), it can be regarded as a good approximation for it. As a matter of fact, we replaced optimization problem on convex set $\{y; \|y\|_p \leq 1\} \times \{z; \|z\|_m \leq 1\}$ with one on a simpler $F \times G$ on its boundary. Similarly, we could replace $\sup_{\|z\|_m \leq 1} \inf_{\|y\|_p \leq 1} \|By - Az\|$ in (1.44) with $\sup_{1\leq i\leq m} \inf_{1\leq k\leq p} \sup_{1\leq i\leq n} \left| b_{ik} - a_{ij} \right|$. Thus, the transformed formula (1.45) becomes the following Hausdorff-based distance:

$$d(A,B) = \max\left\{ \sup_{1\leq k\leq p} \inf_{1\leq i\leq m} \sup_{1\leq i\leq n} \left| b_{ik} - a_{ij} \right|, \sup_{1\leq i\leq m} \inf_{1\leq k\leq p} \sup_{1\leq i\leq n} \left| b_{ik} - a_{ij} \right| \right\} \tag{1.51}$$

The resulted nonlinear function *d* verifies the three main properties of a metric: positivity ($d(A,B) \geq 0$), symmetry ($d(A,B) = d(B,A)$) and triangle inequality ($d(A,B) + d(B,C) \geq d(A,C)$). So, this Hausdorff derived function represents a distance, although it does not represent the standard Hausdorff-Pompeiu metric anymore [36]. It defines a new metric topology on the space of all matrices {*A*}, that is not equivalent but comparable with that induced by the Hausdorff topology [36]. This metric has been successfully used in the classification processes, representing a powerful discriminator between feature vectors.

1.4.2. A special metric for complex feature vectors

The feature vectors corresponding to some media objects do not represent always 1D, 2D or 3D vectors. Often they represent very complex structures, therefore the distances between them cannot be computed using conventional metrics, like the Euclidian distance. For example, some biometrics-related image analysis techniques, such as face [37] and fingerprint recognition [38], could produce this kind of feature vectors. These methods developed by us identify a set of *keypoints* in the image, such as SIFT points (for faces) [37] and minutiae points (for fingerprints) [38], and model a feature vector for each keypoint. Such a feature vector could be a complex structure, whose components may represent names, locations, orientations or codify other information. The global feature vector is composed of all the feature vectors corresponding to the keypoints (see **selected paper 4** [38]).

We have modeled a generic metric for this type of feature vectors that is based on the number of *matches* between them. Therefore, if $v = [v_1,....,v_n]$ and $w = [w_1,....,w_m]$ represent two different-sized feature vectors of this kind, then the distance between them is computed as following:

$$d(v,w) = \frac{m+n}{2} - card(M(v,w)) \tag{1.52}$$

where *card* (*M* (*v*, *w*)) is the number of pairings (matches) between *v* and *w*. Thus, (v_i, w_j) represents a match between these feature vectors if $v_i \cong w_j$, which means these components are closed enough to each other, in terms of the criteria related to that image analysis task [37-39]. The set of the matches is modeled as:

$$M(v,w) = \{(i,j) \mid v_i \cong w_j \ \& \left(\forall(k,t) \in M(v,w) \Rightarrow k \neq i \ \& \ t \neq j\right)\} \tag{1.53}$$

where

$$v_i \cong w_j \Leftrightarrow dist(v_i, w_j) \leq T \tag{1.54}$$

where *dist* is a proper metric that works for the feature vectors v_i and w_j, and *T* is a properly selected low threshold value.

The function *d* satisfies the main properties of a metric [37-39]. The *non-negativity* is demonstrated easily as follows:

$$card(M(v,w)) \leq \min(m,n) \leq \frac{m+n}{2} \Rightarrow d(v,w) \geq 0 \tag{1.55}$$

The *Leibniz rule* is satisfied because:

$$d(v,w) = 0 \Leftrightarrow card(M(v,w)) = \frac{m+n}{2} \Leftrightarrow card(M(v,w)) = m = n \Leftrightarrow v = w \tag{1.56}$$

Obviously, the *symmetry* property is satisfied by *d*:

$$M(v,w) = M(w,v) \Leftrightarrow d(v,w) = d(w,v) \tag{1.57}$$

The *sub-additivity*, or *triangle inequality*, is also verified because we have:

$$d(v,w) + d(w,u) \geq d(v,u) \Leftrightarrow n \geq card(M(v,w)) + card(M(w,u)) - card(M(v,u)) \tag{1.58}$$

We introduced *M* (*u*, *v*, *w*), the set of matches between all the three feature vectors, and $M_u(v,w)$, representing the set of matches between *v* and *w* but cannot be found in *u*. Obviously, $card(M(v,w)) = card(M(u,v,w)) + card(M_u(v,w))$, so (1.58) is equivalent to:

$$n \geq card(M(u,v,w)) + card(M_u(v,w)) + card(M_v(u,w)) - card(M_w(v,u)) \tag{1.59}$$

which is true because $n \geq card(M(u,v,w)) + card(M_u(v,w)) + card(M_v(u,w))$.

1.4.3. Automatic unsupervised classification algorithm

The machine learning techniques represent essential tools for our research. While biometric systems, described in the next chapter, are mostly based on supervised classification (recognition) algorithms, the image analysis methods, described in the third chapter, make use of unsupervised classification models. An unsupervised classification, or clustering, approach must be able to group a set of feature vectors (and consequently the corresponding media objects) in a number of classes (clusters), having no previous knowledge about these classes. In fact the only available knowledge about them could be their number.

If the number of classes is a priori known, or set interactively by the user, then we have a semi-automatic unsupervised classification technique. Semi-automatic clustering methods, such as hierarchical agglomerative clustering and *K*-means algorithms, have been widely used by us. Very often, the number of classes cannot be known, therefore some automatic clustering solutions are required. We have proposed several automatic classification techniques that are described in this subsection and the next one [39-42]. The clustering model described here represents an extended and automatic version of the hierarchical agglomerative clustering, or region growing, scheme [39]. If $\{V_1,...,V_n\}$ represents a sequence of media feature vectors to be classified, the automatic unsupervised classification algorithm developed by us to solve this task is modeled as following:

1. A distance set is initialized: $D = \phi$
2. One starts the classification process with all the feature vectors as the *n* initial clusters: $C_1 = \{V_1\},...,C_n = \{V_n\}$.
3. Each feature vector is labeled: $\forall i \in [1,n], C(V_i) = i$.
4. At each iteration one computes the *overall minimum distance* between clusters and merges those being at that distance from each other:

$$\forall i < j,\ d_{Cl}(C_i, C_j) = d_{\min} \Rightarrow C_i = C_i \cup C_j, C_j = \phi, \tag{1.60}$$

where

$$d_{\min} = \min_{i \neq j \in [1,n]} d_{Cl}\left(C_i, C_j\right) \tag{1.61}$$

and the distance between the clusters could be computed as a *single linkage clustering* metric

$$d_{Cl}\left(C_i, C_j\right) = \min_{v \in C_i, w \in C_j} d\left(v, w\right), \tag{1.62}$$

a *complete linkage clustering* metric

$$d_{Cl}(C_i, C_j) = \max_{v \in C_i, w \in C_j} d(v, w), \tag{1.63}$$

or an *average linkage clustering*, described as

$$d_{Cl}(C_i, C_j) = \frac{\sum_{v \in C_i} \sum_{w \in C_j} d(v, w)}{card(C_i) \cdot card(C_j)}, \tag{1.64}$$

where *d* is a proper metric for the feature vectors *v* and *w* [39].

5. Minimum distance is then registered: $D = D \cup \{d_{\min}\}$.
6. When a single cluster is obtained, a new clustering process is performed on the distance set *D*, using a hierarchical agglomerative clustering (region-growing) algorithm: steps 2 and 3 are applied, then step 4 is repeated until the number of clusters becomes $K = 2$. Two classes containing distance values are thus obtained.
7. One element from each class is randomly selected and the two distance values are then compared. The class corresponding to the greater value represents the set of large distances, let it be D_l. The smaller value belongs to the set of small distances, D_s. Obviously, $D = D_l \cup D_s$.
8. For any small distance, it searches for all pairs of vectors corresponding to it and the feature vectors from each identified pair are inserted in the same class:

$$\forall dist \in D_s, \forall i < j \in [1, n],\ if\ d(V_i, V_j) = dist \Rightarrow C(V_j) = i \tag{1.65}$$

The resulted labeling, $\{C(V_1), ..., C(V_n)\}$, represents the final media feature vector classification result [39]. The described automatic clustering algorithm has been successfully applied in various recognition tasks, and also in important domains like database indexing.

1.4.4. Automatic clustering models based on validity indexes

We also developed some robust automatic unsupervised classification models that use semiautomatic clustering approaches and validation index based measures [40-42]. Thus, we considered the same feature set, $\{V_1, ..., V_n\}$, to be clustered. An integer value $T \in [1, n]$ representing the maximum number of possible feature vector clusters was selected first. A high *T* value could lead to better classification results, but also raises the computation volume and the time complexity of the classification process. Usually, we have used the value $T = \left\lceil \frac{n}{2} \right\rceil$ in our experiments.

For each $K \in [1, T]$ one applied a semi-automatic unsupervised classification procedure to the feature vector set [40-42]. We generally used a *K*-means algorithm [40,42] or a hierarchical agglomerative procedure [41] for this clustering task, but some other unsupervised recognition solutions, like *Fuzzy K-Means* [43] or *Self Organizing Maps* (*SOM*) [44], could also be used.

In the previous sub-section we described how a hierarchical agglomerative clustering algorithm works: each observation starts in its own cluster, and pairs of clusters are merged as one moves up the hierarchy. The *K*-means clustering, proposed by MacQueen in 1967, represents one of the simplest unsupervised learning algorithms [45]. In statistics and machine learning, *K*-means is a method of cluster analysis which aims to partition *n* observations into *K* clusters in which each observation belongs to the cluster with the nearest mean. The clustering procedure is composed of the following steps:

1. One selects K initial centroids, as much as possible far away from each other, each centroid representing a point in the feature vector space.
2. Each feature vector is associated to the closest centroid (in terms of the used distance)
3. The centroids of the obtained clusters are recomputed, as means of the vectors in those clusters.
4. Steps 2 and 3 are repeated until the centroids of the classes no longer change their positions.

In the next phase, one determines the optimal number of clusters, from 1 to T. Some cluster validity indexes are used for this purpose [40-42]. We modeled a measure based on a combination of Dunn and Davies-Bouldin validation indexes in [40]. The Dunn index aims to maximize the inter-cluster distances and minimize the intra-cluster distances [46]. The number of clusters that maximizes the Dunn index is considered the optimal number of clusters. This validity index has a linear time complexity, its computational complexity being O (n), this fact representing an advantage. Its main disadvantage is the vulnerability for noise in the data. The index proposed by Davies and Bouldin is a function of the ratio of the sum of within-cluster scatter to between-cluster separation [47]. Its lowest value indicates an optimal clustering operation. The Davies-Bouldin index becomes computationally expensive when the number of clusters grows very large.

Therefore, for each K we obtain the feature vector clusters $Cl_1,...,Cl_K$. Then, the optimal number of classes is determined by performing the following minimization [40]:

$$K_{optim} = \arg \min_{K \in [1,T]} \left(DB(K) + \frac{1}{D(K)} \right) \tag{1.66}$$

where the Davies-Bouldin index is computed as

$$DB(K) = \frac{1}{K} \sum_{i=1}^{K} \max_{i \neq j} \frac{d(Cl_i) + d(Cl_j)}{d(C_i, C_j)} \tag{1.67}$$

and the Dunn index is obtained as

$$D(K) = \min_{i \in [1,K]} \left\{ \min_{j \neq i} \left\{ \frac{d(C_i, C_j)}{\max\limits_{k \in [1,K]} d(Cl_k)} \right\} \right\} \tag{1.68}$$

where C_i is the centroid of the cluster Cl_i , while $d(Cl_i)$ represents the intra-cluster distance of Cl_i , that is the absolute squared distance between all pairs of points in that cluster. So, the final feature vector classification result is $Cl_1,...,Cl_{K_{optim}}$.

The automatic clustering models described here have been successfully used by numerous media pattern recognition and indexing techniques developed by us. The voice recognition [41], image classification [48], shape recognition [40], image segmentation [42] and media indexing [33] approaches using these clustering solutions are described in the next two chapters.

1.5. Conclusions

In this chapter we described some robust mathematical models that have been developed by us to facilitate the biometric and computer vision techniques presented in the following chapters. These models are grouped into two main categories. The first one contains the PDE-based mathematical models for image and video enhancement, while the second category contains machine learning models.

We proposed in our recently published papers some effective PDE-based image denoising and restoration techniques that provide very good results and outperform not only the conventional filtering methods but also many other PDE-based approaches. Our PDE denoising algorithms are divided into diffusion-based methods and variational approaches. We brought important original contributions in the diffusion-based restoration field, which were described in this chapter. Thus, a linear diffusion technique, based on a 2nd order hyperbolic PDE model, was presented first. It reduces substantially the Gaussian noise and also enhances the image contrast.

Nonlinear diffusion-based smoothing algorithms were also described in this chapter. Thus, we provided a detailed overview of the state of the art nonlinear diffusion techniques derived from the Perona-Malik framework. A novel anisotropic diffusion-based model developed by us is also introduced and compared with those state of the art approaches. Another proposed PDE-image filtering solution, which could be also represented as a variational problem, is based on a diffusion porous media flow and outperforms some influential PDE denoising schemes, like Perona-Malik, TV and Kacur-Mikula models. A 4th-order PDE diffusion model that achieves satisfactory Gaussian and speckle noise reduction results was also described here. Two PDE variational models developed by us are described in this chapter. They provide an efficient noise reduction, obtaining much better results than conventional filters. Also, our techniques overcome the drawbacks of other existing variational models, such as the TV model.

All the PDE-based image filtering solutions described in this chapter represent original and effective denoising techniques developed by us and published in some prestigious international journals [5,15,16,18,24,27,28]. A rigorous mathematical treatment was performed for each proposed PDE model, its convergence and stability being mainly investigated. More detailed mathematical investigations of these models are provided in those papers disseminating our research results in PDE-based image enhancement domain. Robust discretization schemes were constructed for all these differential models and explained in this chapter.

The effectiveness of these numerical approximation algorithms was demonstrated by the successful denoising experiments, some of them described in the chapter. All PDE denoising models proposed by us have also a strong edge-preserving character. Method comparisons were also provided for all our restoration techniques. We have found that our PDE filtering schemes not only achieve much better results than conventional algorithms, but also outperform the influential schemes of the same class. Thus, our nonlinear diffusion methods outperform the Perona-Malik models, while our variational approaches outperform the TV denoising. Since all our described PDE techniques succeed also in removing the staircasing effect, they can represent better denoising solutions than many state of the art PDE-based technologies. Also these methods can be applied successfully to the edge detection domain, and consequently to object detection.

Our original contributions to media feature vector classification domain, disseminated in important scientific publications [31-33,37-39], were then described. The two novel metrics introduced by us represent important contributions in this field, because they can perform some difficult tasks that conventional metrics are unable to solve: measuring the distances between different-sized feature vectors or special feature vectors representing not matrices but complex structures. A robust mathematical treatment is provided by us for each metric. Also, these proposed metrics can be applied successfully to feature vectors belonging to various media, eventually adapted to those media. So, our metric derived from the Hausdorff-Pompeiu metric for sets is used not only for the DDMFCC-based 2D speech feature vectors, but also for 2D video feature vectors. Our second metric represents a similarity metric that is specially modeled for images whose content is characterized by some *key points*. It is applied with some adaptations to both SIFT-based facial feature vectors and minutiae-based fingerprint feature vectors.

The proposed automatic unsupervised classifiers, described in the last section, constitute other significant machine learning contributions. Our media feature vector clustering models, derived from semi-automatic clustering algorithms, like region-growing, or using these semi-automatic clustering solutions in combination with some validation index based measures, are very useful to any automatic unsupervised recognition task. For this reason, our classification approaches are applied successfully to both biometrics and computer vision domains.

2. Biometric authentication techniques

Biometric authentication, or simply biometrics, refers to measuring and analyzing biological data with the purpose of uniquely identify the humans by their physical or behavioral characteristics. The *physiological* biometric identifiers are related to the human body shape and include, but are not limited to: face, fingerprint, palm print, iris, DNA and the odour/scent. The behavioral characteristics, or *behaviometrics*, are related to the individual's behavior of a person, including voice, typing rhythm, gait, signature and handwriting [49].

The most important application areas of biometrics include access control [50], surveillance and security systems [51], law enforcement and missing person searching. The main properties that must be satisfied by a strong biometric identifier are: uniqueness, measurability, performance and acceptability [52]. Each biometric characteristic can be represented through a digital media signal and corresponds to a media pattern recognition process. Thus, we have voice recognition, face recognition, fingerprint recognition, iris recognition, handwriting recognition and other such recognition tasks [53]. While a biometric like voice is described by a 1D sound signal, the most other identifiers are represented by 2D image signals. For this reason, the most biometric recognition tasks belong to the image analysis domain [53].

A *biometric system* represents a computer system that performs person authentication on the basis of one or more biometrics [49-53]. A *unimodal* biometric system is based on a single biometric identifier, while a *multimodal* biometric system uses more biometric characteristics to authenticate the humans. The biometric system performs two major operations: person registration and recognition. It is composed of the following main components: sensor, pre-processing device, biometric database, feature extractor device, classifier and verification system [53].

The first task, related to registration, is performed using the first three components. The input biometric sequences are captured by the media acquisition device of the sensor and transformed into digital signals. The obtained signals, often affected by noise during the acquisition process, are sent to pre-processing device, where some proper filtering procedures, like the PDE-based restoration operations described in previous chapter, are applied on them. Then, the biometric signals are registered in the biometric database. The person recognition process is performed by the next three devices of the system. Biometric recognition consists of two main operations: person identification and verification. Human identification is based on a feature extraction that produces biometric feature vectors, and a classification procedure performed by a supervised classifier that uses a training set obtained from the system's database. The person verification either validates or invalidates a determined identity, usually using some certain threshold values.

We developed both unimodal and multimodal biometric systems based on several biometric identifiers. We used mainly the voice, face and fingerprint for person authentication, our recognition approaches based on these biometrics being described in next sections. We have recently started to conduct research in the iris recognition domain, obtaining some encouraging results [54]. Since our research in this biometric field is in the beginning stages and we do not have enough published results on it [54], the iris analysis has not been detailed in this thesis. Our voice recognition techniques are described in next section. The proposed face recognition models are then presented in the second section, while the fingerprint recognition approaches are described in the third one. The multi-modal biometric authentication systems are discussed in the last section.

2.1. Voice recognition approaches using mel-cepstral analysis

Human voice represents a *behavioural* biometric identifier, although it could also be considered a physiological feature, because every person has a different *pitch*. Voice (speaker) recognition is the computational task of validating users' claimed identity using characteristics extracted from their voices. A speaker recognition system is able to recognize who is speaking on the basis of individual information included in the speech signals [55]. Speaker recognition technology is successfully used in controlling the access to various services such as banking by telephone, database access services, information services, voice mail, security control for confidential information areas, and remote access to computers [55]. Audio surveillance systems also make use of voice recognition techniques.

The voice recognition approaches can be divided into *text-dependent* (*speech-dependent*) and *text-independent* (*speech-independent*) techniques. The former methods discriminate the individuals based on the same spoken utterance and deal with cooperative subjects [31]. The latter techniques do not rely on a specific speech and deal with non-cooperative subjects [56], being useful for surveillance applications.

As any biometric recognition system, the speaker recognition encompasses both person identification and verification. Human voice identification represents the process of determining which speaker provides a given vocal utterance, consisting of a feature extraction process and a classification one. Depending on the character of its classification stage, the speaker recognition can be either *supervised* or *unsupervised*. Speaker verification, on the other hand, represents the procedure of accepting or rejecting the identity claim of a previously identified speaker.

We developed both text-dependent [31] and text-independent voice recognition techniques [57], and also both supervised [36] and unsupervised recognition approaches [41]. We have achieved much better speaker recognition results in the speech-dependent case, so we describe only the text-dependent approaches in this thesis. Since the *Mel Frequency Cepstral Coefficients* (*MFCC*s) represent the dominant features used in speech and speaker recognition domains [58], we proposed a voice feature extraction based on the mel-cepstral analysis for these methods. The MFCC-based vocal feature extraction is described in the next subsection. In the second subsection, a supervised speech-dependent voice recognition approach is proposed. Then, an automatic unsupervised speaker recognition algorithm is described in the last subsection.

2.1.1. MFCC-based speech feature extraction solutions

There are various speech feature extraction solutions used by the voice recognition systems. The most popular are the MFCC analysis, Linear Predictive Coding (LPC) analysis, and the autoregressive (AR) coefficients. The speaker recognition techniques developed by us are based on AR coefficients [59,60] or MFCC analysis [31,36,41,53] in the feature extraction stage.

We describe here a robust MFCC-based voice analysis on whose basis we modeled some efficient speech feature vectors for speaker recognition. Thus, we consider a vocal sequence represented by a 1D digital signal, to be featured, and perform a short-time analysis on it. The speech signal is divided into overlapping frames with 256 samples and overlaps of 128 samples [31,33,57]. Each resulted segment is then windowed, by multiplying it with a Hamming window of 256 coefficients. The spectrum of each windowed sequence was then computed, by applying the FFT (*Fast Fourier Transform*) to it (see **selected paper 2**, Barbu 2005 [31]).

The *cepstrum* of each windowed frame could be determined by applying the inverse Fourier transform to its log-spectrum, but we considered the *melodic cepstrum* a much better featuring solution. The regular frequencies were translated to a scale that is more appropriate for human speech [33,36,53]. The mel-scale approximates the human auditory system's response more closely than the linearly-spaced frequency bands used in the normal cepstrum. The difference between the cepstrum and the *mel-frequency cepstrum* is that in the MFC, the frequency bands are equally spaced on the mel scale. The mel-frequency cepstral coefficients (MFCCs) were obtained as following:

1. The windowed signal was processed using FFT.
2. The powers of the spectrum obtained above were mapped onto the mel scale, using triangular overlapping windows.
3. The logs of the powers were applied at each of the mel frequencies.
4. One computed the DCT (Discrete Cosinus Transform) of the set of mel log powers, as if it were a signal.
5. The MFCCs were obtained as the amplitudes of the resulting spectrum.

Thus, a sequence of mel-cepstral coefficients resulted for each frame, each such MFCC set representing a melodic cepstral acoustic vector. These acoustic vectors could work as feature vectors but we intended to achieve more powerful speech features. A 2D feature vector could be obtained as the MFFCC-based matrix having these acoustic vectors as columns. Another featuring solution proposed by us was the 1D feature vector composed of the *pitch* values of the acoustic vectors [60]. A 2D feature vector having on each column the greatest *n* coefficients of the corresponding acoustic vector was also proposed [60].

Much better recognition results are obtained if the acoustic vectors are further processed. Therefore, a derivation process can be performed on those MFCC acoustic vectors. We compute the *delta mel cepstral coefficients* (*DMFCCs*), as the first order derivatives of the mel cepstral coefficients. Then, the *delta delta mel frequency cepstral coefficients* (*DDMFCC*s) are derived from DMFCCs, thus representing the second order derivatives of the MFCCs [31]. We derive these mel-cepstral coefficients because we intend to model the intra-speaker variability. These computed DDMFC coefficients indicate how fast the voice of a speaker is changing in time.

A DDMFCC acoustic vector is obtained for each frame of the initial vocal signal. Each acoustic vector is composed of 256 samples, but the speech information is encoded mainly in its first 12 coefficients. So, we truncate each vector at its first 12 samples, then consider it as a column of a matrix. This truncated DDMFCC acoustic matrix has been used as a robust 2D voice feature vector and provided satisfactory recognition results [31,57]. Another type of vocal feature vector is determined as the mean of the DDMFCC-based acoustic matrix (1D vector composed of the mean values of the matrix columns) [36].

The notation $V(S)$ was used for the feature vector of the vocal sequence S. These 2D or 1D speech feature vectors have the same number of rows, but a different number of columns depending on their length. Since they cannot be compared using conventional metrics, we used the Hausdorff-derived metric described in 1.4.1 to measure the distance between them [31,41].

2.1.2. Supervised text-dependent voice recognition technique

The existing text-dependent speaker recognition systems classify the speech feature vectors, obtained from voice analysis based on MFCCSs, LPC or AR coefficients, using various classifiers, such as the *K*-Nearest Neighbor (*K*-NN) [61], Hidden Markov Models (HMM) [62], Vector Quantization (VQ) [63], Gaussian Mixture Models [64], various neural networks [65], Dynamic Time Warping (DTW) [66] and ART-based classifiers [60]. In the past we proposed some voice recognition techniques using autoregressive coefficient based feature vectors that are classified by Multi Layer Perceptron (MLP) and RBF (Radial Basis Functions) networks [59]. In the last ten years, representing the period targeted by this thesis, we have developed some robust speaker recognition models using MFCC-based feature vectors and supervised classifiers [67].

A supervised text-dependent speaker recognition approach is proposed in [31]. It classifies properly any input vocal utterance using a speech training set. So, one considers $\{S_1,...,S_n\}$, the set of input same-speech utterances (signals) to be recognized. A set of *N* registered (known) speakers is also considered. Each of them generated a set of vocal utterances having the same spoken text as the input sequences. The *training set* of the system is composed of all the sets of spoken utterances provided by the registered speakers, being modeled as $Sp = \{Sp_1,...,Sp_N\}$, where each $Sp_i = \{s_1^i,...,s_{n(i)}^i\}$ represents the set of vocal sequences corresponding to the i^{th} speaker [31].

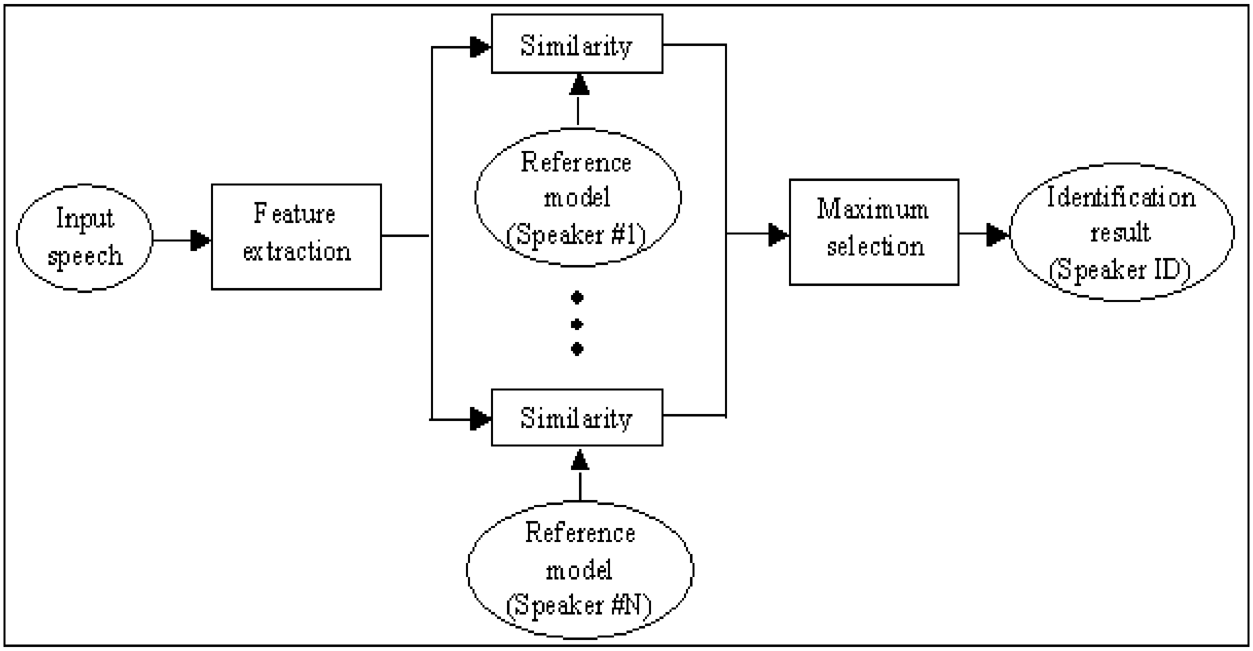
Input speech
Feature extraction
Similarity
Reference model (Speaker #1)
Similarity
Reference model (Speaker #N)
Maximum selection
Identification result (Speaker ID)

Fig. 2.1. Supervised speaker identification scheme

In the identification stage, one applies a melodic cepstral analysis based feature extraction process, like that described in 2.1.1, on both the input and training sets. So, the feature set $\{V(S_1),...,V(S_n)\}$ and the *training feature set* $\{\{V(s_1^1),...,V(s_{n(1)}^1)\},...,\{V(s_1^N),...,V(s_{n(N)}^N)\}$ are determined [31,36]. In selected article [31] the feature vectors are modeled as DDMFCC-based 2D matrices having 12 rows and a variable number of columns.

Then, a supervised classification procedure is performed on these feature vectors. We propose a *minimum average distance classification* technique, representing an extended version of the minimum distance classifier. This algorithm inserts each input vocal sequence S_i in the class of the speaker corresponding to the smallest average distance between the input feature vector and its training vectors. Thus, the closest speaker is identified as the n_i^{th} registered speaker, where:

$$n_i = \arg \min_{j \in [1,N]} \frac{\sum_{k=1}^{n(j)} d(V(S_i), V(s_k^j))}{n(j)} \quad , \forall i \in [1, n] \tag{2.1}$$

where *d* is the special metric given by equation (1.51). The classification result, consisting of *N* classes of speech utterances: $C_1, \ldots, C_N$, represents also the voice identification result [31]. A supervised speaker identification framework is depicted in Fig. 2.1.

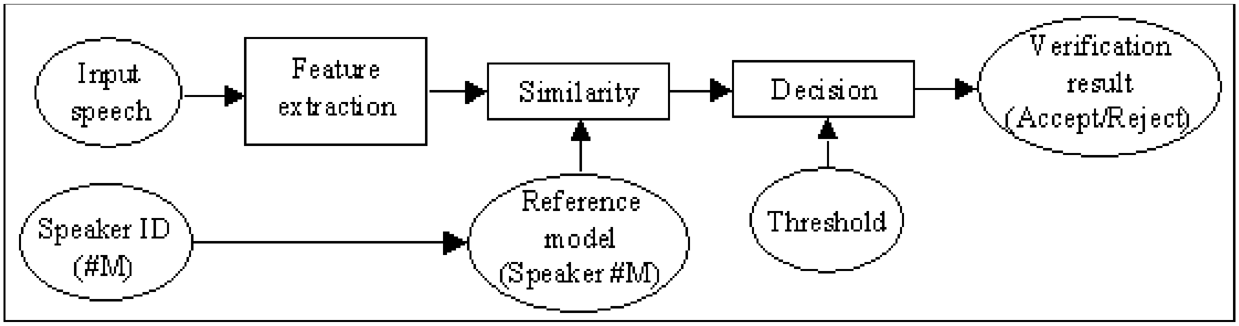

Fig. 2.2 Speaker verification model

The next stage of the recognition process, the speaker verification, decides for each identified sequence if the associated speaker is the one who really produced it. We have proposed a threshold-based verification procedure to be performed within each resulted voice class [31]. So, each average distance computed in any speaker class could not exceed a special chosen threshold value *T*:

$$\forall i \in [1, N], \forall S \in C_i : \frac{\sum_{k=1}^{n(i)} d(V(S), V(s_k^i))}{n(i)} \leq T \tag{2.2}$$

A threshold – based speaker verification scheme is represented in Fig. 2.2. The task of choosing a proper threshold value is solved by developing an *automatic threshold detection* approach [31]. Thus, the overall maximum distance between any two training vectors belonging to the same training feature subset is considered as a threshold. Therefore, a proper threshold value is obtained as:

$$T = \max_{i \leq N} \max_{k \neq t} \sum_{k=1}^{n(i)} d(V(s_k^i), V(s_t^i)) \tag{2.3}$$

A lot of numerical experiments on various speech datasets have been performed, satisfactory recognition results being obtained [31,36]. A high recognition rate, approximately 85%, has been achieved by our speech-dependent voice recognition system that outperforms other speaker recognition techniques. A recognition example based on our method is described in the next figures and table. The 5 input speech signals are displayed in Fig. 2.3, their 2D feature vectors being displayed in Fig. 2.4. The training set of the system is described in Fig. 2.5, where there are displayed the 4 training utterances generated by 3 speakers, and their training feature vectors. All the input and training sequences have the same speech: *Hello!*

The computed average distance values are registered in Table 2.1. From this table, the following voice identification results: Speaker 1 =>$\{S_1, S_3\}$, Speaker 2 =>$\{S_4, S_5\}$ and Speaker 3 =>$\{S_2\}$. We computed the threshold value T = 1.35, which leads to the final recognition result: Speaker 1 =>$\{S_1, S_3\}$, Speaker 2 =>$\{S_5\}$, Speaker 3 =>$\{S_2\}$, Unregistered speaker =>$\{S_4\}$.

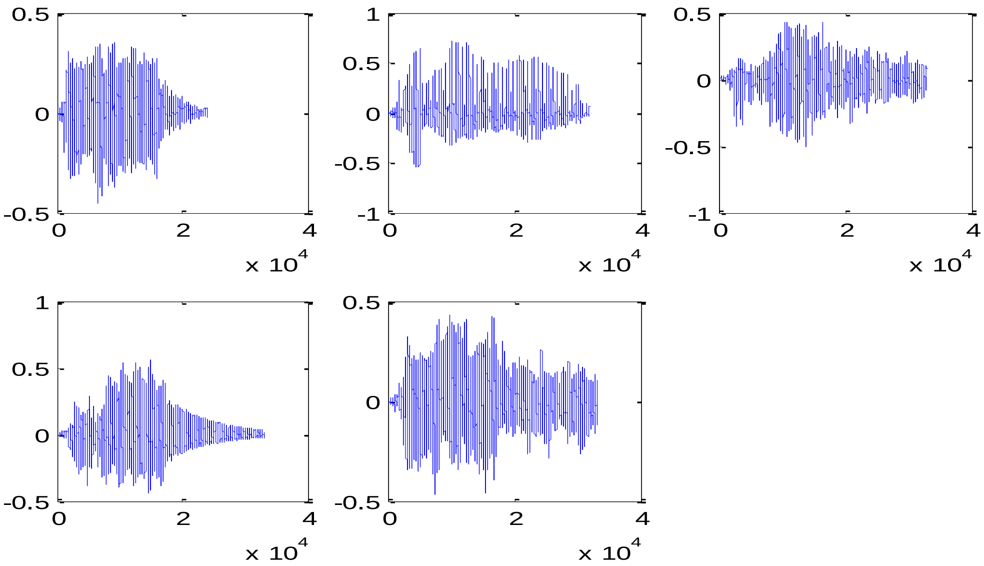

Fig. 2.3. Input vocal sequences

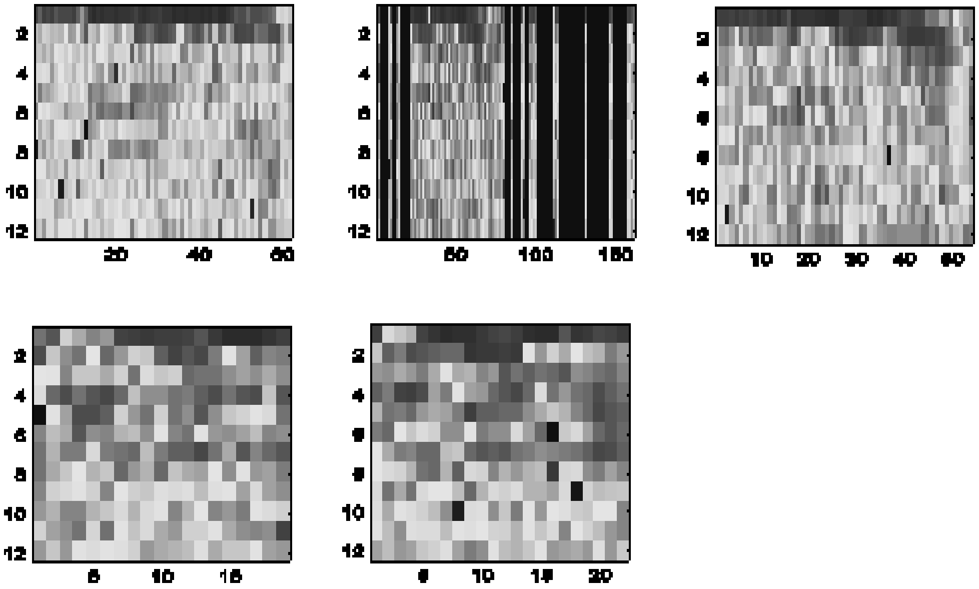

Fig. 2.4. Input DDMFCC-based vocal feature vectors

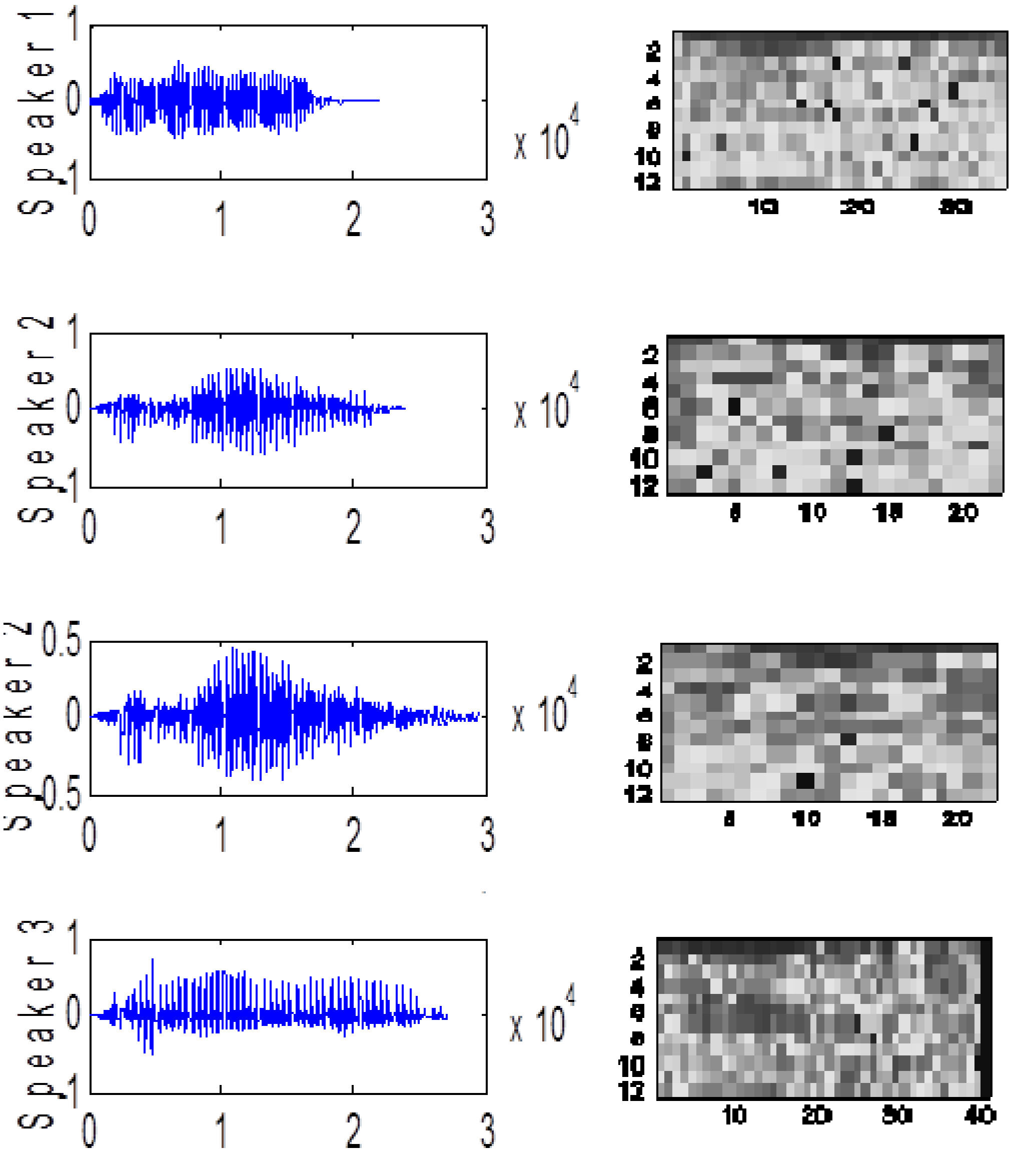

Fig. 2.5. Training set of the system

Table 2.1. Average distance values

	Speaker 1	Speaker 2	Speaker 3
Vocal Input 1	0.7532	1.0857	1.3415
Vocal Input 2	0.9360	0.7495	0.2956
Vocal Input 3	1.2512	1.4123	1.5452
Vocal Input 4	1.7814	1.4814	1.5013
Vocal Input 5	1.4756	1.2137	1.5123

2.1.3. Automatic unsupervised speaker classification model

We also considered the unsupervised speech-dependent voice recognition problem [41], which represents a much more difficult task and has other application areas. While supervised voice recognition is mainly used by the security systems that control access to various services, unsupervised speaker recognition is very useful for voice database indexing and retrieval [68]. Also, this unsupervised recognition could be used to cluster the speakers from unlabeled conversations.

The existing unsupervised voice recognition systems use no a priori knowledge about the identity of the speakers, therefore no voice training set is available to them, but most of them have knowledge about the number of these speakers, as is the case with the SOM-based recognition techniques [44]. Unlike these approaches, the unsupervised recognition method proposed by us has also a completely automatic character [41]. It used no knowledge about the speakers' identities and their numbers, no interactivity being used. This makes our technique appropriate for voluminous sets of vocal utterances.

We formulate the following automatic unsupervised speaker recognition task in [41]. One considers $\{S_1,...,S_N\}$, the set of speech utterances to be recognized. These same-speech voice sequences are generated by an unknown number of speakers. There is no available knowledge about these speakers. All vocal signals S_i, characterized by the same speech (text), have to be clustered in a proper number of classes, each voice class containing all voice sequences produced by a speaker.

A voice feature extraction was performed on these sequences first, the MFCC-based analysis described in 2.1.1 being utilized. In [41] we compute the 2D feature vectors $\{V(S_1),...,V(S_N)\}$ as truncated DDMFCC acoustic matrices. The obtained vocal feature vectors are clustered automatically in a proper number of classes. All the automatic unsupervised classification algorithms described in section 1.4 could be used in this case.

In [41] we use the validation index based automatic clustering technique described in 1.4.4. It applies repeatedly an agglomerative hierarchical clustering algorithm on the feature vector set, until the optimal number of clusters, provided by the validity index based measure from (1.66), is finally achieved. The unsupervised classification result, $C_1,...,C_{K_{optim}}$, represents also the speaker recognition solution.

The developed automatic unsupervised text-dependent voice recognition model has been successfully tested on numerous speech datasets. A high recognition rate (around 80%) and good values for the performance parameters have been obtained. We have recorded tens of speakers at a frequency of 22050 Hertz, with various speeches (spoken words), achieving hundreds of vocal sequences. The automatic voice recognition algorithm has been applied only on sets of same-speech vocal utterances [41].

Its effectiveness is proved by the high values obtained for the performance parameters: *Precision* = 0.88, *Recall* = 0.85 and F_1 = 0.86. These scores indicate there are very few false positives and false negatives (missed hits) produced by the recognition technique [41]. Also, our speaker recognition method executes quite fast, but its speed and recognition rate depend to some extent on the threshold parameter *T* used in the classification process, that is selected as $T = \left\lceil \frac{N}{2} \right\rceil$. If that threshold is increased, then the performance of our technique also rises, but the computational complexity and running time will be increased, too. For example, if we consider the ideal case $T = N$, we get the optimal speaker recognition, but the execution time would be very high for a great number of vocal sequences (high N).

A simple voice recognition example using the described approach is displayed below. A set of speech signals S_{1-8} characterized by the same text, *Start*, is displayed in Fig. 2.6. Their computed DDMFCC-based 2D feature vectors, $V(S_1),...,V(S_8)$, are depicted in Fig. 2.7.

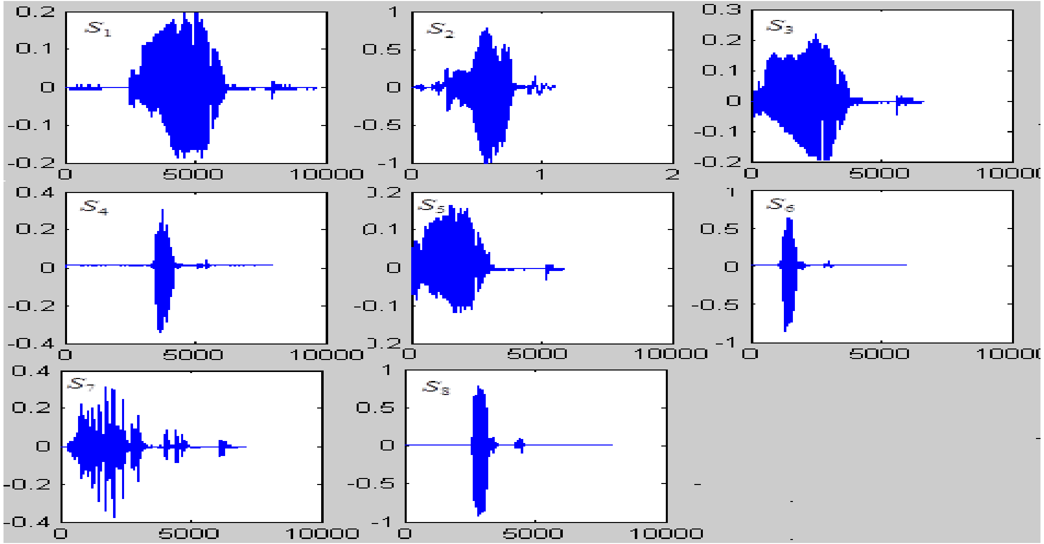

Fig. 2.6. The set of signals to be recognized

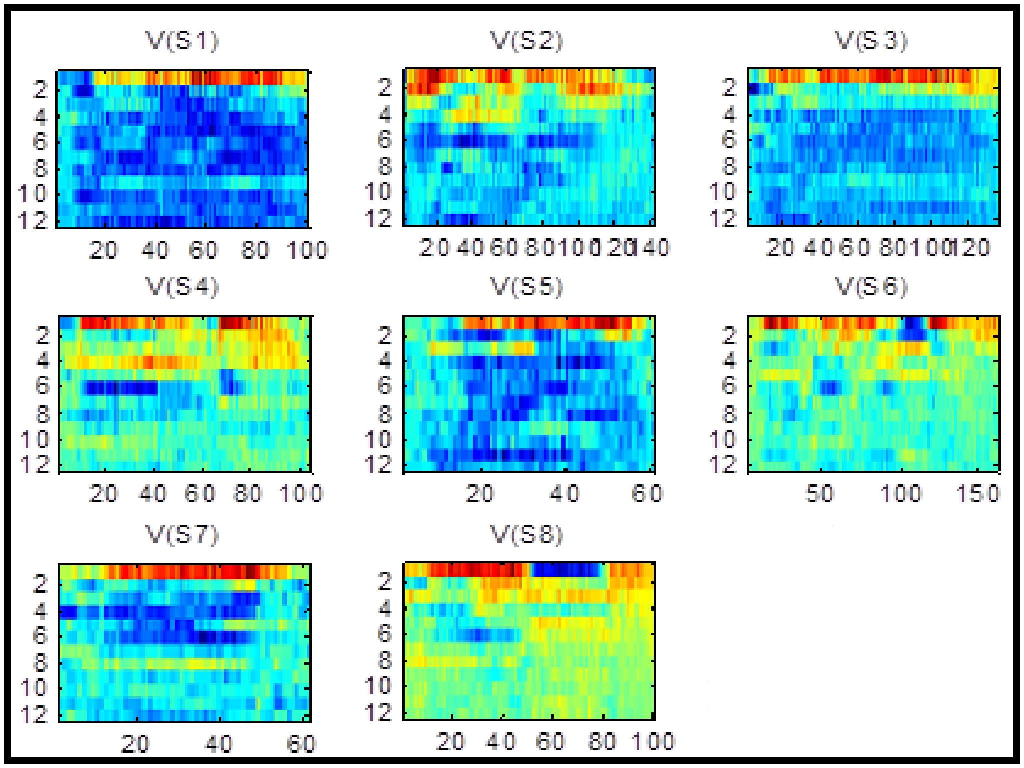

Fig. 2.7. The feature vector set

The values of the distances between these vectors, $d_{ij} = d(V(S_i), V(S_j))$, are registered in Table 2.2. One can see some of these values are low, while others are much higher One applies the automatic feature vector clustering algorithm with these distance values, obtaining $K_{opt} = 3$ and the following voice classes: $\{S_1, S_3, S_5\}$, $\{S_2, S_7\}$ and $\{S_4, S_6, S_8\}$.

Table 2.2. Distances between vocal feature vectors

d_{ij}	S_1	S_2	S_3	S_4	S_5	S_6	S_7	S_8
S_1	0	4.32	0.98	5.09	1.67	4.88	3.87	6.11
S_2	4.32	0	3.96	4.56	4.83	5.32	1.25	4.29
S_3	0.98	3.96	0	3.78	0.95	5.31	5.14	6.01
S_4	5.09	4.56	3.78	0	4.17	1.03	3.28	1.23
S_5	1.67	4.83	0.95	4.17	0	4.61	4.11	5.87
S_6	4.88	5.32	5.31	1.03	4.61	0	3.94	0.91
S_7	3.87	1.25	5.14	3.28	4.11	3.94	0	4.03
S_8	6.11	4.29	6.01	1.23	5.87	0.91	4.03	0

Method comparison have been also performed. We have determined that our automatic speaker recognition technique provides comparable good results to some non-automatic unsupervised recognition approaches, like those using Self Organizing Maps (SOMs) [44], when applied on quite small voice sets. But when applied to medium or large sets of vocal utterances, our method achieves much better recognition results than SOM-based approaches or other techniques which require that speakers' number to be known. Those methods need interactivity, so they become very difficult to apply for large sets.

Also, we have compared the proposed automatic clustering algorithm with other voice classification solutions. Thus, we have replaced the agglomerative hierarchical clustering region-growing procedure with some *K*-means algorithms [45]. We have obtained a faster recognition process with *K*-means and its variants (*C*-means, Fuzzy *K*-means) [43,45] but, unfortunately, the obtained speaker recognition results have been considerable weaker. That means a lower recognition rate, lower values for performance scores and more voice classification errors.

The described unsupervised voice classification technique can be used successfully to cluster-based indexing of large speech databases, given its automatic character. The resulted indexes, composed of feature vector clusters, would facilitate considerably the speaker retrieval process.

2.2. Robust face recognition techniques

Artificial facial recognition represents a very important biometric authentication domain, the human face being a physiological biometric identifier that is widely used in person authentication. A facial recognition system represents a computer-driven biometric application for automatically authenticating a person from a digital image, using the characteristics of its face [69]. As any biometric recognition system, it performs two essential processes: identification and verification. Facial identification consists in assigning an input face image to a known person, while face verification consists in accepting or rejecting the previously detected human identity. Also, the face identification is composed of a feature extraction process and a classification procedure.

Face recognition technologies have a variety of potential applications in commerce and law enforcement, such as database matching, identity authentication, access control for various services, suspect recognition, information security and video surveillance [69]. Also, these technologies can be incorporated into more complex biometric systems, to achieve a better human recognition.

Facial recognition techniques are divided into two main categories: geometric and photometric methods. The geometric approaches represent feature-based techniques and look at distinguishing individual characteristics, such as eyes, nose, mouth and head outline, and developing a face model based on position and size of these features. Photometric techniques are view-based recognition methods. They distill a face image into values and compare these values with templates [69].

Numerous face recognition algorithms have been developed in the last decades. The most popular techniques include Principal Component Analysis (PCA) using Eigenfaces [70,71], Linear Discriminant Analysis (LDA) using Fisherfaces [72], Elastic Bunch Graph Matching (EBGM), Hidden Markov Models (HMM) [73] and the neuronal model Dynamic Link Matching (DLM) [74].

Proposed in 1991 by M. Turk and A. Pentland [71], the Eigenface approach was the first genuinely successful system for automatic recognition of human faces. Their model represented a breakaway from contemporary research trend on face recognition which focused on identifying some individual facial characteristics. I developed an eigenimage-based face recognition technique derived from the influential work of Turk and Pentland, which is described in the next subsection. Then, a face recognition system using 2D Gabor filtering, proposed by us, is described in the second subsection. I also modeled an automatic unsupervised face recognition scheme based on SIFT characteristics and a hierarchical agglomerative clustering algorithm. It is presented in 2.2.3.

2.2.1. Eigenimage-based face recognition approach using gradient covariance

In the **selected paper 3** [75] we proposed an eigenimage-based face recognition method based on the well-known technique of Turk and Pentland [71]. Their approach considered a large set of facial images, representing a training set. Each image was transformed into a vector Γ_i, $i = 1,...,M$, then one computed the average vector Ψ. The covariance matrix was computed next as $C = A \cdot A^T$, where $A = [\Phi_1,...,\Phi_M]$ and $\Phi_i = \Gamma_i - \psi$. The eigenvectors and eigenvalues of C (a very large matrix) were obtained from those of $A^T \cdot A$. Thus, $A \cdot A^T$

and $A^T \cdot A$ have the same eigenvalues and their eigenvectors are related as follows: $u_i = Av_i$. One kept only $M^{'}$ eigenvectors, corresponding to the largest eigenvalues, each of them representing an eigenimage (eigenface). Each face image was projected onto each of these eigenfaces, its feature vector, containing $M^{'}$ coefficients, being obtained. Any new input face image was identified by computing the Euclidean distance between its feature vector and each feature training vector. Next, some verification procedures were applied to determine if the input image represented a face at all or one of the registered persons.

We developed a derived version of this PCA (Eigenface) approach in 2007 [75]. So, in that paper we propose a continuous mathematical model for face feature extraction, first. The 2*D* face image is represented there by a differentiable function $u = u(x, y)$ and the covariance matrix is replaced by a linear symmetric operator on the space $(L^2(\Omega))$ involving the image vector *u* and its gradient ∇u [75]. Thus, Ω represents a 2D domain of R^2 and $u : \Omega \to R$, the face image. We denote by $L^2(\Omega)$ the space of all L^2- integrable functions *u* with the norm $|u|_2 = \left(\int_\Omega u^2(x, y)dxdy\right)^{1/2}$ and by $H^1(\Omega)$ the Sobolev space of all functions $u \in L^2(\Omega)$ with the distributional derivatives $D_x u = \frac{\partial u}{\partial x}, D_y u = \frac{\partial u}{\partial y}$. The norm of $H^1(\Omega)$ is computed as $|u|_{H^1(\Omega)} = \int_\Omega (u^2(x, y) + (D_x u(x, y))^2 + (D_y u(x, y))^2)dxdy = \int_\Omega (u^2(x, y) + |\nabla u(x, y)|^2)dxdy$.

We consider an initial set of facial images, representing the face training set: $\{u_1,...,u_M\} \subset (H^1(\Omega))^M$. The average value is computed as: $\mu(x, y) = \frac{1}{M}\sum_{i=1}^{M} u_i(x, y),\ x,y \in \Omega$. Then, one computes $\Phi_i(x, y) = u_i(x, y) - \mu(x, y),\ i = 1,...,M$ and

$$W_i = \nabla u_i = \{D_x u_i, D_y u_i\},\ \ i = 1,...,M \tag{2.4}$$

We consider the covariance operator $Q \in L((L^2(\Omega))^3, (L^2(\Omega))^3)$ associated with the vectorial process $\{\Phi_i, W_i\}_{i=1}^M$, i.e., for $h = \{h_1, h_2, h_3\} \in L^2(\Omega) \times L^2(\Omega) \times L^2(\Omega)$:

$$\begin{aligned}(Qh)(x, y) = \Bigg\{ &\sum_{i=1}^{M} \Phi_i(x, y)\int_\Omega \Phi_i(\xi)h_1(\xi)d\xi + \sum_{i=1}^{M} W_i^1(x, y)\int_\Omega W_i^1(\xi)h_2(\xi)d\xi + \\ &+ \sum_{i=1}^{M} W_i^2(x, y)\int_\Omega W_i^2(\xi)h_3(\xi)d\xi, \Bigg\}, \forall h_k \in L^2(\Omega), k = 1,2,3\end{aligned} \tag{2.5}$$

where $W_i = \{W_i^1, W_i^2\}, W_i^1(x, y) = D_x U_i(x,y), W_i^2(x, y) = D_y U_i(x,y),\ i = 1,...,M$. Equivalently we view *Q* as covariance operator of the process $\Phi = \{\Phi_i\}_{i=1}^M$ in the space $H^1(\Omega)$ endowed with norm $|\bullet|_{H^1}$. The operator *Q* is self-adjoint in $(L^2(\Omega))^3$ and has an orthonormal complet system of eigenfunctions $\{\varphi_j\}$, i.e., $Q\varphi_j = \lambda_j \varphi_j, \lambda_j > 0$. Moreover, $\varphi_j \in (H^1(\Omega))^3, \forall j$.

We associate with operator Q the $3M \times 3M$ matrix $\tilde{Q} = A^T A$, where $A : R^{3M} \to (L^2(\Omega))^3$ $AY = \left[\sum_{i=1}^{M} \Phi_i y_1^i, \sum_{i=1}^{M} W_i^1 y_2^i, \sum_{i=1}^{M} W_i^1 y_3^i \right]$, $Y = \{y_1^i, y_2^i, y_3^i\}_{i=1}^{M}$ and $A^T : (L^2(\Omega))^3 \to R^{3M}$, which represents the adjoint operator, is provided by $A^T h = \left[\int_\Omega \Phi_1(\xi) h_1 d\xi, ..., \int_\Omega \Phi_M h_1 d\xi, \int_\Omega W_1^1(\xi) h_2 d\xi, ..., \int_\Omega W_M^1(\xi) h_2 d\xi, \int_\Omega W_1^2(\xi) h_3 d\xi, ..., \int_\Omega W_M^2(\xi) h_3 d\xi \right]$ where $h = (h_1, h_2, h_3) \in (L^2(\Omega))^3$. We obtain:

$$A^T A = \left\| \begin{matrix} \int_\Omega \Phi_i \Phi_j d\xi & 0 & 0 \\ 0 & \int_\Omega \Phi_i \Phi_j d\xi & 0 \\ 0 & 0 & \int_\Omega \Phi_i \Phi_j d\xi \end{matrix} \right\|_{i,j=1}^{M} \tag{2.6}$$

We consider $\{\lambda_j\}_{j=1}^{3M}$ and $\{\psi_j\}_{j=1}^{3M} \subset R^{3M}$ a linear independent system of eigenvectors for $\tilde{Q}$, i.e., $\tilde{Q}\psi_j = \lambda_j \psi_j$, $j = 1,...,3M$. Then, we demonstrate in [75] that $\{\varphi_j\}_{j=1}^{3M}$ defined by $\varphi_j = \psi_j \Phi_j$, for $1 \le j \le M$, $\varphi_j = \psi_j W_j^1$, for $M+1 \le j \le 2M$, and $\varphi_j = \psi_j W_j^2$, for $2M+1 \le j \le 3M$ are eigenfunctions of operator Q, i.e., $Q\varphi_j = \lambda_j \varphi_j$, $j = 1,...,3M$. It should be recalled that the eigenfunctions $\{\varphi_j\}$ to covariance operator Q maximizes the variance of projected samples i.e.,

$$\varphi_j = \arg\{\max < Qh, h >_{(L^2(\Omega))^3} ; |h|_{(L^2(\Omega))^3} = 1\} \tag{2.7}$$

In this way the eigenfunctions $\{\varphi_j\}_{j=1}^{3M}$ capture the essential features of the training images. From $\{\varphi_j\}$ we keep a smaller number of eigenfaces $\{\varphi_j\}_{j=1}^{3M'}$, with $M' < M$ corresponding to largest eigenvalues λ_j, and consider the space

$$X = lin\{\varphi_j\}_{j=1}^{3M'} \subset (L^2(\Omega))^3 \tag{2.8}$$

We assume that system $\{\varphi_j\}$ has been normalized (i.e. orthonormal in $(L^2(\Omega))^3$), so we project any initial image $\{\Phi_i, W_i^1, W_i^2\} \in (L^2(\Omega))^3$ on X by formula

$$\Psi_i(x,y) = \sum_{j=1}^{3M'} \varphi_j(x,y) < \varphi_j, T_i >_{(L^2(\Omega))^3}, i = 1,...,3M \tag{2.9}$$

where $T_i = \{\Phi_i, W_i^1, W_i^2\}$, $i = 1,...,3M$ and $< \cdot, \cdot >_{(L^2(\Omega))^3}$ represents the scalar product in $L^2(\Omega) \times L^2(\Omega) \times L^2(\Omega)$ [6]. We compute the weights $w_i^j = < \varphi_j, T_i >_{(L^2(\Omega))^3}, i = 1,...,3M$, and model the feature vector corresponding to image u_i, as following:

$$V(u_i)=(w_i^1,...,w_i^{3M'}),\ i=1,...,3M \tag{2.10}$$

Then, the continuous model proposed in our paper is discretized. One assume that $\Omega=[0,L_1]\times[0,L_2]$ and set $x_i=i\varepsilon, i=1,...N_2$ and $y_j=j\varepsilon,\ j=1,...N_1,\ \varepsilon>0$. Thus one obtains M matrices of size $N_1\times N_2$, representing the discrete images, and denote their corresponding $N_1\cdot N_2\times 1$ image vectors as $I_1,...,I_M$. Also, $\tilde{Q}=A^T\cdot A$, where

$$A=\begin{Vmatrix}\Phi_1,...,\Phi_M & 0 & 0\\ 0 & W_1^1,...,W_M^1 & 0\\ 0 & 0 & W_1^2,...,W_M^2\end{Vmatrix} \tag{2.11}$$

and

$$\begin{cases}\Phi_k=\left\|\Phi_k(x_i,y_j)\right\|_{i,j=1}^{N_2,N_1}\\ W_k^1=\left\|\Phi_k(x_{i+1},y_j)-\Phi_k(x_i,y_j)\right\|_{i,j=1}^{N_2,N_1}\\ W_k^2=\left\|\Phi_k(x_i,y_{j+1})-\Phi_k(x_i,y_j)\right\|_{i,j=1}^{N_2,N_1}\end{cases} \tag{2.12}$$

The obtained matrix has a $3M\times 3M$ dimension. One determines the eigenvectors ψ_i of the matrix $\tilde{Q}$, then, the eigenvectors of the discretized covariance operator Q are computed as:

$$\tilde{\varphi}_i=A\cdot\psi_i,\ i=1,...,M \tag{2.13}$$

We keep only $M'<M$ eigenimages corresponding to largest eigenvalues and considered the space $X=linspan\{\tilde{\varphi}_i\}_{i=1}^{3M'}$. Then, the projection of $[\Phi_i,W_i^1,W_i^2]$ on X, given by the discrete version of Ψ_i, is computed as:

$$P_X([\Phi_i,W_i^1,W_i^2])=\sum_{j=1}^{3M'}w_i^j\cdot\tilde{\varphi}_j,\ i=1,...,3M \tag{2.14}$$

where $w_i^j=\tilde{\varphi}_j^T\cdot[\Phi_i,W_i^1,W_i^2]^T$. So, for each facial image I_i a corresponding feature vector is obtained as $V(I_i)=[w_i^1,...,w_i^{3M'}]^T,\ i=1,...,3M$. We then perform a supervised classification process for these feature vectors. So, we consider an unknown image I to be classified using the face training set $\{I_1,...,I_M\}$.

The input image is normalized, first. So, $\Phi=I-\Psi$, where $\Psi=\frac{1}{M}\sum_{i=1}^{M}I_i$. The vectors W^1 and W^2 are computed from Φ using (2.12). Then it is projected on the eigenspace, by using $P(\Phi) = \sum_{i=1}^{M'} w^i \tilde{\varphi}_i$, where $w^i = \tilde{\varphi}_i^T \cdot [\Phi, W^1, W^2]^T$, its feature vector being computed as $V(I) = [w^1, ..., w^{M'}]^T$ [75]. A threshold-based facial test can be performed to determine if the given image represents a real face or not. So, if $\|P(\Phi) - \Phi\| \le T$, T being a properly chosen threshold, then *I* is a face, otherwise it is not.

We consider *K* registered (authorized) persons whose faces are represented in the training set. We redenote this set as $\{I_1^1, ..., I_1^{n(1)}, ..., I_i^1, ..., I_i^{n(i)}, ..., I_K^1, ..., I_K^{n(K)}\}$, where $K < M$ and $\{I_i^1, ..., I_i^{n(i)}\}$ is the training subset provided by the *i*th authorized person. A minimum average distance classifier, like that described in 2.1.2, is used. The input image is associated to the user corresponding to the minimum mean distance value. That user must be the *k*th registered person, where:

$$k = \arg\min_i \frac{\sum_{j=1}^{n(i)} d(V(I), V(I_i^j))}{n(i)} \tag{2.15}$$

where *d* is the Euclidean metric. After performing this face identification process, a face verification is also conducted in [75]. A threshold-based face verification technique is proposed, the proper threshold value being determined as the overall maximum distance between any two feature vectors belonging to the same training feature subset, like in 2.1.2.

Numerous experiments, using this developed approach, have been performed on various facial datasets, very good face recognition results being achieved [75]. We used Yale Face Database B [76], containing thousands of $[192 \times 168]$ facial images corresponding to many subjects, for the tests. We found that our proposed technique achieves a high recognition rate, of approximately 90%, and get high values for the performance parameters, *Precision* and *Recall*.

Let us describe here one of the performed face recognition experiments. In Fig. 2.8 one can see a set of 10 input faces to be recognized. The training set, containing 30 facial images belonging to 3 persons, is illustrated in Fig. 2.9, where each registered individual has 10 photos positioned on 2 consecutive rows. So, one computes 90 eigenfaces for this training set but only the most important 27 ($M' = 9$) of them are required. They are represented in Fig. 2.10.

The corresponding feature vectors are then determined and the average distance values between these input image feature vectors and the 3 feature subsets are registered in the next table, where each row *i*, marked by D_i, contains the distance values from the 10 feature vectors to the *i*th feature subset.

It results from Table 2.3 that input images 1, 3 and 8 are identified as faces of the third registered person from Fig. 2.8, the images 2, 6 and 10 are identified as faces of the first person and images 4 and 7 are identified as the second person. Also, the face images 5 and 9 are identified as belonging to the first registered person but their distance values, 5.795 and 5.101, are greater than the computed threshold, $T = 2.568$, so the verification procedure labels the person with faces 5 and 10 as unregistered.

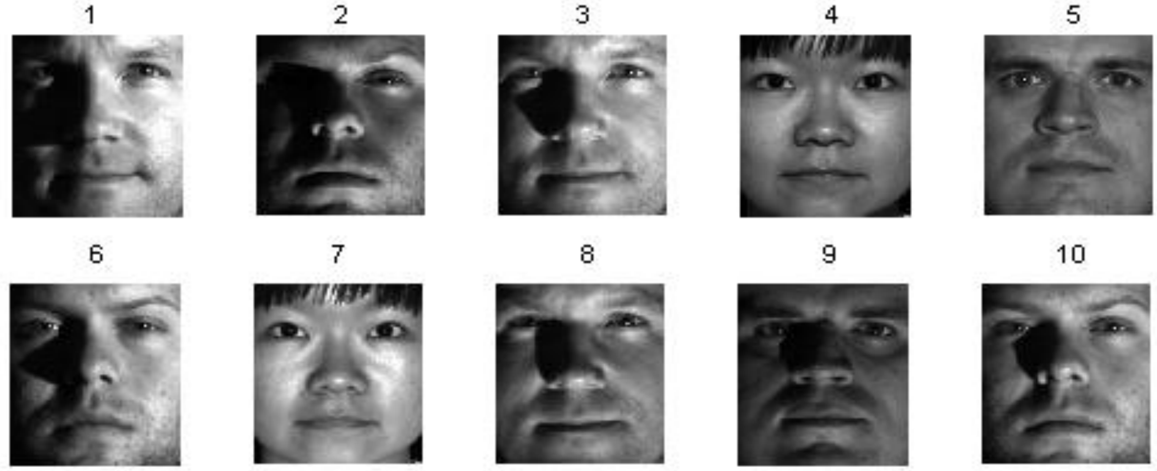

Fig. 2.8. Input facial images

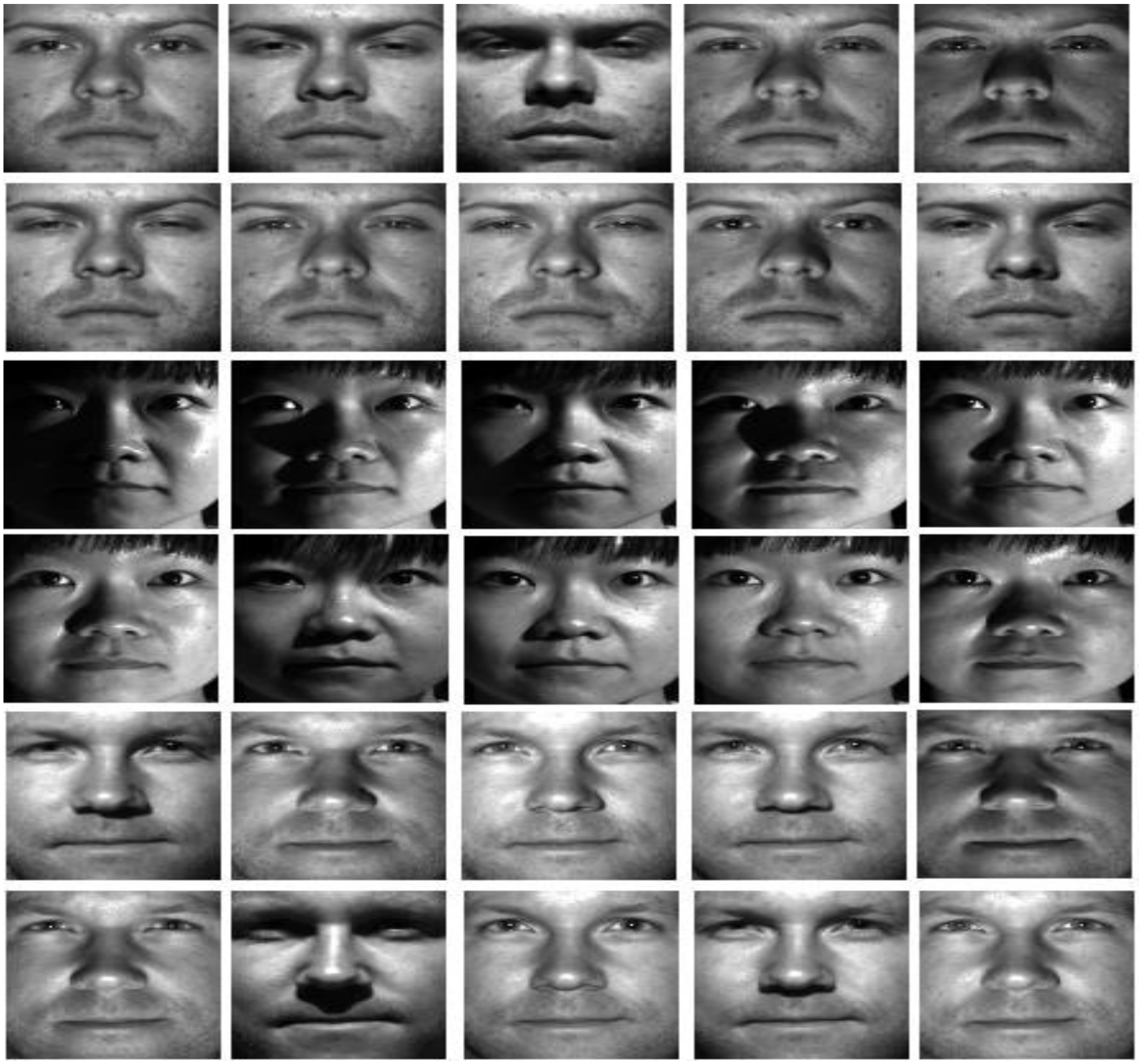

Fig. 2.9. Face training set

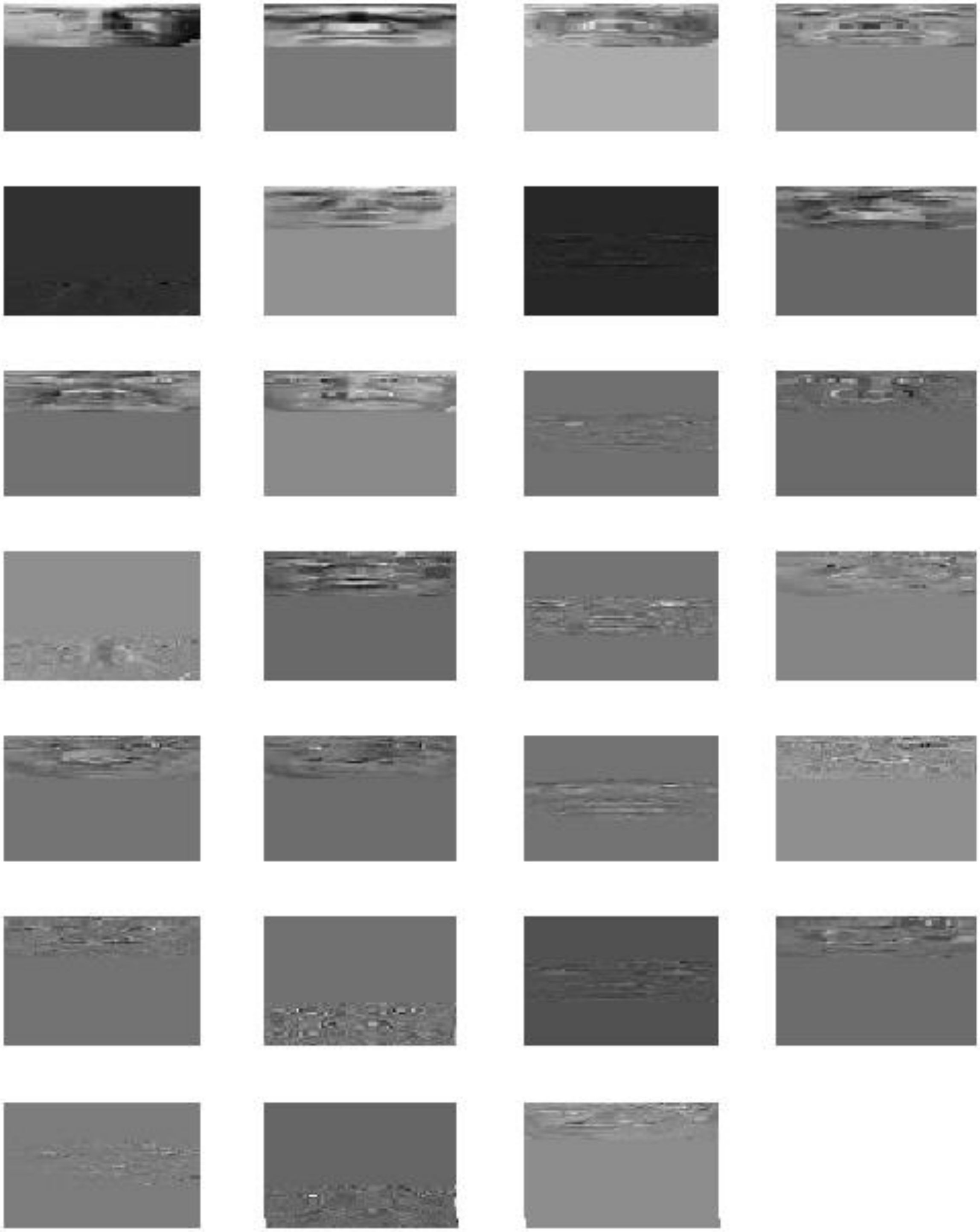

Fig. 2.10. The main eigenfaces

Table 2.3. The mean distance values

	1	2	3	4	5	6	7	8	9	10
D_1	2.573	1.919	2.557	2.736	5.795	2.2702	2.108	3.147	5.101	1.923
D_2	3.090	3.859	2.788	1.954	6.716	2.5956	1.789	2.623	6.959	3.467
D_3	2.351	3.257	2.273	2.534	6.103	3.1354	3.293	2.331	5.143	2.926

2.2.2. Face recognition technique using 2D Gabor filtering

The Gabor filters are successfully used in various image processing and analysis domains, such as: image smoothing, image coding, texture analysis, shape analysis, edge detection, fingerprint and iris recognition. The Gabor filter (Gabor Wavelet) represents a band-pass linear filter whose impulse response is defined by a harmonic function multiplied by a Gaussian function. Thus, a bi-dimensional Gabor filter constitutes a complex sinusoidal plane of particular frequency and orientation modulated by a Gaussian envelope [77]. It achieves an optimal resolution in both spatial and frequency domains. The 2D Gabor filters have been increasingly used in the face recognition domain, too [77,78].

I developed a supervised 2D Gabor filtering-based face recognition technique that is described here [79]. My approach designs 2D odd-symmetric Gabor filters for facial image recognition, having the following form:

$$G_{\theta_k, f_i, \sigma_x, \sigma_y}(x, y) = \exp\left(-\left[\frac{x_{\theta_k}^2}{\sigma_x^2} + \frac{y_{\theta_k}^2}{\sigma_y^2} \right] \right) \cdot \cos\left(2\pi f_i x_{\theta_k} + \varphi \right) \tag{2.16}$$

where $x_{\theta_k} = x\cos\theta_k + y\sin\theta_k$, $y_{\theta_k} = y\cos\theta_k - x\sin\theta_k$, f_i provides the central frequency of the sinusoidal plane wave at an angle θ_k with the x – axis, σ_x and σ_y represent the standard deviations of the Gaussian envelope along the two axes, x and y. We set the phase $\varphi = \pi / 2$ and compute each orientation as $\theta_k = \frac{k\pi}{n}$, where $k = \{1, ..., n\}$ [79,80].

The two-dimensional filters $G_{\theta_k, f, \sigma_x, \sigma_y}$, provided by (2.16), represent a group of wavelets that optimally captures both local orientation and frequency information of the image. Each face image must be filtered with $G_{\theta_k, f, \sigma_x, \sigma_y}$ at various orientations, frequencies and standard deviations. So, we consider some proper value for the filter parameters (variance values, radial frequencies, orientations): $\sigma_x = 2$, $\sigma_y = 1$, $f_i \in \{0.75, 1.5\}$ and n = 5, which means $\theta_k \in \left\{ \frac{\pi}{5}, \frac{2\pi}{5}, \frac{3\pi}{5}, \frac{4\pi}{5}, \pi \right\}$. So, we construct 2D Gabor filter bank $\left\{ G_{\theta_k, f_i, 2, 1} \right\}_{f_i \in \{0.75, 1.5\}, k \in [1, 5]}$, composed of 10 channels [79,80].

The modelled filter set is applied to the current face, by convolving that facial image with each Gabor filter from this set. The resulted Gabor responses are then concatenated into a three-dimensional feature vector. If I represents a $[X \times Y]$ face image, then the proposed feature extraction model can be expressed as:

$$V(I)[x, y, z] = V_{\theta(z), f(z), \sigma_x, \sigma_y}(I)[x, y] \tag{2.17}$$

where $x \in [1, X]$, $y \in [1, Y]$ and

$$\theta(z) = \begin{cases} \theta_z, & z \in [1, n] \\ \theta_{z-n}, & z \in [n+1, 2n] \end{cases}, \quad f(z) = \begin{cases} f_1, & z \in [1, n] \\ f_2, & z \in [n+1, 2n] \end{cases} \tag{2.18}$$

and

$$V_{\theta(z), f(z), \sigma_x, \sigma_y}(I)[x, y] = I(x, y) \otimes G_{\theta(z), f(z), \sigma_x, \sigma_y}(x, y) \tag{2.19}$$

A fast 2D convolution could be performed using the *Fast Fourier Transform* (*FFT*) [2], therefore (2.19) is equivalent to $V_{\theta(z), f(z), \sigma_x, \sigma_y}(I) = FFT^{-1}[FFT(I) \cdot FFT(G_{\theta(z), f(z), \sigma_x, \sigma_y})]$. For each facial image *I* one obtains a 3D face feature vector *V* (*I*), having a $[X \times Y \times 2n]$ dimension and representing a robust content descriptor [79]. A face image (marked with a red rectangle) and its 10 Gabor representations (components of the corresponding feature vector) are displayed in Fig. 2.11.

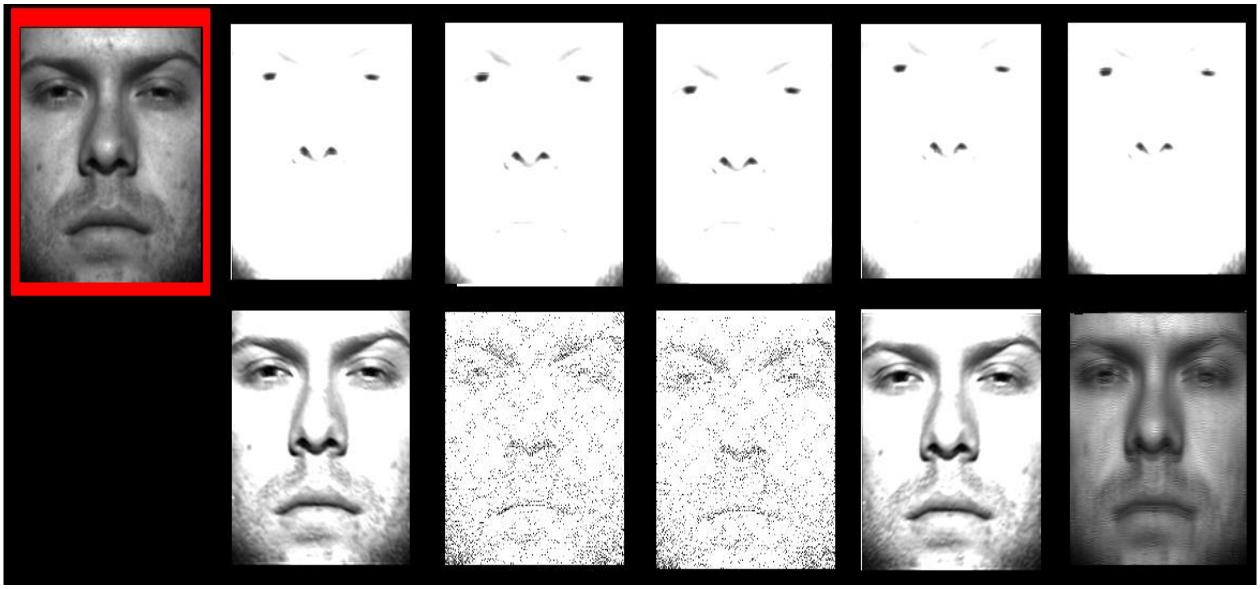

Fig. 2.11. Face image and its 2D Gabor representations (feature vector components)

Feature vector classification represents the second step of the face identification process. In [79] I provide a supervised classification approach for these Gabor filter-based 3D feature vectors. The training set of this classifier is created first. Thus, one considers *N* registered individuals, each of them providing a set of faces of its own. The training face set is modeled as $\left\{\left\{F_j^i\right\}_{j=1,\ldots,n(i)}\right\}_{i=1,\ldots,N}$, where F_j^i represents the *j*th face image of the *i*th user and *n*(*i*) is the number of training faces of the *i*th user. Next, one computes the training feature vector set as $\left\{\left\{V(F_j^i)\right\}_{j=1,\ldots,n(i)}\right\}_{i=1,\ldots,N}$. A minimum average distance classification based on this training vector set is then performed on the input face set, each face being inserted in the class of the user corresponding to the minimum average distance. The classification model is described as:

$$Class(j) = \arg\min_{i \in [1,N]} \frac{\sum_{t=1}^{n(i)} d(V(I_j), V(F_t^i))}{n(i)}, \forall j \in [1, K] \tag{2.20}$$

where $Class(j) \in [1, N]$ represents the index of the face class where input I_j is introduced and d is the squared Euclidian metric. The facial identification result, represented by the obtained classes $C_1,...,C_N$, is followed by a threshold-based face verification process [79,80], modeled as:

$$\forall i \in [1, N], \forall I \in C_i : \frac{\sum_{j=1}^{n(i)} d(V(I), V(F_j^i))}{n(i)} > T \Rightarrow C_i = C_i - \{I\} \tag{2.21}$$

where the threshold value is automatically computed as $T = \max_{i \leq N}\left(\max_{j \neq k \in [1, n(i)]} d\left(V(F_j^i), V(F_k^i)\right)\right)$.

The performed recognition experiments demonstrate the effectiveness of the described approach [79,80]. A high face recognition rate (over 80%) is achieved by our technique, on the basis of experiments involving hundreds frontal images. We have obtained high values for the performance parameters, *Precision* and *Recall*. We have used *Yale Face Database B*, containing thousands of $[192 \times 168]$ facial images at different illumination conditions, representing various persons, for our recognition tests [76]. While we obtain very good recognition results for frontal faces, considerable lower recognition rates are achieved for images representing rotated or non-frontal faces.

Method comparisons have been also performed. The performance of this approach has been compared with those of Eigenface-based systems. We have tested the Eigenface algorithm of Turk & Pentland [71], the Eigenface method proposed by us [79] and this Gabor filter based technique, on the same face dataset. The values of statistical parameters *Precision* and *Recall*, computed for these algorithms, are registered in Table 2.4. As one can see in this table, the three face recognition techniques provide comparable good results. The original Eigenface-based technique performs slightly better than our two methods.

Table 2.4. Performance parameter comparison

	Eigenface (T&P)	Eigenface (Barbu)	Gabor filter based method
Precision	0.95	0.85	0.88
Recall	0.94	0.85	0.90

A face recognition example is described next. A small facial training set, composed of the faces of three authorized persons, is represented in Fig. 2.12. A small sized input image set, with K = 6, is displayed in Fig. 2.13. The computed average distance values are registered in Table 2.5.

From this table, it results the following face identification: *User* 1 => $\{I_2, I_4\}$, *User* 2 => $\{I_1, I_5\}$, *User* 3 => $\{I_3, I_6\}$. We also compute T = 0.9759, so, the face verification provides the final recognition result: *User* 1 => $\{I_2, I_4\}$, *User* 2 => $\{I_1\}$, *User* 3 => $\{I_3, I_6\}$, *Unregistered* => $\{I_5\}$.

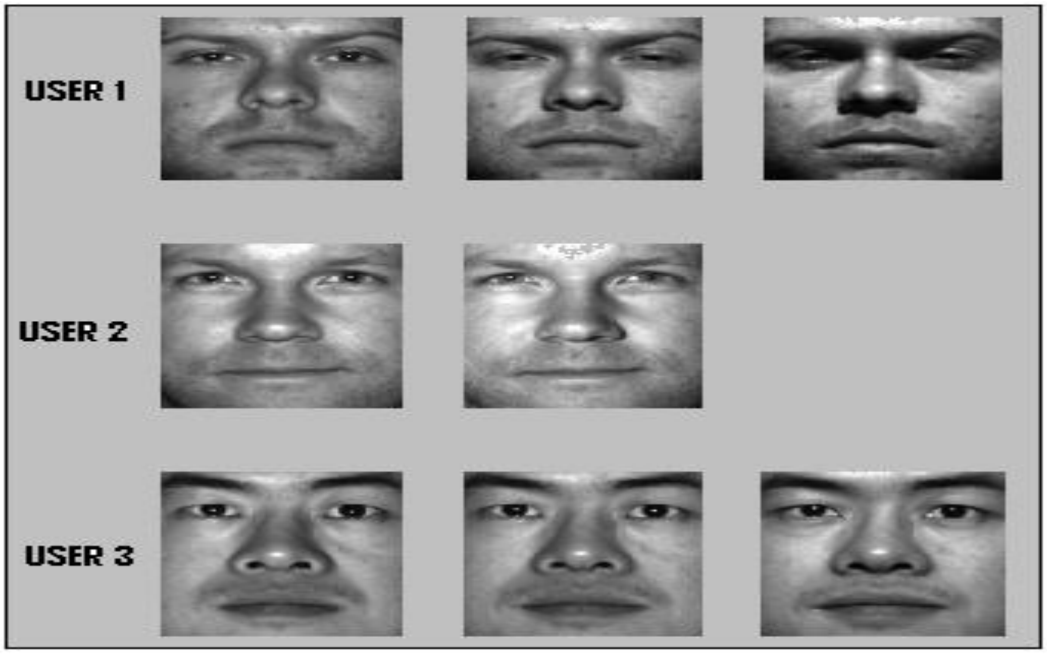

Fig. 2.12. Face training set

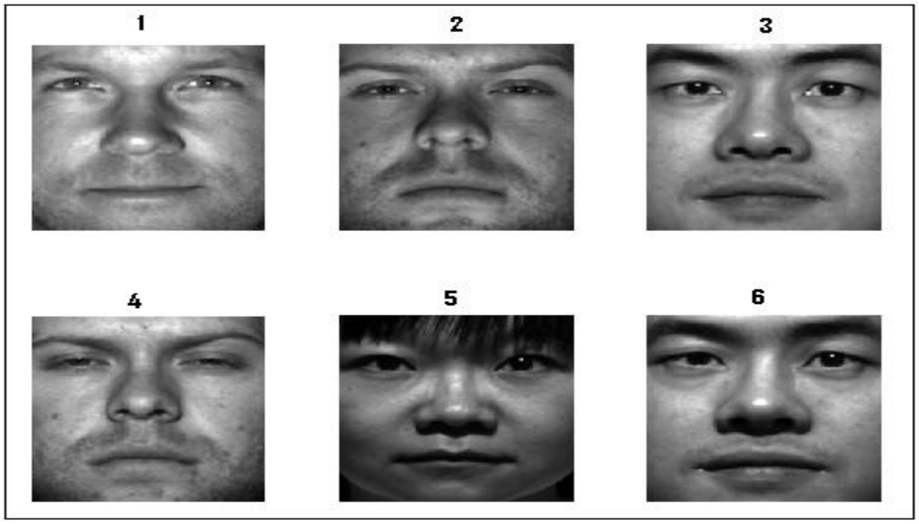

Fig. 2.13. Input face set

Table 2.5. Resulted average distance values:

	I_1	I_2	I_3	I_4	I_5	I_6
User 1	1.0970	0.6208	1.5475	0.7779	1.6175	1.0379
User 2	0.5581	1.4291	1.7623	1.2103	1.1313	1.2551
User 3	1.2154	1.0946	0.9278	1.2548	1.3562	0.6333

2.2.3. Automatic unsupervised face recognition system

In the previous subsections we described two supervised facial recognition techniques that work properly for cooperative human subjects, being very useful for access control. Now we describe an unsupervised face recognition method that could deal with non-cooperative subjects and can be successfully used by the surveillance systems [51].

Most of the existing face authentication techniques perform the recognition in a supervised manner, but numerous unsupervised methods have been developed recently. Thus, we mention the SOM-based face recognition techniques [81], the unsupervised methods based on PCA or ICA (Independent Component Analysis) [82], and the unsupervised face recognition by associative chaining [83]. We modeled an unsupervised facial recognition system having also an automatic character [37].

In [37] we considered the following unsupervised recognition task. The set of faces $\{F_1, \ldots, F_n\}$ must be clustered automatically, on the similarity basis. The faces from each resulted cluster have to belong to the same person. Because of the unsupervised character of the process, the persons are unknown and no facial training set is available. Even the number of these persons is unknown, given the automatic character of the process.

A robust SIFT-based facial feature extraction is performed on F_i images [37]. Published by David Lowe in 1999, Scale Invariant Feature Transform represents a computer vision algorithm that locates and describes local image features [84]. SIFT characteristics are widely used in computer vision areas like object tracking and recognition. The SIFT algorithm determines the main keypoints from the image to produce a proper feature description. The extracted features are invariant to scaling, orientation, affine transforms and illumination changes [84], so they are well-suited for face description.

The SIFT characteristics of a face image are obtained in several steps. First, one computes the maxima and minima values of the result of Difference of Gaussians (DoG) filters applied at different scales on the face image. Then, the low contrast points are discarded. A dominant orientation is then assigned to each of the identified keypoints. For each keypoint one computes a local feature descriptor on the basis of the local image gradient, transformed according to keypoint orientation to obtain orientation invariance. So, one obtains a SIFT feature vector of 128 coefficients for each face keypoint. The face feature vector corresponding to F_i is modeled as follows:

$$V(F_i) = \left(\begin{bmatrix} v_1(F_i) \\ \ldots \\ v_{n_i}(F_i) \end{bmatrix}, \begin{bmatrix} loc_1(F_i) \\ \ldots \\ loc_{n_i}(F_i) \end{bmatrix} \right) \tag{2.22}$$

where $v_k(F_i)$ is the feature vector of the k^{th} keypoint of F_i and $loc_k(F_i)$ is a pair of coordinates representing its location in the face image [37]. The keypoints are positioned in the feature vector given by (2.22) from left to right and from top to the bottom. Since $V(F_i)$ represent complex feature vectors, the distances between them could not be measured using the Euclidean metric or other conventional metrics. So, the special metric introduced in subsection 1.4.2 is used for this purpose [37]. The set of matches used by that metric and given by (1.53) is replaced in this case with:

$$M_{ij} = \{(k,t) \mid d_E(v_k(F_i),v_t(F_j)) \le T_1 \,\&\, d_E(loc_k(F_i),loc_t(F_j)) \le T_2\} \tag{2.23}$$

where the threshold values T_1 and T_2 are detected empirically, and d_E represents the Euclidean metric.

The face feature vector classification is performed in [37] by applying the validity index-based automatic clustering model described in 1.4.4 on the feature set $\{V(F_i)\}_{i=1,\dots n}$. The clustering algorithm used repeatedly in that model is now a hierarchical agglomerative one that computes the distance between clusters using the average linkage clustering approach, and the distances between facial feature vectors are computed using (1.52) and (2.23).

The described unsupervised facial recognition method has been tested on the same *Yale Face Database B*, containing thousands of 192 × 168 faces, used in the previous cases [76]. A high face recognition rate, of approximately 90%, is obtained, being influenced also by the threshold value selection. The optimal values used in (2.23) are $T_1 = 0.65$ and $T_2 = 15$. High performance parameters values have been also achieved: *Precision* = 0.93, *Recall* = 0.91 and F_1 = 0.92. These values prove that our recognition technique produces very few missed hits and very few false positives.

An unsupervised face recognition example is described next. Image set displayed in Fig. 2.14 contains 8 faces, $\{F_1,...,F_8\}$, belonging to 3 persons (2 males, 1 female). Face feature vectors, $V(F_{1-8})$, are obtained from (2.22). The automatic clustering process is applied, resulting the optimal number of clusters $K_{optim} = 3$ and the final recognition result: $C_1 = \{F_1, F_6, F_8\}$, $C_2 = \{F_2, F_4\}$ and $C_3 = \{F_3, F_5, F_7\}$. These classification results are displayed in Fig. 2.15, each row of it containing the faces from a class and their SIFT characteristics: keypoints and their orientations.

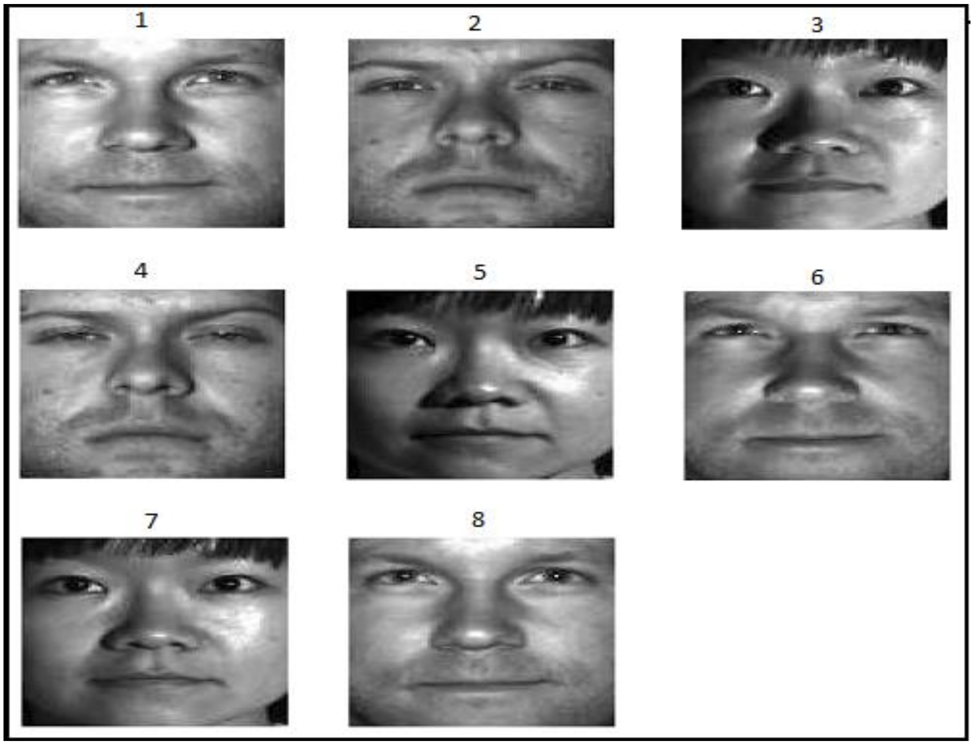

Fig. 2.14. The set of faces to be recognized

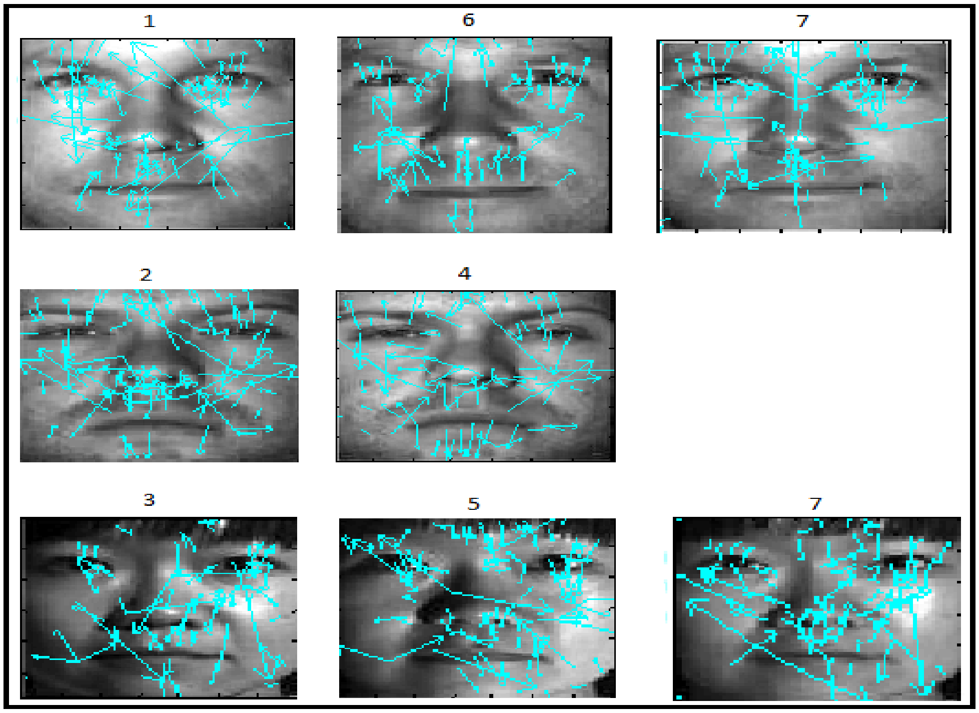

Fig. 2.15. SIFT characteristics and face clustering result

Method comparison was also performed [37]. Because of its automatic character, the proposed recognition technique executes much faster and provides better results for large face sets than non-automatic approaches. Also, our SIFT-based method produces better recognition results than unsupervised techniques using other face features, such as Eigenfaces [70,71] or 2D Gabor filtering based characteristics [78,79]. We also considered some other versions of the automatic classification algorithm. Thus, we tested it with various *K*-means algorithms [45] and Self-Organizing Feature Maps (SOFM) [81], instead of the region-growing procedure, on the same face feature sets, but achieved weaker recognition results and also slower execution times.

The performance parameters of several face recognition techniques are registered in the next table. One can see their values for this SIFT-based unsupervised method, the PCA (Eigenface) algorithm [70,82], the ICA-based technique [82], unsupervised version of Barbu's 2D Gabor filtering approach [80], and an algorithm using SIFT characteristics with *K*-means clustering. As it results from Table 2.6, the recognition technique provided here achieves the highest values for *Precision*, *Recall* and F_1, which means it outperforms the other approaches.

Table 2.6. The performance parameters for several face recognition approaches

	This method	Eigenface (PCA)	ICA	Unsupervised Gabor filter-based	SIFT/*K*-means
Precision	0.93	0.92	0.90	0.88	0.88
Recall	0.91	0.90	0.88	0.86	0.91
F_1	0.9199	0.9099	0.8899	0.8699	0.8947

The recognition techniques measured by performance parameters registered in Table 2.6 have been tested on hundreds [192 × 168] faces of *Yale Face Database B*. Their corresponding RPC (*Recall versus Precision Curves*) are displayed in Fig. 2.16. The RPC of our model, marked in blue, also proves its performance.

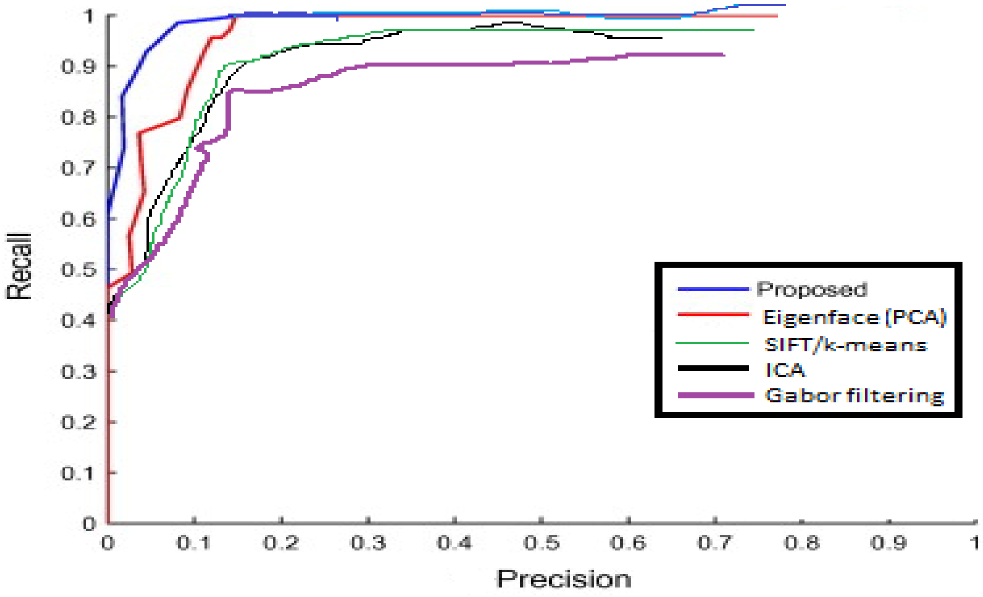

Fig. 2.16. RPC curves for several face recognition approaches

Because of its automatic and unsupervised character, the facial recognition technique described here can be successfully applied not only for non-cooperative subjects in video surveillance systems [85], but also for voluminous face sets. So, an important application area of our unsupervised recognition approach is face database indexing and retrieval. Some robust clustering-based face indexing methods [86] can be developed using our face recognition system.

2.3. Person authentication via fingerprint recognition

The fingerprint represent one of the most known forms of biometrics used to authenticate human persons. Because of their uniqueness and consistency over time, fingerprints have been used for person recognition for over a century [87].

Fingerprint recognition represents the computerized automated process of determining the identity of an individual using the characteristics of his fingerprints. Obviously, a fingerprint recognition system is a biometric authentication system that performs two main operations: fingerprint identification and verification. Fingerprint identification associates each input fingerprint with a registered user of the system, consisting of a fingerprint feature extraction and a feature vector classification. Fingerprint verification represents the task of validating the associated identity of a fingerprint, usually using proper threshold values.

The main application area of fingerprint recognition systems is law enforcement. Another important application field of fingerprint authentication is access control to various services, numerous security systems being based on fingerprints [88].

The fingerprint recognition approaches are divided into two major categories: *minutiae-based* [89] and *pattern-based* techniques [90]. We developed recognition methods from both categories. Thus, a robust minutiae-based fingerprint authentication model is described in the next subsection. Then, a pattern-based fingerprint recognition technique using 2D Gabor filters is presented in 2.3.2. Another pattern-based recognition approach, but based on 2D Wavelet Decompositions, is described in the last subsection.

2.3.1. Minutiae-based fingerprint authentication approach

The fingerprint is composed of *ridges* and *valleys*. The minutia points represent unique features found within the fingerprint patterns. There are various types of minutia details such as: ridge endings, bifurcations, short ridges, dots, crossovers, spurs and islands [38,89]. The most important fingerprint points are the ridge endings, short ridges and bifurcations.

Most modern fingerprint recognition technologies are based on minutiae matching [89]. The idea of minutiae-based matching is if one can find enough minutiae in one image that have corresponding minutiae in another image, then those images are most likely from the same fingerprint. The most commonly used minutiae points by the existing fingerprint recognition approaches are the ridge endings and bifurcations. Any minutiae-based fingerprint recognition technique performs a *minutiae detection* process before *minutiae matching*.

We proposed several minutiae based recognition methods in our past works [38,53,91]. The same minutiae detection procedure was performed by each of them. First, a fingerprint image enhancement process, consisting of denoising and restoration operations, was applied. While there exist some direct minutiae extraction techniques that identify the fingerprint minutia points by following the ridge line in the grayscale image of the fingerprint [92], we considered a binarization-based solution. The enhanced image was converted from grayscale to the binary format using a thresholding algorithm.

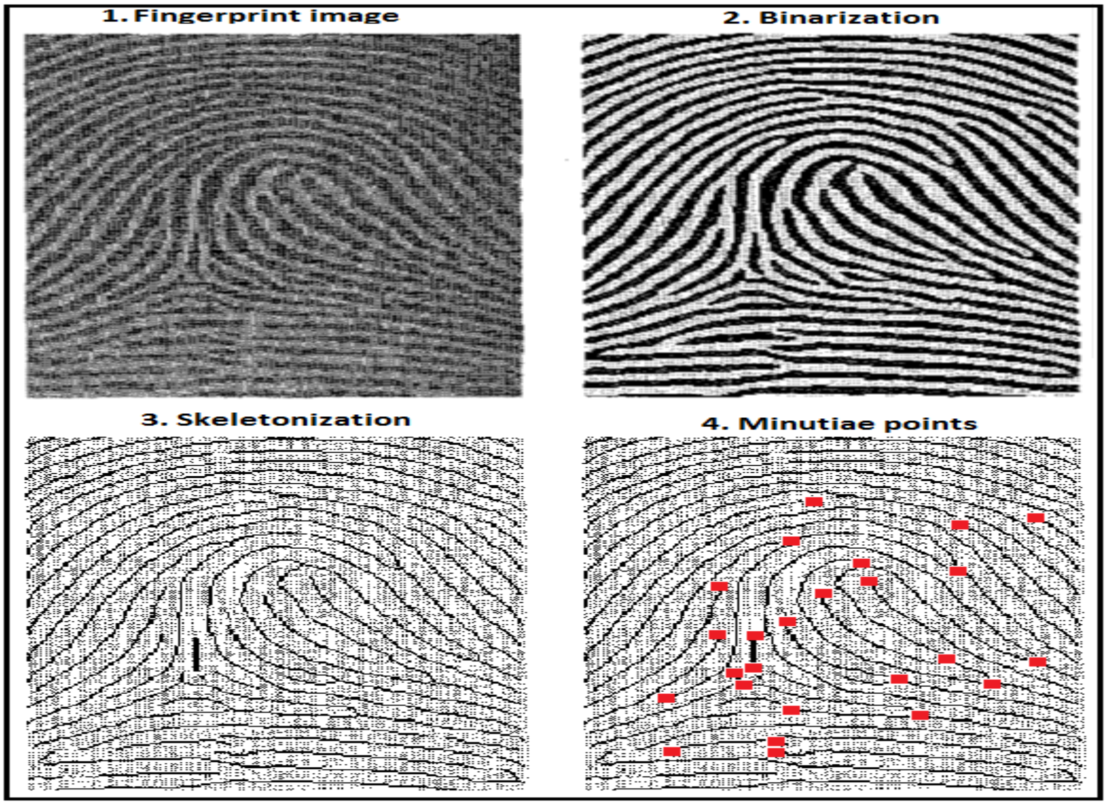

Fig. 2.17. Minutiae detection process

Then, the *skeletonization*, performed using a *thining* algorithm, produced the *morphological skeleton* of the binary image of the fingerprint [93]. Image thinning represents a morphological process that is similar to erosion and opening and produces very thin ridges, having a width of one pixel [93]. The most popular thinning algorithms are medial axis method, contour generation method, local thickness based thinning approach, sequential and parallel thinning [94].

The thinned ridges facilitated the fingerprint minutiae detection task. We considered *8 – neighborhoods* of black pixels in this identification process. For each black pixel (0 value) of the skeleton, one determined if it represents either a minutia point or an ordinary pixel. The detection algorithm counted the number of neighbours of the current black pixel. There could be three possible situations. If the pixel has only one neighbour, then it represents a ridge ending. If the pixel has at least 3 neighbours, then it represents a bifurcation. If the pixel has 2 neighbours, then it is an intermediary pixel. A minutia point detection process is described in Fig. 2.17.

The identification process is followed by the minutiae matching. In [91] we develop some minutiae-based fingerprint matching approaches based on neural networks. The modeled NN-based classifiers operated on minutiae-based feature vectors obtained using some Zernike moments. We will not insist on those NN-based recognition techniques here, describing the most recently developed fingerprint matching approach instead.

So, in **selected paper 4** (Barbu 2011[38]) we introduce a robust fingerprint recognition system based on minutia point matching. In its feature extraction stage, one models the fingerprint feature vector on the basis of the feature vectors corresponding to the detected minutiae [38]. The sequence of the minutia points identified in the fingerprint *F* is noted as $\left\{M_1^F,...,M_{m(F)}^F\right\}$. The fingerprint feature extraction process is modeled as follows:

$$V(F)=\left[V(M_1^F),...,V(M_{m(F)}^F)\right] \tag{2.24}$$

where $V(M_i^F)$ represents the feature vector of M_i^F, $i\in\left[1,m(F)\right]$. Each of these vectors contains the essential information related to the corresponding minutia: its *type* (ridge ending, bifurcation), its *position* (provided by coordinates) and its *orientation,* representing the angle of the minutia tangent and orizontal axis [89,95]. So, the feature vector of a fingerprint minutia is constructed as:

$$V(M_i^F)=\left[Type_i^F,x_i^F,y_i^F,\theta_i^F\right] \tag{2.25}$$

where $Type_i^F$ represents the minutia type of M_i^F, x_i^F and y_i^F are its coordinates, and θ_i^F represents the orientation of M_i^F. These measures of a minutia, which compose the feature vector, are represented in Fig. 2.18.

From relations (2.24) and (2.25) we determine the final form of the feature vector of fingerprint *F*:

$$V(F)=\left[\left(Type_1^F,x_1^F,y_1^F,\theta_1^F\right),...,\left(Type_{m(F)}^F,x_{m(F)}^F,y_{m(F)}^F,\theta_{m(F)}^F\right)\right] \tag{2.26}$$

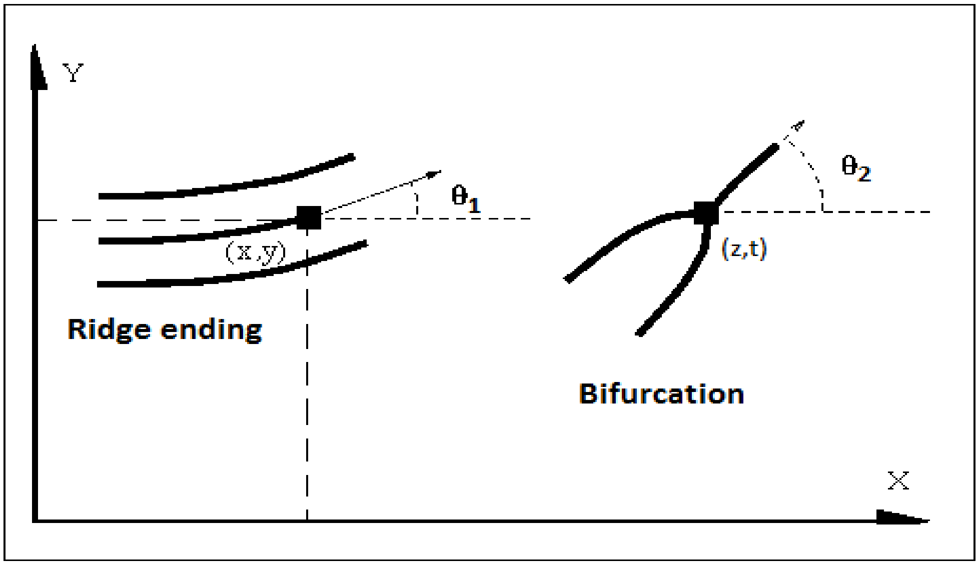

Fig. 2.18. The minutiae used in the matching process

The components M_i^F are arranged in the sequence corresponding to F in the order given by their coordinates. They were aligned from left to right and from top to the bottom, as follows:

$$\begin{cases} x_1^F \leq \ldots \leq x_i^F \leq \ldots . \leq x_{m(F)}^F \\ x_i^F = x_{i+1}^F \Rightarrow y_i^F < y_{i+1}^F \end{cases} \tag{2.27}$$

Obviously, the fingerprint feature vectors computed by (2.26) represent complex structures that cannot be classified using conventional metrics. We use the special metric described in 1.4.2 to measure the distances between these feature vectors [38]. The metric given by (1.52) took in this case the next form:

$$d(V(F_1),V(F_2)) = \frac{m(F_1)+m(F_2)}{2} - p(V(F_1),V(F_2)) \tag{2.28}$$

where

$$p(V(F_1),V(F_2)) = card\left\{ i \leq \min\left(m(F_1), m(F_2)\right) \middle| Type_i^{F_1} = Type_i^{F_2}, x_i^{F_1} \cong x_i^{F_2}, y_i^{F_1} \cong y_i^{F_2}, \theta_1^{F_1} \cong \theta_1^{F_2} \right| \right\} \tag{2.29}$$

Then, a supervised fingerprint classification is performed, using the minimum average distance classifier [38] or the K-NN [61]. So, we may consider a set of input fingerprint images $\{F_1,...,F_n\}$ to be authenticated. We model a training set composed of templates representing the fingerprints of N registered individuals. The training set is obtained as $\left\{\left\{T_j^i\right\}_{j=1,...,n(i)}\right\}_{i=1,...,N}$, each T_j^i being the jth template of the ith registered user. Each fingerprint is associated to the registered user corresponding to the minimum average distance between the fingerprint's feature vector and the training vectors of that user. Thus, the class of the current input fingerprint results as $C_{ind(j)}$, where $ind(j) = \arg\min_{i\in[1,N]} \frac{\sum_{k=1}^{n(i)} d(V(F_j),V(T_k^i))}{n(i)}, \forall j \in [1,n]$ and the distance function *d* is given by (2.28) - (2.29). Next, a fingerprint verification process is performed within the resulted *N* fingerprint classes, $C_1,...,C_N$, to validate the identifications [38]. The verification procedure uses a properly chosen threshold.

We have performed numerous fingerprint recognition tests using the described authentication approach. Satisfactory results have been obtained and a high recognition rate, of approximately 90%, has been achieved for this minutiae-based method. One of the FVC2004 fingerprint databases has been used for our recognition experiments. It contains 80 fingerprints of 10 different fingers, and was created using low cost fingerprint scanners [95].

Our technique produces a low number of false positives and false negatives (missed hits), obtaining high values for the performance parameters such as *Precision*, *Recall* (almost 1) and the combined F_1 measure. Also, we have compared this minutiae-based technique with some other fingerprint recognition algorithms, and found it provides a lower execution time and better recognition results.

2.3.2. Fingerprint pattern matching using 2D Gabor filtering

The basic fingerprint patterns are *arch*, *whorl* and *loop*. The pattern-based authentication algorithms compare these basic patterns between a input fingerprint image and a previously stored template. This is done by registering digital fingerprint images based on a so called “core point” identified as a reference point in the pattern of fingerprints [96]. Then the fingerprint image is globally represented by using 2D Gabor filters [90], Fourier descriptors, Wavelet transforms [99] or the quantified co-sinusoidal triplets.

We approached the pattern-based fingerprint recognition in several papers [53,97-99], efficient matching techniques based on Gabor filtering and Wavelets being developed. A two-dimensional Gabor filter based fingerprint pattern matching technique modeled by us is described in this subsection, while a 2D Wavelet Transform based recognition approach will be described in 2.3.3.

Some fingerprint pre-processing operations must be performed before the feature extraction, in order to improve the fingerprint image to a certain standard. We apply three techniques of preprocessing: normalization, segmentation and reference point detection. By normalization we improved the contrast of the fingerprint and this was done by distributing the range of gray levels in the image through the entire [0, 255] range [53,97]. The normalization form of the initial grayscale image *A* of dimension [$M \times N$] is computed as:

$$A^{'}(i,j) = 255 \cdot \frac{A(i,j) - \min(A)}{\max(A) - \min(A)}, \forall i \in [1,M], \forall j \in [1,N] \qquad (2.30)$$

By segmentation one gets the region of interest where the fingerprint is positioned inside the image, as fingerprint images could contain white regions around the real fingerprints. One divides the image in [8x8] blocks, computing the percentage of gray level pixels as opposed to white pixels in each of these blocks and applying a threshold in order to qualify such a block as belonging to the region of interest (percentage higher than the threshold value) or not.

The *reference point*, or *core point*, of the fingerprint, used as the center of the feature map corresponding to the fingerprint, is detected as the point where the curvature of the fingerprint ridge is the most accentuated [53,90]. We construct an orientation map of all ridges in the fingerprint image and then on this map one detects the pixels for which their orientation is more different than the one of its neighbors [90,97].

As we have already mentioned, the 2D Gabor filtering represents a very useful tool for many areas of image processing and analysis. We use it here to extract global and local features of the fingerprint valleys and ridges. These two-dimensional filters capture local orientation and frequency information, very useful in characterizing fingerprint patterns [90]. We model an even symmetric 2D Gabor filter, given by:

$$G_{\theta_i, f, \sigma_x, \sigma_y}(x, y) = \exp\left(-\left[\frac{x_{\theta_i}^2}{\sigma_x^2} + \frac{y_{\theta_i}^2}{\sigma_y^2}\right]\right) \cdot \cos\left(2\pi f x_{\theta_i}\right), \tag{2.31}$$

where $x_{\theta_i} = x\cos\theta_i + y\sin\theta_i$ and $y_{\theta_i} = y\cos\theta_i - x\sin\theta_i$ [53, 98]. The parameter f is determined in relation with the frequency of the ridges, which corresponds to the average distance between the ridges. For a 500 dpi image, the average distance between ridges is 8 pixels, hence we considered the value $f = 1/8 = 0.125$. We also set $\sigma_x = \sigma_y = 4$ as a compromise between the robustness to noise and the filtering precision [98]. We also consider 8 orientations for filtering, therefore $\{\theta_1, ..., \theta_8\} = \{0^\circ, 22.5^\circ, 45^\circ, 67.5^\circ, 90^\circ, 112{,}5^\circ, 135^\circ, 157{,}5^\circ\}$. The fingerprint image is filtered by convolution with the modeled 2D Gabor filter set, for the 8 considered orientations.

Due to performance reasons, the results of the Gabor filtering cannot be used directly as feature vectors. Instead, the Gabor filtered image is processed through a grid centered in the core point of the fingerprint [53]. That rectangular grid is composed of [10 x 10] cells, each cell having 16 by 16 pixels.

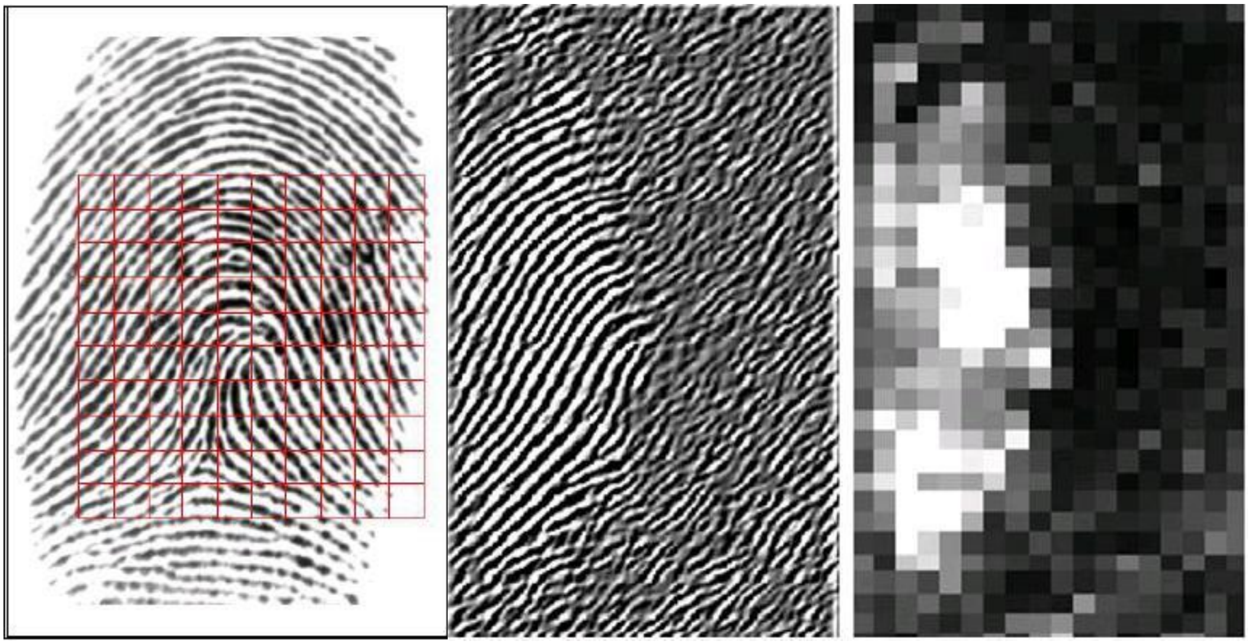

Fig. 2.19. Rectangular grid applied to fingerprint (L), Gabor filtered fingerprint (C), feature map (R)

For each rectangular cell we calculate the standard deviation of the filtered fingerprint, which corresponds to the local energy of the Gabor filter response [53]. The collection of standard deviation values extracted from the grid forms a feature map for the fingerprint. There are obtained 8 such feature maps, one for each orientation. In Fig. 2.19 one can see the applied grid, the filtering result and the obtained feature map.

On the basis of these feature maps, we create a tridimensional feature vector for each fingerprint [53,98]. Therefore, for the analyzed fingerprint *A*, its 3D feature vector is modeled as follows:

$$V(A)[x,y,i] = H_i(A), \forall i \in [1,8] \tag{2.32}$$

where $H_i(A)$ is the feature map of fingerprint *A* corresponding to the θ_i orientation of the Gabor filter defined by (2.31). To measure the distance between two such feature vectors, the *sum of absolute differences* (*SAD*) between the vector components is used as a metric.

This pattern feature extraction is followed by a supervised classification of these 3D fingerprint feature vectors. The input fingerprints $\{A_1,\ldots, A_n\}$ are classified using a training set of fingerprints $\{\{Amp_j^i\}_{j=1,\ldots,n(i)}\}_{i=1,\ldots,N}$ corresponding to *N* registered persons, like in the minutiae-based recognition case. Each fingerprint A_j has to be inserted into the fingerprint class $C_{ind(j)}$, where $ind(j) = \arg\min_{i\in[1,N]} \frac{\sum_{n=1}^{n(i)} d\left(V(A_j), V(Amp_n^i)\right)}{n(i)}, \forall j \in [1,n]$ and function *d* is the SAD metric. The fingerprint verification process is performed using the already described threshold-based algorithm, the proper threshold value being detected automatically, as in (2.3).

A lot of fingerprint recognition experiments have been performed using the proposed approach, satisfactory results being obtained. The described recognition method has been applied to a database of 140 fingerprint images of 300 by 600 pixels including multiple images selected for each finger of 5 individuals. The experiments produced an authentication rate of over 80%.

Using a larger number of orientations for the Gabor filters can increase the recognition rate of our technique at the expense of computational time. The complexity of the 2D Gabor filtering in one direction is of the order *O*(*n*), as it is normalization and segmentation, while the detection of the reference point has a complexity of $O(n^2)$.

2.3.3. Pattern-based fingerprint recognition using 2D Wavelet Decomposition

The wavelet features are used by certain minutiae-based recognition techniques. While minutiae-based fingerprint authentication uses both 1D and 2D wavelet analysis [100], the pattern based fingerprint recognition uses the two-dimensional wavelet transforms only [101, 102]. In [99] we proposed a fingerprint authentication technique based on 2D – DWT.

The *2D Discrete Wavelet Transform* (*2D DWT*) represents a multi-resolution analysis technique for two-dimensional signals. Applying a multi-level 2D DWT decomposition on a digital image produces its conversion from the spatial domain into the frequency domain, while providing a series of sub-images known also as sub-bands [101]. The implementation of the Discrete Wavelet Transform is performed by using two filters for 2D signal processing: a low-pass filter and a high-pass filter. The discrete wavelet analysis passes the two-dimensional signal through these two complementary filters, the result of this processing being two 2D distinct signals. The first filter extracts the low frequency components, the most important ones, known as *approximations* of the 2D signals. The second one extracts the high frequency components, known as the *details* of such signals. In Fig. 2.20 one describes the block diagram of the decomposition of a two-dimensional discrete signal *S* on the basis of these two types of digital filters. The two resulted component signals are *A*, containing the approximations of signal *S*, respectively *D*, containing the details of the same signal [53,99]. The decomposition process may continue iteratively on several levels, the approximations' component signal, *A*, being the one reprocessed through DWT. At each level the approximations' signal is filtered and decomposed in the two 2D signals of lower resolution, and so on.

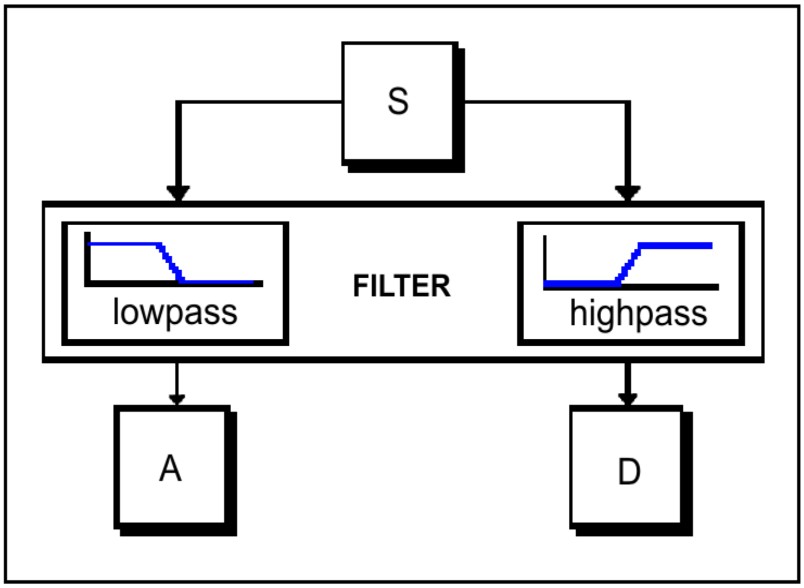

Fig. 2.20. Wavelet decomposition of a signal

The wavelet decomposition tree corresponding to an image *I* is schematically represented in Fig. 2.21. In the next figure one can see 3 decomposition levels.

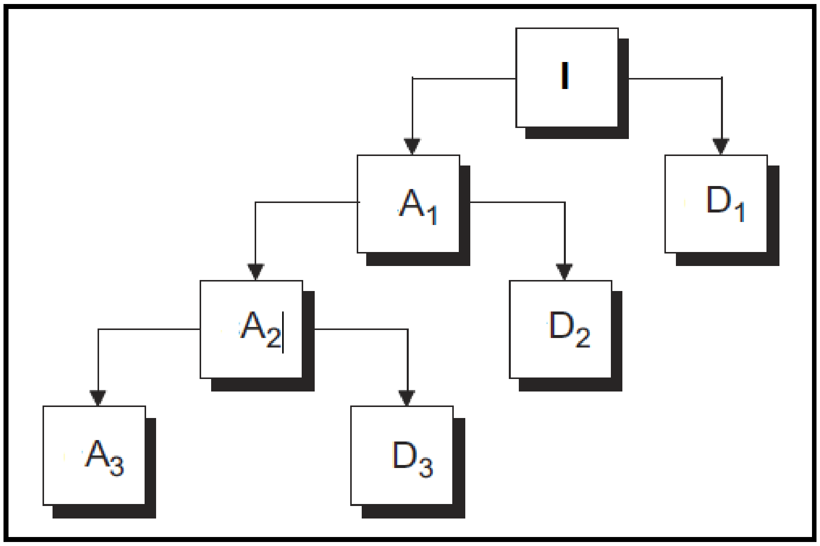

Fig. 2.21. DWT decomposition tree of the digital image *I*

We applied such DWT decompositions in the process of their recognition. In Fig. 2.21 there is represented an example of Discrete Wavelet Transformation on 4 levels for a fingerprint image.

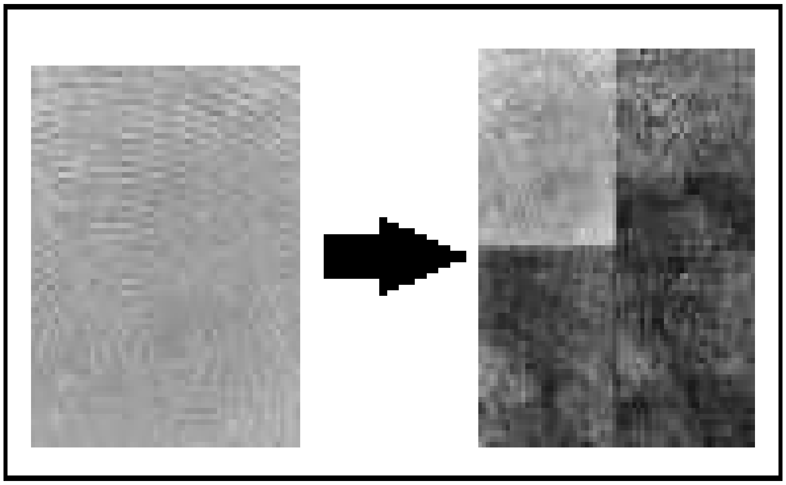

Fig. 2.22. DWT decomposition of a fingerprint

The preprocessing operations described in 2.3.2 are performed in this case, too. The most important of them is reference point detection. After preprocessing stage one models a feature vector on the basis of the wavelet characteristics of the preprocessed image. In our approach [99], we cut a $[M \times N]$ rectangular region inside the fingerprint *F*, centered on the identified reference point. Resulted image was then divided into non-overlapping $[K \times K]$ blocks [99].

For each B_i from the sequence of resulted blocks $\{B_1,...,B_n\}$, we apply the multi-resolution 2D-DWT analysis down to the *k* level. So, we start with $A_0^i = B_i$, and on each level *j* the current block A_{j-1}^i is decomposed in the sub-images A_j^i and D_j^i, corresponding to approximations and details. From here on we take into consideration only the sub-images corresponding to the resulted details, $\{D_1^i,..., D_k^i\}$, for each of them computing the normalized energy. The obtained sequence of the *k* values is considered as the feature vector of the block B_i. The feature vector of the fingerprint results by concatenating the vectors belonging to each component block, and this is done by placing them on the rows of a matrix [53,99]. The model of the wavelet-based feature extraction for the *F* fingerprint image is given by:

$$V(F)[i, j] = V(B_i)[j], \ \forall i \in [1, n], j \in [1, k] \tag{2.33}$$

where

$$V(B_i)[j] = \frac{\left\|D_j^i\right\|_2}{\sum_{t=1}^{k}\left\|D_t^i\right\|_2}, \forall i \in [1, n], j \in [1, k] \tag{2.34}$$

and $\|\cdot\|_2$ represents the Euclidean norm of the signal taken as an argument [53,99].

The 2D fingerprint feature vector $V(F)$ resulted from (2.33), has a $[n \times k]$ dimension and a high discrimination power between fingerprints because it approximates the energy of the fingerprint image on several levels. The distances between these fingerprint feature vectors can be measured using the Euclidean distance (and its variants) or SAD.

The fingerprint identification is performed by applying a similar minimum average distance based supervised classification procedure to these DWT-based feature vectors [99]. A *K*-NN feature vector classification could also be performed in this case. A threshold-based fingerprint verification operation is performed next, to validate the identifications [53,99].

The pattern-based authentication technique described here has been tested on many fingerprint datasets. The numerous performed experiments produced satisfactory results. A high fingerprint recognition rate, of approximately 85%, has been achieved and also high values have been obtained for *Precision* and *Recall* parameters. The same database as in the previous case, containing 140 fingerprint images of size [300 x 600], including 10 images per finger of 5 individuals, has been used for these tests. These images have been selected from database based on the fingerprint pattern inside the image, being preferred those having the reference point located close to image center. The poor quality images or those having the core point too close to their margins have been rejected. The reference point detection process executes quite fast, its execution taking approximately 1.5 seconds. The detection algorithm has a complexity of $O(n^2)$.

2.4. Multi-modal biometric technologies

The unimodal biometric systems must deal with various problems, such as the noisy biometric data, intra-class variability, inter-class similarity, restricted degrees of freedom, non-universality, spoof attacks and unacceptable error rates. Multimodal biometrics was introduced to address some of these limitations [103].

A multimodal biometric system can be understood in various ways. Thus, one distinguishes the following multimodal biometric system categories: *multi-sensor systems*, which have multiple sensors (optic, chip-based, ultrasound-based and others); *multi-method systems*, using multiple feature vector classification techniques; *multi-sample systems*, using various samples of the same identifier; *multi-characteristic systems*, using data from multiple biometric identifiers [103].

The architecture of a generic biometric system consists of four main modules: sensor module, feature extraction module, matching (classification) module and decision (verification) module. Biometric information fusion represents an important process performed within a multimodal biometric system. The information fusion can occur in any of the mentioned modules [103,104]. The fusion at the sensor level consists of fusing the biometric data originating from multiple sources (sensors). The fusion at the feature extractor level unifies the feature vectors computed for multiple identifiers. Classifier level fusion consists of combining the results generated by more classifiers. The decision level fusion combines the obtained authentication decisions using techniques like that based on *majority vote* [103,104].

Obviously, performing the integration of the biometric information at the first levels would produce optimal recognition results, because the feature set contains more information about input data than the matching score or the output decision. Unfortunately, the low level fusion is difficult to achieve because of incompatibilities between feature vectors corresponding to different biometric identifiers. Also, the fusion at the decision level is considered too rigid due to the availability of limited information. For this reason, the fusion is performed more often at the matching module level [103,104].

Combining multiple classifiers can be performed using fusion techniques such as *simple sum rule* [105], HyperBF networks [106], Borda count based methods [107], and other approaches [103,104]. The fusion strategies at the decision level include, besides the already mentioned majority voting, the behavior knowledge space method [108], the AND/OR rules [109] and weighted voting based on Dempster-Shafer theory of evidence [110].

In our 2012 book we provided an overview of the multimodal biometrics. Also, we considered multimodal biometric systems based on the three biometric identifiers (voice, face and fingerprints) and their corresponding authentication techniques [53]. Various multimodal biometric systems could be developed using voice, face and fingerprints [111], or combinations of two of the three biometrics. Thus, there exist numerous bimodal systems based on speech and face [112], voice and fingerprint [113], or face and fingerprint [114].

We have combined the unimodal biometric systems described in the previous sections of this chapter to obtain more complex multimodal recognition systems. Thus, in [91,115] we describe some multimodal biometric systems based on voice, face and fingerprint recognition methods. Our multi-characteristic systems contain some text-dependent voice authentication components based on the described DDMFCC-based speech analysis. The facial recognition is performed by using parts-based representation methods and a manifold learning approach. The fingerprint recognition performed within these systems is approached by minutiae detection and matching technique using neural networks [91]. The biometric information fusion is applied at the decision level, the final decision being taken by using a majority voting technique applied to the three biometric identifiers [91,115]. The developed multimodal biometric authentication approach achieved a high person recognition rate, of about 92%.

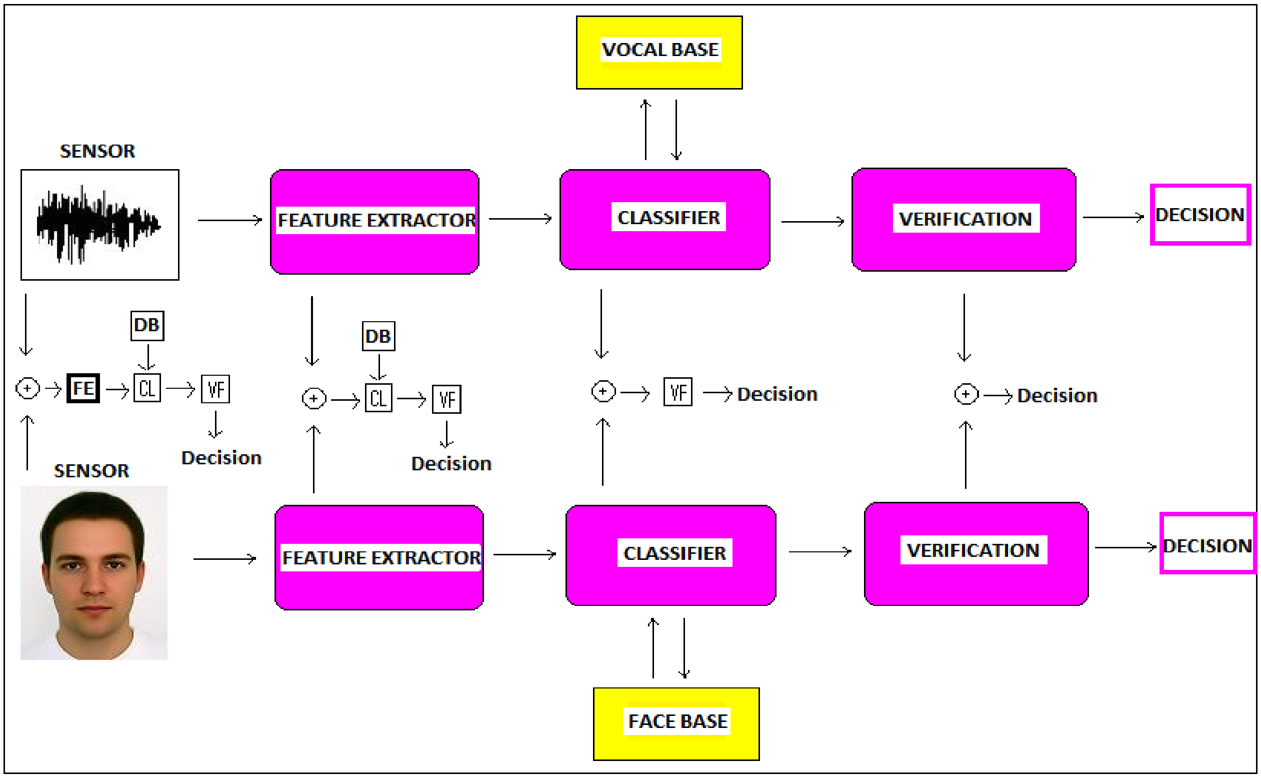

Fig. 2.23. Bimodal biometric system based on voice and face identifiers

Bimodal recognition solutions are also proposed in some of our papers. Thus, such a biometric system, using DDMFCC – based voice recognition and minutiae-based fingerprint matching, and a majority voting based decision, is proposed by us in [113].

Another bimodal biometric system developed by us, which combine a mel-cepstral based voice recognition technique and an eigenimage-based facial recognition approach is provided in [116]. The architecture of such a bimodal authentication system, based on speech and face, is described in our 2012 book [53], its scheme being displayed in Fig. 2.23. In this figure there are represented the possible fusion processes performed at the four modules of the multimodal biometric system [53].

We also developed several multimodal biometric systems having a multi-method character. Thus, in [59] we model an improved speaker recognition system using a combination of voice authentication techniques. These recognition approaches, based on DDMFCC analysis, LPC analysis, AR coefficients with trained NN (such as ART, MLP and RBF networks), and vowel preponderance, are executed and their recognition results are weighted and aggregated in a decision system [59,60].

Another multi-method biometric system constructed by us represents a bimodal pattern-based fingerprint matching system [53,97]. The modeled fingerprint authentication technology combines the two pattern-based fingerprint recognition algorithms, based on 2D Gabor filtering and the 2D Wavelet Decomposition, respectively. The flow diagram of the resulted aggregated fingerprint recognition scheme is displayed in Fig. 2.24.

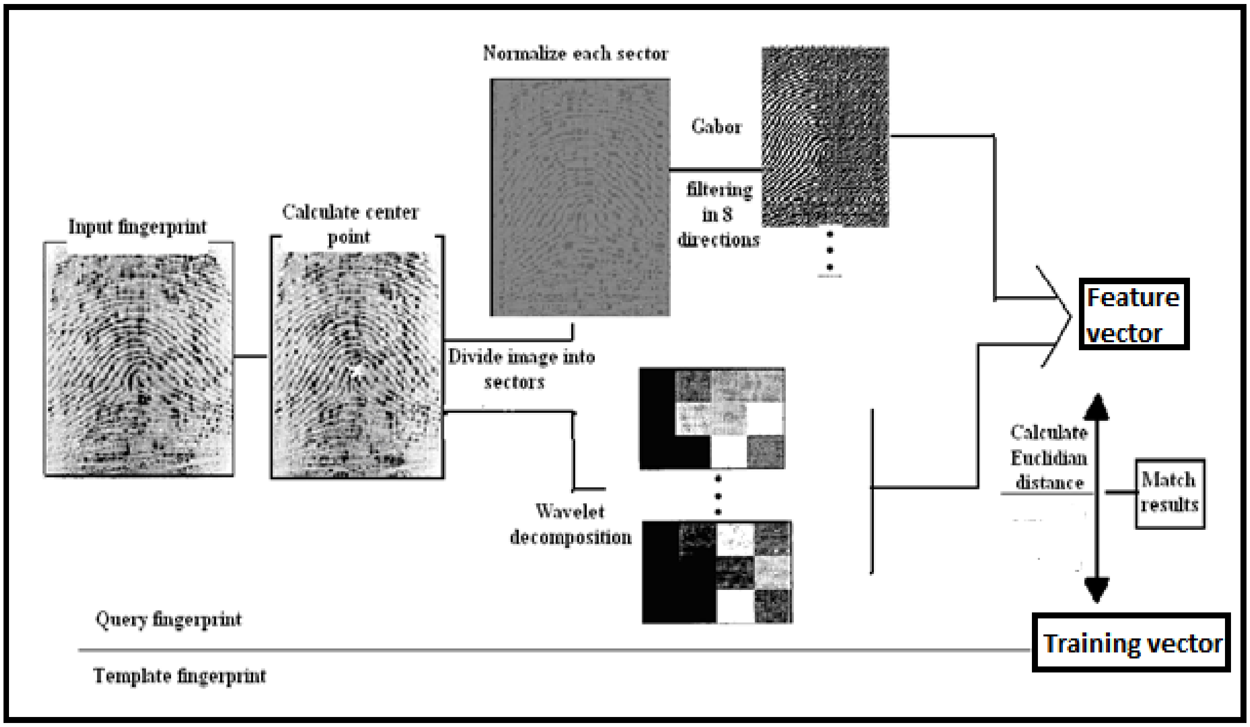

Fig. 2.24. Bimodal fingerprint recognition system based on 2D Gabor filters and Wavelet Decomposition

We also combined these two multi-method bimodal systems into a more complex multi-characteristic biometric system based on voice and fingerprint identifiers [97]. Its biometric fusion technique performed the correlation of the person authentication results produced by the voice recognition system and the fingerprint matching system. Those results were correlated at the decision module level, using a weighted inference system based on Dempster-Shafer evidence theory [97].

Combining multiple biometrics and biometric recognition approaches could enhance considerably the performance and accuracy of the human authentication process. Our multimodal biometric systems achieve much better recognition results and obtain higher recognition rates than each of their unimodal authentication components.

Our biometric authentication could be improved further by adding new identifiers and algorithms. Thus, we intend to obtain more satisfactory results in the iris recognition subdomain [54,117], such that to successfully include the person authentication techniques based on this biometric identifier (iris) into much more complex multimodal biometric systems that make also use of speech, face and fingerprint biometrics.

2.5. Conclusions

We have conducted extensive research in the biometrics domain in the last ten years. The most important research results, disseminated in 25 scientific publications (books, chapters, articles published in international journals and conference proceedings) have been described in this chapter. We brought important contributions to this research field, developing many unimodal and multimodal person authentication techniques based on various biometric identifiers.

The most reliable biometric recognition results were obtained for three identifiers: voice, face and fingerprints. We performed three types of tasks in this area: development of unimodal biometric systems; modeling unsupervised person recognition approaches; development of multimodal biometrics technologies. Each unimodal biometric system being based on a supervised recognition technique involving a single identifier, we developed several supervised voice, face and fingerprint recognition models that outperform existing approaches.

While most speaker recognition systems use same-sized 1D vocal feature vectors, our proposed (text-dependent) voice recognition models compute robust different-sized 2D feature vectors through an original DDMFCC-based voice analysis. Since conventional metrics do not work for these speech feature vectors, we have created the Hausdorff-derived metric described in previous chapter, especially for them. While the eigenimage-based face authentication system represents our main contribution in the face recognition domain, the 2D Gabor filter-based facial recognition technique constitutes another original contribution, too. We also developed some novel and effective fingerprint recognition systems. The complex minutiae-based fingerprint feature vectors, modeled by our minutia matching system and classified by using a special metric, represent our most important contribution in this field. We also constructed pattern-matching based fingerprint recognition models using feature vectors obtained from 2D Gabor filter-based and 2D-DWT based feature extractions. All these biometric authentication systems perform supervised feature vector classification processes that use a minimum average distance classifier developed by us, besides the well-known *K*-NN classifier.

The proposed unsupervised biometric recognition methods, representing also important contributions, are based on voice and face identifiers and use the validity-index based automatic clustering algorithms developed by us. The special metrics constructed for the DDMFCC-based 2D voice feature vectors and the SIFT-based face feature vectors are applied in the clustering processes. Because of their automatic character, these unsupervised person recognition approaches could be used successfully for indexing voluminous voice and face databases, by constructing speaker and face cluster-based indexes. Some unsupervised biometric recognition models based on fingerprints can also be developed, by applying our automatic clustering procedures to minutia-based or pattern-based fingerprint feature vectors.

We also developed some effective multimodal biometric solutions based on various combinations of voice, face and fingerprints or various combinations of biometric authentication techniques. These multi-characteristic and multi-method biometric systems produce enhanced person recognition results. Usually, our multimodal person authentication techniques perform the biometric information fusion at the classifier or decision level. The fusion at lower levels will be investigated during our future research in multimodal biometrics domain.

Some part of my research in the biometrics field has been only mentioned and not described in this thesis. For example, our iris recognition and text-independent voice recognition results were not described here. This is due to space reasons, since this part of the thesis is limited to a number of characters, and also because I am not satisfied enough with these results and intend to further improve those recognition techniques in the future.

3. Image analysis based computer vision models

The goal of the computer vision domain is to duplicate the human vision. It includes real-world image and video acquiring, processing, analyzing and interpretation techniques in order to produce representation of objects in the world [118]. Computer vision field has important applications in several strongly related domains such as artificial intelligence, robotics and human-computer interaction. Digital signal processing is also closely related to computer vision, but mainly through its 2D signal processing and analysis techniques. While unidimensional signals are rarely used in computer vision applications, image analysis represents the most closely related field to computer vision.

A typical computer vision system performs an image/video acquisition process first, using its sensors, then it executes some pre-processing operations on the acquired data, such as image denoising/restoration or contrast enhancement. Next, certain image and video analysis tasks are performed by the system. Some typical tasks of a computer vision system include image reconstruction, object and event detection, motion estimation, video tracking, object and action recognition, learning, or content-based indexing and retrieval.

We have investigated most of these computer vision domains, the image analysis techniques related to them and developed by us being described in the following sections of this chapter. The image segmentation field is approached in the next section, where our region-based and contour-based segmentation solutions are described, while the video segmentation domain is described in 3.2, where our automatic temporal video segmentation technique is presented. Image reconstruction, or inpainting, is approached using some robust variational PDE models that are detailed in the third section. In 3.4 we consider the object recognition domain, presenting some methods of recognizing objects from digital images and video sequences. Multimedia information indexing and retrieval, another important computer vision area, is considered in section 3.5, where we describe some content-based media indexing and retrieval techniques developed by us. In the last section of this chapter, our proposed image and video object detection and tracking approaches are presented.

3.1. Novel image segmentation techniques

Image segmentation represents an important image analysis domain that is useful to many other computer vision fields. The segmentation refers to the process of partitioning a digital image into multiple segments, or regions, which represent sets of pixels [118]. All the pixels in a region are similar with respect to some characteristic or computed property, such as color, intensity, or texture. Obviously, image object detection constitutes the main application area of image segmentation.

The image segmentation algorithms can be classified into two major categories: *region-based* and *contour-based* techniques. Region-based methods provide a set of regions that collectively cover the entire image. They include histogram-based [119], clustering based [120], graph partitioning based [121], watershed based and neural network based techniques. The contour-based segmentation approaches provide a set of contours extracted from the image. Most of them use edge detection filters [122], partial differential equation-based models [123] or active contours (snakes) for the segmentation process [124].

Region-based image segmentation domain is approached in the next subsection. We developed some robust region-based segmentation techniques using pixel clustering, which are described in 3.1.1. Then, in 3.1.2, our contributions in the contour-based image segmentation field are illustrated. A developed robust variational PDE contour tracking model is described there.

3.1.1. Automatic region-based image segmentation methods

We proposed several region-based image segmentation techniques in our past papers [33,42,125], all of them representing clustering-based approaches. The segmentation methods from this category compute a content-based feature vector for each image pixel. Such a feature vector may contain information of color, intensity, texture or other image content characteristics. All the pixel feature vectors are grouped in a number of classes using a clustering algorithm. The image segments (regions) are determined on the basis of the obtained pixel clusters.

The segmentation approaches proposed by us are based on color/intensity regions and textured regions, respectively [125,126]. They consider a [*n* x *n*] neighborhood, where *n* is an odd value, for each pixel. Then, a feature vector that describes properly the content of this neighborhood is computed. If the image does not contain textured regions, then the feature extraction becomes a quite easy task. A statistic value of the neighborhood, such as the mean or the median, can be considered as a feature vector [125]. Otherwise, a texture analysis is required to obtain the proper feature vectors.

Image texture, defined as a function of the spatial variation in pixel intensities, is useful in a variety of applications and constitutes a subject of intense study by many researchers. Texture segmentation, representing the process of dividing the image space into texture regions, has been a topic of intensive research for over four decades [127]. Texture analysis has been approached using various techniques based on Gabor filtering [128], Wavelet Transforms [129], image moments [127], Fourier descriptors [130], geometrical approaches [131], co-occurrence matrices [132] or correlation operations [127].

In [33,42] we provided some moment-based texture segmentation techniques. Our methods are based on the *representation theorem* that says a texture region is unique determined by an infinite set of moments. The image to be segmented is converted into the grayscale form. Then, it is enhanced, by applying some denoising and restoration operations. Let *I* be such an enhanced $[X \times Y]$ grayscale image. For each pixel of *I* we consider a square $[(2N+1)\times(2N+1)]$ neighborhood having that pixel located at its center, the value of *N* depending on texture density. So, for the *i*th pixel of the image, the discrete area moment of order (*p*+*q*) of its neighborhood is

$$m_{pq}(i) = \sum_{x=x_i-N}^{x=x_i+N} \sum_{y=y_i-N}^{y=y_i+N} I(x,y)\cdot x^p \cdot y^q, \;\; p,q \geq 0 \tag{3.1}$$

where (x_i, y_i) returns the position of the *i*th pixel in the image. In [33] we model the texture-based pixel feature vector as a sequence of 9 particular image area moments up to the order 4:

$$V(i) = [m_{00}(i), m_{01}(i), m_{02}(i), m_{10}(i), m_{11}(i), m_{12}(i), m_{20}(i), m_{21}(i), m_{22}(i)] \tag{3.2}$$

or as a matrix $V(i) = [m_{jk}(i)]_{(3x3)}$. We obtain the feature set $\{V(i)\}_{i=1,\ldots,XY}$ and perform an unsupervised classification of its components. We consider both automatic and semi-automatic clustering solutions for these moment-based feature vectors [33].

In the semi-automatic case, the user indicates the number of texture clusters, *K*, after visualizing the displayed image. Then, a *K*-means algorithm or a region-growing procedure that stops when the number of clusters becomes *K* is applied to the pixel feature vector set [33,125]. In the automatic clustering case no interactivity is required and the image is not displayed. The automatic unsupervised classification algorithm described in 1.4.3 is used to cluster the feature vectors $V(i)$ [33]. The Euclidian metric is used in the classification processes to measure the distance between feature vectors.

Each obtained class (cluster) of pixels represents a certain texture. The *K* classes being determined, the identification of the textured regions becomes an easy task. Any two 4-adjacent pixels from the same class must belong to the same image region (segment).

This moment-based texture segmentation approach produced quite satisfactory results but we have been trying to improve it by modifying the moment-based feature extraction and the clustering solution. Thus, in a following paper [126] we develop more complex texture feature vectors, based on discrete modified centered area moments up to order 5. The feature vector corresponding to the i^{th} pixel is computed as the next 6-uple:

$$V(i) = \left[\hat{\mu}_{00}(i), \hat{\mu}_{01}(i), \hat{\mu}_{11}(i), \hat{\mu}_{12}(i), \hat{\mu}_{22}(i), \hat{\mu}_{23}(i)\right], i \in [1, X \cdot Y] \tag{3.3}$$

where the modified centered moments are obtained as:

$$\hat{\mu}_{pq}(i) = \sum_{x=x_i-N}^{x=x_i+N} \sum_{y=y_i-N}^{y=y_i+N} I(x,y) \cdot \left(\frac{x-C_x}{\sigma_x}\right)^p \cdot \left(\frac{y-C_y}{\sigma_y}\right)^q, \; p,q \geq 0 \tag{3.4}$$

where the coordinates of the center of gravity (centroid) are computed as:

$$C_x = \frac{m_{10}}{m_{00}}, C_y = \frac{m_{01}}{m_{00}} \tag{3.5}$$

and the standard deviations in the *x* and *y* directions are

$$\sigma_x = \sqrt{\frac{\mu_{20}}{m_{00}}}, \sigma_y = \sqrt{\frac{\mu_{02}}{m_{00}}} \tag{3.6}$$

where the centered moments are

$$\mu_{pq}(i) = \sum_{x=x_i-N}^{x=x_i+N} \sum_{y=y_i-N}^{y=y_i+N} I(x,y) \cdot (x-C_x)^p \cdot (y-C_y)^q, \; p,q \geq 0 \tag{3.7}$$

As resulting from the moment representation theorem, if more higher order $\hat{\mu}_{pq}(i)$ moments are included into $V(i)$ sequence, this feature vector would become a more powerful texture descriptor [126]. The main disadvantage of more complex feature vectors is the high computational cost of the texture analysis process. The computing of these texture feature vector coefficients $\hat{\mu}_{pq}(i)$ is time-consuming, requiring many operations. Its algorithm has a polynomial time complexity. The computational complexity for each moment has the order $O(p \cdot q \cdot n^2)$, where *n* represents here the number of pixels from a neighborhood. So, we get $n = (2N + 1)^2$ and the time complexity is $O(p \cdot q \cdot (2N + 1)^4)$.

The feature vector classification process is then performed in [126] by using the validation index-based automatic clustering technique described in 1.4.4. It applies repeatedly a *K*-means algorithm on the feature set $\{V(i)\}_{i=1,\dots,XY}$ until the optimal number of clusters *K* is finally achieved. The final image segmentation result is obtained easily from the determined *K* texture classes. A robust investigation of the feature vector clustering process complexity is also provided in my paper [126].

This centered moment-based approach provides better texture recognition results than the previously described moment-based technique. We performed a lot of experiments, testing this method on tens images containing textures. Satisfactory results were obtained, a high texture recognition rate, over 80%, being achieved. We set the values *T* = 25 (see 1.4.4) and *N* = 2 for the tests, but if the analyzed texture has quite large structural units, then *N* should be increased. The homogeneous (intensity) regions are also successfully detected using this approach. Our segmentation model outperforms other techniques based on moments [127], Gabor filters [128] or DWT-2D [129], as resulting from our method comparison.

Such a texture recognition example is depicted in Fig 3.1. The color textured image displayed in (a) is converted to the grayscale form in (b). The 3 detected texture classes are represented in (c) and the resulted 4 texture regions are depicted in (d). One can see that 2 identified texture regions of the image, which are labeled with 1, belong to the same texture class.

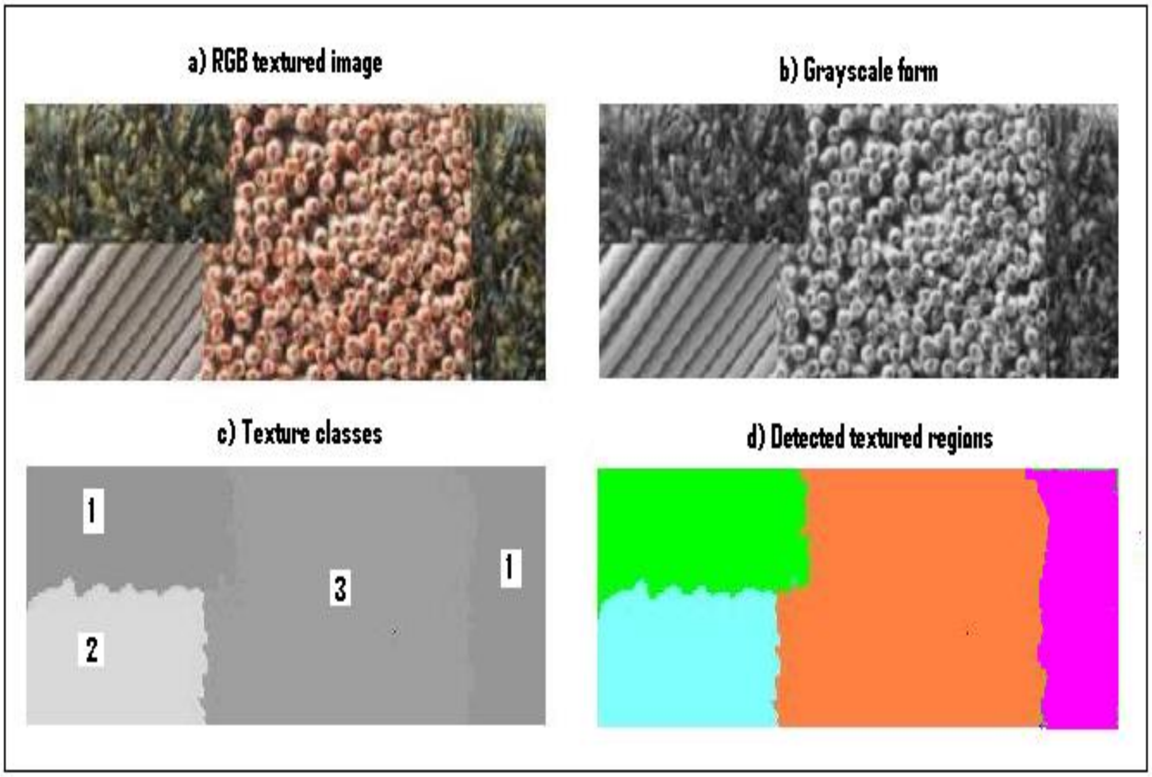

Fig. 3.1. Texture segmentation example

3.1.2. Level set based contour tracking model

The contour-based image segmentation domain has also been widely investigated during our research. Thus, our PDE–based restoration models described in the second chapter could be applied successfully in this research field. The nonlinear diffusion-based techniques presented in 1.2 [8] and the variational PDE denoising models described in 1.3 [11] have a strong edge-preserving character, therefore they can be used for image edge detection. The region boundaries and these identified edges being closely related, the image segmentation process becomes a quite easy task.

Other PDE-based segmentation solutions are based on parametric, fast marching [133] and level-set techniques [123]. We developed a robust level-set based image segmentation approach that is described in the **selected paper 5** published in [134]. Initially introduced by Osher and Sethian in 1988 to track the moving interfaces [135], the level-set algorithms have since become a powerful tool for performing contour evolution. The central idea of the level-set based method is to represent the evolving contour using a signed function whose zero level corresponds to the actual contour.

The variational level-set techniques perform image object contour tracking by considering a level set function that minimizes some energy functional. A very popular variational level-set algorithm is the one elaborated by Chan and Vese [136]. Their algorithm is based on the classical Mumford-Shah segmentation model [137] and the level sets. It represents a geometric active contour model that uses variational calculus approaches to evolve the level set function. Our contour-based PDE segmentation technique is derived from this Chan-Vese level-set model, representing an improved version of it. Also, in [134] we provide a rigorous mathematical justification for the proposed level-set based contour detection procedure and for Chan-Vese model also. We consider the following energy functional:

$$\begin{aligned} F_\varepsilon(\varphi) = \mu\int_\Omega \left|\nabla H_\varepsilon(\varphi)\right| dxdy + \nu\int_\Omega H_\varepsilon(\varphi) dxdy + \lambda_1\int_\Omega (u_0 - C_1(\varphi))^2 H_\varepsilon(\varphi) dxdy + \\ + \lambda_2\int_\Omega (u_0 - C_2(\varphi))^2 (1 - H_\varepsilon(\varphi)) dxdy + \lambda_3\int_\Omega \varphi^2 dxdy \end{aligned} \tag{3.8}$$

where $\varphi(x,y)$ is a level-set function defining the contour $\partial\omega = \{(x,y)\in\Omega; \varphi(x,y)=0\}$, $\Omega \subseteq R^2$, $H_\varepsilon(u) = \varepsilon u + \frac{1}{2} + \frac{1}{\pi}\arctan\left(\frac{u}{\varepsilon}\right)$, $\mu,\nu,\lambda_i > 0$, $C_1(\varphi) = \int_\Omega u_0 H(\Omega) dxdy \left(\int_\Omega u_0 H(\Omega) dxdy\right)^{-1}$ and $C_2(\varphi) = \int_\Omega u_0 (1 - H(\varphi)) dxdy \left(\int_\Omega (1 - H(\Omega)) dxdy\right)^{-1}$. The last term is added in order to regularize the problem and, more precisely, the Euler-Lagrange equations, for giving the mathematical justification. Then, the functional is rewritten as:

$$\begin{aligned} F_\varepsilon(\varphi) = \mu\int_\Omega \delta_\varepsilon \left|\nabla\varphi\right| dxdy + \nu\int_\Omega H_\varepsilon(\varphi) dxdy + \lambda_1\int_\Omega (u_0 - C_1(\varphi))^2 H_\varepsilon(\varphi) dxdy + \\ + \int_\Omega (\lambda_2 (u_0 - C_2(\varphi))^2 (1 - H_\varepsilon(\varphi)) + \lambda_3\varphi^2) dxdy \end{aligned} \tag{3.9}$$

Then, we consider in [134] the following minimization problem that has to be solved:

$$\varphi_\varepsilon = \arg\min\{F_\varepsilon(\varphi); \varphi \in BV(\Omega)\} \tag{3.10}$$

where $BV(\Omega)$ is the space of functions with bounded variations in Ω. In our paper we demonstrate that there is at least one minimizer φ_ε for (3.10) (see [134] for more). The Euler-Lagrange equations corresponding to this minimization problem are then determined as:

$$\begin{aligned}&-\mu div(\delta_\varepsilon(\varphi_\varepsilon)\operatorname{sgn}(\nabla\varphi_\varepsilon)) + \mu|\delta_\varepsilon(\varphi_\varepsilon)| + \nu\delta_\varepsilon(\varphi_\varepsilon) + 2\lambda_\varepsilon\varphi_\varepsilon + 2(\lambda_1(C_1(\varphi_\varepsilon)-u_0))C_1^{'}(\varphi_\varepsilon) + \\ &+\lambda_2(C_2(\varphi_\varepsilon)-u_0)C_2^{'}(\varphi_\varepsilon))(1-H_\varepsilon(\varphi_\varepsilon)) + (\lambda_1(C_1(\varphi_\varepsilon)-u_0)^2 + \lambda_2(C_2(\varphi_\varepsilon)-u_0)^2)\delta_\varepsilon(\varphi_\varepsilon) = 0\end{aligned} \tag{3.11}$$

We use the steepest descent method to compute the solution of (3.11) and obtain the evolution equation:

$$\begin{cases}\dfrac{\partial\varphi_\varepsilon}{\partial t} + F_\varepsilon^{'}(\varphi) = 0, in\ (0,T)\times\Omega \\ \varphi_\varepsilon(0,x,y) = \varphi_0(x,y), in\ \Omega \\ \dfrac{\partial\varphi_\varepsilon}{\partial\overline{n}} = 0, in\ (0,T)\times\partial\Omega\end{cases} \tag{3.12}$$

Then, (3.12) is solved by the following iterative sequence of equations:

$$\begin{cases}\dfrac{\partial\varphi_\varepsilon^k}{\partial t} + F_{\varepsilon_k}^{'}(\varphi) = 0, in\ (0,T)\times\Omega \\ \varphi_\varepsilon^k(0,\cdot) = \varphi_0, in\ \Omega \\ \dfrac{\partial\varphi_{\varepsilon_k}}{\partial\overline{n}} = 0, in\ (0,T)\times\partial\Omega\end{cases} \tag{3.13}$$

where $\varphi_\varepsilon^k = \frac{1}{T}\int_0^T \delta_\varepsilon(\varphi_\varepsilon^{k-1}(t))dt.$ In [134] one proves rigorously that the Cauchy problem given by (3.13) is well-posed in the space $BV(\Omega)$ and the following gradient descent algorithm is convergent:

$$\varphi_\varepsilon((k+1)\Delta t) = \varphi_\varepsilon(k\Delta t) - \Delta t F_\varepsilon^{'}(\varphi_\varepsilon((k+1)\Delta t)) \tag{3.14}$$

This level-set based segmentation model is then discretized, and the following numerical scheme that computes the level-function φ_ε is obtained:

$$\frac{\varphi_{i,j}^{n+1}-\varphi_{i,j}^{n}}{t}=\frac{\mu}{h^2}\Delta_{-}^{x}\left(\frac{\Delta_{+}^{x}\varphi_{i,j}^{n+1}\delta_h(\varphi_{i,j}^{n})}{\sqrt{\frac{\left(\Delta_{+}^{x}\varphi_{i,j}^{n}\right)^2}{h^2}+\frac{\left(\varphi_{i,j+1}^{n}-\varphi_{i,j-1}^{n}\right)^2}{(2h)^2}}}\right)+\frac{\mu}{h^2}\Delta_{-}^{y}\left(\frac{\Delta_{+}^{y}\varphi_{i,j}^{n+1}\delta_h(\varphi_{i,j}^{n})}{\sqrt{\frac{\left(\Delta_{+}^{y}\varphi_{i,j}^{n}\right)^2}{h^2}+\frac{\left(\varphi_{i+1,j}^{n}-\varphi_{i-1,j}^{n}\right)^2}{(2h)^2}}}\right)$$

$$\left(-\nu+\lambda_1(u_{0,i,j}-C_1(\varphi^n))^2+\lambda_2(u_{0,i,j}-C_2(\varphi^n))^2\right)\delta_h(\varphi_{i,j}^{n})-2\lambda_3\varphi_{i,j}^{n}-\frac{\mu}{h}\sqrt{\left(\Delta_{+}^{x}\varphi_{i,j}^{n}\right)^2+\left(\Delta_{+}^{x}\varphi_{i,j}^{n}\right)^2}+(3.15)$$

$$+2\left(\lambda_1(C_1(\varphi^n)-u_0)C_1^{'}(\varphi^n)H_h(\varphi^n)+\lambda_2(C_2(\varphi^n)-u_0)C_2^{'}(\varphi^n)\right)\left(1-H_h(\varphi^n)\right)$$

where $\Delta_{-}^{x}\varphi_{i,j}=\varphi_{i,j}-\varphi_{i-1,j};\Delta_{+}^{x}\varphi_{i,j}=\varphi_{i+1,j}-\varphi_{i,j};\Delta_{-}^{y}\varphi_{i,j}=\varphi_{i,j}-\varphi_{i,j-1};\Delta_{+}^{y}\varphi_{i,j}=\varphi_{i,j+1}-\varphi_{i,j}$.

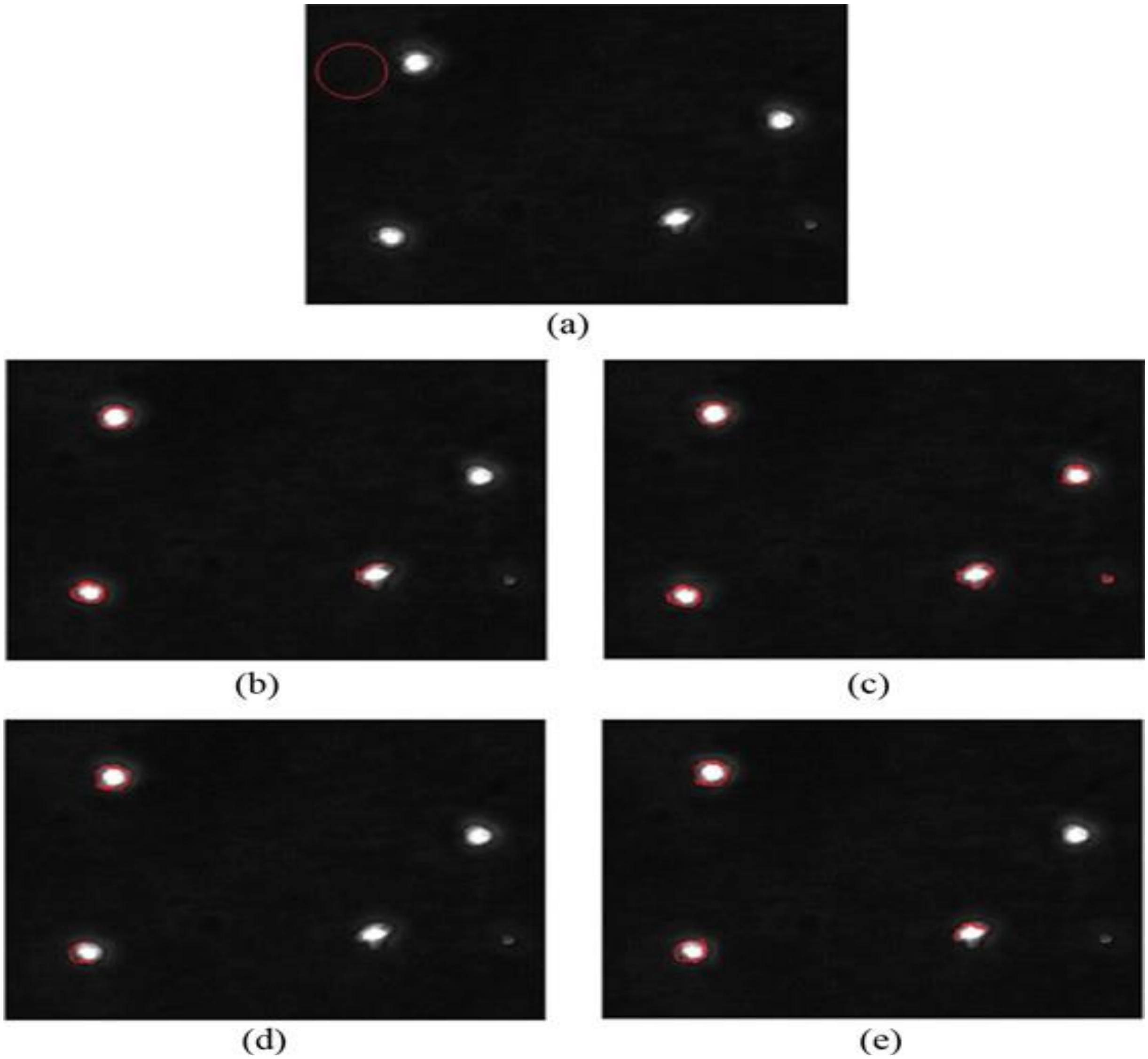

Fig. 3.2. Method comparison: a) Image to be segmented and initial contour at first step; b) Our method: step 300; c) Our method: step 800; d) Chan-Vese algorithm: step 300; e) Chan-Vese algorithm: step 800.

The obtained iterative algorithm has been tested on various image datasets, being applied with the following parameters: $\lambda_1 = \lambda_2 = \lambda_3 = 1, \mu = 0.2, \nu = 0.1, t = 1, \Delta t = 0.1$ and *N* = 1000. A lot of contour tracking experiments have been performed, satisfactory results being achieved. A high object detection rate, of approximately 90%, is reached, and high values for the performance parameters are also obtained: *Precision* = 0.91 and *Recall* = 0.85. So, the proposed technique tracks the most relevant objects while identifying more relevant results than irrelevant.

Method comparisons have also been performed. The contour tracking approach described here provides much better results than other active contour based methods. The performed experiments prove that our level-set segmentation technique performs better than influential Chan-Vese contour-based model [136]. Thus, it provides a higher object detection rate and also executes somewhat faster, identifying the contours in a lower number of iterations. Thus, our variational approach can be seen as an improved variant of the Chan-Vese model.

A contour tracking example and method comparison is represented in Fig. 3.2. In (*a*) there is displayed an image containing human cells that must be segmented. The initial contour is also depicted in red. The cell segmentation results obtained by our level-set based approach after 300 and 800 iterations are described in (*b*) and (*c*). One can see that all the cells are detected. The cell tracking results produced by the Chan-Vese method are displayed in (*d*) and (*e*). The parameters used for Chan-Vese procedure are $\lambda_1 = \lambda_2 = 1, \mu = 0.5, \nu = 0, \Delta t = 0.1$. The Chan-Vese algorithm cannot segment all these cells in the same number of steps.

Also, the method described here outperforms also other active contour based techniques [124,138]. This image segmentation technique using contour tracking has important computer vision application areas, such as robotics, video object detection and tracking, object interpretation, biometrics and medical computer vision.

3.2. Temporal video segmentation approaches

While in the previous section we described several segmentation solutions for digital images, the segmentation of the video sequences is described in this section. We approached in some of our papers the temporal video segmentation domain [33,139,140]. Temporal video segmentation has been an area of active research in the last decades. It represents a key step in video analysis, being successfully applied in various important video analysis domains, such as video key frame extraction [141], video compression, video indexing [142], video content browsing and retrieval [143], or video object detection and tracking [144].

This type of video segmentation consists in partitioning the movie in temporal segments, like shots and scenes. The video shot, sometimes referred as *basic scene*, represents the elemental unit of the video clip and refers to a continuous sequence of frames, shot uninterruptedly by one camera. The video scene represents a succession of several semantically-correlated shots. Shot transitions are the mechanism used to change from one shot to the next in a video production. The video shots are assembled during the editing phase using a variety of technologies that produce different types of shot transitions.

These transition types can be broken basically into three categories: hard cuts, soft cuts and digital effects. A *hard cut*, simply referred as cut, represents a sudden transition from one video shot to another, and is the most common shot transition. A *soft cu*t represents a gradual transition between two shots, which means a sequence of video frames that belongs to both the first and the second video shot. There exist two types of soft cuts: *fades* and *dissolves*. A fade comes in two varieties: fade-in and fade-out. A fade-in starts from a solid color screen and slowly transitions to a shot. A fade-out starts with a shot and transitions to a solid color. A dissolve (cross-fade) occurs when the two video shots overlap for a period of time, the first one dissolving into the second one. *Digital effects* for shot transition include wipes, color replacement, animated effects, pixelization, focus drops, lighting effects, pushes, page peels, spirals, irises and others.

Obviously, a shot-based video segmentation (video shot detection) process consists of identifying all the shot transitions within a video sequence. Video cut detection methods can be grouped in the following categories: pixel-difference based techniques, histogram comparison based methods, edge-oriented models, motion-based techniques and statistical feature-based approaches.

In my **selected paper 6** [139] a review of all these categories, describing their video shot identification techniques, is provided. Some histogram-based approaches considered by us are described in the next subsection. A much more efficient video segmentation technique, which uses a 2D Gabor filtering based frame feature extraction and an automatic video frame classification, is described in 3.2.2.

3.2.1. Histogram comparison based shot detection techniques

The most popular video cut detection techniques are those based on different types of histograms. Intensity and color histogram based methods represent a good alternative to pixel-based approaches, providing better results.

Numerous distance formulas have been modeled for measuring the similarity of grayscale (color) histograms corresponding to consecutive frames in a movie. Besides Euclidian metric, we must mention the *histogram differences*, the *histogram intersection* and the *histogram quadratic distance*. Also, other types of image histograms, like *YUV histograms*, *weighted histograms* [145] or *multiresolution histograms* [146] are used as well by the video cut detection algorithms.

A histogram-based video cut detection technique is proposed in my 2006 book [33]. The grayscale histogram of each video frame is considered as a frame feature vector. The distances between these feature vectors are computed using Euclidean metric or SAD. Then, two solutions for frame grouping are provided. The first one represents a semi-automatic approach that sets interactively the number of videoshots, N, first. Then, the highest N - 1 feature vector distance values are determined. The values of these locations correspond to the N - 1 video shot transitions from the analyzed clip. Given the locations of the video cuts, the shot detection process becomes an easy task.

The other grouping solution is an automatic technique based on *local adaptive thresholding* [33]. A video cut is identified whenever the inter-frame difference metric value exceeds a threshold value. The used threshold is detected automatically, its value depending on the current pair of consecutive frames.

Both versions of this histogram-based segmentation method were tested on many videos. They outperform the pixel-difference based techniques using SAD metric, producing much less false hits and having a higher precision rate. Histogram comparison algorithms provide better segmentation results than pixel-based approaches because they are not as sensitive to minor changes within video scenes as pixel based methods. The main drawback of the histogram-based video cute detection is that the spatial distribution of information is disregarded. Thus, two images may have quite similar color histograms while their content differs extremely. For example an image describing a sunflower field beneath a blue sky and an image depicting a sand beach near the sea, could have almost the same histogram. Obviously, a lot of missed hits (video cuts) may result from this situation.

We tried to overcome this disadvantage of color/intensity histograms, by combining various histograms into a frame feature vector. So, in [147] we model the video frame feature vectors as the sum of two normalized histograms. The color, or grayscale histogram, is combined to the DCT histogram into a more efficient image content descriptor.

The video frame feature vectors, computed as $V(I_i) = \frac{H_c(I_i) + H(DCT(I_i))}{M \cdot N}$ for each $[M \times N]$ frame I_i, are categorized using the semi-automatic grouping approach based on the number of shots. We obtain better cut detection results using this improved technique, which are next used for other video analysis processes, like keyframe extraction and video recognition [147]. More results from this paper [147], related to this computer vision processes, will be presented in 3.4.2.

I have treated the histogram-based video segmentation algorithms very succinctly in this short subsection because they do not contain more original contributions. My major contribution in the temporal video segmentation domain is described in the following, much larger, subsection.

3.2.2. Automatic feature-based video cut identification model

We developed an automatic feature-based video cut detection technique that is described in [139]. The most important part of our technique is the feature extraction stage, which produces some content-based feature vectors that provide an optimal frame characterization. We considered a two-dimensional Gabor filtering-based feature extraction to obtain some good frame content descriptors. So, the selected paper [139] considers an even-symmetric 2D Gabor filter having a quite similar form to that given by (2.31):

$$G_{\theta,f}(x,y) = \exp\left(-\frac{1}{2}\left[\frac{x_\theta^2}{\sigma_x} + \frac{y_\theta^2}{\sigma_y}\right]\right)\cos(2\pi f x_\theta), \tag{3.16}$$

where $x_\theta = x\sin\theta + y\cos\theta$ and $y_\theta = x\cos\theta - y\sin\theta$. Filter $G_{\theta,f}$ optimally captures both local orientation and frequency information from a video frame.

Each frame of the analyzed movie is then filtered by applying $G_{\theta,f}$ at various orientations and a given frequency. A set of proper values for the filter's parameters, obtained from our experiments, are used [139]. Thus, we set the following values for frequency and the two standard deviations: *f* = 16, $\sigma_x = 3, \sigma_y = 4.5$. Also, we propose the following sequence of six angle orientations: $\theta_1 = \frac{\pi}{6}; \theta_2 = \frac{\pi}{3}; \theta_3 = \frac{\pi}{2}; \theta_4 = \frac{2\pi}{3}; \theta_5 = \frac{5\pi}{6}; \theta_6 = \pi.$ As a result, we obtain the following Gabor filter set: $\{G_{\theta_i,f}\}_{i\in[1,6]}$. This even-symmetric 2D Gabor filter set is described in the next figure, Fig. 3.3, where each filter kernel $G_{\theta_i,f}$ is represented as a 3D surface plot.

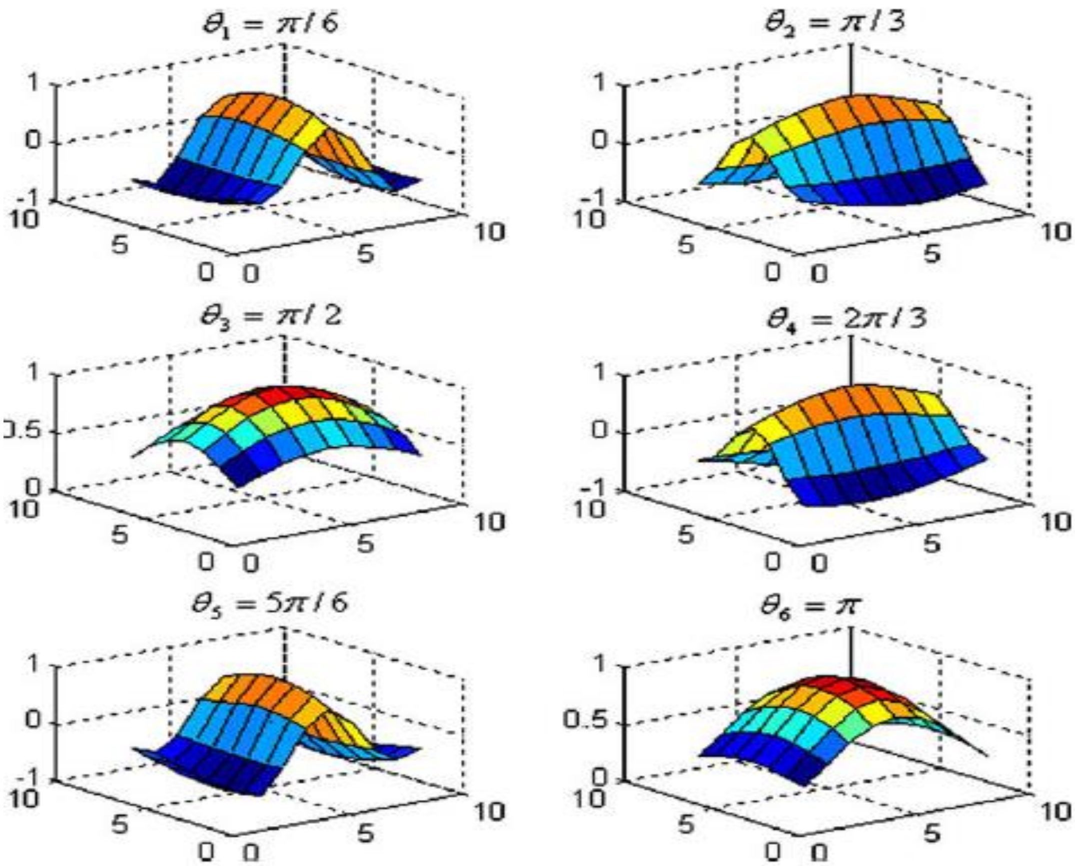

Fig. 3.3. The proposed even-symmetric 2D Gabor filter set

Let $Vid = \{I_1,...,I_n\}$ be the videoclip to be segmented, represented as a video frame sequence. A 3D feature vector is then computed for each $[M \times N]$ frame I_i, by processing it with each filter from the set $\{G_{\theta_i,f}\}_{i\in[1,6]}$. The feature extraction process can be expressed as follows:

$$V(I_i)[x,y,j]=V_{\theta_j,f}\left(I_i\right),\ \forall x\in[1,M],y\in[1,N],i\in[1,n],j\in[1,6] \qquad (3.17)$$

where

$$V_{\theta_j,f}\left(I_i\right)=I_i * G_{\theta_j,f} = FFT^{-1}\left\lfloor FFT(I)\cdot FFT(G_{\theta_j,f})\right\rfloor, \qquad (3.18)$$

The 3D feature vector $V(I_i)$, characterized by a $[M \times N \times 6]$ size, constitutes an optimal image content descriptor for frame I_i. These Gabor filter based feature vectors are useful tools for detecting the visual discontinuities in the video content. Similar frames have very closed feature vectors, while dissimilar frames correspond to quite distanced vectors. The distances between the 3D feature vectors can be measured using metrics like the Euclidean distance or SAD [139].

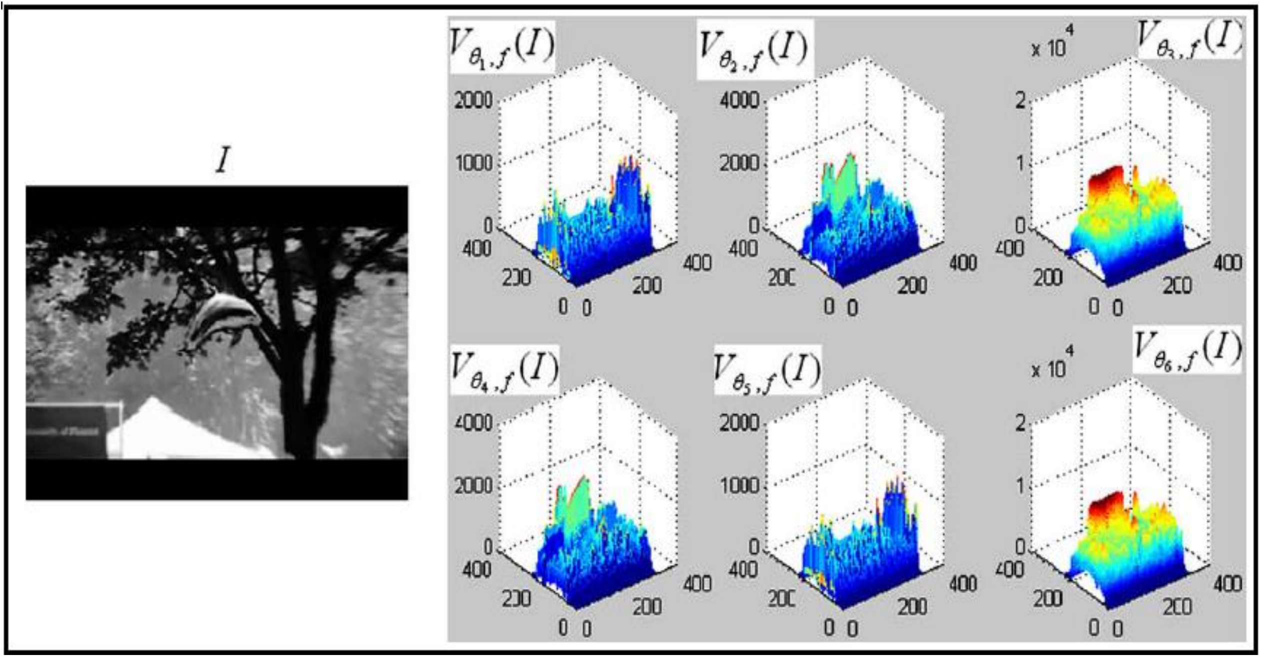

Fig. 3.4. The proposed even-symmetric 2D Gabor filter set

A grayscale image (frame) *I* and the six components, which (correspond to the angle orientations), of its feature vector are displayed in Fig. 3.4. The two-dimensional components, $V_{\theta_j,f}(I)$, are represented as 3D surfaces.

The next stage of our video cut detection process consists of grouping the frames in the proper videoshots. In [139] one provides also some frame clustering solutions. The videoshots have the following property: any two consecutive frames within a shot have very similar content and any two consecutive frames belonging to different shots have very different content. This means that any distance between two consecutive feature vectors corresponding to a video cut must be substantially higher than any distance between two consecutive feature vectors not related to a cut. This condition can be formalized as follows:

$$\min_{i \in S} d(V(I_i), V(I_{i+1})) > \max_{j \notin S} d(V(I_j), V(I_{j+1})), \tag{3.19}$$

where *d* is a proper metric (Euclidian, SAD) and *S* represents the cut position set ($i \in S$ means a cut between I_i and I_{i+1} [139,140]. We compute the distance value set $D = \{d_1, ..., d_{n-1}\}$, where $d_i = d(V(I_i), V(I_{i+1}))$. While the semi-automatic frame clustering solution described in the previous subsection can be applied here easily, using these d_i values, we consider in [139] two automatic no-threshold based feature vector clustering approaches.

As it results from (3.19), the position set *S* determines two kinds of distance values in the set *D*: large distances and small distances. We get $D = D_l \cup D_s$, where $D_l = \{d_i \mid i \in S\}$ and $D_s = \{d_i \mid i \notin S\}$. First approach is based on a condition, usually satisfied by the distances between frame feature vectors, requiring that for each value from *D*, the closest distance value belongs to the same subset, D_l or D_s [139]. All the performed experiments indicate that this condition is true for our Gabor filter-based feature vectors. So, the values from D are sorted in ascending order, the largest absolute difference between two consecutive values in the sorted vector being identified. The lower value is the greatest distance from D_s, while the higher one is the lowest distance from D_l, the two distance subsets thus being determined [139].

The other automatic frame clustering solution applies an hierarchical agglomerative classification procedure using average linkage clustering to the distance set D, until the number of distance clusters becomes $K = 2$. The cluster containing the larger values has to be D_l, the distance subset that determines the cut position set S and the video break detection result (see [139]).

The described temporal video segmentation technique has been tested on hundreds video sequences. The performed experiments have provided very good segmentation results. A very high video cut detection rate and high values for the performance parameters have been achieved. Thus, we have got the following values *Precision* = 0.94, *Recall* = 0.96 and F_1 = 0.949, respectively.

Method comparison has been also performed. Our automatic feature-based cut detection technique outperforms the video cut identification methods based on pixel differences, color (grayscale) histograms, edge histograms, basic statistical features or likelihood ratio. Those segmentation algorithms produce more false hits and missed hits, therefore providing lower values for the three quality measures.

Precision, *Recall* and F_1 values obtained from cut detection experiments using the SAD-based pixel differences, color histograms (CH), edge histograms (EH), simple statistical measures (dispersion, mean, variance) (ST) and likelihood ratio (LHR) are registered in Table 3.1. One can see in this table that our cut identification algorithm get much higher values for the performance parameters.

The techniques using pixel difference and those based on histograms execute somewhat faster than our algorithm, the complex Gabor filtering related computations performed by our feature extraction approach requiring more processing time [139]. The segmentation models based on edge histograms or statistical measures are considerably slower than our video cut identification technique.

Table 3.1. Method comparison: performance measures of various shot detection algorithms

Technique	Precision	Recall	F_1
Our method	0.94	0.96	0.949
SAD	0.78	0.76	0.769
CH	0.75	0.70	0.724
EH	0.80	0.74	0.768
ST	0.64	0.61	0.624
LHR	0.60	0.59	0.595

In the next figure there is displayed one of our many temporal videoclip segmentation results [139]. The determined shot cuts of a movie are represented as pairs of frames in Fig. 3.5. For example, the first two images determine a video break, the third and the fourth indicate another break and so on. While our technique described here identifies correctly all the 24 shot cuts of this film, no cuts being missed and no false cuts being detected, the other segmentation models obtain much weaker results.

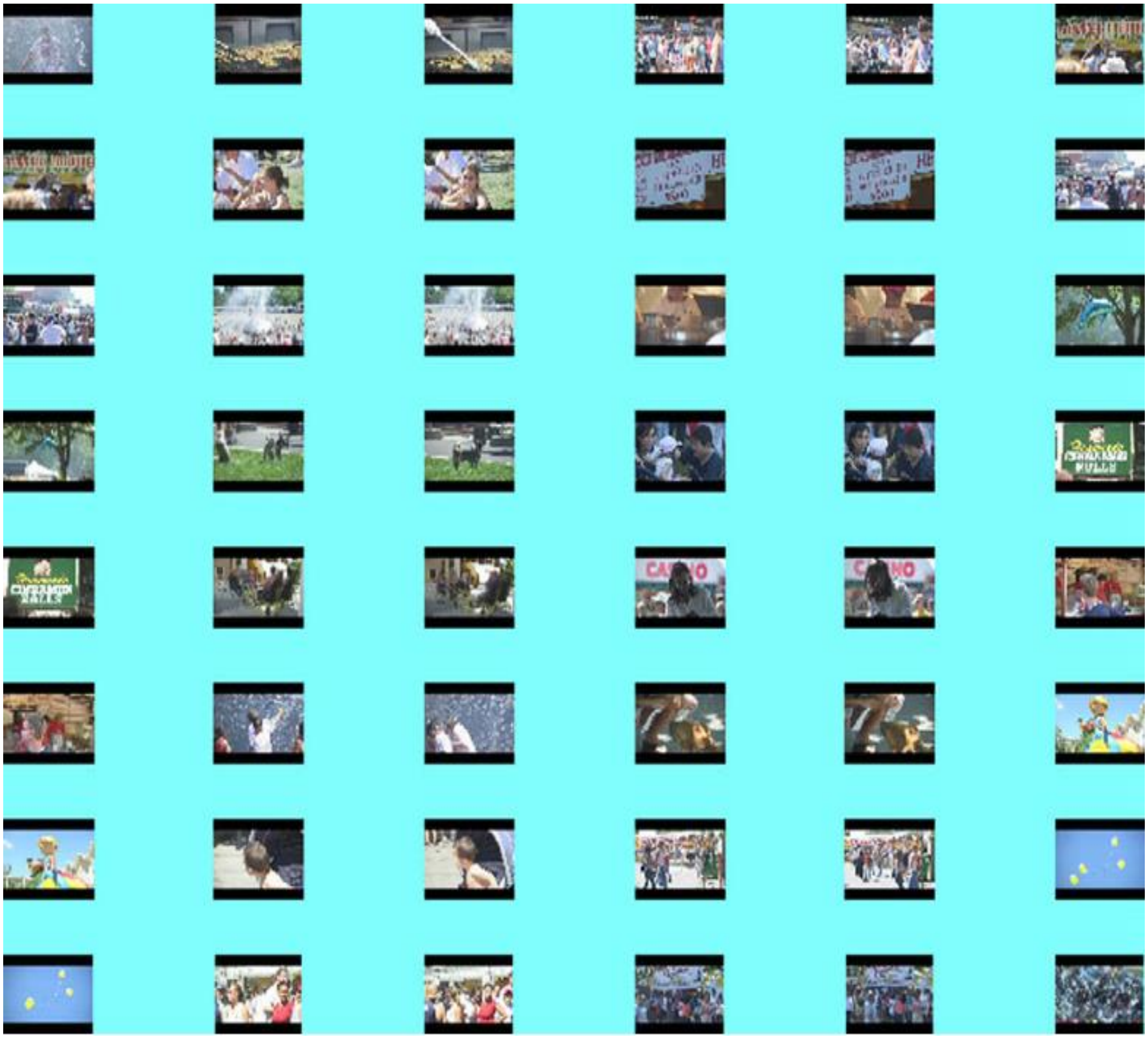

Fig. 3.5. Video cuts (as pairs of frames) corresponding of a movie composed of 25 shots.

The positions of the video cuts described in Fig. 3.5 are displayed in Fig. 3.6. As one can observe in the last figure, there are many differences between the data represented in the graphs corresponding to the 6 techniques. The highest 24 distance values are marked in each graph on the first column of the figure. It is obvious that many high distances displayed in the graphs of SAD, CH, EH, ST and LHR algorithms do not correspond to video cuts. There are 5 such distance values for SAD, 8 for CH, 3 for EH, 12 for ST and 14 for LHR [139].

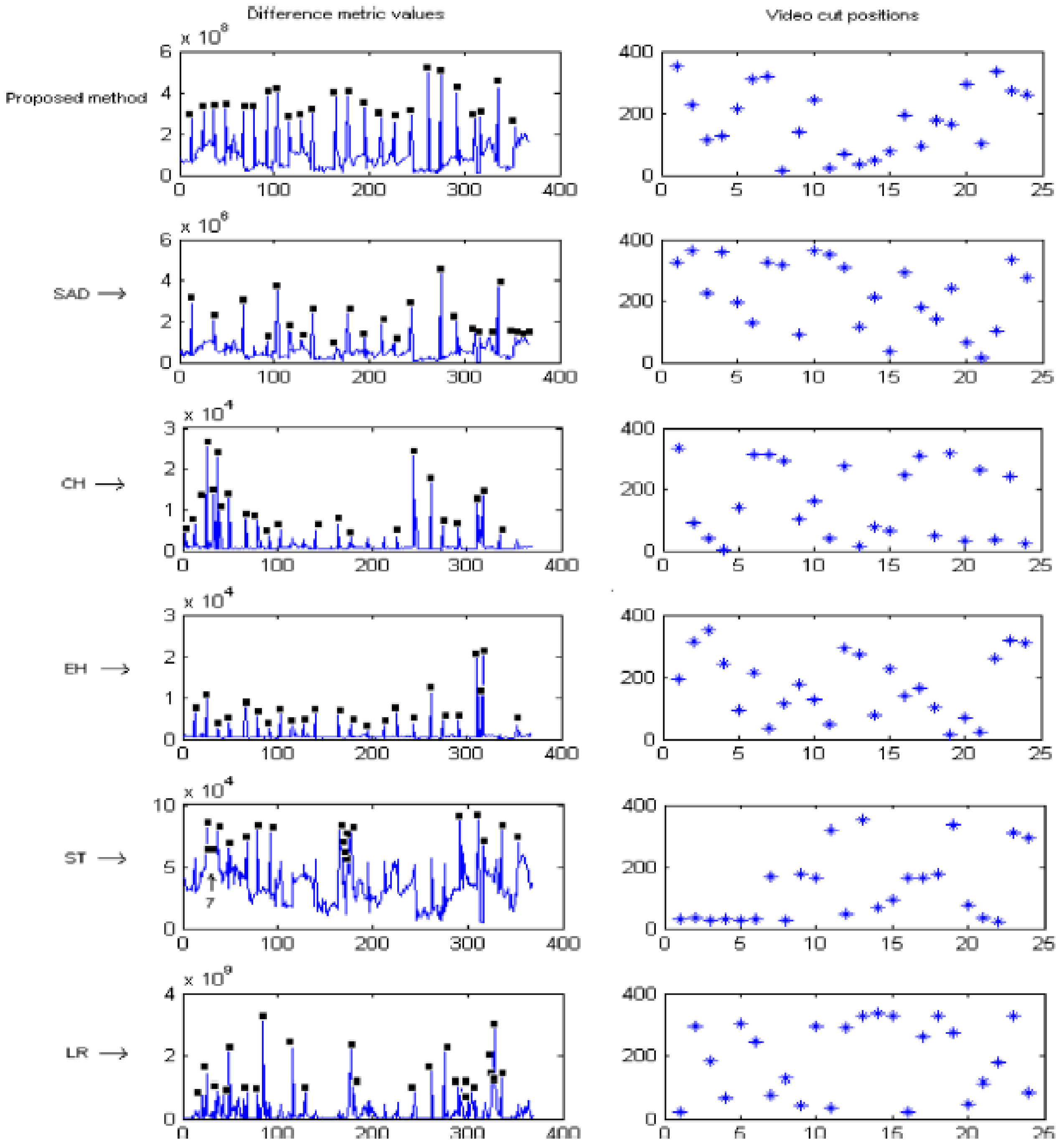

Fig. 3.6. Method comparison: the video cut detection results of 6 approaches

The method described here has also been tested for other shot transition types. While it produces optimal cut detection results, our approach performs weaker when applied to gradual transitions or some digital effects. However, the performed experiments have indicated a relatively good identification of the starting points of soft transitions like fades and dissolves. Extending this Gabor filtering based approach in the direction of soft cut detection will constitute an important task of my future work.

3.3. Variational PDE models for image reconstruction

Image reconstruction, known also as *image inpainting*, represents the computer vision process of restoring the missing areas of a damaged image as plausibly as possible from the known zones around them. The image reconstruction techniques are divided into the following categories: structural inpainting, textural inpainting, and combined approaches that perform simultaneous structure and texture inpainting.

Texture-based inpainting is highly connected with the problem of texture synthesis. A lot of texture inpainting algorithms have been proposed since an influential texture synthesis model was developed by A. Efros and T. Leung [148]. In their approach texture is synthesized in a pixel by pixel way, by taking existing pixels with similar neighborhoods in a randomized fashion. Many other texture synthesis algorithms improving the speed and effectiveness of the Efros-Leung scheme have been elaborated in the last 15 years [149].

Structural inpainting uses PDE-based and variational reconstruction techniques. The PDE methods follow isophote directions in the image to perform the reconstruction. The first PDE-based inpainting model was introduced by Bertalmio et al. in [150]. Variational methods for image reconstruction, which are closely related to the variational denoising models, have been introduced since 2001, when the Total Variation (TV) inpainting model was proposed by T. Chan and J. Shen [151]. Their variational scheme fills the missing image regions by minimizing the total variation, while keeping close to the original image in the known regions. It uses an Euler-Lagrange equation and anisotropic diffusion based on the strength of the isophotes. The TV inpainting model has been extended and considerably improved in numerous other papers [152].

We have proposed a robust variational PDE technique that restores a degraded image that is observed in a number of points in **selected paper 7** [153]. Our approach uses a variational problem considered in the Sobolev distribution space for which the corresponding Euler-Lagrange equation is a nonlinear elliptic diffusion equation.

Thus, in [153] the reconstructed image is determined from the following energy functional minimization:

$$\min\left\{\int_{\Omega} g(u(x,y))dxdy + \frac{1}{2}\|u-u_0\|_{-1}^{2}; u \in L^1(\Omega), u-u_0 \in H^{-1}(\Omega)\right\}, \qquad (3.20)$$

where g: R—> R represents a convex and lower semi-continuous function, u is the restored image and u_0 is the observed image, characterized by missing zones, on bounded domain $\Omega \subseteq R^2$. The Euler–Lagrange optimality conditions in (3.20) are given by the elliptic boundary value problem:

$$\begin{cases} -\Delta\beta(u) + u = u_0, \text{ in } \Omega \\ \beta(u) = 0, \text{ on } \partial\Omega \end{cases} \qquad (3.21)$$

where β is the subdifferential of g defined as:

$$\beta(r) = \{w \in R; w(r-s) \geq g(r) - g(s), \forall s \in R \qquad (3.22)$$

and representing a maximal monotone (multivalued) function. In [153] we then demonstrate, providing a rigorous mathematical proof, that the minimization problem (3.20) has a unique solution *u**, which satisfies the equation given by (3.21). We prove that the steady-state solution *u** to the following evolution equation:

$$\begin{cases} \dfrac{\partial u}{\partial t} - \Delta\beta(u) + u \ni u_0, \text{ in } (0,\infty)\times\Omega \\ u(0,x,y) = u_0(x,y), \qquad (x,y)\in\Omega \\ u = 0, \qquad\qquad\qquad \text{on } (0,\infty)\times\partial\Omega \end{cases} \tag{3.23}$$

represents also the solution to the equation (3.21) and, respectively to the minimization problem (3.20) (see [153] for more). The discrete version of the equation (3.23) is provided by the following steepest descent algorithm:

$$2u_{k+1} - \Delta\beta(u_{k+1}) = u_0 + u_k, k = 1,... \tag{3.24}$$

Then, by using $Au = -\Delta\beta(u)$, this implicit finite difference scheme is next transformed into the next explicit finite difference scheme:

$$u_{k+1} = -hA\beta(u^k) + u^k, k = 0,1,...,N \tag{3.25}$$

where *N* is the number of iterations, $t\in[0,T]$ and *Nh* = *T*. By replacing *A* to the discretized second order operator, $Au \cong \frac{1}{4}\left(u^k_{i-1,j} + u^k_{i+1,j} + u^k_{i,j-1} + u^k_{i,j+1} - 4u^k_{i,j}\right)$, where $u^k_{i,j} = u^k(i,j)$, one obtains:

$$u^{k+1}_{i,j} = u^k_{i,j} + \frac{h}{4}\left(\beta(u^k_{i-1,j}) + \beta(u^k_{i+1,j}) + \beta(u^k_{i,j-1}) + \beta(u^k_{i,j+1}) - 4\beta(u^k_{i,j})\right) \tag{3.26}$$

If $\beta(r) = r^{\varepsilon+1}$, instead of (3.26) we consider the following explicit finite difference scheme:

$$u^{k+1}_{i,j} = u^k_{i,j} + \alpha\left(u^k_{i,j}\right)^{\varepsilon}\left(u^k_{i-1,j} + u^k_{i+1,j} + u^k_{i,j-1} + u^k_{i,j+1} - 4u^k_{i,j}\right) \tag{3.27}$$

where $\alpha \le 1$ and $\varepsilon \in (0,1)$ respectively.

The image is reconstructed by applying the iterative algorithm given by (3.27) for *k*=0,1,…, *N* – 1. The degraded image $u^0 = u_0$ is transformed into the restored image u^N, that is closed to the original image, in several tens steps [153].

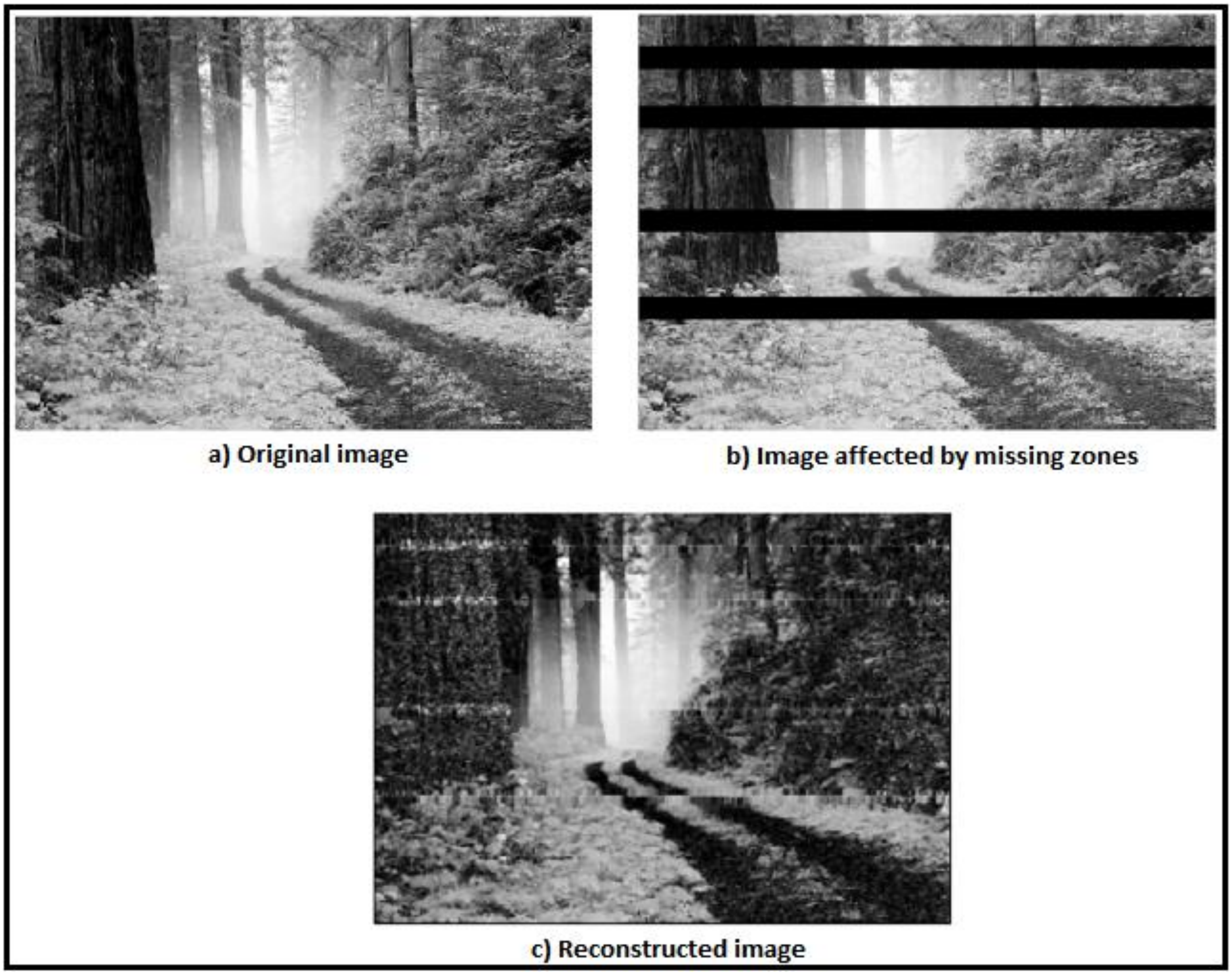

Fig. 3.7. Image inpainting performed by our variational approach

We have performed numerous inpainting experiments by using this image restoration algorithm. Our PDE variational technique has been applied on hundreds image containing missing zones and produced satisfactory reconstruction results. The optimal inpainting results are obtained for a number of iterations $N = 100$.

In Fig. 3.7 there is described such an image reconstruction example. The original image is displayed in (a). In (b) one can see a deteriorated version of that image, containing several missing zones (black rectangle regions). The image inpainted by the iterative algorithm (3.27) is displayed in (c). The proposed PDE-based reconstruction technique executes also quite fast, being characterized by a low time complexity. The running time of our algorithm is less than 1 second.

Method comparisons have also been performed (see [153]). We have compared the performance of our restoring technique with performances of some other inpainting techniques, such as TV inpainting [151] and those based on Gaussian processes [154]. We have found that our restoration approach runs faster that many other algorithms, while producing comparable good results.

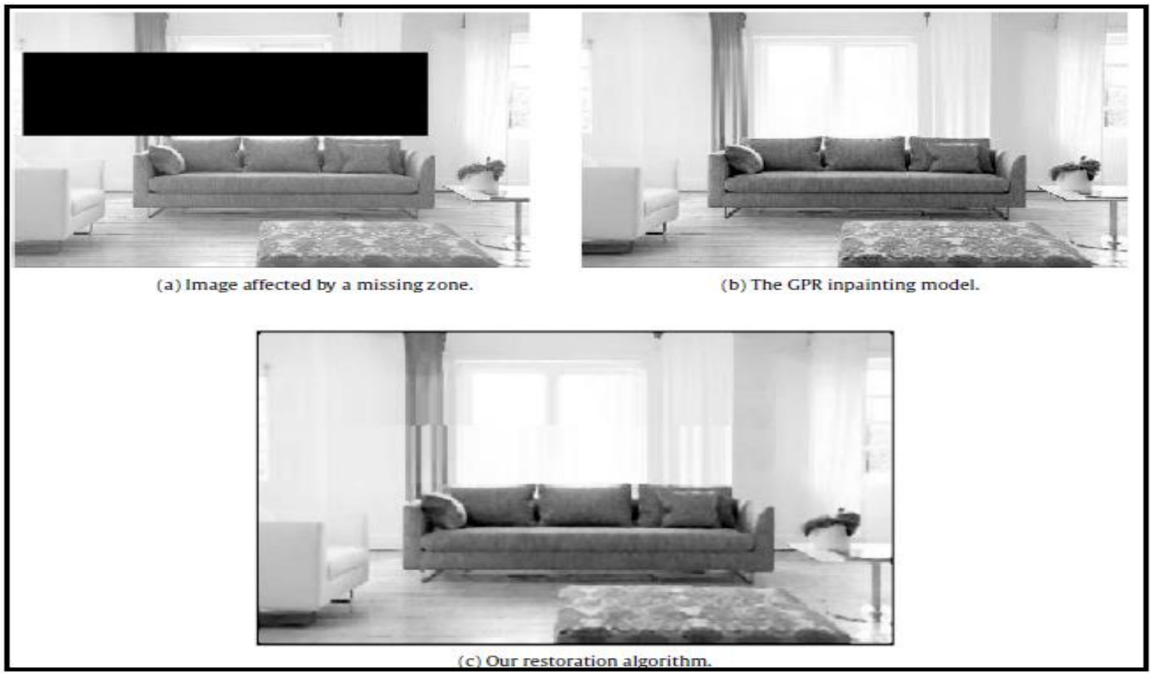

(a) Image affected by a missing zone.

(b) The GPR inpainting model.

(c) Our restoration algorithm.

Fig. 3.8. Method comparison: inpainting results produced by our method and GPR models

The Gaussian processes represent a powerful prediction method for image inpainting, being very useful in restoring the missing parts of an image. These non-parametric models can reconstruct both the structure and texture of the degraded image. Our PDE inpainting approach has been tested against GP-based restoring techniques for various grayscale images affected by missing zones [154]. Such a comparison example is represented in the next figure, where our variational PDE-based restoring algorithm is compared with the Gaussian Process Regression (GPR) Model [154]. A grayscale image containing a missing region (see the black rectangled area) is displayed in Fig. 3.8 (a). The image inpainting result produced by the GPR model is displayed in Fig. 3.8 (b), while the image reconstructed successfully by our variational technique is represented in Fig. 3.8 (c).

Thus, important theoretical and experimental results have been provided in our selected paper treating this variational reconstruction model [153]. We intend to improve these results in our forthcoming works in this domain. Also, we have improved the existing PDE inpainting models [151, 152], by developing novel variational inpainting schemes based on PDE-based smoothing. Since variational inpainting is closely related to variational denoising, we have modified our nonlinear 2nd-order diffusion-based denoising schemes so that to work properly for reconstruction. Those variational models are successfully adapted for inpainting by incorporating inpainting masks into their energy functionals. We get the next class of reconstruction processes:

$$u^* = \arg\min_u \int_\Omega \left(\alpha \cdot \psi_u\left(\|\nabla u\|\right) + \lambda\!/\!_2 \left(1 - 1_\Gamma\right)\left(u - u_0\right)^2\right) d\Omega, \quad (3.28)$$

where $\alpha \in (0,1)$ assures a minimal smoothing outside the missing region related to Γ mask and ψ_u is a properly selected edge-stopping function (for example, similar to 1.13). We have also obtained effective inpainting models from 4th–order PDEs. These new denoising-derived image inpainting results are disseminated in papers under consideration at journals and conferences.

3.4. Image and video recognition methods

Media pattern recognition represents an important computer vision domain, which have been widely investigated during our research activity. In this section we describe our results obtained in the pattern recognition subdomains related to image and video data. Image and video recognition field is strongly correlated to other computer vision domains approached by us and described in the next sections, such as: image and video retrieval, image object detection and video object tracking.

The recognition of any media entity represents the process of classification of that entity on the basis of its extracted features. Depending on the character of the classification approach, the recognition process can be either supervised or unsupervised. Image and video recognition area include recognition techniques for images, videos, image objects and video objects. A lot of such recognition methods were proposed in my past papers. I present some of these approaches in the following subsections. Several automatic image recognition techniques are described in the next subsection. Then, in 3.4.2, a video sequence recognition approach is presented. Next, some image and video object recognition models are discussed in the last subsection.

3.4.1. Automatic image recognition techniques

We considered the task of automatic recognition of entire images in some of our past papers [33,155-159], developing both supervised and unsupervised recognition methods. The automatic classification algorithms used for image recognition are those described in 1.4, so we focus on image feature extraction instead. The existing image featuring approaches use various histograms [160,161], Gabor filtering [77], 2D Wavelets [162], SIFT characteristics [84] and others. We have provided better feature extraction solutions during our research in this field.

A supervised image recognition system classifies any input image using a training image set. A feature extraction process is performed on the (input) images to be classified and the registered images from the training set. Then, any input feature vector is compared to the vectors from the training feature set. The most supervised image recognition techniques developed by us are related to biometrics [53]. In the sections 1.2 and 1.3 of the second chapter we have treated the recognition of images representing biometric identifiers such as faces and fingerprints. The numerous biometric authentication systems described there, using PCA [75], Gabor [79,80,97], or Wavelet [97-99] features, and performing identification and verification of faces and fingerprints, represent examples of efficient supervised image recognition systems.

An unsupervised image recognition procedure performs a clustering within a set of images, on the basis of their content similarity. It uses no training set and if it has also an automatic character, no knowledge about clusters' number is available. We have proposed several automatic unsupervised image recognition approaches, using various feature extraction and classification algorithms [33,37,155-159]. Each image is featured by computing a proper content descriptor for it that is used as a feature vector. Then, all feature vectors are clustered automatically by using the unsupervised classification techniques described in 1.4.

Thus, in [157] we propose an automatic image recognition method using *dispersion-based* features. The task to be solved is formulated for all recognition techniques as following: given a large image set $S = \{I_1, ..., I_n\}$, its images have to be categorized in some classes, whose number is not a priori known.

A grayscale conversion is operated on these images first. Then, each image I_i is decomposed into [*a* x *b*] blocks, usually considering *a* = *b*. If a perfect division is not possible, the image could be padded with zeros. The statistical dispersion (standard deviation) of each block is then computed as the square root of its variance, a *dispersion matrix* thus being obtained for each image [155,157]. This matrix is utilized as the image feature vector $V(I_i)$.

The 2D feature vector classification is performed using the region-growing based automatic clustering algorithm from 1.4.3 [39]. The obtained classes represent a reliable image recognition result, each class containing similar regions while non-similar images belong to different clusters [157]. The performed numerical experiments produced good recognition results and a quite high recognition rate. Although this approach works properly for large image sets, we provide here, as an example, a recognition process applied to a small image set. The color images to be clustered are displayed in Fig. 3.9. The 2D feature vectors are represented as 3D plots in Fig. 3.10, the distances between them being registered in Table 3.2. The clustering process using the values of this table provides the image recognition result: $I_1 \approx I_3 \approx I_5$, $I_2 \approx I_4$.

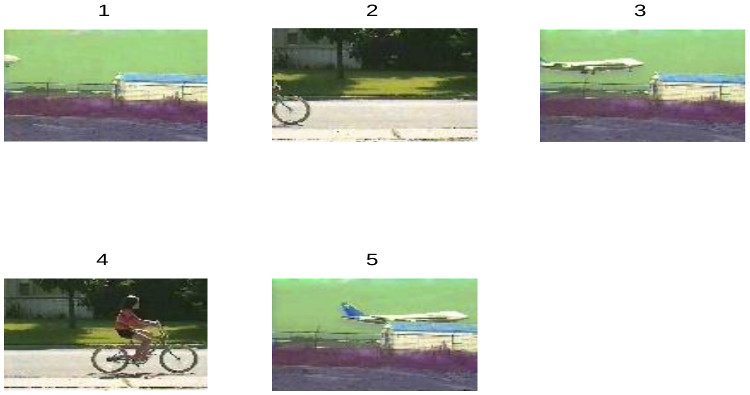

Fig. 3.9. The color image set

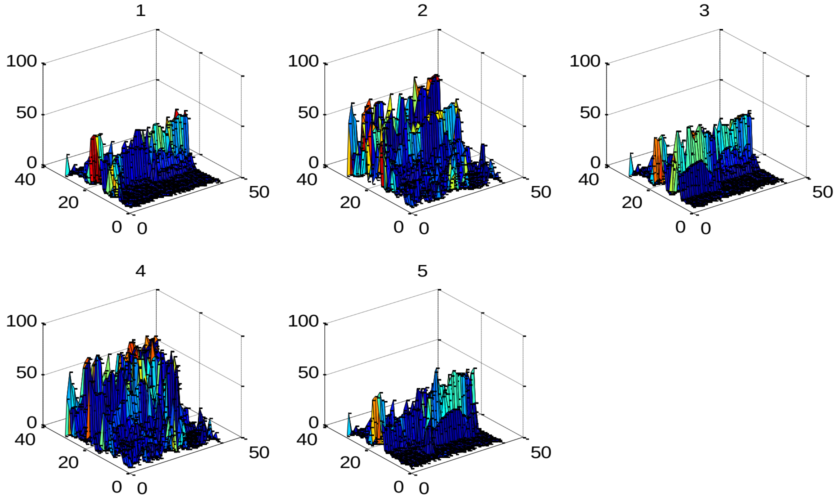

Fig. 3.10. The feature vector set

Table 3.2. Distances between image feature vectors

	$V(I_1)$	$V(I_2)$	$V(I_3)$	$V(I_4)$	$V(I_5)$
$V(I_1)$	0	571.3183	293.0381	675.6527	319.3169
$V(I_2)$	571.3183	0	599.5098	359.3718	618.9163
$V(I_3)$	293.0381	599.5098	0	686.5573	361.6215
$V(I_4)$	675.6527	359.3718	686.5573	0	712.8829
$V(I_5)$	319.3169	618.9163	361.6215	712.8829	0

We also developed some *moment-based image recognition* approaches [156,158,159]. The area moments represent not only good texture descriptors but also very good content descriptors, given the fact that image content is composed of textures, colors and shapes.

Thus, in [158] we propose an automatic moment-based image recognition technique. A moment-based image analysis similar to that described in subsection 3.1.1 is performed to each image I_i. Its feature vector is modeled as a sequence of 12 moment-based coefficients, representing normalized centered discrete area moments:

$$V(I_i) = (\eta_{00}, \eta_{01}, \eta_{02}, \eta_{03}, \eta_{10}, \eta_{11}, \eta_{12}, \eta_{13}, \eta_{20}, \eta_{21}, \eta_{22}, \eta_{23}) \tag{3.29}$$

where

$$\eta_{pq}(I_i) = \frac{\hat{\mu}_{pq}(I_i)}{\mu_{00}{}^{\gamma}(I_i)} \tag{3.30}$$

where $\gamma = \frac{p+q}{2} + 1$, the improved centered moment of (*p*+*q*)th order $\hat{\mu}_{pq}$ is given by (3.4) and the centered moment of (*p*+*q*)th order μ_{pq} is computed as in (3.7).

The computed feature vector provides a robust image content description [158]. Next, an automatic feature vector clustering is performed within the feature set $\{V(I_1),...,V(I_n)\}$. The automatic unsupervised classification algorithm presented in 1.4.4, here using a hierarchical agglomerative procedure with average linkage clustering and a validity index-based measure, is successfully applied in this case. Euclidian metric is used for measuring the distances between feature vectors. Automatic clustering makes this method work properly for very large image sets.

We have conducted a lot of recognition experiments, testing the proposed technique on hundreds large image data sets, and achieved quite satisfactory image recognition results. A high recognition rate, of approximately 80%, has been also obtained [158,159]. Let us describe a small recognition example performed by using this moment-based approach.

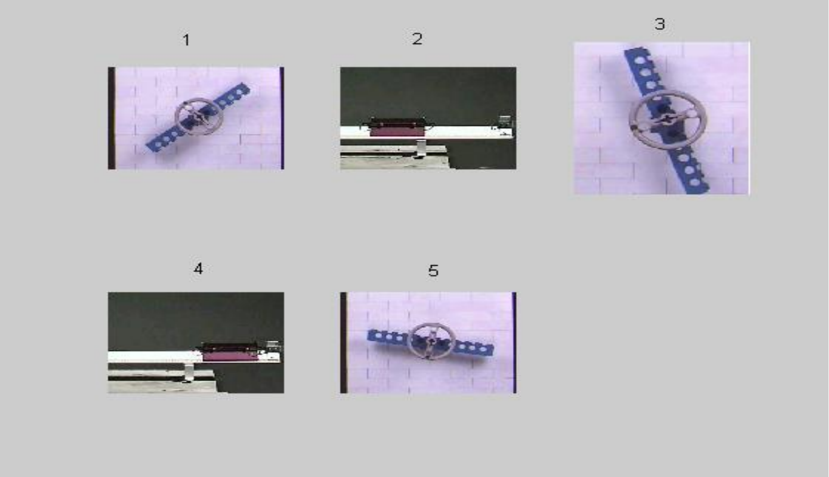

Fig. 3.11. Images to be clustered

The distances between feature vectors of the images to be recognized, displayed in Fig. 3.11, are: $d(V(I_1),V(I_2)) = 7.14$, $d(V(I_1),V(I_3)) = 2.26$, $d(V(I_1),V(I_4)) = 6.45$, $d(V(I_1),V(I_5)) = 2.77$, $d(V(I_2),V(I_3)) =$ 7.91, $d(V(I_2),V(I_4)) = 7.51$, $d(V(I_2),V(I_5)) = 7$, $d(V(I_3),V(I_4)) = 7.17$, $d(V(I_3),V(I_5)) = 2.14$, $d(V(I_4),V(I_5))$ = 6.29. The image clusters obtained on the basis of these values are $\{I_1, I_3, I_5\}$ and $\{I_2, I_4\}$.

Another automatic moment-based image recognition technique developed by us is provided in [156]. The feature vectors are modeled as sequences of normalized centered area moments, but having different forms than sequences given by (3.29). In the classification stage it uses the automatic feature vector clustering algorithm from 1.4.3 [39] and provides very good image categorization results [156].

Other image feature vector models, such as those based on various types of histograms, are provided by us in [147]. Image color/intensity histogram does not represent a satisfactory content descriptor, for the reasons explained in 4.2.1, so it has to be combined to other image histograms, such as DCT histogram, to obtain better content descriptors [147]. Also, the 2D Gabor filtering-based 3D feature vectors modeled for the video shot detection process described in 3.2.2 can be successfully used for unsupervised content-based image recognition, because they represent robust image content descriptors [139]. In section 3.5 we will describe some efficient feature vectors based on Gabor filters, which are used for content-based image retrieval [163].

Image clustering can also be performed by using various *image similarity metrics* [164]. In [164] we develop a robust image similarity metric based on SIFT characteristics. The proposed content similarity metric could be used successfully for performing efficient automatic image recognition.

Another category of image recognition techniques constructed by us is that of *color-based recognition* approaches [165]. We have developed several automatic image recognition methods using *LAB color features* in the last four years [165-167]. We have replaced RGB color space with LAB in our image analysis because the characteristics of the LAB color space makes it more suitable for extracting global color features from a digital image.

Thus, a robust unsupervised color-based image recognition system is proposed in [165]. The images from a given set $S = \{I_1, ..., I_n\}$ are clustered in several categories on the color similarity basis. First, all these images are converted from RGB to LAB. A certain color is defined in LAB space by a triplet (*L*,*a*,*b*), where (*a*,*b*) can be viewed as a pure color, while *L* coordinate gives its darkness or lightness. A reduction of the number of colors is required in order to obtain global characteristics [166]. With the LAB color space, such a reduction can be done by considering only several *ab* planes from the total of 256. We use 8 *ab* planes corresponding to the following central *L* values: 16, 48, 80, 112, 144, 176, 208 and 240. Any value of *L* in an image is forced to take the nearest value from this set. Then, for each of the 8 *ab* planes, we construct one planar histogram, having [256 x 256] bins, one for each (*a*,*b*) pair. We clear the bins containing less than 20 points, the planar histogram becoming scarce in values (with many empty bins). So, we compute one important color for several subsets of possible colors. The colors in a *ab* plane are distributed as in Fig. 3.12: red colors in upper right quadrant, and here, at the border of upper left quadrant, yellow color at higher luminance values; violet nuances in the lower right quadrant, blue colors in lower left quadrant and green colors in upper left quadrant. Black and white appear in planes with the lowest and highest luminance, and gray tones appear mostly toward center of *ab* planes.

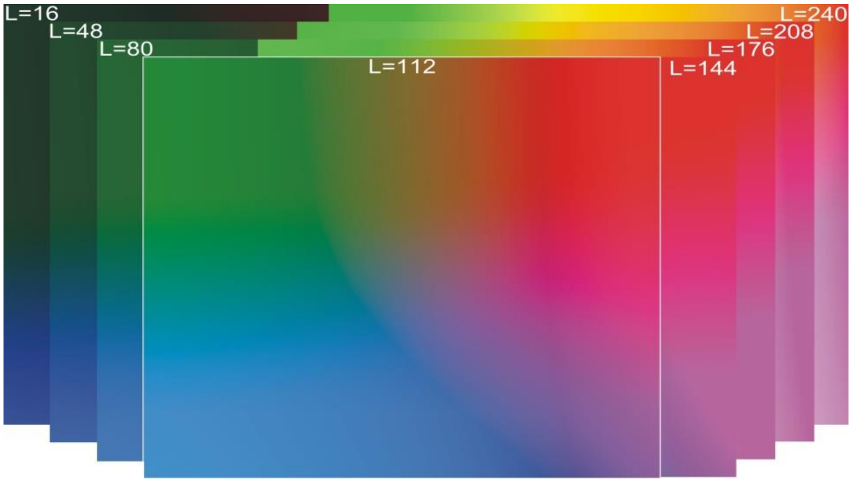

Fig. 3.12. Color distribution for *L*=134 *ab* plane

So, we consider each quadrant of an *ab* plane as an independent subset of colors. As we take into consideration 8 *ab* planes, we have 32 quadrants where we must identify the most important colors. For each quadrant a list of (*a*,*b*) pairs with corresponding nonzero bins in the planar histogram is constructed. Then the (*a*,*b*) pairs are ordered according to the values in the bins, the colors with a greater number of corresponding pixels in the image being on top of this list. Then colors very close in the *ab* planes are merged in these lists, which became a list of fewer colors, but with larger counts of pixels. Finally, the top (*a*,*b*) pair is taken as the most important color in the corresponding quadrant. Collecting all the 32 important colors provides us the following 2D feature vector:

$$V(I_i) = \begin{bmatrix} a_1^i \ldots a_j^i \ldots a_{32}^i \\ b_1^i \ldots b_j^i \ldots b_{32}^i \end{bmatrix} \tag{3.30}$$

each column representing an important (a_i, b_i) color. In order to facilitate the image comparison process, the feature vector components are arranged in order, from lower luminance *ab* planes to higher luminance, and clockwise from upper right quadrant to upper left quadrant. This assures that comparing two similar color components of two images means comparing the distance between two points in the same *ab* plane and the same quadrant [165].

Euclidean metric is used for these 2D feature vectors in the classification process. These color-based feature vectors are clustered automatically by applying the validation index based unsupervised classification model described in subsection 1.4.4. In this case that clustering technique uses the *K*-means algorithm as the semi-automatic clustering procedure to be executed repeatedly [165].

We have obtained satisfactory image clustering results, as resulting from our recognition experiments. Such a color-based image recognition example is represented in Fig. 3.13. The 9 color images are categorized successfully in 4 classes, representing flowers, horses, vestiges and beaches, on the color similarity basis. A high image recognition rate (over 80%) and high values for *Precision* and *Recall* performance parameters have been also achieved.

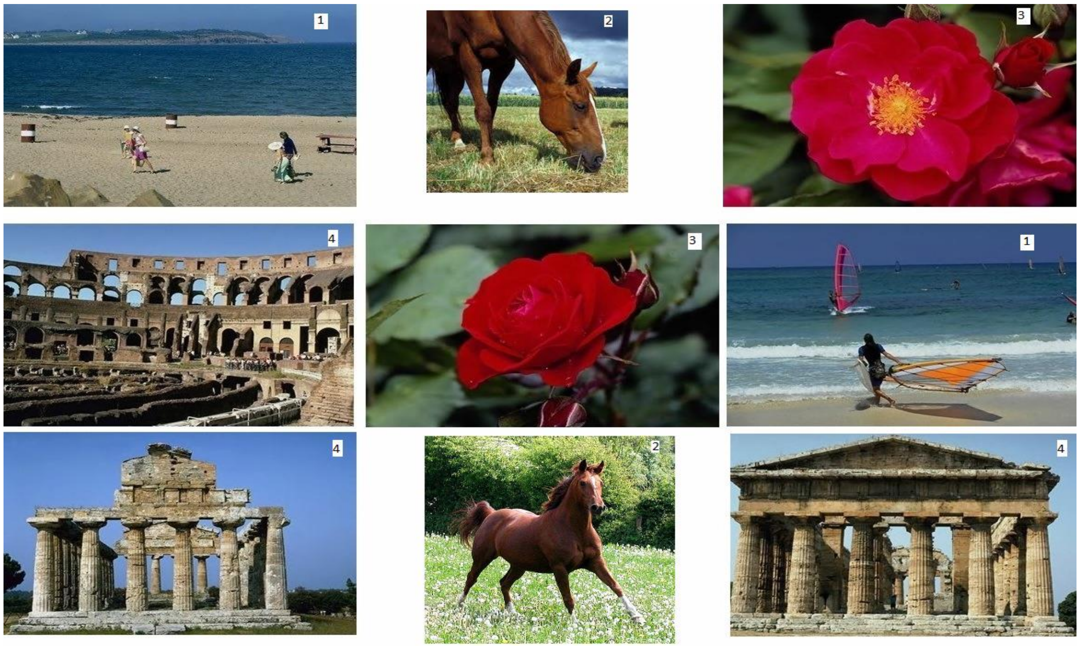

Fig. 3.13. Images clustered in 4 color-based classes

Another successfully variant of this LAB color space based recognition approach is proposed in [166]. A quite similar feature extraction process is performed, but the LAB color-based image feature vectors are classified by using the hierarchical agglomerative clustering solution, instead of *K*-means, within the automatic clustering technique from 1.4.4. Another efficient LAB color feature based method developed by us is described in [167]. These LAB color characteristics are also used by us in the biometric domain, for iris clustering [54]. A color-based iris image recognition system is proposed in [54]. From the performed method comparison we have found that our color-based recognition methods outperforms other color image clustering approaches, such as those based on color histograms or some similarity metrics.

We have described here some robust automatic image recognition approaches using statistics-based, moment-based, Gabor filtering-based, SIFT-based and LAB color-based feature extraction processes. They provide good results and high recognition rates, outperforming some state-of-the-art image recognition techniques. Also, because of their automatic character, our unsupervised recognition methods work properly for very large image sets or databases. For this reason they can be applied successfully in content-based image indexing and retrieval areas. So, cluster-based image indexing as well as content-based image retrieval (CBIR) can be easily performed using the image recognition results described here, as we will see in the next section.

3.4.2. Video sequence recognition approach

Besides static image recognition, we have considered developing some video image recognition solutions. An unsupervised content-based movie recognition technique is provided in [147]. Our approach clusters successfully the video sequences on the basis of their content-similarity.

So, in [147] we consider a set of videos, $\{Vid_1,...,Vid_N\}$, that must be classified in several similarity clusters. Each video sequence Vid_i could be composed of one or more video shots [147]. The proposed video analysis algorithm consists of the following processes:

- Video frame feature extraction
- Temporal video segmentation
- Video keyframe extraction
- Movie feature vector modeling
- Video feature vector clustering

In the frame feature extraction stage one computes powerful frame content descriptors that can be used as feature vectors in the next video analysis processes. Feature extraction could be performed using the numerous image featuring techniques described in this thesis. In our 2005 paper [147] we considered a histogram-based frame feature extraction, but since then we have provided much more efficient featuring approaches [155-157,163-166]. We already mentioned in 3.2.1 the feature extraction process from [147], which computes a normalized combination of color (intensity) histograms and *DCT* (*Discrete Cosinus Transform*) histograms. The feature vectors are obtained as $V(I_i) = \frac{H_c(I_i) + H(DCT(I_i))}{M \cdot N}$ for each $[M \times N]$ frame I_i [147].

A temporal video segmentation process is then performed on each videoclip Vid_i, to determine its shots. In [147] a semi-automatic video cut detection approach, like those described in 3.2.1, is used. Obviously, our automatic videoshot detection technique developed in 2009 and presented in 3.2.2 [139] would represent a better segmentation solution in this case.

The analyzed clips may have a large size, which means a great number of frames, therefore some resumed forms of the videos are used in the recognition process. A resumed form of the movie Vid_i is determined by computing its *keyframes* [147]. The video keyframes comprise the essence of the movie content. The easiest video keyframe detection solution consists of considering the first frame of each identified videoshot as a keyframe, but this does not represent always a proper solution.

We could extract more keyframes from each shot by performing a frame clustering operation within that shot. In [147] we use a semi-automatic hierarchical agglomerative clustering procedure for frame grouping, the number of clusters being set interactively after watching the videoshot. This region-growing algorithm could be replaced with one of the automatic clustering techniques described in 1.4. The first video frame of each cluster is considered a keyframe of the videoshot [147]. The keyframe set of the movie sequence includes all keyframes of all the videoshots.

A video feature vector is then modeled for each movie. Therefore, if $\{I_1^i,...,I_{n(i)}^i\}$ represents the keyframe set of Vid_i, then the movie feature extraction process is expressed as [147]:

$$V(Vid_i) = \begin{bmatrix} V(I_1^i) \\ \dots \\ V(I_{n(i)}^i) \end{bmatrix}, \forall i \in [1, N] \tag{3.31}$$

Each 2D video feature vector $V(Vid_i)$ is a $[n(i) \times 256]$ matrix that represents a good content descriptor of the corresponding movie. So, all these feature vectors are characterized by the same number of columns and a number of rows depending on the number of keyframes from each video. Therefore, the distances between them cannot be measured by using Euclidian metric or other conventional metrics. In this case, which requires a special metric to be used in the classification process, the Hausdorff-derived metric, described in 1.4.1 and used also for speaker recognition tasks, can be successfully used.

An unsupervised videoclip classification is then performed by clustering these 2D feature vectors. In [147] a semi-automatic feature vector clustering procedure, based on a hierarchical agglomerative algorithm, is applied to the feature set $\{V(Vid_i)\}_{i=\overline{1,N}}$. The number of the video classes, *K*, is set interactively after one visualizes these videos [147]. Obviously, an automatic clustering algorithm [39], like those presented in 1.4, can be used in this case, instead of the semi-automatic region-growing approach, too.

We have tested the proposed recognition approach on numerous video sets, obtaining quite good results. This main disadvantage of this unsupervised video recognition technique consists of its non-automatic character. Because of the interactivity that is used in several stages of the recognition process, our approach executes quite slowly. Also, because of the same interactions, it is quite difficult to perform clustering within very large movie sets. For small and medium sets of videos, this recognition approach works properly, as resulting from the following example, too. We consider the small video set $\{Vid_1, Vid_2, Vid_3\}$, to be clustered. The keyframes of these videos and the keyframe feature vectors are displayed in the next three figures. The values of distances between movie feature vectors $V(Vid_{1-3})$ are included in Table 3.3. By using the values in this tables, the videos are clustered in 2 classes: $\{Vid_1, Vid_3\}$ and $\{Vid_2\}$.

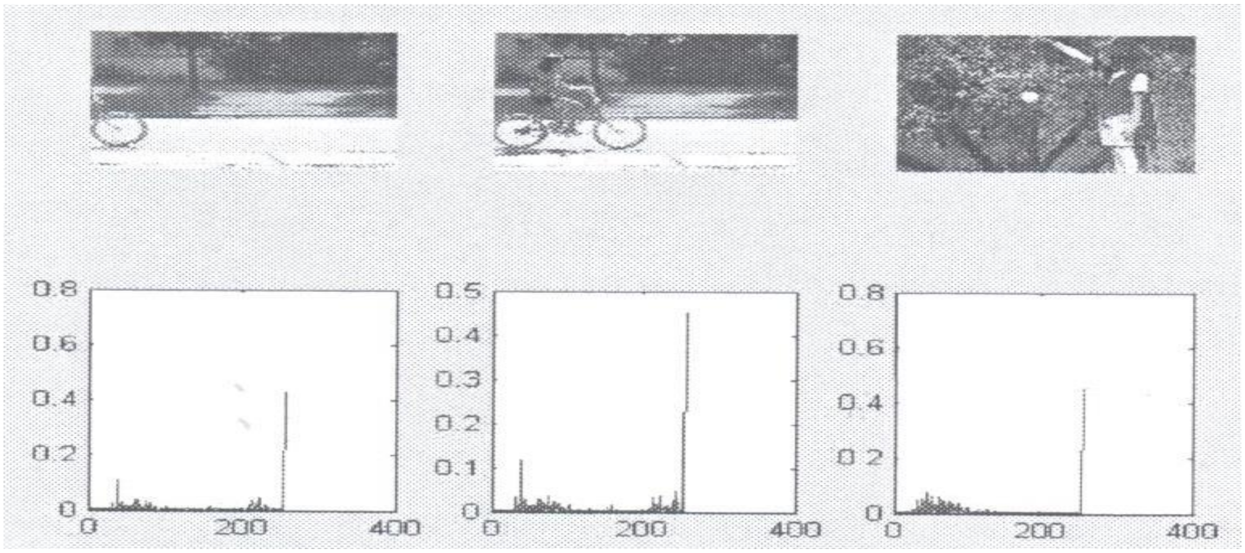

Fig. 3.14. Keyframes of the 1st movie and their feature vectors

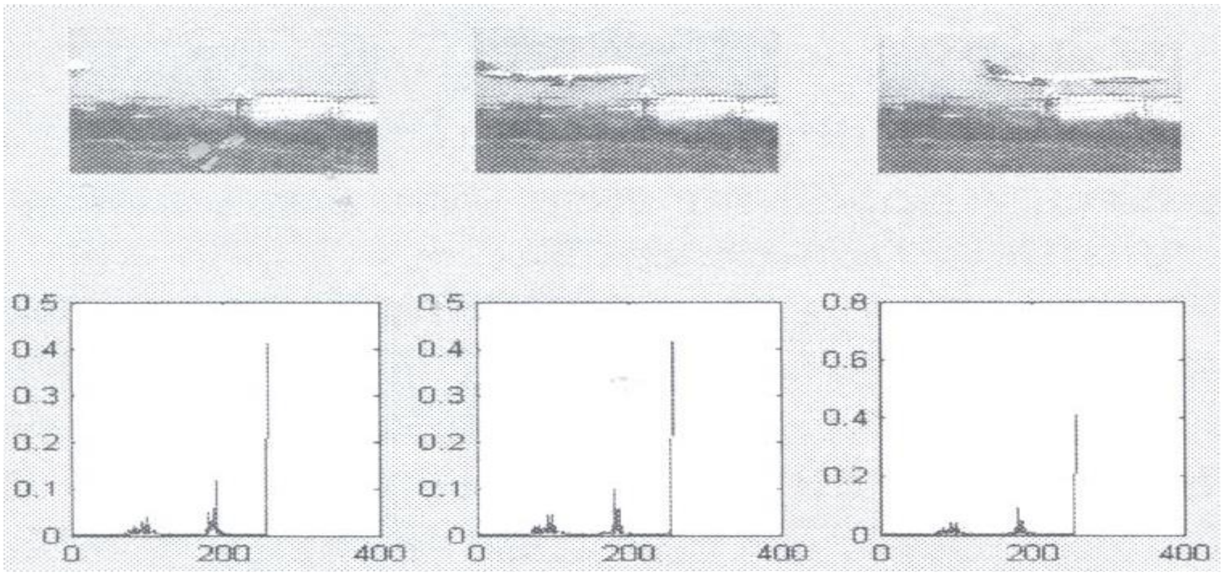

Fig. 3.15. Keyframes of the 2nd movie and their feature vectors

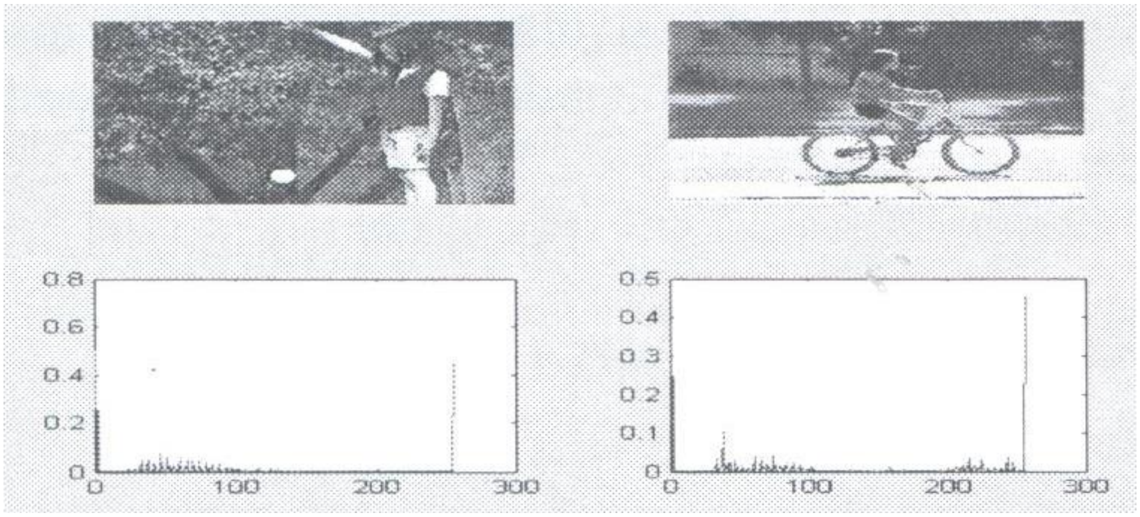

Fig. 3.16. Keyframes of the 3rd movie and their feature vectors

Table 3.3. Distances between video feature vectors

	$V(Vid_1)$	$V(Vid_2)$	$V(Vid_3)$
$V(Vid_1)$	0	0.1168	0.0191
$V(Vid_2)$	0.1168	0	0.1147
$V(Vid_3)$	0.0191	0.1147	0

This video recognition method can be improved considerably by transforming it into an automatic approach. We have already indicated where our automatic clustering algorithms can replace the used semi-automatic clustering procedures, so that the recognition technique becomes completely automatic. An automatic version of this approach can be applied successfully in the video indexing, where it may provide cluster-based indexing solutions, and retrieval domains.

3.4.3. Image and video object recognition models

Object recognition represents a challenging computer vision field that is strongly related to object detection, discussed in the last section. The image object recognition task consists of classifying the objects in proper classes on the basis of their extracted features. The classification process can be either supervised or unsupervised.

The recognition techniques described here work for image objects that have been already detected in digital images or video sequences by using locating methods like those presented in 3.6. The image object, representing a semantic region of an image or frame, can be detected exactly as it is or as the sub-image corresponding to its bounding rectangle. If the objects are obtained as such sub-images, they can be treated as *images* in the recognition process. So, all the image recognition techniques described in 3.4.1 can be applied successfully to objects, in this case.

I have already presented some image object recognition methods in this thesis. The supervised and unsupervised biometric recognition techniques mentioned in sections 2.2 and 2.3, and published in our papers [37,38,53,54,75,79,80,97-99], represent efficient object recognition approaches that work for objects representing faces, fingerprints or irises. These biometric objects have been featured by using 2D Gabor filters, PCA, DWT-2D, SIFT or minutia-based solutions.

Other image object recognition solutions proposed by us are based on Histograms of Oriented Gradients (HOGs) or cross-correlation procedures [168]. We will discuss more about these approaches in the last section of the chapter.

If the image objects are considered in their current shape, the recognition process becomes a much more difficult task. We proposed several content-based object recognition solutions in our past works [33,169,170]. In our vision, such a shape-based image object recognition technique must perform the following operations:

- A shape recognition process is performed first
- A content-based recognition is conducted within each shape class

Shape recognition represents a very important computer vision domain, consisting of recognizing image objects, based on their shape information [169-180]. While supervised shape recognition classifies the objects by matching their shapes against the registered template shapes, unsupervised shape recognition clusters a set of objects, based on their shape similarity. A successful shape recognition approach requires a robust shape descriptor that captures the shape features in a concise manner and is invariant to all geometric transformations. Shape analysis approaches are divided into two main categories: *region-based* and *contour-based* methods.

The descriptors used by region-based techniques are derived using all the pixel information inside a shape region, while the contour-based descriptors express the shape information of the object outline. The most important region-based recognition approaches are based on the Angular Radial Transform Descriptor (ARTD) [171], Zernike moments [172] and Legendre moments [173]. Contour-based shape recognition includes techniques based on Fourier Descriptors [174], Curvature Scale Space Descriptors (CSSD) [175], Contour Trees [176], Reeb Graphs [177] and invariant moments [178-180].

We have approached the object shape recognition domain by developing an automatic moment-based recognition model [40]. This models uses feature vectors representing robust shape descriptors, which are translation, scaling, rotation and reflexion invariant measures. We consider a set $\{Ob_1,...,Ob_n\}$ containing the image objects to be recognized by their shape information.

The following moment-based image object feature extraction process is considered in [40]:

$$V(Ob_k) = \left[(\eta_{30}(k)+\eta_{12}(k))^2 + (\eta_{03}(k)+\eta_{21}(k))^2, \eta_{24}(k)+\eta_{42}(k)\right], \forall k \in [1,n] \qquad (3.32)$$

where $\eta_{ij}(k) = {\mu_{ij}(k)}\big/{\mu_{00}^{(i+j)/2+1}(k)}$ represents a scaling invariant moment and $\mu_{ij}(k) = \sum_x \sum_y f_k(x,y)\cdot(x-C_x)^i \cdot (y-C_y)^j,\ i,j \geq 0$, where $f_i(x,y) \in \{0,1\}$ is the gray-value function of the object area Ob_k , $C_x = \frac{m_{10}}{m_{00}}, C_y = \frac{m_{01}}{m_{00}}$ and $m_{ij}(k) = \sum_x \sum_y f_k(x,y)\cdot x^i \cdot y^j$.

Similar moments are used for image segmentation and recognition processes. The resulted feature vector $V(Ob_k)$ is invariant to the geometric transforms: scaling, translation, rotation and mirroring. The first component of it, $(\eta_{30}(k)+\eta_{12}(k))^2 + (\eta_{03}(k)+\eta_{21}(k))^2$, represents a Hu moment used to express the shape eccentricity [180]. The second component, $\eta_{24}(k)+\eta_{42}(k)$, constitutes also an invariant moment-based parameter [33,169]. The modeled feature vector represents a powerful shape descriptor of the image object. The Euclidean distance is used for these feature vectors in the classification process.

An automatic unsupervised classification process is performed next within the feature set $\{V(Ob_1),...,V(Ob_n)\}$. These moment-based feature vectors are clustered automatically in a proper number of classes that is not a priori known [40]. One applies the validation index – based automatic unsupervised feature vector classification technique described in 1.4.4, in the version executing repeatedly the region-growing algorithm [40]. One sets a threshold *T*, then run the hierarchical agglomerative algorithm for each $N \in [1,T]$, until an optimal value N_{optim} is achieved and the final classes $C_1,...,C_{N_{optim}}$ result.

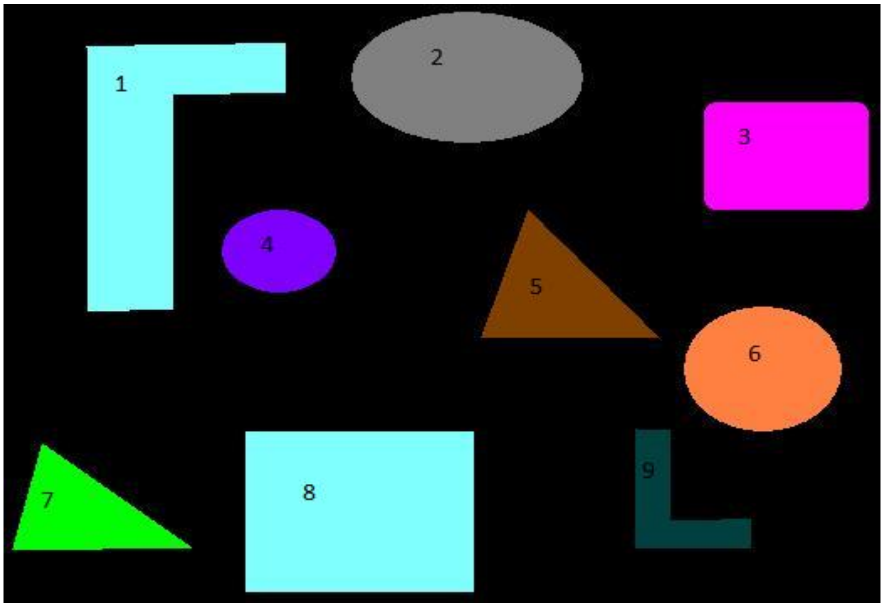

Fig. 3.17. Image containing several shapes

Many experiments have been performed using the described shape recognition approach, very good results being obtained. A high recognition rate, of approximately 85 %, is produced by our technique. This recognition rate rises if one increases the threshold value, usually set as $T = \lceil n/2 \rceil$, but the procedure complexity and time execution rise too.

We obtain high values for the performance parameters (*Precision*, *Recall* and F_1) of this recognition process. Thus, we get *Precision* = 0.85, *Recall* = 0.84, which means our shape recognition approach produces quite few missed hits or false positives. A shape recognition example is described in the two figures. Thus, in Fig. 3.17 there is displayed an image containing objects which can be segmented easily. Each Ob_i is marked with the *i* value in the picture, *i* = 1,…,9. The shape classes corresponding to the image from Fig. 3.17 are represented in Fig. 3.18, where each shape is labeled with its class number. The 4 detected shape classes, representing the final recognition result, are: $\{Ob_1, Ob_9\}$, $\{Ob_2, Ob_4, Ob_6\}$, $\{Ob_3, Ob_8\}$ and $\{Ob_5, Ob_7\}$.

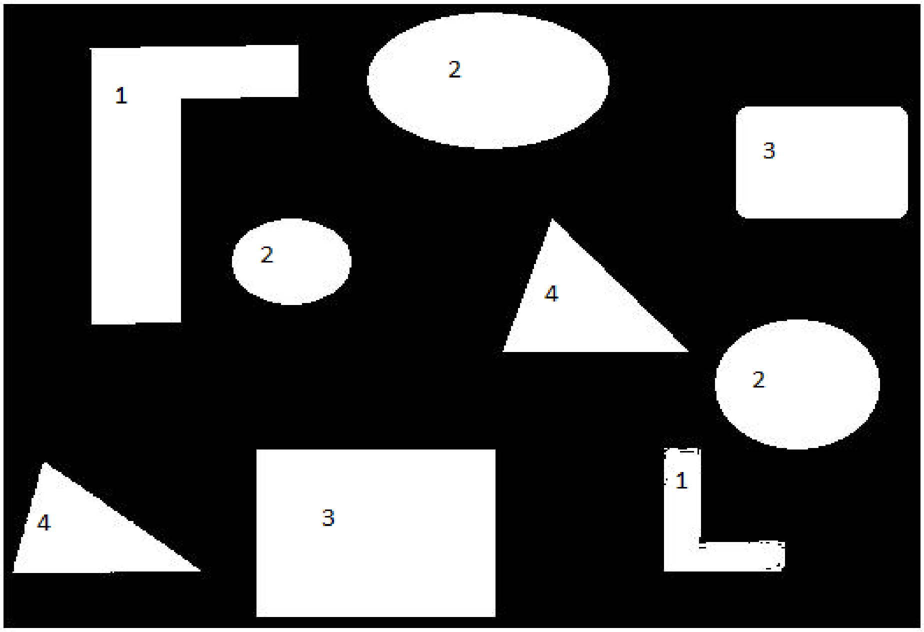

Fig. 3.18. The detected shape-based classes

Our moment-based shape analysis approach outperforms other recognition techniques, like those based on Hu moments [180], Zernike moments [172] or Fourier descriptors [174]. Also, its automatic character makes it better than any non-automatic shape recognition approach, because it works properly for very large sets of shapes. Therefore, it becomes very useful in some important computer vision application areas, such as shape-based indexing of image databases and object retrieval from these databases.

In the next stage of object recognition, a content-based recognition is performed within each *shape-based class*, C_i, $i \in [1, N]$. All the image objects from such a class have similar shapes but could have different contents. Besides its shape, the object content is characterized by the colors and textures. Various featuring techniques can be used to obtain a proper image object content descriptor. A histogram-based feature extraction can be used, the feature vector of an object from a shape class being computed as a given type of histogram of that object or as a combinations of more histograms. Color, or intensity, histograms, DCT histograms, edge histograms, weighted histograms or combinations of these image histograms can be used for this purpose. Such a histogram-based object featuring is proposed by us in our 2006 book [33]. We have obtained quite good recognition results using these histogram-based feature vectors, but, since 2006, more powerful image feature vectors that can be applied successfully for image objects have been modeled by us. So, the feature vectors based on 2D Gabor filters [139], 2D Discrete Wavelets [99], SIFT characteristics [39,164], statistical features [157] and LAB color-based characteristics [165-167] can be easily adapted in order to work for image objects.

The content-based feature vectors are clustered automatically using any of the clustering approaches from 1.4. As a result of this content-based object recognition, each shape class C_i is divided into several content-based sub-classes. All these content classes could be considered the final object recognition result, although in [33] we consider one more recognition level. Thus, a *structure-based* object recognition is performed within each content-based class [33]. The object structure is defined there as formal model that defines the way color/intensity and texture regions are arranged into that object. Some structure-based object feature vectors are computed and clustered in a number of classes [33]. These structure-based classes, containing objects characterized by the same shape, content and structure, represent the final object recognition result [33].

The image object recognition approach based on shape, content and structure features represents a quite good idea, given the satisfactory recognition results it produces [33]. But the structure-based recognition level has been mainly necessary because of the histogram-based feature vectors used in [33,169], which do not represent very powerful object content descriptors. For example, two objects may have exactly the same shape and similar color histograms, but they could have somewhat different contents because of the different structures (different arrangements of color regions). We have found that the more complex and robust image feature vectors constructed by us since 2006, representing much better content descriptors, make the structure-based recognition process unnecessary, the object recognition being performed successfully in two stages only.

The recognition methods discussed here can be applied also for video image objects. If the video objects are defined as image objects contained by video frames, the video object recognition process becomes equivalent to the video tracking process that is described in the last section. But if we consider the video object as an entity composed from all its instances in the frames and its trajectory, the recognition process becomes a more difficult task. In [33] we consider a recognition solution for such spatio-temporal video objects. Two objects are similar if they have both similar states and similar trajectories. Similarity measures between object trajectories are modeled in [33].

These image object recognition methods can be successfully applied not only in image indexing and retrieval, and video tracking domains, but also in a high-level image analysis and computer vision field that is *image and video interpretation* [33]. In [33] we perform also semantic object analysis, providing some image and video interpretation (understanding) approaches. A supervised object recognition system is used for this purpose. Its training set contains registered objects, labeled with their semantic (for example *people*, *car*, *building*, …). A object feature extraction is performed, then a supervised classification is applied to the feature vectors [33]. Each input object is inserted in a class representing a semantic (label) by using the minimum average distance or the *K*-Nearest Neighbors classifier. The classified (recognized) object receives the label of that class. An image is interpreted by associating to it the sequence of labels of its objects. The interpretation of a video results from its frame interpretations [33].

3.5. Content-based image indexing and retrieval systems

Multimedia information indexing and retrieval represents an important computer vision domain that includes two strongly correlated sub-domains. *Information indexing* is generally considered an essential requirement for any efficient *information retrieval* system. The indexing process develops some structures, called indexes, which facilitate the direct access to required information from a large data collection. Information retrieval represents the process of extracting the relevant information to an information need from data collections, eventually using the index structures.

Multimedia retrieval aims to extract relevant media entities, such as sounds, images, videos or image/video objects, from multimedia data collections, such as the multimedia databases [181]. Multimedia indexing and retrieval processes may have a *concept-based* character or a *content-based* character. The concept-based indexing/retrieval is based on metadata, which refers to the textual descriptions or annotations associated to the media entities. The content-based indexing/retrieval use the content characteristics, expressed as feature vectors, of those entities and not their metadata. In [33] we investigated this computer vision domain, providing some solutions for multimedia database organizing, indexing and retrieval.

Content-based image indexing and retrieval represents the most important and researched sub-domain of multimedia indexing and retrieval. Some image indexing techniques are described in the next subsection, while content-based image retrieval approaches are presented in subsection 3.5.2.

3.5.1. Content-based image indexing models

The *content-based image indexing* (*CBII*) has been introduced to overcome the disadvantages of metadata-based indexing. Content-based image indexing replaces the search keys, used by annotation-based indexing, with feature vectors characterizing the image content given by colors/intensities, textures and shapes. An efficient content-based image storing is also necessary for a flexible retrieval from image databases. The purpose of storing an image indexing structure is to optimize speed and performance in identifying relevant digital images for a search query.

A lot of indexing techniques have been developed in the last three decades for the multidimensional spaces like the content-based image feature vector spaces. *Spatial Access Methods* (*SAM*) based on various *tree* structures are used for indexing high-dimension spatial data. Some well-known tree-based indexing methods that work properly for digital images are the R*-tree [182], K-D-tree [183], VP (Vantage-Point)-tree [184], M-tree and MVP-tree [185]. These content-based indexing solutions treat the image retrieval tasks as multidimensional Nearest-Neighbor (NN) searches.

The content-based image and object feature vectors modeled by us and described in previous sections can be successfully used with these SAM-based indexing structures in the retrieval processes [181]. So, in [186] we have developed a color-based image indexing method using LAB color features and a K-D tree structure, which recursively partition the space into two subspaces. Each non-leaf node of the K-D tree generates a splitting plane dividing the space into two half-spaces. The color-based feature vectors $V(I_i)$, which will be described in 3.5.2, are inserted in the nodes of this K-D tree as following: the tree is traversed starting from its root and moving to either the left or the right child-node depending on whether the point to be inserted is on the *left* or *right* side of the splitting plane. Once one reaches the node under which the child-node must be located, insert the new point, representing a feature vector, as either the left or right child of the leaf node, again depending on which side of node's splitting plane contains the new node. This K-D tree based index facilitates considerably the image retrieval process, by solving the *K*-NN Search task [186]. The image feature extraction and the content-based retrieval using the K-D-tree based index are described in 3.5.2 [186].

We also consider some cluster-based indexing approaches in [33]. Since the image content is composed of textures, colors/intensities and shapes, the content-based image indexing include color-based indexing, texture-based indexing and shape-based indexing procedures [33]. So, an index is constructed for each content component (color, texture or shape).

The idea of our image indexing approach is to model a content-based image database recording and to perform a clustering process at the level of each field of that recording [33]. So, let $I_1,...,I_N$ be the images from a large collection. A robust image analysis process, applying the image segmentation, object detection and image/object featuring operations described or to be described in this thesis, is performed on each image. As a result, one obtains feature vectors for the image content as a whole, texture classes, main object shapes and contents.

Then, one organizes an image database composed of three tables: T_1 for images, T_2 for objects and T_3 for textures, respectively. For each I_i we model in the image-related table, the record $T_1(I_i)$ containing a number of *fields* $F_1^j(i)$. Each field registers a content-based feature vector $V(F_1^j(i))$, representing an image descriptor. For example, $F_1^1(i)$ may refer to moment-based feature vectors, $F_1^2(i)$ to Gabor filter-based feature vectors, $F_1^3(i)$ to SIFT-based feature vectors, $F_1^4(i)$ to color-based feature vectors, and so on. Therefore, each image table recording is modeled as following:

$$T_1(I_i) = \{V(F_1^1(i)),...,V(F_1^K(i))\}, \forall i = 1,..., N \tag{3.33}$$

where *K* represents the number of content characterization solutions.

Let $Ob_1,...,Ob_n$ represent all the objects of interest detected in the images $I_1,...,I_N$. The recording of each object Ob_i in the table T_2 is given as:

$$T_2(Ob_i) = \{V(F_2^1(i)),...,V(F_2^k(i))\}, \forall i = 1,..., n \tag{3.34}$$

where the fields $F_2^j(i)$ record feature vectors $V(F_2^j(i))$, representing shape or object content descriptors for $j < k$, while $V(F_2^k(i)) = m$ if Ob_i belongs to I_m.

If $t_1,...,t_l$ represent all the textures identified in the images $I_1,...,I_N$, then the database record of each texture t_i in the table T_3 is modeled as following:

$$T_3(t_i) = \{V(F_3^1(i)),...,V(F_3^p(i))\}, \forall i = 1,..., l \tag{3.35}$$

where the fields $F_3^j(i)$ record feature vectors $V\left(F_3^j(i)\right)$ representing texture descriptors for $j <$ p, and $m \subset V\left(F_3^p(i)\right)$ if t_i can be found in I_m.

Indexing structures based on feature vector clustering are created for all the three tables T_{1-3} [33]. Each table T_s can be indexed by any field of it, F_s^j. All the feature vectors from this table corresponding to that field, $\left\{V\left(F_s^j(1)\right),...,V\left(F_s^j(N)\right)\right\}$ are clustered automatically in a number of classes. In [33], the region-growing based automatic clustering algorithm described in 1.4.3 is used [39], but the automatic unsupervised classification techniques described in 1.4.4 and based on validation indexes could also be applied here. The resulted feature vector clusters are noted $C_s^j(1),....,C_s^j(n(j))$. For each of them, a representative feature vector, $V\left(C_s^j(i)\right)$, is determined (as cluster's centroid, for example). A list of indices is also determined as follows:

$$l\left(C_s^j(i)\right) = \left\{ind \mid V(F_s^j(ind)) \in C_s^j(i)\right\} \tag{3.36}$$

With these results, the table indexing structures are modeled as the next sets of indexes:

$$Index\left(T_s\right) = \left\{Index_1^s,..., Index_{n(T_s)}^s\right\}, s \in \{1,2,3\} \tag{3.37}$$

where $n(T_s)$ is the number of content-based fields of T_s, and the index of the j^{th} field of T_s is organized as a table with 2 fields, related to the representative feature vector and the list of indices. An entry in such a index table is modeled as following:

$$Index_j^s(i) = \left[V\left(C_s^j(i)\right); l\left(C_s^j(i)\right)\right], \forall i = 1,..., n(j) \tag{3.38}$$

These feature vector clustering based table indexing structures facilitate considerably the image entity search during the retrieval process. In the next subsection we will discuss more about the working of the proposed image indexing model in the retrieval context. The architecture of a modeled table and its indexing structures are represented in Fig. 3.19.

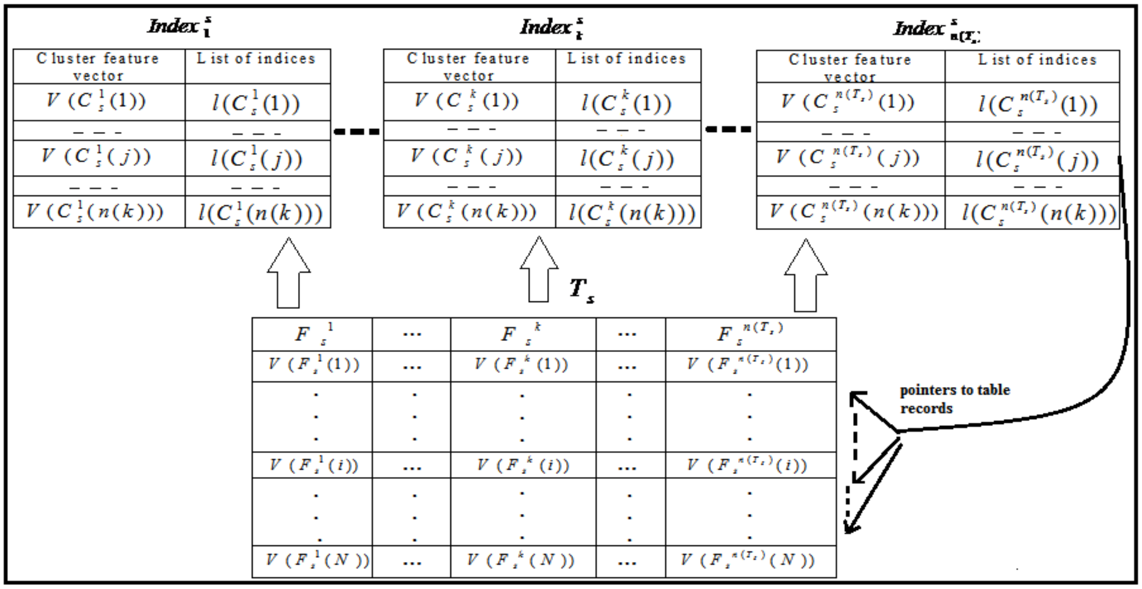

Fig. 3.19. Table indexation scheme

3.5.2. Content-based image retrieval techniques

Content-based image retrieval (*CBIR*) domain has originated in 1992, numerous CBIR technologies being developed since then. In recent years there has been a growing interest in content-based retrieval because of the limitations inherent in annotation-based image retrieval systems [187]. The CBIR techniques analyze the actual image content, which refers to colors, textures and shapes, rather than the metadata such as keywords, tags or descriptions associated with the image.

A CBIR system extracts the needed image entities from a large database, on the basis of their visual content. The content-based retrieval process performs two major operations: *querying* and database *searching*. The *query* represents a solicitation addressed by the user to the system. Most important querying techniques are: query by example, query by multiple examples, query by image region, querying by direct feature specification, multimodal query and semantic query. The image search process is strongly related to the content-based image database indexing described in the previous subsection.

Also, numerous content-based retrieval systems make use of *relevance-feedback* mechanisms, which progressively refines the image search results by repeating the search, with some output used as the new input [187,188]. Most retrieval systems use low-level image content features, such as image color, texture and shape characteristics. More sophisticated CBIR systems use medium-level descriptors, such as those related to image objects and the spatial relationships between them, and high-level features, related to image semantics.

Content-based image retrieval technologies have been successfully applied in various domains, such as medical diagnosis, crime prevention and law enforcement, art collections and engineering design. Some of the most popular CBIR systems are: Google Image Search, Bing Image Search, QBIC, FIRE, CIRES, Visual SEEK and GNU Image Finding Tool [188].

The CBIR domain has been widely investigated by us in the last years, many image retrieval approaches being proposed [33,163,186,189-191]. Our querying approach has been based on examples, in the most cases. The content-based retrieval tasks considered by us have the following general form: given an image entity (image, object, texture) as an input, identify all the relevant entities from an image collection. The relevant entities for a given input could represent: all images, objects or textures registered in a database that are similar by content to an example image, object or texture; all registered images containing objects or textures that are similar to an input object or texture class; all the registered image objects having similar shapes to a given input shape.

We use both the cluster-based and SAM-based content-based indexing structures to solve these image retrieval tasks [33,186]. So, if the image collection is organized and indexed as described in 3.5.1, the image retrieval becomes a quite easy task. An effective CBIR system using the clustering-based image indexes is developed in our 2006 book [33]. The proposed content-based retrieval model is composed of an interrogation (querying) device and a search engine. The database interrogation process is based on single and multiple examples [33].

If *I* is an input image given as example, the search engine looks for images that are similar to it in the image-related table of the database, T_1. The index corresponding to that table is then searched. The input image can be featured in various ways, some feature vectors *V*(*I*) being obtained. If *V*(*I*) is computed through a feature extraction process corresponding to the field F_1^j , then $Index_j^1$ structure is searched. One compares *V* (*I*) to all representative feature vectors registered by that index, $Index_j^1(i)[1] = V(C_s^j(i)), i = 1,...,n(j)$, by computing the distances to them. The index entry corresponding to the minimum distance value is determined from the next relation:

$$ind(j) = \arg\min_{i\in[1,n(j)]} d\left(V(I), Index_j^1(i)[1]\right) \tag{3.39}$$

where *d* is a metric that works properly for these feature vectors. The list of indices (table positions) $Index_j^1(ind(j))[2] = l\left(C_1^j(ind(j))\right)$ is then determined. The registered images having these table recording positions represent the content-based retrieval result that can be formalized as $\{I_i \in T_1 \mid i \in Index_j^1(ind(j))[2]\}$. This retrieval result corresponds to a single image feature extraction method, related to the *j*th field. If one considers all the fields of the table, one obtains a retrieval result for each of them. The final image retrieval result is then achieved as the intersection of all these results: $\bigcap_{j=1}^{K}\{I_i \in T_1 \mid i \in Index_j^1(ind(j))[2]\}$, where *ind* (*j*) is given by (3.39).

If one considers another entity type, instead of a whole image, as a query example for a content similarity based retrieval, the searching process is performed similarly [33]. The tables T_2 or T_3, and their corresponding indexing structures, are used instead of T_1, if the input represents an image object or a texture.

The second retrieval type consists of extracting the images containing objects or textures that are similar to a given input. Let us describe the image object case here only, the texture case being performed similarly. If *Ob* represents the input object, then all the registered objects which are similar by both the shape and image content to it are firstly retrieved from the corresponding table as $\bigcap_{j=1}^{n(T_2)}\left\{Ob_{ind} \in T_2 \mid ind \in Index_j^2\left(\arg\min_{i\in[1,n(j)]} d\left(V(Ob), Index_j^2(i)[1]\right)\right)[2]\right\}$. The images containing objects that are similar to *Ob* are then determined, using the reference field of T_2, as:

$$\left\{I_m \mid m = V\left(F_2^{n(T_2)+1}(ind)\right) \mid ind \in \bigcap_{j=1}^{n(T_2)}\left\{Index_j^2\left(\arg\min_{i\in[1,n(j)]} d\left(V(Ob), Index_j^2(i)[1]\right)\right)[2]\right\}\right\}$$

.

The last retrieval task requires the search for all registered objects characterized by a given input shape, *S*. Let $F_2^1,...,F_2^{Sh(T_2)}$ represent the shape-related fields of any object recording from T_2. Then, the set of the image objects which are similar in shape to *S* is determined as following: $\left\{Ob_{ind} \in T_2 \mid ind \in \bigcap_{j=1}^{Sh(T_2)} Index_j^2\left(\arg\min_{i\in[1,n(j)]} d\left(V(S), Index(i)[1]\right)\right)[2]\right\}$. Other retrieval tasks can be also formulated and solved using our cluster-based image indexing and retrieval model.

We have also developed some content-based image retrieval techniques based on relevance-feedback schemes [163,186,189-191]. They retrieve images from large collections on the content similarity basis, but they could work for image objects and textures also. Query by example is used for the image database interrogation, while the image searching process is based on a relevance-feedback mechanism and can be facilitated by the SAM-based image indexing structures.

Our methods compute robust image content-based descriptors by using various feature extraction methods. If $I_1,...,I_n$ represent the registered images, the corresponding feature vector set can be obtained by applying the image featuring approaches described in 3.4.1 [155-159,164-170]. We provide here other image feature extraction solutions that work properly for both recognition and retrieval of digital images.

Thus, we proposed some color-based image retrieval techniques using histogram-based feature extractions and various metrics for the feature vectors, several years ago. In [189] we consider the color histograms as feature vectors and the *histogram intersection*, $histin(H_I, H_J) = \sum_t \frac{\min(H_I(t),H_J(t))}{\max(H_I(t),H_J(t))}$, as the metric used in the retrieval process. In [190] the *Chi-squared measure* is used as an image similarity metric in the CBIR process. It is expressed as $d(V(I_i),V(I_j)) = \sum_n \frac{(H_{I_i}(k) - H_{I_j}(k))^2}{H_{I_i}(k) + H_{I_j}(k)}$, where H_{I_i} and H_{I_j} are the histograms of I_i and I_j, respectively. The image retrieval results obtained by the two similarity metrics are compared in [191]. These color-based retrieval techniques perform the image searching by using an effective relevance-feedback scheme that will be described next [191]. They achieve quite good results, but we have obtained considerably better content-based image retrieval by using some other feature extraction solutions.

One of these featuring solutions is based on a two-dimensional Gabor filtering process. We consider an even-symmetric 2D Gabor filter, $G_{\theta,f}(x,y) = \exp\left(-\frac{1}{2}\left[\frac{x_\theta^2}{\sigma_x^2} + \frac{y_\theta^2}{\sigma_y^2}\right]\right) \cdot \cos(2\pi f x_\theta)$ with $x_\theta = x\sin\theta + y\cos\theta$ and $y_\theta = x\cos\theta - y\sin\theta$, *f* giving the frequency of the sinusoidal plane wave at an angle θ with $x-$axis, and σ_x, σ_y the two standard deviations (see [163]).

Each image I_i is filtered by applying $G_{\theta,f}$ at various orientations, frequencies and standard deviations. We have obtained empirically a set of proper values for filter parameters, which are: the orientations $\theta_1 = \pi/3$, $\theta_2 = 2\pi/3$ and $\theta_3 = \pi$; the frequencies $f_1 = 4$, $f_2 = 8$ and $f_3 = 16$; the standard deviations along $x-$ axes $\sigma_x^1 = 2$, $\sigma_x^2 = 2.5$ and $\sigma_x^3 = 3$; the standard deviation values along the $y-$ axes $\sigma_y^1 = 4$, $\sigma_y^2 = 4.5$ and $\sigma_y^3 = 5$. So, each image is processed with the filter bank $\{G_{\theta_i,f_i,\sigma_x^i,\sigma_y^i}\}_{i\in[1,3]}$. This image feature extraction process is modeled as: $V(I_i)[x,y,j] = V_{\theta_j,f_j,\sigma_x^j,\sigma_y^j}(I_i)[x,y]$, where $V_{\theta_j,f_j,\sigma_x^j,\sigma_y^j}(I_i) = FFT^{-1}[FFT(I_i) \cdot FFT(G_{\theta_j,f_j,\sigma_x^j,\sigma_y^j})]$ [169].

The resulted 3D feature vectors represent robust image content descriptors that can be used successfully in an image recognition process, as we mentioned in 3.4.1. They are obtained in a similar way as the Gabor filter-based feature vectors used for temporal video segmentation [139], but by applying a lower number of filters with a different set of parameters. In [139] we use a SAD difference metric for these image feature vectors, but other conventional metrics, such as the Euclidian distance, could be applied as well.

The relevance-feedback based CBIR model proposed in my **selected paper 8** [163] is quite similar to that represented in the next figure. Besides the just described feature extraction component, it consists of a query device, search engine and image database.

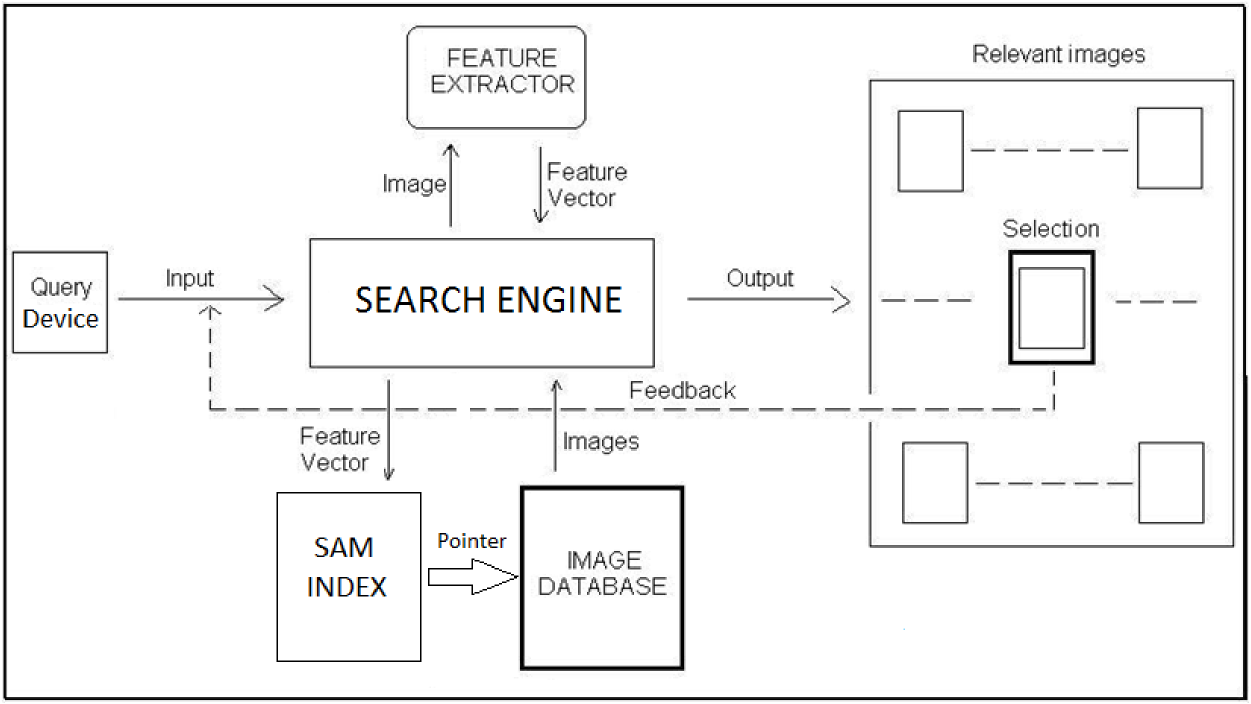

Fig. 3.20. Relevance-feedback based CBIR system

The proposed CBIR system performs the following retrieval task: finding the desired images from a large collection (database) by using an input example image, *I* [163]. Options for providing query images to the system include:

- A preexisting image may be supplied by the user or chosen from a random set.
- The user draws a rough approximation of the image he is looking for.

Our content-based image retrieval technique operates in the following way. First, the input image is compared to images registered by the collection. The most relevant images, representing those having a similar visual content to the input image, are extracted and displayed. If the desired image can be found in the retrieved set, then the searching process ends. Otherwise, the relevance-feedback mechanism is used. The image that is closest to the goal, in terms of content similarity, is interactively selected from the displayed set and becomes the new input.

The retrieval process continues this way until a final decision is made by user. An optimal moment to stop this search procedure is when the current query image becomes more similar to the desired image than all images retrieved in that step. Then, either that input image can be considered the desired one, or no image from the collection is acceptable and the retrieval process is abandoned [163].

The searching for the most relevant images, performed at each step, represents a quite difficult task to be solved. The search engine has to extract the most similar *K* registered images to the input *I*. A high-computational solution consists of computing the distances $d_i = d(V(I_i), d(V(I))$, where $i \leq n$, and sorting the distance value set $D = \{d_i\}_{i=\overline{1,n}}$ in ascending order [163]. To avoid this costly approach, that searching task must be treated as a *K*-Nearest Neighbor Search problem. The K-NN search is a generalization of the Nearest Neighbor search, a problem that can be solved by using Spatial Access Methods.

For this reason, a SAM-based image indexing structure should be added to the retrieval scheme, as in Fig. 3.20. The index can be modeled as a search tree data structure, whose nodes contain feature vectors. A successfully NN search can be performed using a *space-partitioning tree* structure, such as VP-tree or K-D tree. The nearest point to $V(I)$ from the feature vector space is thus determined, then the next closest one is identified, and so on, until the *K*-NNS problem is solved. Obviously, the determined closest *K* feature vector points correspond to the most relevant *K* images.

The proposed content-based image retrieval technique has been successfully tested on several image databases, containing thousands of [384 x 256] digital images with different contents. We have performed hundreds experiments, each of them being related to a different input query image, and achieved satisfactory retrieval results (see [163]). Our CBIR system provides high values for the performance parameters *Precision* and *Recall*, of approximately 85%. Also, it provides much better image retrieval results than the previously described color-based retrieval approaches, because the Gabor filter-based 3D feature vectors represent more powerful content descriptors than the histogram-based feature vectors.

In our experiments we usually set $K = 5$, the number of relevant images retrieved at each step. One of the image retrieval tests is described in the next figures. Let us assume we are interested in an image depicting a *herd of horses*. We select the input image *I*, representing a user-made drawing of a horse and displayed in Fig. 3.21.

The set of relevant images obtained for this query image is displayed in Fig. 3.22. They are ranked in order of their similarity to *I*, a lower label number indicating a greater content similarity. As one can see in the figure, almost all the retrieved images are depicting horses, the only exception being the last one. We are searching for images containing *more* horses, so the optimal image to be selected as an input for the new retrieval step is the fourth one, marked by a red rectangle in the figure.

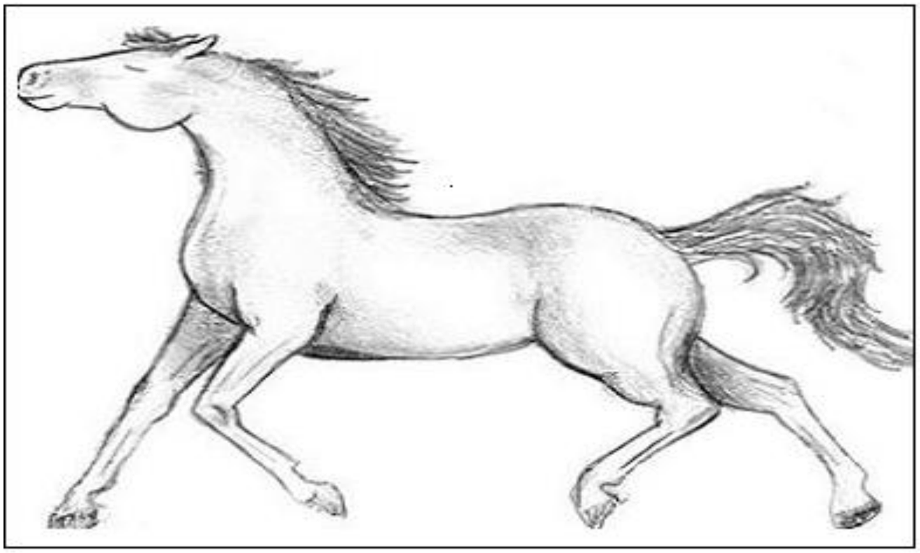

Fig. 3.21. User-made drawing used as query image

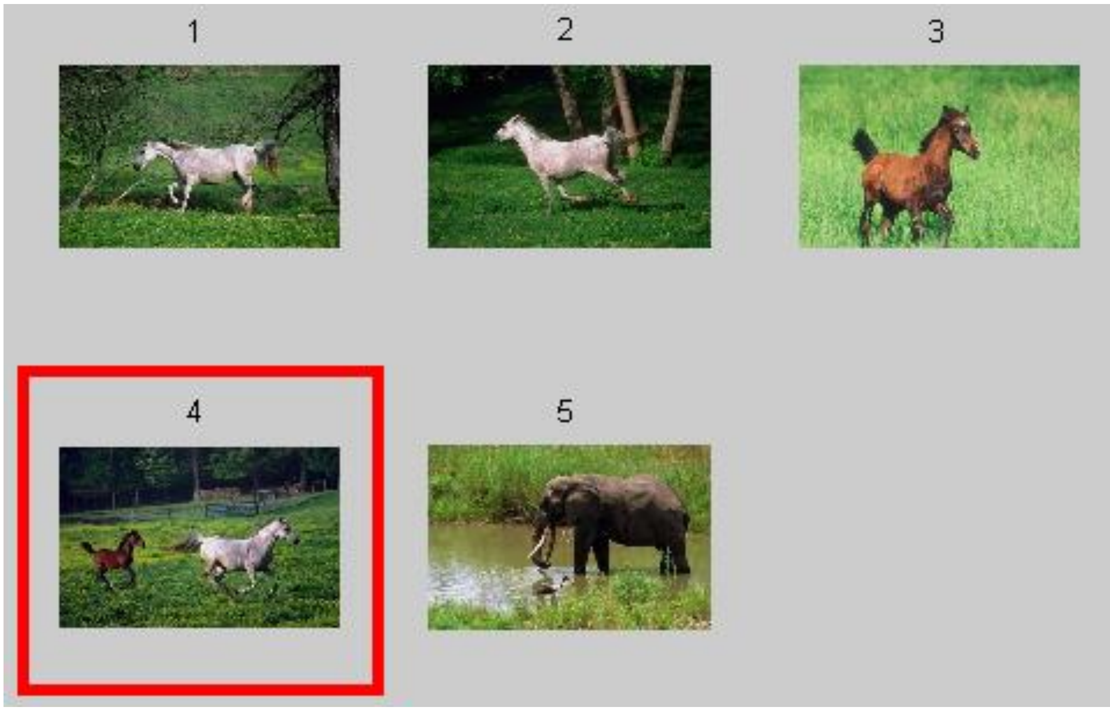

Fig. 3.22. Images retrieved in the first step

The images retrieved by using this new query image are displayed in the next figure. The best of them is the fourth image, representing a horse farm. It is selected as the goal image, being surrounded by a blue rectangle in Fig. 3.23, and the retrieval process ends.

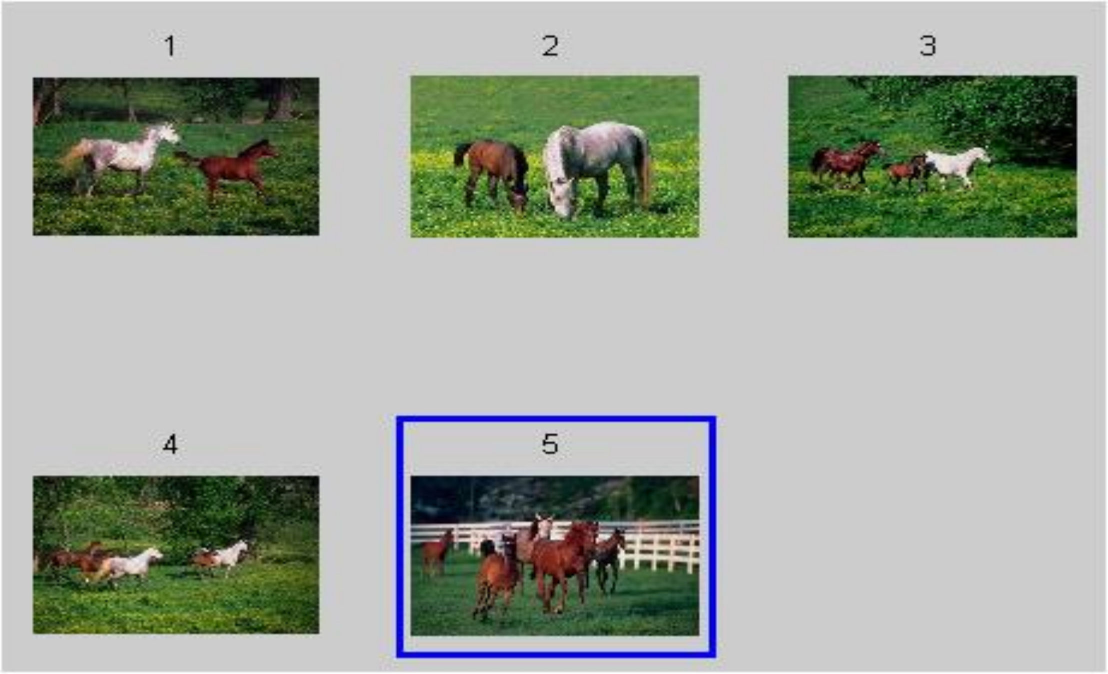

Fig. 3.23. Images retrieved in the second step

Another content-based indexing and retrieval system based on a relevance-feedback mechanism is provided by us in [186]. The LAB color-based feature extraction described in this paper can also be used successfully for image recognition [54,167]. We have mentioned it in 3.4.1, where another LAB-based image feature extraction approach, producing 2D feature vectors, is described in detail.

So, in [186] we consider another approach that divides each *ab* plane in 12 particular regions and constructs a histogram with only 12 bins for each plane, as in Fig. 3.24. This produces only 96 bins for the LAB histograms, considering all the 8 *ab* planes. To compute the histogram based on the 8 *ab* planes and the 12 regions for each plane, we simply browse all the pixels of an LAB converted image and for each pixel one unit is added to the corresponding bin. First we find the *L* value and select the corresponding *ab* plane, then the corresponding color region in that plane is identified by testing the *a* and *b* values of each pixel. The feature vector with 96 components is then modeled by putting the 12 values for each plane in the order indicated in Fig. 3.24, and then by concatenating the values for each plane in the order of their specific *L* value, from low values (16) to high values (240) [186]. For an image *I*, the color-based feature vector is computed as:

$$V(I) = \left(n_1(I), n_2(I), ..., n_{12}(I), n_{13}(I), ..., n_{24}(I), n_{25}(I), ..., n_{96}(I)\right) \tag{3.40}$$

where $n_i(I)$, i = 1,…,96, are the number of pixels counted as corresponding to each color region in the above described configuration [186]. The distances between these feature vectors can be measured by using the well-known Euclidian metric or other conventional metrics.

A SAM-based image indexing process is then performed in [186]. The respective color-based image indexing technique has been described briefly in 3.5.1. A K-D tree based indexing structure is build upon the feature vector set $\{V(I_1), ..., V(I_n)\}$, with each $V(I_i)$ computed by (3.40).

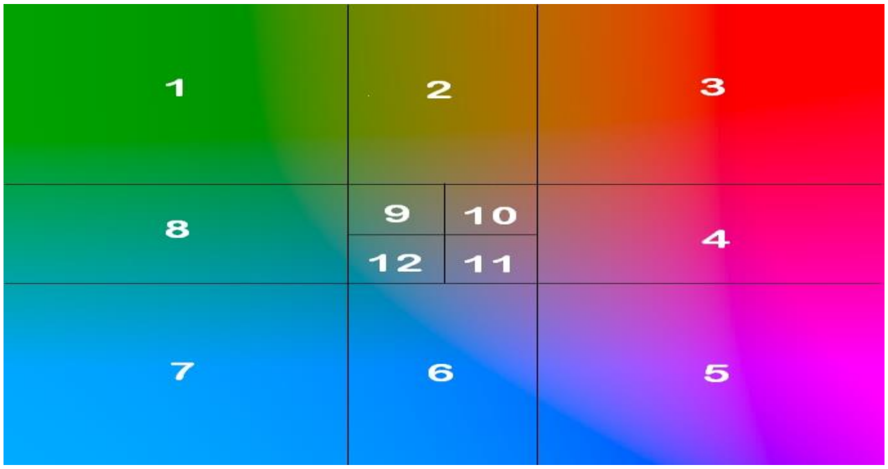

Fig. 3.24. The choice for splitting an *ab* plane into 12 regions

Next, the image retrieval process is performed by using a CBIR framework similar to the previous one [186]. The relevance-feedback based image search scheme represented in Fig. 3.20 is applied in this case with the SAM-based indexing component structured as a K-D tree [186]. The same interrogation procedure is performed, an example image being used as a query. At each step, *K* relevant images are retrieved, one of these output images becoming the new input.

The most similar *K* registered images are extracted from the database by performing a K-Nearest Neighbor Search using the K-D tree-based database index. The NN finding algorithm starts with K-D tree root, then moves down the tree recursively, going left or right depending on whether the point is less than or greater than current node in the split dimension. Once the algorithm reaches a leaf node, it saves that node point as the *optimal*. The algorithm performs the next steps at each node: if the current node is closer than optimal, then it becomes the current optimal. The algorithm checks whether there could be any points on the other side of the splitting plane that are closer to the search point than the *optimal*. This task is performed by intersecting the splitting hyperplane with a hypersphere around the search point that has a radius equal to the current nearest distance. If the hypersphere crosses the plane, there could be nearer points on the other side of the plane, so the algorithm has to move down the other branch of the tree from the current node looking for closer points, executing the same recursive process. If the hypersphere does not intersect the splitting plane, then the procedure continues walking up the tree, the entire branch on the other side of the node being eliminated. When the procedure for the root node finishes, then the search is completed. The nearest point to $V(I)$ from the feature vector space is thus determined, then the next closest one is identified, and so on, until *K*-NNS task is solved.

This color-based image indexing and retrieval method has been tested on various image datasets. A lot of experiments have been performed by us on several databases, containing thousands [256×384] color images. We have considered several hundreds of input images as examples, each experiment being related to an initial query image.

Our CBIR system achieves high retrieval rates and high values for the performance parameters. We have obtained values around 0.8 - 0.85 for the *Precision* and *Recall* parameters. The parameter value $K = 5$ has been usually used in our experiments. Method comparison has also been performed. The LAB color-based indexing and retrieval approach proposed here outperforms other relevance-feedback based algorithms that use weaker featuring methods. For example, this CBIR model provides much better retrieval results than some systems using various histogram-based feature vectors [186].

In Fig. 3.25, there are described parts of an experiment performed by us that prove the effectiveness of the developed system. One can see the initial input, representing an orange rose and the *K* retrieved images representing roses. If the reddest rose is selected as new query, *K* new red roses are retrieved. If the rose containing mostly yellow is selected, one gets *K* yellow roses.

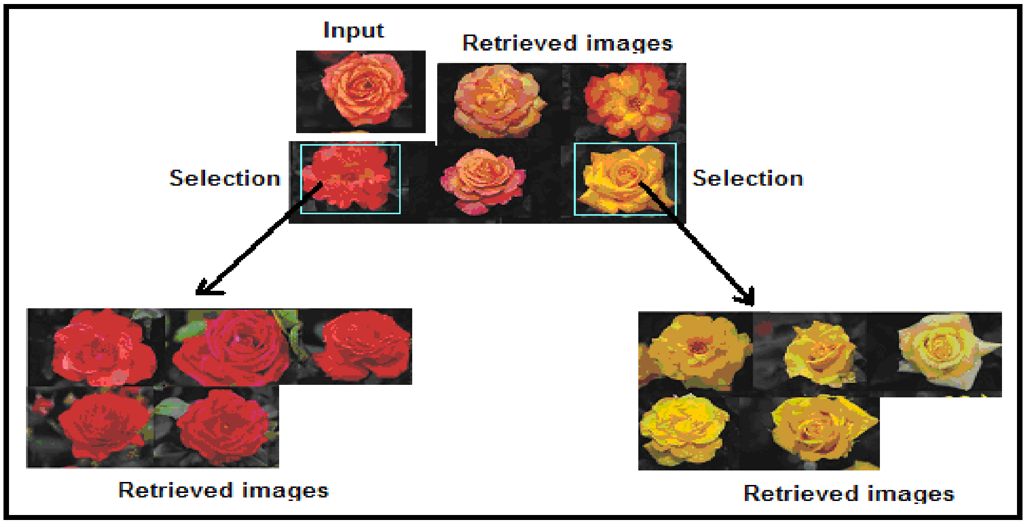

Fig. 3.25. Color-based retrieval example

3.6. Image and video object detection and tracking solutions

In this chapter we present our recent research results in some important and strongly-related computer vision domains, such as object detection and tracking. Object detection represents a high-interest computer vision research area that can be divided into two sub-domains: *image object* detection and *video object* detection. Also, video object detection is closely related to another important computer vision field that is video object tracking.

We describe each of these three areas in the next subsections, insisting upon our contributions in these domains. The image object detection approaches proposed by us are described in 3.6.1. Our results in the video object detection field are presented in 3.6.2, while the proposed object tracking algorithms are discussed in 3.6.3.

3.6.1. Automatic image object detection techniques

Image object detection represents the computer vision process that deals with locating semantic objects in static images. A sub-domain of object detection is *object-class detection*, which aim to locate semantic objects from a certain class, such as humans, vehicles, buildings or animals.

Many image object detection approaches have been proposed in the last decades. They can be divided into several main categories: point-based, segmentation-based and supervised learning based techniques [192]. The methods from the first category are based on point detectors, like Moravec detector [193], Harris detector [194] and SIFT [84]. The segmentation-based detection techniques use the image segments, obtained by edge-based methods, color/texture-based algorithms [195], Active Contours [124,138] and other segmentation approaches, for semantic image object detection. Object detection is also performed by using some well-known supervised learning techniques. We have to mention here the Adaptive Boosting algorithms, such as AdaBoost [196], LPBoost or GentleBoost, and Support Vector Machines (SVM) [197], which provide very good image object detection results.

We have approached the object detection domain, developing both segmentation-based and supervised learning-based techniques. Also, some object-class detection approaches have been proposed [53,168,198].

The variational PDE image segmentation technique described in 3.1.2, and representing the level-set based object contour tracking model proposed in [134], constitutes an effective image object detection approach. We also developed an object detection method based on color/texture-based segmentation [126]. So, the moment-based image segmentation proposed in [126] and described in 3.1.1 can be applied successfully to image object detection. The various combinations of the segmented regions produce the image objects [33]. These objects could be categorized as semantic or non-semantic by performing some recognition processes on them. So, a supervised recognition technique, using a training set that contains semantic objects, can be applied to the input image objects, which are thus associated to some proper semantic object classes [33].

We have investigated the object-class detection domain, developing some robust detection techniques for several classes of image objects, such as faces, human skin and human cells. Each of them will be detailed in this subsection.

Face detection represents a computer technology that determines the locations and sizes of human faces in arbitrary digital images, constituting a very important image object detection sub-domain. The main application area of face detection is biometric authentication, face finding being considered the first step of *facial recognition* [53]. *Video surveillance* represents another important application area of face detection [51].

The face detection approaches can be divided into the following categories: *knowledge-based* techniques, *feature-based* methods, *appearance-based* approaches and *template matching* methods. The knowledge-based methods encode human knowledge of what constitutes a typical face, usually the relationships between facial features. A face is modeled using a set of coded rules that are used to guide the face search process. [199]. The feature based approaches aim to detect invariant face features, which are structural features that exist even when the pose, viewpoint or lighting conditions vary. Let us mention here the *Random Graph Matching* based approaches [200] and the *Feature Grouping* techniques [201]. Appearance-based techniques train various classifiers, like Multilayer Perceptrons [202], HMM [203], Bayes classifiers [204], SVM, Sparse Network of Winnows (SNoW) [205], PCA and Adaptive Boosting [206].

The template matching based techniques use stored face templates [207]. Usually, these approaches use correlation operations to locate faces in images. The templates are hand-coded, not learned and must be created for different poses. A template matching-based face detection technique for color images is also proposed in my **selected paper 9** [168]. It also performs ***human skin detection*** and uses the identified skin regions for face detection.

Human skin color represents a useful face detection tool [207]. Our skin-based face finding approach identifies the skin regions of the image, then determines those of them representing faces. Besides face detection, there exist other important application areas of skin detection, such as image content filtering and finding illegal internet content [208], content-aware video compression or image color balancing. Numerous skin color localization techniques have been developed in the last two decades. An influential skin detection model is the algorithm proposed by Fleck and Forsyth in 1996 that uses a skin filter [208].

While it is one of the most used color spaces for image data processing and storing, RGB is not a favorable choice for skin color analysis, because of the high correlation of its 3 channels and the mixing of luminance and chrominance data [168,198]. For this reason, most skin segmentation algorithms work with other color spaces. In [198] we propose a skin detection technique using the HSV and $YC_r C_b$ color spaces. The RGB image is converted into the Hue Saturation Value format, by computing the three components using the known conversion equations. We obtain the components, H, S and V, as 3 matrices with coefficients in the [0,1] interval. We are interested mainly in the hue value, H.

The $YC_r C_b$ color model represents a family of color spaces. In fact, it is not an absolute color space, but a way of encoding the RGB information. In this format Y represents the luminance, while C_r and C_b are the blue-difference and red-difference chroma components. These 3 components of the color space are computed as linear combinations of R, G and B values. The computation formulas of the chroma components have the general form $\alpha \cdot R + \beta \cdot G + \gamma \cdot B + 128$, where $\alpha, \beta, \gamma \in [-0.5, 0.5]$. We choose empirically some proper values for α, β, γ and get:

$$\begin{cases} C_r = 0.15 \cdot R - 0.3 \cdot G + 0.45 \cdot B + 128 \\ C_b = 0.45 \cdot R - 0.35 \cdot G - 0.07 \cdot B + 128 \end{cases} \tag{3.41}$$

Our method defines explicitly the skin-colored segments, by applying a set of restrictions on these 2 components and on the hue, to determine the skin regions. Thus, we have determined a skin related interval for each component. In our approach, each pixel of the image I belongs to a human skin segment if the corresponding values in C_r, C_b and H are situated in those intervals.

One constructs a binary image Sk, having the same size as I, whose white regions correspond to the skin segments. The proposed skin segmentation process is modeled as follows:

$$Sk(i,j)=\begin{cases}1, if\ C_r(i,j)\in[150,165]\ \propto\ C_b(i,j)\in[145,190]\ \propto H(i,j)\in[0.02,0.1]\\ 0, \hfill otherwise\end{cases} \tag{3.42}$$

where $i \in [1, M]$ and $j \in [1, N]$, I representing a $[M \times N]$ image. The connected components of Sk represent the detected skin regions [168]. The proposed detection method provides very good results, although some skin identification errors could appear, because of some skin-colored regions not representing real skin. In Fig. 3.26 (a), there is displayed an RGB image depicting human persons. The result of the HSV conversion is displayed in Fig. 3.26 (b), while the obtained skin detection result is depicted in Fig. 3.27. See [168] and [198] for more results.

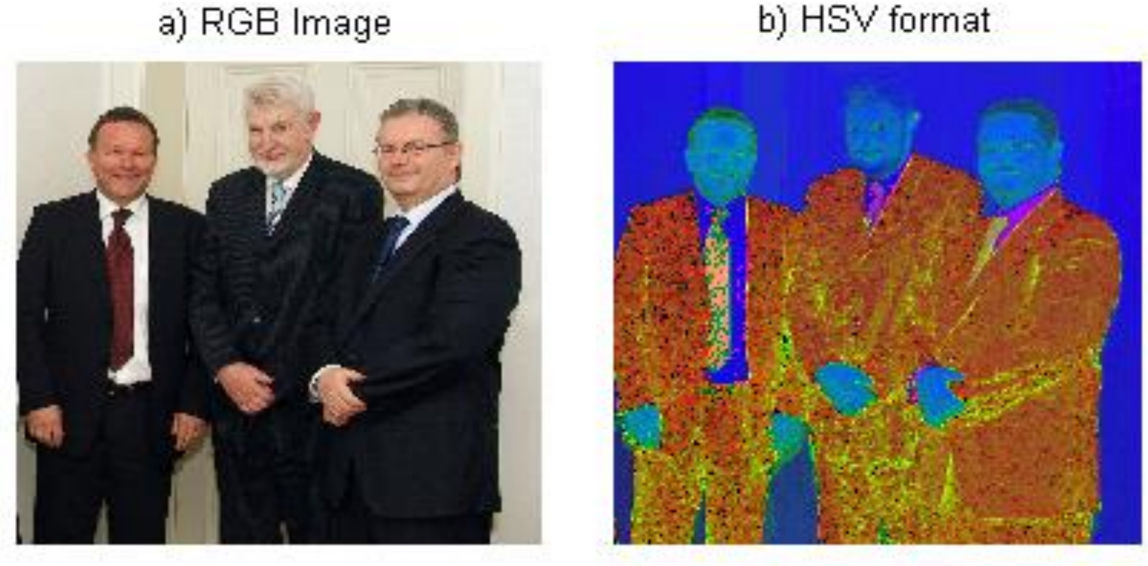

Fig. 3.26. Digital color image conversion: RGB to HSV

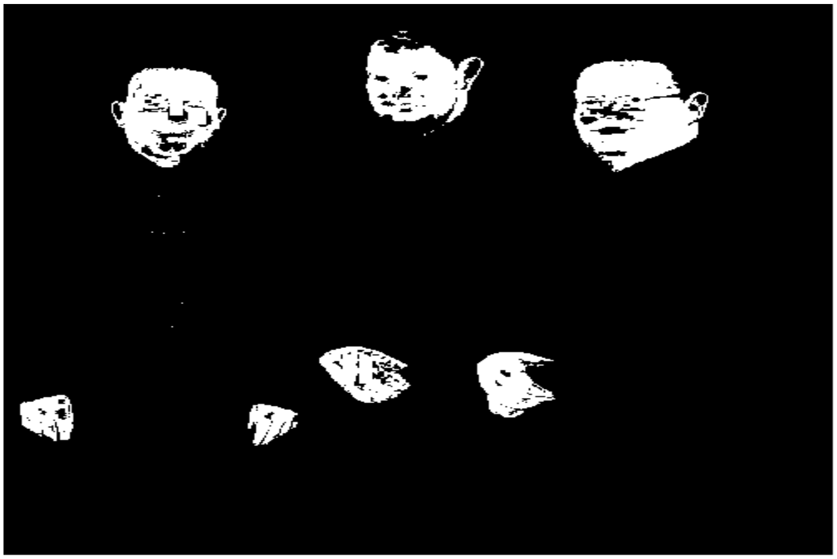

Fig. 3.27. Skin detection result

The detected skin regions are then used in the face identification process. For each skin segment one must decide if it represents a face, or not. First, several necessary pre-processing operations are performed. A task that has to be solved is the separation of faces from adjacent or occluding skin regions. Our detection task cannot identify properly the faces that are occluded by other skin-like *objects*. Usually, this situation appears in group photos, like that displayed in Fig. 3.28 (a). So, we provide a separation technique involving some morphological operations performed on the binary image *Sk*. Thus, we apply two successive *erosions* on it. First, the binary image is eroded with a structuring element *L*, representing a vertical line of 5 pixels in length:

$$Sk' = Sk \ominus L = \bigcap_{l \in L} Sk_{-l} \tag{3.43}$$

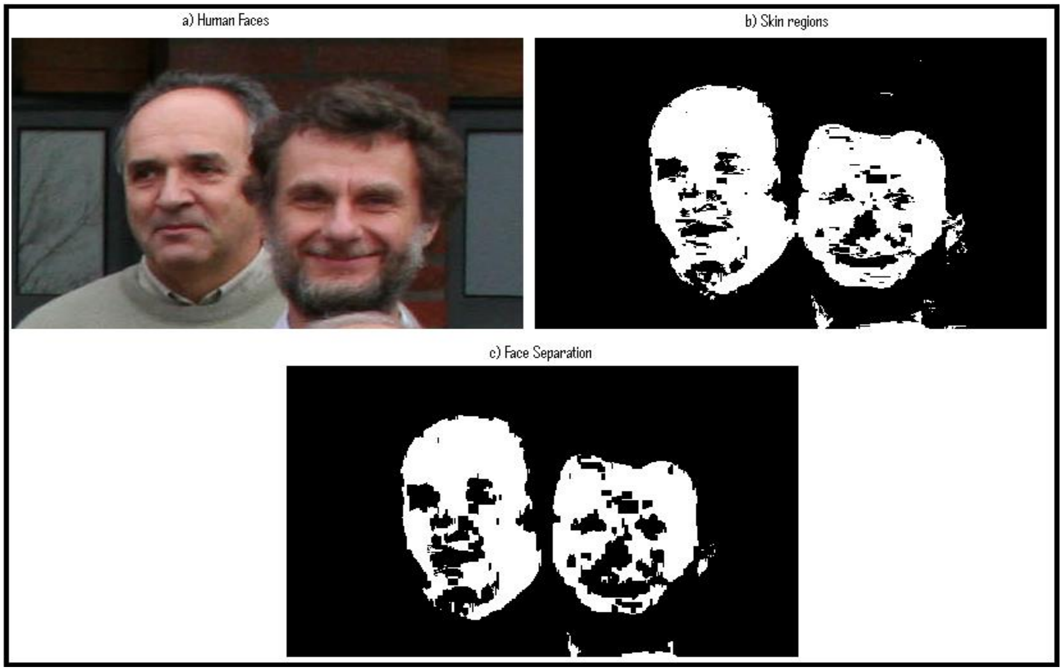

Fig. 3.28. Face separation example

Then, another erosion operation is applied on Sk', by using a structuring element *Sq*, representing a small square area (for example, containing a single pixel):

$$Sk'' = Sk' \ominus Sq = \bigcap_{p \in Sq} Sk'_{-p} \tag{3.44}$$

Such a skin separation example is depicted in Fig. 3.28. In (b) the skin segments corresponding to faces from (a) form a single connected component. The result of the morphology-based process, given by the relations (3.43) and (3.44), is displayed on (c). The 2 greatest skin regions are clearly separated in the final binary image, Sk''. Unfortunately, there could be some situations when the face separation is not possible in the binary image. The binary image Sk''contains a set of skin segments, representing connected sequences of white pixels. Let this set of regions be $\{S_1, \dots, S_n\}$. Now, we have to decide which of these regions could qualify as *face candidates* for the template matching process. So, we have established a set of candidate criteria for these S_i segments [168].

First condition requires that each skin region exceeds a given area. We have decided to not take into consideration the small area white spots, because they cannot represent serious face candidates. If a white region area is below a given threshold value, it is labeled as non-face. The second condition is related to the *solidity* of the skin regions. A connected component S_i has to be rejected as non-face, having a non-facial shape, if the *solidity* (the ratio between region's area and its *bounding box* area) of its *filled* version is below an established threshold. We consider the filled versions of skin regions because their solidities are affected by holes representing eyes, eyebrows, mouth, nose or ears. So, we perform a black hole filling process on Sk'', first. Also, a face is characterized by some limits of its *width to height ratio*. None of the two dimensions of a face, width and height, can be *much* larger than the other, so another condition requires the width to height ratio of the face candidates to be restricted to a certain interval [168]. For each $S_i, i \in [1, n]$, the described face candidate identification process is formally expressed as follows:

$$Area(S_i) \geq T_1 \propto \frac{Area(Fill(S_i))}{Area(Box(S_i))} \geq T_2 \propto \frac{Width(Box(S_i))}{Height(Box(S_i))} \in [T_3, T_4] => S_i = candidate \quad (3.45)$$

where *Area* ( ) computes the number of white pixels of the region received as argument, *Fill* ( ) performs the filling process, *Box* ( ) returns the bounding rectangle, *Width* ( ) and *Height* ( ) return the dimensions of a rectangle. We have considered the following threshold values: area threshold $T_1 = 130$, solidity threshold $T_2 = 0.65$, width to height thresholds $T_3 = 0.6, T_4 = 1.8$.

A face candidate identification example is described in Fig. 3.29. In (a) one can see a boy flexing his muscles. The corresponding binary image resulted after skin detection, erosion operations, small region removing and hole filling process is depicted in (b). The bounding boxes of the 3 skin regions are depicted in c), d) and e). The one representing the right arm is rejected because of its low solidity, the skin segment of the left arm is rejected because of a wrong width to height ratio, and the one representing the skin of head and neck is accepted as a right face.

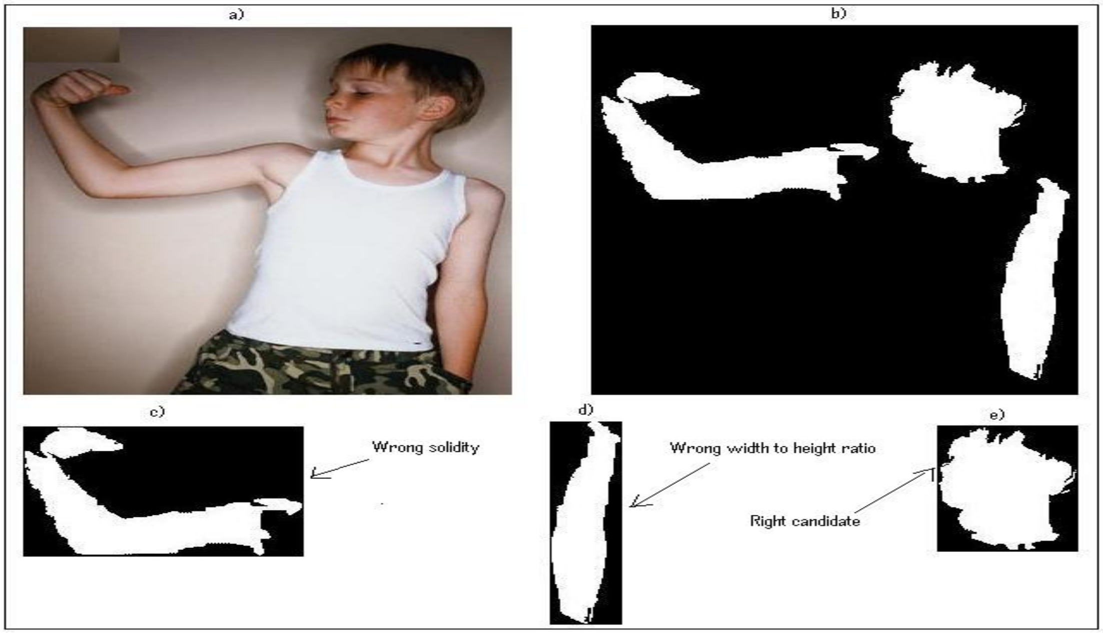

Fig. 3.29. Face candidate identification example

In its next stage, the facial detection approach determines which of the face candidates represent human faces. First, one converts the denoised RGB image I into a 2D grayscale form, let it be I'. If there is a set of K face candidates, where $K \leq n$, we determine the set of the sub-images of I' corresponding to their bounding rectangles. The face detection process can be affected by the head hairline of the person and by the skin zone of the neck and upper chest. So, a narrow upper zone and a narrow bottom zone from each image are removed. In our tests, the height of each removed zone represents one 11th of the bounding box height [168].

Let the set of the truncated *skin images* be $\{I_1, \ldots, I_K\}$, where $I_i \subset I', \forall i \leq K$. Then, we perform a correlation-based template matching process on this set. Our template-based approach works like a supervised classification algorithm. We create a face template set, containing faces of various sizes, orientations, poses, genders, ages and races. Let the template set be $\{F_1, \ldots, F_N\}$, with N large enough, where each F_i represents a grayscale image. Next, an edge detection operation is performed on both the skin images and templates. A Canny filter can be used for edge extraction, but some edge detection solutions derived from our nonlinear diffusion based smoothing methods could also be used [15,16]. For each skin image I_i and each face F_j, a binary image representing its edges results. Let I_i^e and F_j^e be the *edge images* related to I_i and F_j.

Then, for each candidate (skin image), one computes the 2D *cross-correlation coefficients* [209] between its edge image and the edge images of the templates, and then, the average value of this sequence of coefficients [168]. Let us note $v(I_i)$, the resulted correlation-based value corresponding to I_i. We propose a threshold-based approach, so, the computed 2D average correlation coefficient corresponding to a facial skin image must exceed a properly chosen threshold value. The face detection process is modeled mathematically as follows:

$$\forall i \in [1, K],\ I_i = face \Leftrightarrow v(I_i) \geq T \tag{3.46}$$

where

$$v(I_i) = \frac{1}{N}\sum_{j=1}^{N} \frac{\sum_x \sum_y \left(I_i^e(x,y) - \mu(I_i^e)\right)\left(F_j^e(x,y) - \mu(F_j^e)\right)}{\left(\sum_x \sum_y \left(I_i^e(x,y) - \mu(I_i^e)\right)^2\right)\left(\sum_x \sum_y \left(F_j^e(x,y) - \mu(F_j^e)\right)^2\right)} \tag{3.47}$$

where $\mu(\,)$ computes the average of a matrix and threshold value T is determined empirically. If T is not exceeded for any I_i, then the color image I contains no human faces [168].

In [168] we propose also a no-threshold automatic face finding method that replaces the threshold with an automatic clustering procedure applied to $v(I_i)$ values. Thus, the set $\{v(I_1), \ldots, v(I_K)\}$ is divided into 2 classes by using a region-growing algorithm (see [168]). This method works properly when the correlation-based values related to faces are *much* higher than those related to non-facial images. For this reason, the threshold based method is a better solution. The sub-images of the RGB image I corresponding to the detected faces I_i are provided as output by the face detection system.

We have performed a lot of face detection experiments using this system. Our tests involved tens of RGB images containing faces and produced satisfactory results. A high face detection rate, which is approximately 90%, has been achieved by our system. A threshold value T = 0.185 has been used in our tests. We have also constructed a template face set containing 25 grayscale images of various scales, orientations, poses and imaging conditions, representing both male and female faces, and people of various ages and races, some of them having structural elements. The template set can be extended, by adding new faces, but while a large set may improve the detection results, it also produces a high computation complexity. Our approach produces a low number of *false negatives* (missed faces) and very few *false positive* (non-facial image regions detected as faces), which means high values for the performance parameters *Precision* and *Recall*. The performances of the proposed face detection system are comparable with those of the face detection techniques mentioned in introduction. It achieves better detection results for frontal faces, than for faces characterized by various orientations.

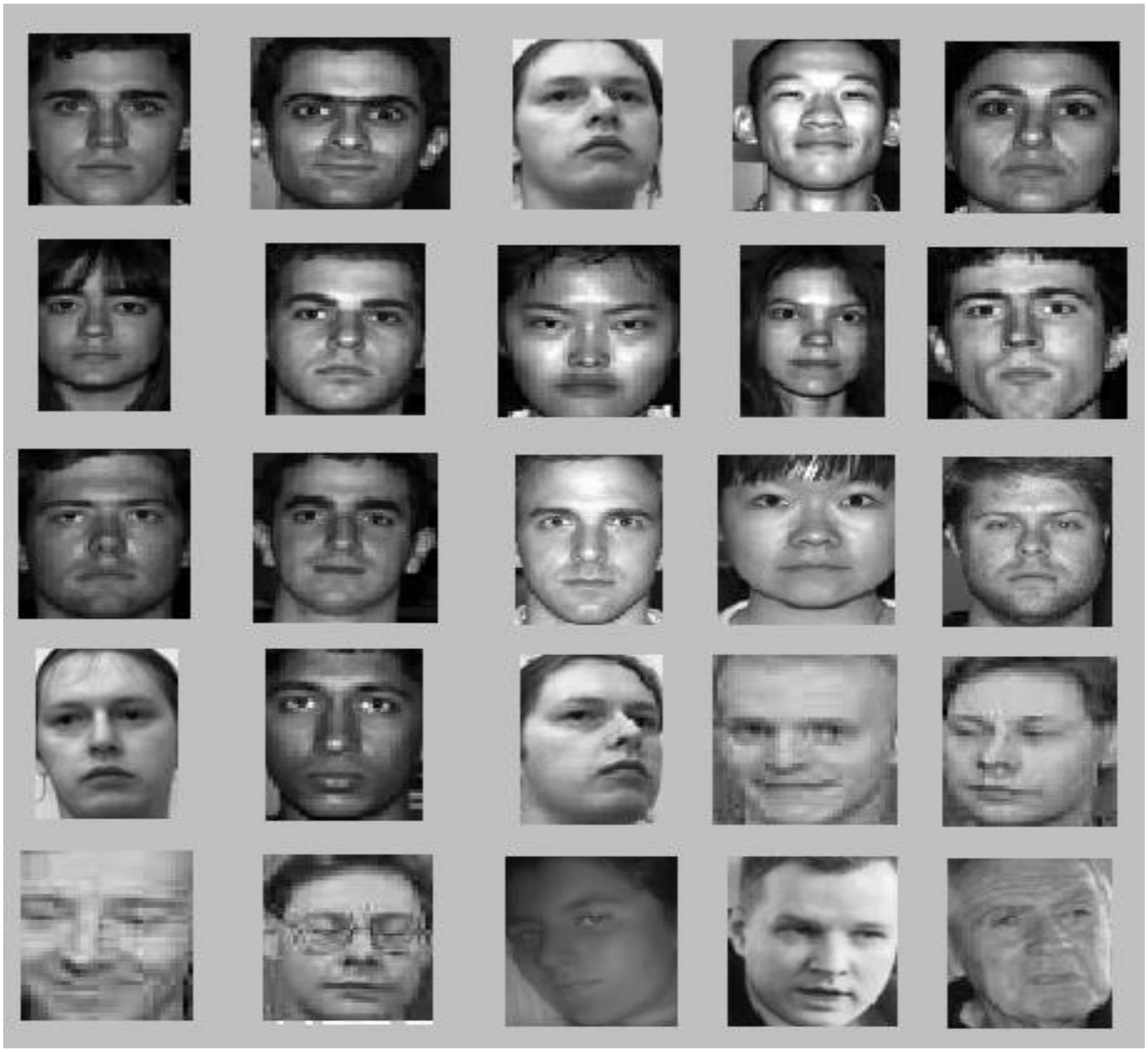

Fig. 3.30. Facial template set

A face detection example is displayed in the next figure. The skin detection process depicted in Fig. 3.26 and Fig. 3.27 is continued with the face detection process represented in Fig. 3.31. In (a) there are displayed the main skin regions obtained by performing the morphological operations, hole filling and small region removing on the binary image from Fig. 3.27. One of them is rejected because of its low solidity, the remaining regions being accepted as face candidates, as one can see in (b). The template matching process is performed by using the template face set represented in Fig. 3.30. One can see the resulted average correlation coefficient values in (c), those greater than the threshold (0.185) corresponding to the detected faces, which are surrounded by black rectangles in that grayscale image. The final face detection result for the RGB image is displayed in (d), the human faces being marked by red bounding boxes [168].

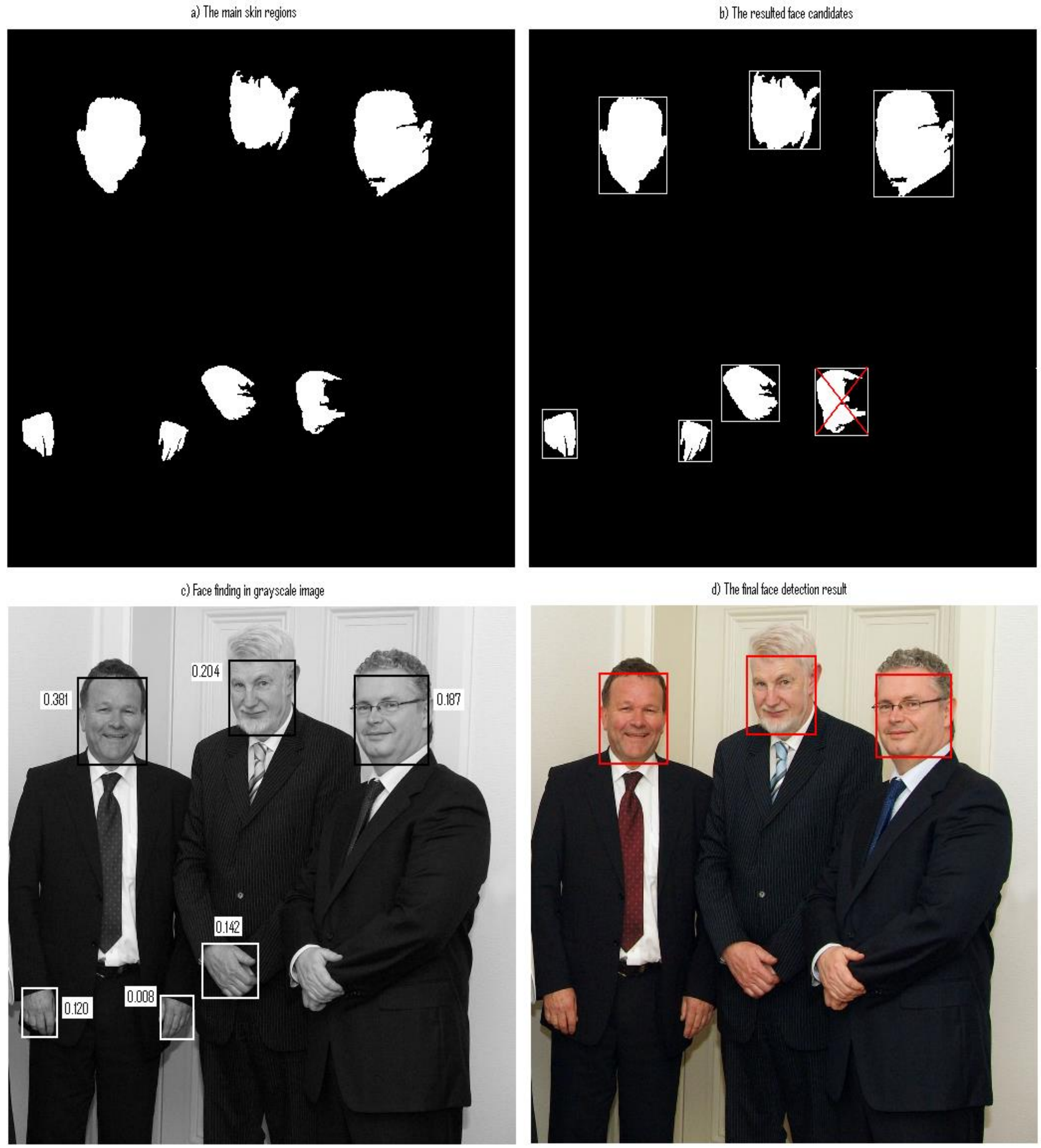
a) The main skin regions
b) The resulted face candidates
c) Face finding in grayscale image
d) The final face detection result
0.381
0.204
0.187
0.142
0.120
0.008

Fig. 3.31. Face detection example

Another object-class detection technique developed by us represents a ***human cell detection*** algorithm [210]. Although our detection approach aims to locate cells in static images and video frames, it could be used successfully to detect other image object classes, such as humans or vehicles. The proposed object detection model uses a sliding-window based object searching approach, a HOG-based feature extraction and a SVM-based feature vector classification technique.

Histograms of Oriented Gradients (*HOG*) represent a robust feature descriptor used in the computer vision domain for object detection. They prove to be very useful for human detection [211], but we use them successfully for cell featuring in this work [210]. We compute HOG characteristics for the sub-images corresponding to the cells' bounding boxes. A HOG-based feature vector is modeled for such an image [210]. First, one determines the image gradient values, representing directional changes in the intensity or color. The gradient vector is formed by combining the partial derivatives of the image *I* in the *x* and *y* directions:

$$\nabla I = \left(\frac{\partial I}{\partial x}, \frac{\partial I}{\partial y} \right), \tag{3.48}$$

The gradients in the two directions can be computed by applying the 1*D* centered, point discrete derivative mask in the horizontal and vertical directions:

$$\begin{cases} \dfrac{\partial I}{\partial x} = I * \begin{bmatrix} -1 & 0 & 1 \end{bmatrix} \\ \dfrac{\partial I}{\partial y} = I * \begin{bmatrix} -1 & 0 & 1 \end{bmatrix}^T \end{cases} \tag{3.49}$$

The gradient orientations of the image are computed as $\theta = \arctan\left(\frac{\partial I}{\partial x}, \frac{\partial I}{\partial y} \right)$. The image *I* is then divided into cells, and for each cell, one computes a local 1*D* histogram of gradient directions (orientations) over the pixels from that cell [210,211]. We consider 9 bins for the local histogram. The histogram channels are evenly spread over 0 to 180 degrees, so each histogram bin corresponds to a 20 degree orientation interval. The obtained cell histograms are then combined into a descriptor vector of the image [210].

First, these cells have to be locally contrast-normalized, due to the variability of illumination and shadowing in the image. That requires grouping the cells together into larger, spatially-connected blocks. Once the normalization is performed, all the histograms can be concatenated in a single feature vector, representing the HOG descriptor. We use [3x3] cell blocks of [6x6] pixel cells with 9 histogram channels. The feature vector of the image is computed as its HOG descriptor, having 81 coefficients. This could be expressed as $V(I) = HOG(I)$ [210]. The detection process uses a supervised classification of these feature vectors, which is performed through a SVM-based approach.

Support Vector Machines (*SVM*) represent supervised machine learning models, widely used in object detection tasks [197]. They can perform efficiently both linear and non-linear feature vector classification. Using a set of training examples, each marked as belonging to one of two classes, a SVM training algorithm predicts, for each given input, which of two possible classes must represent the correct output [197].

Any image object-class detection task can be formulated as a binary linear classifier problem. It can be solved by considering two classes, containing objects and non-objects respectively, then applying a SVM on them. We develop a non-linear SVM training model for human cell detection, because non-linear SVMs are consistently found to be better suited for the object detection task [197,210].

The training image set constructed by us contains the following two subsets: the set of *positives*, containing bounding rectangles of biological cells, and the set of *negatives*, containing non-cell images of various sizes. A training set example is described in the next figure. Its positive samples are displayed in Fig. 3.32 (a), while the negative samples are represented in Fig. 3.32 (b).

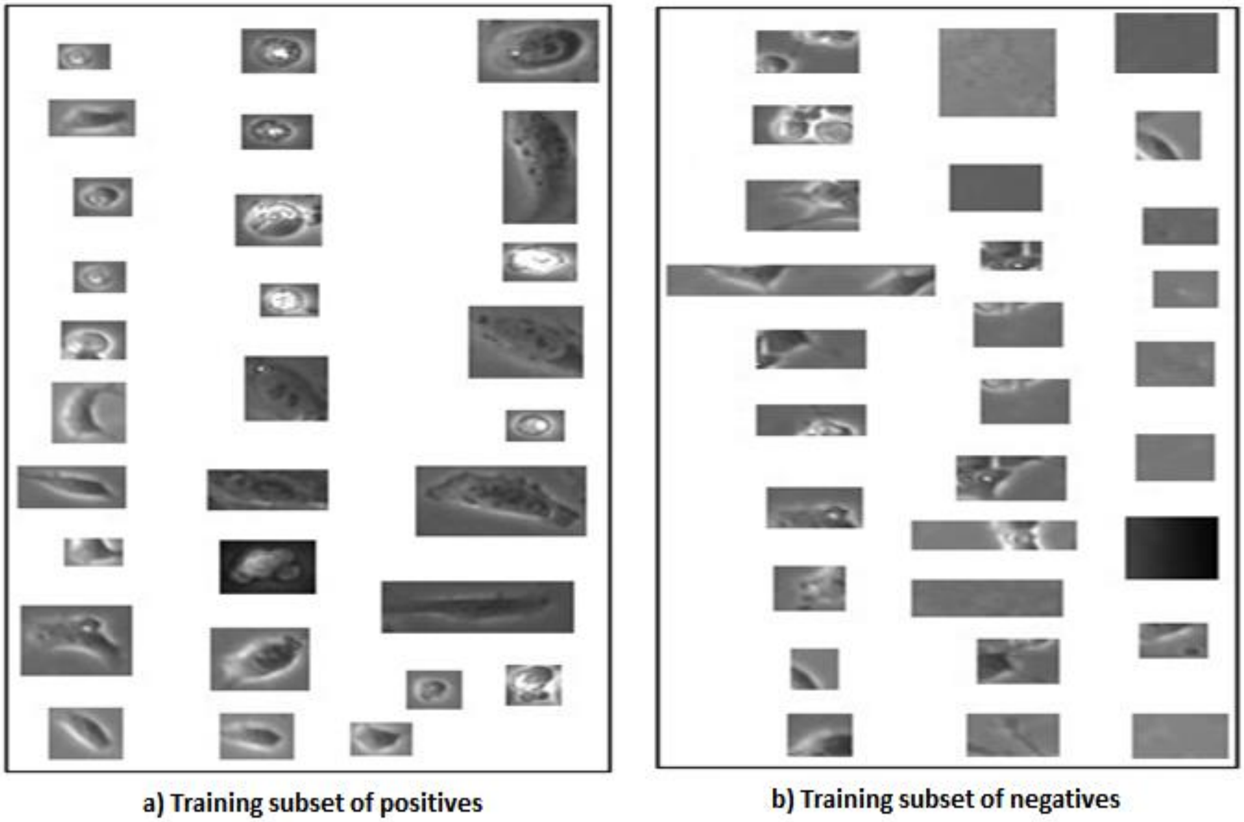
a) Training subset of positives
b) Training subset of negatives

Fig. 3.32. The training set of the system

The training set could be expressed in the following form:

$$S = \{(T_1, x_1),\ldots,(T_n, x_n)\},\ x_{\mathrm{i}} \in \{-1,1\} \tag{3.50}$$

where T_i represent the training samples, and their labels are:

$$x_{\mathrm{i}} = x(T_i) = \begin{cases} 1, \text{if } T_i - positive \\ -1, \text{if } T_i - negative \end{cases} \tag{3.51}$$

The described HOG-based feature extraction is performed on these training subsets, the system's feature training set being composed of the feature vectors $V(T_i), i = 1,..., n$. One must identify the maximum-margin hyperplane that divides the objects characterized by $x_{\mathrm{i}} = 1$ from those having $x_{\mathrm{i}} = -1$. We consider a quadratic programming technique to separate hyperplane identification [210]. Also, our non-linear classification algorithm uses a nonlinear kernel function instead of the *dot product* used in the linear case. So, a quadratic kernel is considered to map the training data *S* into the kernel space. If this SVM classifier is applied to an input object represented by its bounding image *I*, the SVM-based classification of its feature vector will produce the object labeling that can be expressed formally as: *x*(*I*) = *SVM* (*V*(*I*)).

One has to solve the following computer vision task: locate all objects representing human cells from a given image *Im*. We detect the bounding boxes of those cells by performing a sliding-window scanning over the grayscale version of the respective image [210]. We propose a cell search algorithm that scans *Im* using a variable sized sliding window. At each step, one computes the HOG-based feature vector of the sub-image corresponding to current window. The SVM classification algorithm is then applied to the feature vector, the analyzed sub-image being labeled as either positive or negative [210]. We introduce the following condition: if a positive is identified, the next search must be performed far enough from it. So, the positions of pixels of the detected cell are marked as *visited*, this approach reducing the searching complexity [210].

We consider that the widths and heights of the cells vary between some minimum and maximum values, $w_{\min}, w_{\max}, h_{\min}, h_{\max}$, so, the sliding-window size has to vary accordingly. Let us note *Subim*(*Im*, *x, y*, w_1, w_2 , h_1, h_2) the set of all subimages of *Im* having the upper-left pixel *Im*(*x*,*y*), the width in interval [w_1, w_2] and the height in [h_1, h_2]. This set of subimages can be determined recursively. We construct a searching algorithm expressed by next pseudocode [210]:

```
Detect_cells (Im)
 $S = \phi$; mark = 0 matrix with the same size $[M \times N]$ as Im;
  for i = 1 to M - $h_{min}$
   for j = 1 to N - $w_{min}$
    if mark (i, j) = 0
    for each $I \in Subim(Im, i, j, w_{\min}, w_{\max}, h_{\min}, h_{\max})$
     Compute V (I) = HOG(I);
     Apply SVM classifier to V(I): x(I) = SVM(V(I));
      if x(I) = 1 then
       $S = S \cup \{I\}$ ;
       for each pixel location $(a,b) \in I$
        mark(a,b) = 1; (mark location as visited)
        end
      end
    end
   end
  end
 end
 Return S.
```

The result of a cell searching process is displayed in Fig. 3.33. The stem cells from the grayscale image are identified and marked with red rectangles. In that figure, one can see also a blue rectangle marking a subimage representing a non-cell example.

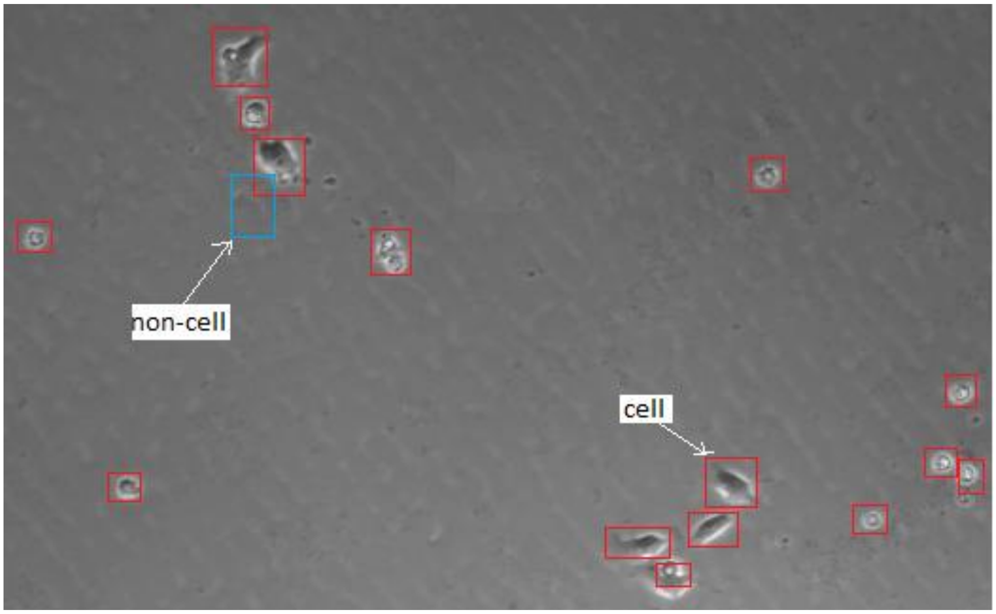

Fig. 3.33. Example of a cell detection result

We have performed many cell detection experiments using the proposed technique. The numerical tests performed on hundreds images, containing various types of cells, have produced satisfactory detection results that prove the effectiveness of our method. It has achieved a high detection rate, of approximately 90%, and also, high values are obtained for the performance parameters. We get values around 0.9 for both the *Precision* and *Recall* parameters. Therefore, almost all the detected objects returned by our approach are relevant, very few false positives being returned. Also, the high *Recall* value indicates that almost all true positives are returned.

We have developed and tested many appropriate SVM training sets, containing cells and non-cell objects. One of those training data sets is described in Fig. 3.31 being composed of 29 positives and 29 negatives. While the proposed detection technique provides satisfactory cell identification results, it does not execute fast enough. That is because of the high complexity and computational cost of the sliding-window based search algorithm. In our tests we apply this algorithm with the parameters $w_{\min} = 20, w_{\max} = 50, h_{\min} = 20, h_{\max} = 50$, M = 512 and N = 672. Lower values may reduce its complexity, but also its effectiveness. The values of parameters related to HOG computing, also may influence the computational complexity of the detection.

Method comparisons have also been performed. Thus, our object searching procedure is considerably faster than methods based on Exhaustive Search (ES), but slower than approaches that do not perform image scanning. Thus, we have also compared the obtained detection results with those produced by other object identification techniques that are based on image segmentation, using edge detection or threshold values and some morphological operations [212]. From our tests, we have found that the approach described here outperforms them, obtaining a higher *Recall* value, but also it is somewhat slower. While the segmentation-based methods often fail to return all the positives, producing a higher number of missed biological cells, they execute faster than the approach presented here [210].

3.6.2. Video object detection approaches

Video object detection represents an important and challenging computer vision domain, which is closely related to the video object tracking described in the next subsection. A video object of a movie constitutes a sequence of image objects that represent the instances (states) of the video object in a succession of frames of that movie. So, the video object detection process involves locating the instances of the video objects in the frames of a video sequence. Object detection and tracking has a wide variety of computer vision application domains. The most important of them are the video compression, video surveillance, human-computer interaction, video indexing and retrieval.

Numerous video object detection techniques have been developed in recent years, and they could be divided in two categories. Video object detection can be performed using the image object detection approaches described in 3.6.1. Thus, the image objects from each video frame can be detected by using techniques based on active contour models [138], segmented regions [126], Hough transforms [213], adaptive boosting or SVM. These techniques belong to the first video object detection category.

The second category contains the video motion-based object detection approaches. Thus, the video objects presenting the most interest are the *moving objects* of a video sequence and not the static objects, whose detection reduces to image object detection. The moving object detection techniques are based on background subtraction [214], frame-differencing [215] or motion estimation [33].

We also proposed some moving object detection algorithms in our past papers [33,217]. A background subtraction based video object detection technique is provided in [217]. We will not insist here on this approach from 2005, describing in detail a more recent detection method instead [218-220].

An automatic multiple moving object detection technique is proposed in the **last selected paper** [219]. My developed model detects efficiently the video objects from a static-camera movie by using a novel temporal differencing algorithm and several mathematical morphology-based operations. I have also developed some *video object-class detection* techniques, such as pedestrian detection [218,219] and sonar object detection approaches [220], based on this moving object detection algorithm.

So, in [219] the video frames of the analyzed color movie are converted into the grayscale form, the set $\{Im_1,...,Im_n\}$ being obtained. One considers a temporal differencing-based video motion estimation approach. The difference of two consecutive frames indicates the motion between them, the resulted non-black image zones representing the moving regions. Such a moving region may not represent an entire image object, because both the foreground and the background of the frame can be composed of more homogeneous regions, characterized by various intensities. The frame difference is noted as $Fd(i, j) = Im_i - Im_j, \forall i, j \in [1, n], i \neq j$. Each moving object present in Im_i and Im_j, is represented in $Fd(i, j)$ by some non-black regions. Its high-intensity pixels (having greater values than background) are displayed in $Fd(i, j)$ at the locations occupied in Im_i, while its low-intensity pixels are displayed in $Fd(i, j)$ at their positions in Im_j. Frame difference is then converted into the binary format by setting to 1 all pixels exceeding a properly selected threshold value, *T*:

$$Fd_b(i,j)=\begin{cases}1, & \text{for } Fd(i,j)\geq T\\ 0, & \text{for } Fd(i,j)<T\end{cases}, \forall i,j\in[1,n], i\neq j \tag{3.52}$$

A mathematical morphology based process is next applied to image $Fd_b(i,j)$. The dilation morphological operation is very useful in this case, producing the dilated binary image as:

$$Fd_m(i,j)=Fd_b(i,j)\oplus Sq=\bigcup_{s\in Sq} Fd_b(i,j)_s \tag{3.53}$$

where $\oplus$ represents the dilation morphological operator and *Sq* is a $[k\times k]$ structuring element [221]. The connected components of the dilated image $Fd_m(i,j)$ are then determined, those representing errors provided by redundant noise or undesired camera motion being removed. We consider the following connected components to be discarded: small white spots – connected components whose area is under a low threshold; components whose bbox has a dimension under a threshold value; low solidity components. The resulted image is noted $Fd_m^p(i,j)$ [218].

The proposed detection algorithm identifies the moving objects from Im_1 to Im_{n-1}, first. At *i*th step, it determines the video objects of Im_i, using the next 2 frames, Im_{i+1} and Im_{i+2}. The corresponding morphologically processed frame difference images $Fd_m^p(i,i+1)$ and $Fd_m^p(i,i+2)$ are computed, and their intersection is then determined as:

$$(Fd_m^p(i,i+1)\bigcap Fd_m^p(i,i+2))[x,y]=\begin{cases}Fd_m^p(i,i+1)[x,y], \text{for } Fd_m^p(i,i+1)[x,y]=Fd_m^p(i,i+2)[x,y]\\ 0, \qquad\qquad\qquad\quad \text{for } Fd_m^p(i,i+1)[x,y]\neq Fd_m^p(i,i+2)[x,y]\end{cases} \tag{3.54}$$

The connected components of the intersection $Fd_m^p(i,i+1)\bigcap Fd_m^p(i,i+2)$ correspond to all high-intensity regions of the moving objects from Im_i. The low-intensity components of its moving objects are determined by using a similar procedure. They correspond to the connected components of $Fd_m^p(i+1,i)\bigcap Fd_m^p(i+2,i)$. The moving objects of Im_i are detected by computing the next sum of image intersections:

$$Ob(i)=(Fd_m^p(i,i+1)\bigcap Fd_m^p(i,i+2))+(Fd_m^p(i+1,i)\bigcap Fd_m^p(i+2,i)) \tag{3.55}$$

The connected components of the binary image *Ob*(*i*) correspond to the moving objects of the frame Im_i. The last step of the detection task consists of the localization of these objects in Im_n. We apply a backward identification process that is modeled as follows:

$$Ob(n)=(Fd_m^p(n,n-1)\bigcap Fd_m^p(n,n-2))+(Fd_m^p(n-1,n)\bigcap Fd_m^p(n-2,n)) \tag{3.56}$$

Each binary image *Ob* (*i*) contains the same number of connected components. For each component, one identifies its bounding box. The sub-images of frame Im_i corresponding to these bounding rectangles represent its moving objects (foreground) (see [219]). Such a foreground detection example is represented in Fig. 3.34.

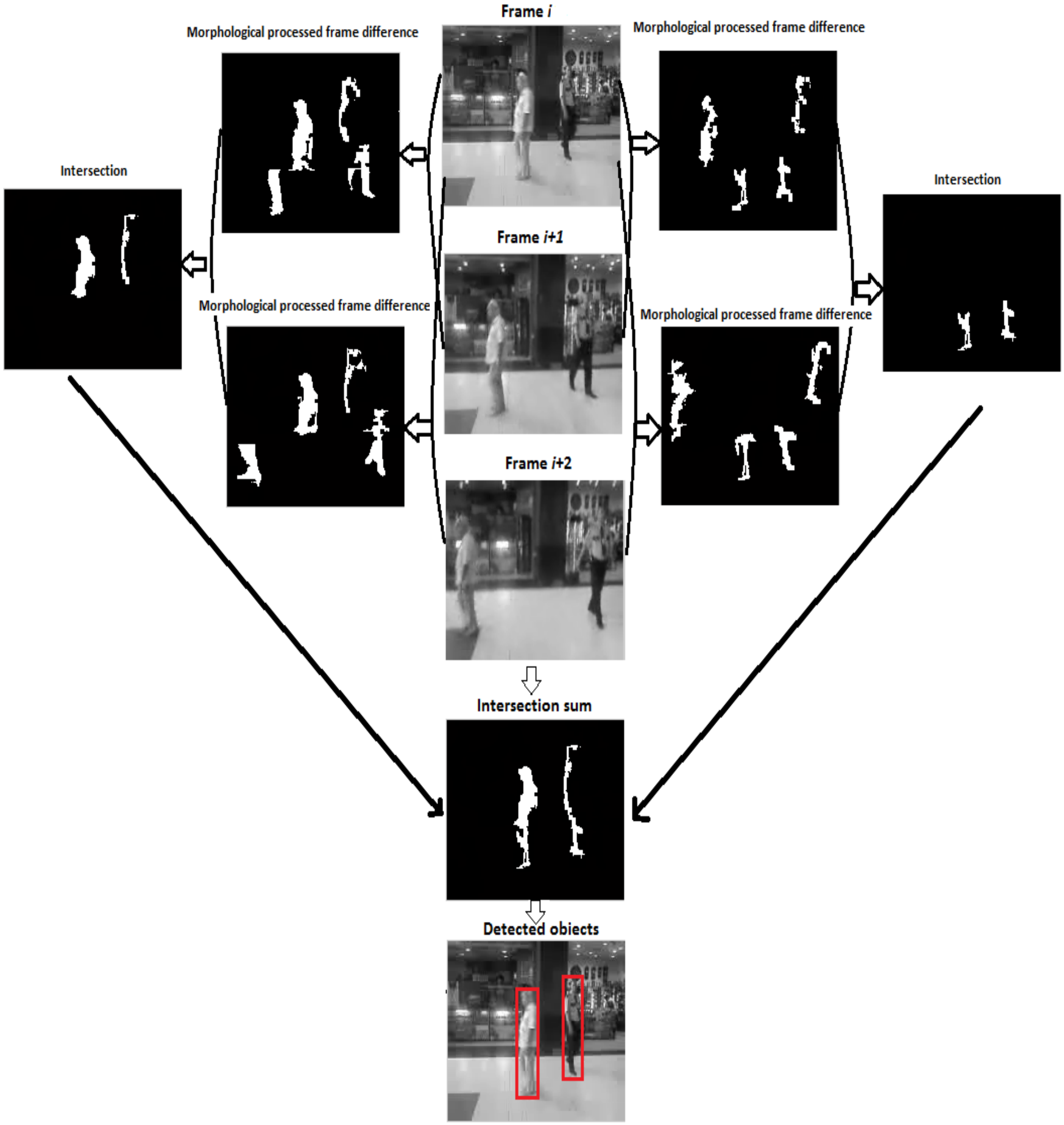
Frame *i*
Morphological processed frame difference
Morphological processed frame difference
Intersection
Intersection
Frame *i*+1
Morphological processed frame difference
Morphological processed frame difference
Frame *i*+2
Intersection sum
Detected objects

Fig. 3.34. Moving object detection example

So, as a result of the described automatic detection process, one obtains a set of identified image objects on each frame, representing instances of moving objects. The next operations that can be performed on these objects are the video object tracking and, the video object class detection and tracking. The video tracking approaches are described in the following subsection, 3.6.1.

The most important video object class detection domain, ***human detection*** in video sequences, has been successfully approached in some of our articles [218,219]. More exactly, we consider the *moving person detection and tracking* task. Detecting walking persons, or *pedestrians*, in video images represents a very challenging task, complicated by various factors, like camera position, variable people appearance, wide range of poses adopted by human beings, variations in brightness, illumination, contrast levels or backgrounds, and person occlusions [222].

Over the last decade the problem of detecting and tracking humans has received a very considerable interest. Significant research has been devoted to detecting, locating and tracking people in videos, since many applications involve persons' locations and movements [222]. Also, human detection and tracking has a wide variety of computer vision application areas, the most important of them being video surveillance and security systems, biometrics, law enforcement, human-computer interaction (HCI), video indexing and retrieval, medical imaging, robotics and augmented reality.

Our proposed approach decides which of the detected moving objects represent pedestrians. We set several conditions related to human body that have to be satisfied by each object representing a pedestrian. The first condition is that the height of the bounding rectangle of the image object representing a human must be at least two times greater than its width. The second condition is that the object solidity has to be over 50%. If $\{ob_1,...,ob_{n_i}\}$ are the objects corresponding to $Ob(i)$, and $\{I(ob_1),...,I(ob_{n_i})\}$ the set of their sub-images, the above conditions can be formalized as follows:

$$\begin{cases} h(ob_j) \geq 2 \cdot w(ob_j) \\ h(ob_j) \cdot w(ob_j) \leq 2 \cdot Area(ob_j) \end{cases}, \ \forall j \in [1, n_i] \tag{3.57}$$

where $h(ob_j)$ and $w(ob_j)$ are the height and the width of image $I(ob_j)$. Let $Obj(i) \subseteq Ob(i)$ the binary image containing the connected components satisfying (3.57) only.

Our third condition is related to the presence of skin regions. So, any video object must contain skin regions to be considered a moving person [218]. A skin detection process is performed on each video frame. Some skin identification techniques based on explicitly defined skin segments, therefore working similarly to the skin detection model described in 3.6.1 [198], are introduced for this purpose [218].

For each frame I_i we get a binary image S_{I_i}, that is similar to *Sk* given by (3.42), whose connected components correspond to its skin regions. If these skin segments are identified in the moving object locations, then those objects must represent humans. So, for each *i*, our approach computes the intersection $\boldsymbol{Obj(i) \cap S_{I_i}}$ and determines its connected components. The moving objects containing these components are considered pedestrians [218,219].

A pedestrian detection example is described in Fig. 3.35. In (a) one displays the moving object detection result for a given frame. The skin segmentation result for that color frame is provided in (b). Obviously, the skin regions in (b) are located within the red bounding rectangles from (a). Also, the two moving objects detected in (a) satisfy the conditions related to width to height ratio and solidity. So, the detected moving video objects represent walking persons. The moving object detection example from Fig. 3.34 leads also to a pedestrian detection result, the two detected image objects representing human beings.

While our human detection approach works successfully for identification of non-occluded side view pedestrians [223], it performs somewhat weaker on occluded people [224], front-view or rear-view moving people. Also, it is not appropriate for non-pedestrian human detection and cannot locate persons that are not moving in upright position.

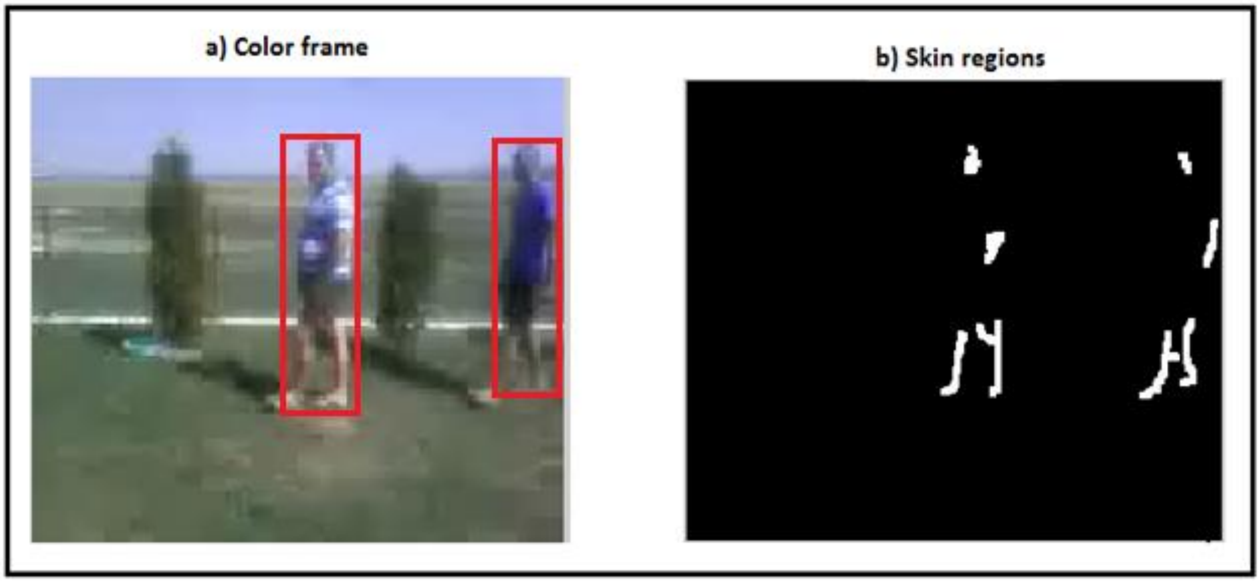

Fig. 3.35. Pedestrian detection example

An automatic temporal differencing based object detection technique is also used for multiple sonar object detection in ultrasound movies [220]. The video tracking of these moving objects is also described in 3.6.3.

The automatic character of my video object detection technique and its capability to perform multiple moving object detection represent important advantages of the described technique. The sensitivity to undesired camera motions represents the major limitation of this detection approach that is well-suited for fixed camera videos. Because of the used temporal differencing procedure, our moving object detection method is quite sensitive to camera movements. Even the presence of a small camera motion may affect the entire object detection process [219].

3.6.3. Video tracking methods

The video object tracking represents the video analysis process of monitoring the spatial and temporal changes of the video object during the movie sequence, including its presence, position, size and shape. A video tracking approach has to solve the temporal correspondence problem that is the task of matching the target object in successive video frames [144,192].

State of the art video object tracking techniques include: mean-shift based tracking [225], kernel tracking [192,226], statistical methods, like those based on Kalman filtering [192,227], particle filtering [192,228] and HMM [229], object matching based tracking [230], optical flow based tracking [231], eigentracking [232] and contour evolution based tracking. Video tracking is often a difficult process, due to some factors such as abrupt object motion, objects' variable form, object occlusions, camera motion and scene illumination changes [144].

We have approached two video tracking types. The first one is based on image object matching and uses the objects already detected in video frames. The tracking processes of the second type begin with detecting the initial instance of the video object, then identifying that image object repeatedly in subsequent frame sequence. Obviously, we consider tracking of moving objects only, since the tracking of static video objects represents a trivial task.

The object-matching based video tracking approaches proposed by us track successfully multiple objects across movie sequences. These methods determine the correspondences between image objects from different frames. As a result of the multiple moving object detection process, all image objects representing video object instances are located within movie. The tracking process identifies for each object of the current frame, the unique object corresponding to it from the next frame.

Let us suppose there are K detected objects on each frame, the detected object set corresponding to I_i is $\{Ob_1^i,...,Ob_K^i\}, i \in [1,n]$, where each object Ob_j^i is considered in the sub-image form. For each $i \in [1,n-1], j \in [1,K]$ one must determine the value $k \in [1,K]$ such that Ob_k^{i+1} corresponds to Ob_j^i, as the next instance of the same moving object. Our tracking approaches are based on object content similarity, therefore we have $Ob_k^{i+1} \approx Ob_j^i$. The next instance of a video object must be the image object from next frame, which is most similar to the current instance, therefore corresponding to the minimum value of a similarity metric.

So, the object matching based video tracking process becomes equivalent to a supervised object recognition process. All the image objects Ob_j^i can be characterized by using the content-based feature extraction approaches described in section 3.4. The object matching process is modeled as follows:

$$ind = \arg\min_{k \in [1,K]} d(V(Ob_j^i), V(Ob_k^{i+1})), \forall i \in [1,n-1], j \in [1,K] \tag{3.57}$$

where *ind* is the optimal value of *k* (index of the next instance), *d* represents a metric that works properly for the feature vectors $V(Ob_j^i)$. Any tracked video object is obtained an ordered sequence of similar image objects.

The video object feature extraction could depend on the class of moving objects to be tracked. Thus, in [220] we consider a multiple moving object detection and tracking process for sonar movies. A 2D Gabor filter-based texture analysis is performed on the image objects that represent video instances detected through a temporal differencing based algorithm [218-220].

Each object Ob_j^i is filtered with a two-dimensional Gabor filter at various orientations (angles), radial frequencies and standard deviations. Thus, the 6-channel 2D Gabor filtering bank $\{G_{\theta_k, f_i, 2, 1}\}_{f_i \in \{0.75, 1.5\}, k \in [1,3]}$, where $\theta_k = \frac{k\pi}{n}$ and $G_{\theta_k, f_i, \sigma_x, \sigma_y}(x,y)$ is computed as in (3.31), is applied to the object. A 3D feature vector $V(Ob_j^i)$ representing a proper content descriptor is obtained for each object (see [220] for more).

The considered Gabor filter-based sonar object featuring produces satisfactory video tracking results. Thus, the tracking algorithm is characterized by a high object recognition rate, exceeding 80%. The performance parameters are *Precision* = 0.80, *Recall* = 0.85. This means there is a small number of false positives and false negatives too. A sonar object tracking example is provided in the next figure. There are two vehicles that are tracked in the ultrasound movie. The two resulted moving objects are marked in red and blue, respectively.

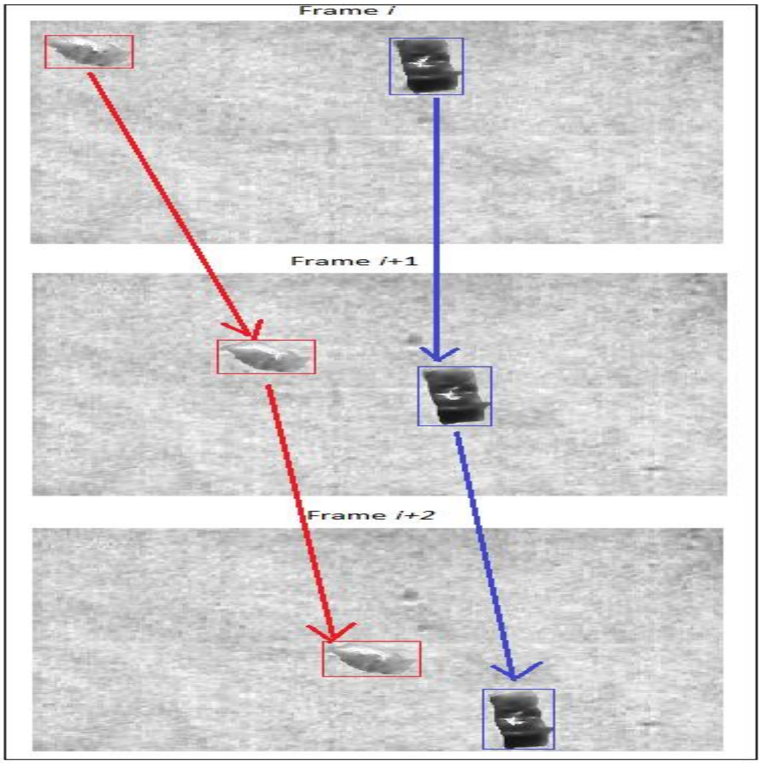

Fig. 3.36. Object matching process in a sonar video

Another video object tracking task uses a HOG-based feature extraction [219]. While the characteristics based on Histogram of Oriented Gradients are widely used for human detection in static images, our technique uses the HOG-based features for human tracking in video images [219].

The moving objects are detected by using the temporal differencing procedure described in 3.6.2. Then, those moving objects representing pedestrians are identified using the human body related conditions described there [219]. An object matching process is then performed for tracking the detected moving persons, H_j^i . The feature vector of a *human* object is computed as the Histogram of Oriented Gradients of its corresponding sub-image, as described in 3.6.1 [210, 211]. So, $V(H_j^i) = HOG(H_j^i), i \in [1,n], j \in [1,K]$. The Euclidean metric is used to measure the distances between these HOG-based feature vectors having 81 coefficients.

The human matching process is performed similarly to the object matching given by (3.57). So, the proper match for H_j^i is determined as the human $H_{ind_i(j)}^{i+1}$ of the next frame, where $ind_i(j) = \arg\min_{t\in[1,K]} d\left(V(H_j^i), V(H_t^{i+1})\right), \forall i \le n, j \le K$. Therefore, any tracked pedestrian is obtained as a sequence $\left\{H_j^1, H_{ind_1(j)}^2, \ldots, H_{ind_i(j)}^{i+1}, \ldots, H_{ind_{n-1}(j)}^n\right\}\Big|_{j\in[1,K]}$ [219].

The detected moving objects from Fig. 3.34 are then identified easily as humans. The corresponding human tracking process is represented in Fig. 3.37. The matching is represented by arrows linking objects from different frames and marked by the distances between their HOG-based feature vectors. The colored arrows, corresponding to lower distance values, indicate correct matches, while the white ones, marked by higher values, represent wrong matches. The instances of each person are marked with the same color and linked by arrows of that color.

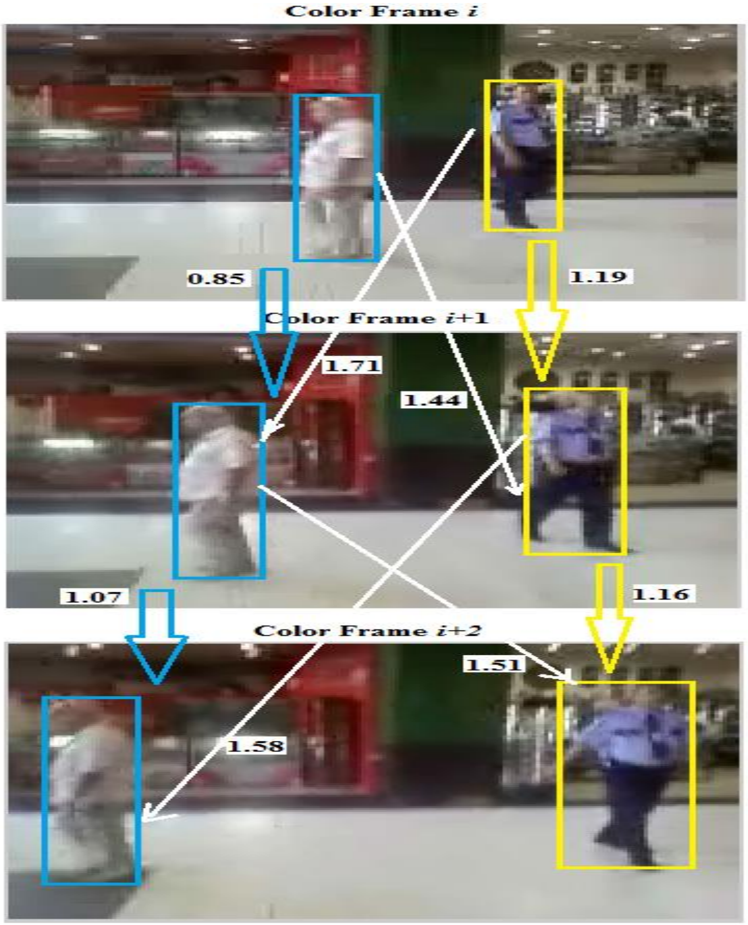

Fig. 3.37. Pedestrian tracking example

The proposed video tracking solution is characterized by a high person matching rate, of approximately 90 %. The resulted performance parameters are *Precision* = 0.90, *Recall* = 0.85 and F_1 = 0.874, which means that very few false positives and false negatives are produced by this pedestrian tracking technique.

Another effective moving person tracking method is proposed in [218]. The pedestrians are detected similarly in the video frames, for each I_i a moving person sequence $\{P_1^i, \ldots, P_K^i\}$ being obtained. We consider a normalized correlation-based human matching approach for video tracking, therefore no feature extraction process in performed [218]. Our approach computes the 2D cross-correlation coefficients between the current object (person) of the current video frame and all the human objects of the successive frame. Its optimal match is determined as the moving person corresponding to the *maximum correlation coefficient* value. So, we have:

$$match_i(j) = \arg\max_{k\in[1,K]} \frac{\sum_x \sum_y \left(P_j^i(x,y) - \mu(P_j^i)\right) \cdot \left(P_k^{i+1}(x,y) - \mu(P_k^{i+1})\right)}{\left(\sum_x \sum_y \left(P_j^i(x,y) - \mu(P_j^i)\right)^2\right) \cdot \left(\sum_x \sum_y \left(P_k^{i+1}(x,y) - \mu(P_k^{i+1})\right)^2\right)}, \forall i \in [1,n], j \in [1,K] \quad (3.58)$$

Therefore, a tracked pedestrian could be modeled through the following sequence: $\{P_j^1, P_{match_1(j)}^2, \ldots, P_{match_i(j)}^{i+1}, \ldots, P_{match_{n-1}(j)}^n\}\Big|_{j\in[1,K]}$ [218].

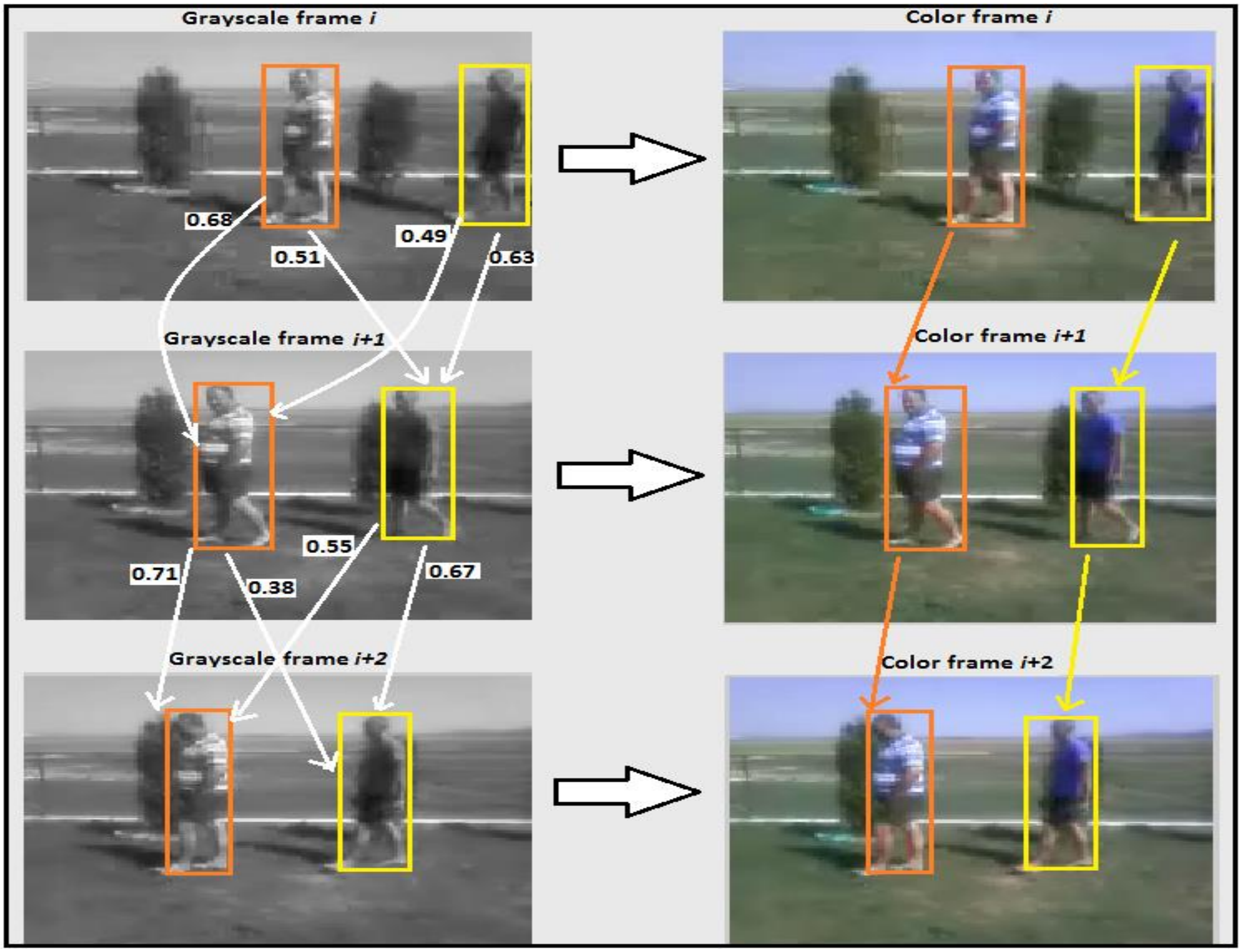

Fig. 3.38. Correlation-based human tracking example

Another considered human matching solution uses the edges of the P_j^i image objects [218], instead of these objects in the correlation procedure given by (3.58). Unfortunately, computing the edge information raises substantially the complexity of the video tracking process. A correlation-based human tracking example is displayed in Fig. 3.38. On the left column one can see the identified humans, two for each grayscale frame, bounded by colored rectangles. The human matching process is represented by arrows linking objects of different frames and marked by the computed 2D correlation results [218]. The arrows corresponding to the higher correlation values indicate the correct matches. On the right column there are displayed the final tracking results: the identified and tracked moving persons in the initial color video frames [218].

We have tested this correlation-based human tracking technique on hundreds video, getting satisfactory results. Our tracking approach is also characterized by a high person matching rate that exceeds 80 percent. The performance parameters are *Precision* = 0.85 and *Recall* = 0.85 [218]. Both the HOG-based and the correlation-based pedestrian matching techniques provide comparable good tracking results and outperform other methods. From the performed method comparisons, we have found that pixel differencing based matching approaches, like those using SAD, MAD, MSD or various histograms, achieve poorer tracking results. Also, our human matching models have lower time complexity than point tracking techniques [192], like those using Kalman filters or particle filters, while producing comparable satisfactory results.

Let us now describe the second video object tracking type, which is not based on previously detected objects, presenting our results. The idea of this kind of video tracking is to select or detect a semantic image object in a given frame and then track it across subsequent frames.

Thus, in the past we proposed some video object tracking algorithms based on motion estimation [33,217]. In those papers some procedures for estimating the video motion or *optical flow* [231], such as the *block-matching algorithm*, were considered. The motion vectors between any two successive video frames are determined by applying the block-matching procedure, each such a vector representing a pair of offsets (*dx, dy*) corresponding to a pixel. The next instance of a moving object is detected easily by applying the corresponding motion vector to each pixel of the current video object instance [33,217].

A much more important video tracking result is obtained in [233], where a robust object tracking technique is provided. Our developed method is able to locate the instances of any video object in a movie sequence, no matter if the movie is recorded with a fixed or moving camera [233]. The first state of the target object could be selected interactively or determined automatically using the image object detection approaches. Then, one detects the video object location in the next frame, by using a sliding-window based object detector [233]. The classic sliding-window method, consisting of a full-search and using fixed-size sliding windows, is computationally expensive and does not treat the object scaling effect. So, we propose an object localization approach based on a variable-sized sliding-window and an improved *N*-step search algorithm [233].

Unlike other video tracking techniques, our proposed model takes into consideration not only the object position changes, but also the possible shape and scale transformations. The object scaling aspect is treated using a variable sized sliding-window while the object translation is approached using a template matching based on an *N*-Step Search algorithm. Since any object in a frame cannot differ much in shape and size from its state in the previous frame, the values of the width and height of that object's bbox must be situated in some neighborhood intervals of the width and height of its previous state. In [233] there is provided an algorithm that locates all image objects determined by these intervals. It works as applying a variable-sized sliding-window on a object's neighborhood. So, one has to determine all objects modeled as following:

$$Ob_{k,t,s,l} = [x_1(Ob) + k, y_1(Ob) + t, x_2(Ob) + l, y_2(Ob) + s], \qquad (3.59)$$

where the current object is codified by the coordinates of the upper-left and bottom-right corners as $Ob = [x_1(Ob), y_1(Ob), x_2(Ob), y_2(Ob)]$, $k, l \in [-M, M]$, $t, s \in [-N, N]$, and $M, N \geq 0$ represent quite small number of pixels. All image objects modeled by (3.59) contain the next sub-image:

$$Ob_{M,N} = [x_1(Ob) + M, y_1(Ob) + N, x_2(Ob) - M, y_2(Ob) - N] \qquad (3.60)$$

So, the set of needed objects is composed of $Ob_{M,N}$, the objects containing $Ob_{M,N}$ padded with an *upper zone*, those containing $Ob_{M,N}$ padded with a *bottom zone*, those containing $Ob_{M,N}$ padded with a *left zone* and those containing $Ob_{M,N}$ padded with a *right zone*. In [233] one provides a recursive object locating algorithm, in pseudo-code, that is applied to $Ob_{M,N}$ and produces $S(Ob_{M,N})$, which is the set of objects $Ob_{k,t,s,l}$.

At each step, the next instance of *Ob* has to be identified in a search area from the next frame, by performing an effective search of the corresponding objects contained by $S(Ob_{M,N})$, in that search window. Besides the full-search approach, or *Exhaustive Search* (*ES*), that is too computationally expensive, various search algorithms for motion estimation have been developed recently, such as the block matching based techniques 3-Step Search, 4-Step Search and their variants [234]. In [233] we propose a *N*-step searching method derived from the 3-step search (*TSS*) approach. One introduces the notation Ob^c for the object in next frame, having the same size as *Ob* and center *c* = (*x*,*y*). Its objects resulted from padding operations are included as rows in $S(Ob^c_{M,N})$, each of them referred as $S(Ob^c_{M,N})[i], i \in \left[1, n(Ob^c_{M,N})\right]$. A *N*-Step Search example is described in Fig. 3.39. The steps of the proposed method are:

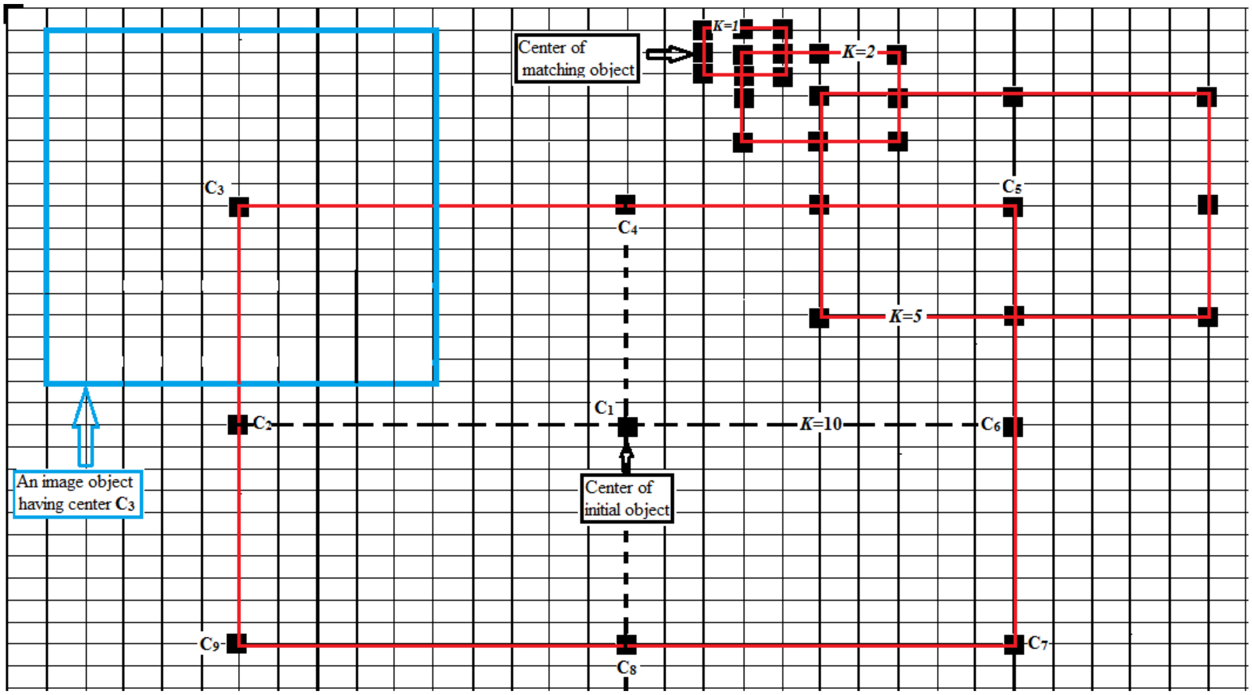

Fig. 3.39. Object matching example: *N*-step search with parameters 4 steps, initial *K*=10 and *T*=1

1. A square search area is set by selecting an initial step size *K*, depending on the motion size
2. One determines 9 points as pairs of coordinates: c_1 is the same as the center of *Ob* in the previous frame and the center of search square. The other points are positioned at the corners and the middle of the square's edges: $d(c_i, c_{i+1}) = K, \forall i \in [1,7]$, *d* being the Euclidean metric.
3. One locates the image objects Ob^{c_i} and computes the sets $S(Ob^{c_i}_{M,N})$.
4. A HOG-based feature extraction is performed and best match from all these objects is found, by computing the distances between their feature vectors and feature vector of initial object:

$$\begin{cases} [i_K, j_K] = \arg \min\limits_{i \in [1,9],\, j \in [1, n(Ob^{c_i}_{M,N}]} d(V(Ob), V(S(Ob^{c_i}_{M,N})[j])) \\ \min(K) = \min\limits_{i \in [1,9],\, j \in [1, n(Ob^{c_i}_{M,N}]} d(V(Ob), V(S(Ob^{c_i}_{M,N})[j])) \end{cases} \quad (3.61)$$

5. One computes the center of $Ob(K) = S(Ob^{c_{i_K}}_{M,N})[j_K]$ and assigns its value to c_1.

6. The step size is halved, $K \to \lfloor K/2 \rfloor$, and another search square, based on the new step size, is set up around c_1. The new $c_2,...,c_9$ center positions are determined.
7. One determines the sets of objects $S(Ob^{c_i}_{M,N}), \forall i \in [2,9]$.
8. If $\min(K) < \min\limits_{i\in[2,9],\, j\in[1,n(Ob^{c_i}_{M,N}]} d(V(Ob),V(S(Ob^{c_i}_{M,N})[j]))$ or $K/2 < T$ (a threshold), then $Ob(K)$ is the match of *Ob*, else

$$\left\{ [i_{K/2}, j_{K/2}] = \arg \min_{i\in[2,9],\, j\in[1,n(Ob^{c_i}_{M,N}]} d(V(Ob),V(S(Ob^{c_i}_{M,N})[j]) \right. \tag{3.62}$$

and returns to step 5 to continue the search similarly.

9. The search process stops when the match (next state) of *Ob* is identified.

The main advantage of this video tracking technique is that it is not influenced at all by the camera motion. Unlike the other proposed object tracking methods, this approach provides satisfactory results regardless of the presence of desired or undesired camera movements, as proven by the hundreds video tracking experiments using this technique [233]. Very good object tracking results have been achieved for both static and moving camera videos, and also a high matching rate, of approximately 90%. Choosing a high value for *K* and a low value for *T* increases the tracking rate, but also the computational complexity. The used parameter values are $T = 3$, $M, N < 5$ and an initial *K* value depending on the target size: half of the object's diagonal.

Given the Histogram of Oriented Gradient features used by it, our approach can be used successfully for human tracking. From the performed method comparison, we have found that it provides better results than pixel differencing based matching methods [215]. Also, the developed object search algorithm outperforms other sliding-window based solutions. Our approach runs much faster than Exhaustive Search based methods, given its lower computational complexity, and provides better tracking results than TTS and 4-Step Search [233,234].

One of our video tracking experiments, related to traffic monitoring [233], is described in Fig. 3.40. The moving car is interactively selected in the first frame, where is marked in red. The initial search square and *K* value are also displayed. In the second frame some results of our *N*-step search procedure are displayed. One can see that the orange bounding rectangle corresponds to the minimum distance value (0.84) between feature vectors. In the next 2 frames, the detected states of the target object are marked in orange and corresponding distance values are displayed.

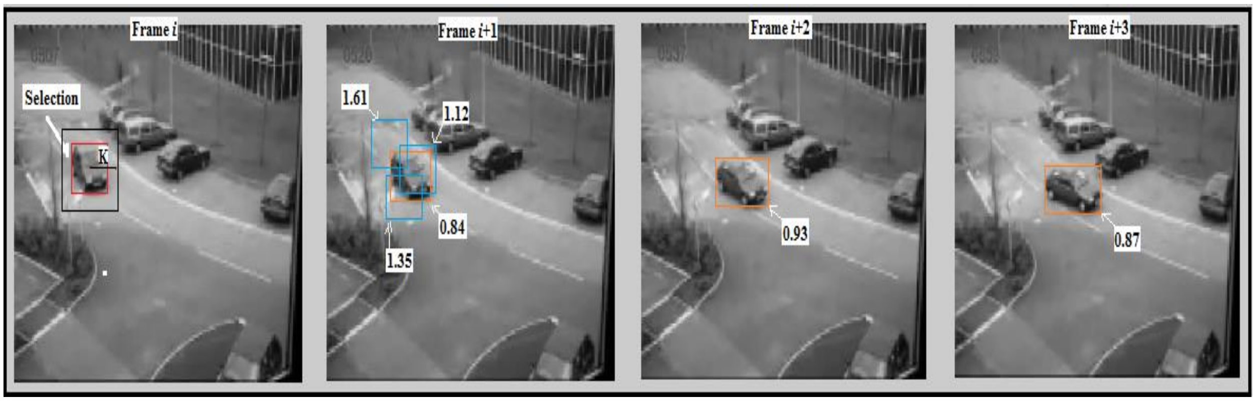

Fig. 3.40. Example of a target object tracking in a short video sequence converted to grayscale

3.7. Conclusions

In this chapter we have described the most important results of our research conducted in the last years in the computer vision domain. These results were disseminated in 2 books, 15 articles published in recognized international journals and 20 articles published in the volumes of international scientific events. We brought major contributions in the next computer vision fields: image and video segmentation, image reconstruction, image and object recognition, content-based image indexing and retrieval, object detection and tracking.

The image segmentation task was treated by proposing original region-based and contour-based approaches. Our automatic region-based segmentation techniques, which use various moment-based pixel feature vectors and the automatic clustering algorithms developed by us, provide very good results and execute quite fast. They represent better solutions than many other state of the art segmentation methods because of their automatic character that is an important advantage. The contour-based segmentation method developed by us represents an effective PDE variational level-set based technique that improves the influential Chan-Vese level-set model. A rigorous mathematical treatment of the proposed contour tracking PDE model was also provided.

We also constructed a novel automatic temporal video segmentation technique, based on a robust Gabor filter-based feature extraction producing 3D frame feature vectors, and some automatic no-threshold based frame clustering solutions. From our many experiments and method comparisons we found that our approach outperforms the other state of the art cut detection methods. It could be improved to work properly for other shot transitions, besides cuts.

Important results were also obtained in the image reconstruction domain. We developed a PDE variational image inpainting approach characterized by a nonlinear elliptic diffusion Euler-Lagrange equation, which restore properly the missing regions. The mathematical investigation of this PDE model, performed by us, represents also an important contribution in this field.

We developed various image, video and object recognition techniques, which were described in this chapter. Our main contributions in the image recognition area are the automatic recognition models computing moment-based, LAB color based and 2D Gabor filter based feature vectors that are next clustered by our unsupervised classification methods. The most important contribution in the object recognition domain is our automatic moment-based shape recognition technique, followed by a content-based analysis in the object recognition process. Because of their automatic character, our recognition models are much more effective than other existing techniques and more useful for content-based image indexing and retrieval, which is another domain successfully approached by us. We proposed effective content-based feature vector indexing solutions, developing both SAM-based indexing structures and cluster-based image indexing models. Consequently, the corresponding CBIR techniques were obtained. We developed an original cluster-based retrieval system that extracts relevant images and objects from a database by using the indexes created through our automatic feature vector clustering algorithms. We also constructed relevance-feedback based CBIR schemes that perform effective *K*-NN searches at each step by using the tree-based SAM indexing structures.

Some significant detection and tracking results were also provided. Original object class detection models, performing skin, face and human cell detection, were developed by us. The temporal differencing-based multi moving object detection method is another major contribution in this field. Novel object-matching based tracking approaches, using correlation-based, Gabor filter-based and HOG-based features, were also proposed. Our pedestrian tracking models and the motion-insensitive *N*-SS based tracking technique represent important contributions as well.

(ii) Professional, scientific and academic career evolvement and development plans

In the main part of this thesis, *b*(*i*), there were presented the most important scientific achievements of my research activity conducted in the period 2005-2014. In this second part, *b*(*ii*), my professional, scientific and academic career evolvement and development plans are outlined.

I began the research in image processing, biometrics and computer vision areas before 2005 and intend to continue it in the future. Several important results were obtained in the respective areas before being awarded the PhD degree, some of them being already mentioned in this thesis. Thus, in the image pre-processing field, we developed an application of the fractional step algorithm for computing the Riccati equation's solutions to image denoising and restoration [235]. An effective restoration model for blurred and noisy images is provided in [235]. A numerical approximation of the Riccati equation via fractional steps method, which can be also applied to image filtering, is described in [236].

In the biometrics domain we modeled some person authentication techniques based on voice and fingerprints. Our speaker recognition models using auto-regressive (AR) coefficient based feature vectors classified using MLP, RBF [59] or various ART classifiers [60] were mentioned in section 2.1. Also, some pattern-based fingerprint recognition techniques using 2D Gabor filters, Wavelet Transforms and a combination of the two were proposed in [97]. Bimodal biometric solutions based on voice and fingerprints were also considered. Some important results were also achieved in the computer vision field. A moment-based image segmentation technique developed in 2003 was shortly discussed in 3.1.1 [125]. An image object detection method using the segmentation results obtained in [125] was proposed in [126]. Also, some image object recognition and interpretation techniques are provided in that paper [126]. Another computer vision system for image object recognition was proposed in 2004 [170].

Obviously, our research in these domains has intensified considerably following the PhD award. We have tried to unify the research in these scientific fields, which are strongly related anyway. So, the biometrics and computer vision represent the major domains of interest, while image preprocessing and machine learning have been viewed as important *helping* domains for them. So, the mathematical models for image processing and machine learning presented in first chapter have the role to facilitate the biometrics and computer vision tasks. It is obvious that our feature vector classification models are required by the recognition tasks of the two major domains, while the images enhanced by pre-processing operations facilitate considerably any image analysis process from the biometrics or computer vision domain. This relationship between these research areas is also expressed in thesis title, which says that image processing and analysis methods, and also the signal analysis used in voice recognition, are applied in the two major fields.

As a unifying aspect, we have approached subdomains that could be part of more than one domain. Since computer vision represents an extremely vast scientific domain that is closely related to a lot of signal processing based research fields, it has significant overlaps with the other three approached domains. For this reason some of our techniques described here can be considered as belonging to two domains, instead of one. For example, some may consider the clustering technologies of machine learning as part of computer vision, the image reconstruction field could be also considered as an image pre-processing subdomain, some biometric authentication processes described here, such as face recognition, represent also object recognition tasks related to computer vision, while some of our computer vision tasks representing object detection procedures, like face detection that is viewed as the first step of face recognition, could also be included in biometrics.

Another important unifying element brought by us is the presence of mathematical models in all the approached fields. Thus, PDE models are introduced to solve all our image processing tasks, some PDE models are used in the biometric authentication domain (see our eigenimage-based approach) and other PDE-based approaches are used in some computer vision subdomains, such as image inpainting and contour tracking. Some mathematical models, although not PDE-based, are used also by the proposed classification algorithms and their metrics. Strong mathematical treatments are provided in all cases involving these models, proving the superiority of partial differential equation based solutions to other approaches.

Our future research will focus on further improving these PDE models and developing new PDE-based solutions for the tasks of the considered domains. As previously mentioned, the main research directions of our future activity will remain essentially the same, but new subdomains of image pre-processing, biometrics and computer vision can be approached. Let us present now our future research plans in each of these fields.

So, I intend to develop new PDE-based techniques for image denoising and restoration and to obtain improved versions of our existing models. For example, the image denoising technique using hyperbolic second-order equations proposed in [5] can be further transformed into a more sophisticated nonlinear filter, as already mentioned in 1.1. We will derive novel and effective nonlinear PDE hyperbolic models from it, such as that given by (1.6), to achieve better image filtering solutions. Another application of our hyperbolic model is a filtering technique that extracts the coherent and incoherent components of a forced turbulent flow and to identify coherent vortices [7].

The nonlinear anisotropic diffusion based image denoising and restoration techniques described in 1.2 will also be improved. Thus, we are investigating successfully new edge-stopping functions for our PDE models. Novel anisotropic diffusion schemes, like (1.19), will also be modeled. Mathematical treatment of well-posedness, stability and consistency will be performed for each of them. More effective discretization schemes will be also considered for these PDE models, rigorous mathematical demonstrations of their convergence being provided.

The image noise removal approach based on diffusion porous media flow presented in 1.2.2 could also be modified. Thus, we will consider the following equation:

$$\begin{cases} \dfrac{\partial u}{\partial t} - \Delta\beta(x,u) = 0, \text{in } (0,\infty)\times\Omega, \\ \beta(0,x) = 0, \text{in } (0,\infty)\times\partial\Omega \end{cases} \tag{1}$$

where β will be a carefully chosen maximal monotone function. A robust mathematical investigation of this nonlinear diffusion equation will be performed. We will try to demonstrate that equation (1) has a unique strong solution in certain conditions. The numerical approximation of this PDE will be performed using an implicit finite difference scheme. A stochastic variant of this PDE model will also be studied. Thus, the stochastic equation $\dfrac{\partial u}{\partial t} - \Delta\beta(x,u) = udW$ may be considered.

We also intend to improve our fourth-order diffusion-based image denoising approaches [24], which are inspired by the influential You-Kaveh isotropic scheme [237], by modeling new diffusivity functions. Also, we will develop nonlinear fourth-order anisotropic diffusion models that outperform the Y-K algorithm and other state-of-the-art 4th-order PDEs, providing much better despeckling and deblurring results. They will outperform also the second-order PDE models, removing more successfully the staircase effect. These novel restoration solutions could be achieved by mixing nonlinear 2nd-order and 4th-order diffusions. Such a combined 4th –order PDE model has just been disseminated in an accepted article [238], and more denoising schemes of that type will be investigated as part of our future research.

Our future research in image enhancement domain will also focus on modeling novel variational schemes for image restoration. The PDE variational techniques described in section 1.3 can be further modified to obtain improved versions. New variants of the regularizer function, which produce a better smoothing effect while preserving the image edges and reducing the staircasing effect, will be proposed. Thus, we will investigate a modified version of the variational PDE model presented in 1.3.2, which is based on the minimization of a convex energy functional of gradient under minimal growth conditions [28]. A new image denoising solution would be based on the following minimization problem:

$$\min\left\{\int_{\Omega}\left(\psi(\nabla u)+\frac{1}{2}\|u-u_0\|^2\right)dx; u\in W^{1,1}(\Omega)\right\}, \tag{2}$$

where $\psi : R \rightarrow [-\infty,+\infty]$ is chosen as a convex lower semicontinuous function such that

$$\psi(\gamma)=\begin{cases} g_0(\gamma),\ for\ |r|\leq\alpha \\ +\infty,\ for\ |r|>\alpha \end{cases} \tag{3}$$

where $g_0(\gamma)\in C^1(R)$. In this case, the corresponding elliptic equation has the following form:

$$-div(g(\nabla u)\ -div(\eta(u))+u-u_0=0 \tag{4}$$

where $\eta(u)$ is the normal cone to $\{u; u_1+u_2\leq a\}, u=(u_1,u_2)$. This is an elliptic variational inequality. This new denoising procedure refers to situation where one imposes a magnitude constraint on the gradient of intensity that is a constant on variation of luminosity of the image.

In the biometrics domain our future research activity will focus on developing new person authentication strategies based on the same identifiers (voice, face and fingerprints) and also considering biometric recognition techniques based on new identifiers. So, we are going to continue the research in the voice recognition area, paying particular attention to the text-independent speaker recognition subdomain, where we have achieved considerably weaker results. A MFCC-based speech signal analysis could be performed in the feature extraction stage, but we will also investigate other voice feature extraction solutions, like those using *linear predictive cepstral coefficients* (LPCCs) [239], for example. In the feature vector classification stage, Vector Quantization (VQ) [63] or Gaussian Mixture Models (GMM) [64] can be applied.

New face recognition solutions will also be explored. So, I consider proposing some facial recognition approaches based on tools that have been less utilized in our research, such as

Independent Component Analysis (ICA), Linear Discriminant Analysis (LDA) and Local Non-negative Matrix Factorization (LNMF) [240].

In the fingerprint authentication domain we aim to extend the conventional recognition from a supervised to an unsupervised framework. The unsupervised fingerprint recognition field has been increasingly investigated in the last years [241]. We consider developing some unsupervised fingerprint recognition techniques that outperform the existing approaches, our technologies being endowed with an automatic character. The planned methods use both minutia-based and pattern-based feature vectors. Our automatic clustering algorithms will be applied to the fingerprint feature vectors, eventually using some special similarity metrics in the minutia-based case.

As previously mentioned, our biometrics related research will also focus on a fourth biometric identifier that is the *human iris* [242]. Our research in the iris recognition domain is still in the early stage, a few results being achieved and disseminated [54,117]. An automatic unsupervised iris recognition approach that classifies LAB color-based feature vectors by using a hierarchical agglomerative clustering algorithm is proposed in [54]. A supervised iris-based authentication model using other LAB color features and a *K*-NN classifier is provided by us in a very recent paper [117]. Although the color analysis in LAB colorspace provides us encouraging iris featuring results and we will continue the research in this area by improving the color-based feature vectors, we are going to investigate other iris feature extraction solutions, too. Thus, the future recognition approaches will take into consideration the iris texture information. Some robust texture analysis based iris feature extraction solutions using two-dimensional Gabor filters and Discrete Wavelet transforms will be constructed as part of our research. Next, we will try to combine the color-based and texture-based features to obtain more powerful iris feature vectors and consequently, much better recognition results.

New multimodal biometric recognition solutions will also be considered in the future. So, adding the new biometric that is iris to our existing unimodal and multimodal biometric systems based on various combinations of voice, face and fingerprints [53,59,60,91,97,113,116] would improve considerably the authentication results. Also, some improved multi-method biometric systems will be obtained by adding new voice, face, fingerprint and iris recognition techniques to the existing models. As mentioned in 2.5, we will also try new biometric information fusion solutions. Thus, we consider performing the fusion at lower levels than the decision level or even the classification level.

My research activity in the computer vision domain will continue in the described subdomains, but new computer vision areas will be also approached. Also, we intend to solve more computer vision tasks by using the PDE models. We will consider new region-based and contour-based image segmentation solutions. So, novel pixel clustering based segmentation techniques can be obtained by using other feature extraction processes instead of the moment-based analysis used in 3.1.1. The feature vector characterizing the neighborhood of a pixel can be also modeled using other well-known image analysis tools, such as the 2D Gabor filters and DWT-2D. Also, we will further investigate the level-set based segmentation domain [136], trying to achieve new contour tracking-based image segmentation solutions.

We could search for some better featuring approaches in the video segmentation case, too, but our main challenge in this case is to develop some temporal segmentation algorithms that work properly not only for hard cuts, but also for other types of shot transitions. So, we will try to improve the automatic video shot detection technique described in 3.2.2 [139], so it works properly for soft cuts, like fades or dissolves, or some digital effects.

Image reconstruction will remain an important focus of my future computer vision research. I consider developing more PDE-based inpainting techniques improving the well-known TV inpainting model and the variational reconstruction model proposed in [134]. So, novel variational inpainting models can be obtained from (3.28) if new proper edge-stoppping functions are determined. Also, more effective variational reconstruction solutions will be achieved by adapting the nonlinear fourth-order diffusion-based models to inpainting:

$$u^* = \arg\min_u \int_\Omega \left(\alpha \cdot \varphi\left(\nabla^2 u\right) + \lambda/2 \left(1 - 1_\Gamma\right)\left(u - u_0\right)^2\right) d\Omega \qquad (5)$$

where function φ must be properly selected. Models combining 2nd and 4th order PDEs may be also adapted for inpainting. Another idea is to construct an inpainting model based on the Cahn-Hilliard equation [243]. So, we will investigate the PDE:

$$\begin{cases} \dfrac{\partial u}{\partial t} = \gamma\left(\Delta^2 u - u^3 - u\right), \text{in } (0,T) \times \Omega, \\ \\ u(0,x,y) = u_0(x,y) \end{cases}, \qquad (6)$$

corresponding to a variational model based on next minimization:

$$\underset{u}{Min}\left\{\int_\Omega (u - u_0)^2\, dxdy + E(u)\right\} \qquad (7)$$

where $E(u) = \int_\Omega \left(\|\nabla u\|^2 + \gamma\left(u^2 - 1\right)\right) dxdy$

We also intend to obtain new results in the image and object recognition field. A novel image recognition approach would imply either a new image featuring solution or a new feature vector classification method. New and possibly improved content-based feature vectors will be modeled by performing new color and texture analysis procedures. Thus, we will continue to investigate the LAB color-based image analysis, trying to achieve better color feature vectors. Also, new texture-based image analysis operations based on 2D Gabor filters, 2D-DWT and Fourier descriptors will be performed. Novel image similarity metrics will be considered for these feature vectors. We will also perform new research in the machine learning domain, focusing mainly on identifying automatic unsupervised classification solutions. Obviously, any new feature vector classification approach would produce not only novel image recognition solutions, but also many new biometric authentication methods. Novel object recognition models will also be considered, new shape descriptors being modeled for this purpose. High-level image analysis will also be a focus of my research, new object interpretation models being investigated.

Our future research in content-based image indexing and retrieval domain is closely related to content-based image/video and object recognition research. We intend to implement new versions of the relevance-feedback based CBIR system represented in Fig. 3.20, by considering new SAM-based high-dimensional data indexing solutions. Thus, various search tree-based structures, such as VP-tree, M-tree or MVP-tree, will be used for the new modeled content-based image feature vectors.

Novel object detection and tracking solution will be developed during our future research, too. As previously mentioned, the PDE level-set based contour tracking techniques for image segmentation and object detection in static images will be further investigated. Other object detection tools, such as the point detectors, various Hough Transforms or boosting procedures, will be applied. New object-class detection tasks will be also performed. I am going to continue the research in the face detection domain, providing other solutions to this task. For example, the proposed face detection model using skin identification results can be further modified [168]. Thus, the face candidates are determined using the same conditions given in (3.45). These candidates represent filled connected components, so their original (unfilled) versions are then analyzed. Those of them characterized by holes that could represent essential facial features such as eyes, eyebrows, nose and mouth, are labeled as faces. Some geometric approaches can be used to identify these individual face characteristics.

Human detection in static images will constitute another important goal of our computer vision research. An idea is to extend the skin-based solution used in the cases of faces for detecting entire human bodies. Obviously, the detected skin regions representing face, neck, arms, hands, legs and feet could determine the location of a person. The task becomes more difficult if some of these body parts are covered by clothes. Another solution is to apply a technique that is similar to the SVM-based approach proposed for cell detection [210]. Our sliding-window based image scanning algorithm, or an improved version of it, and the HOG-based feature extraction will be used successfully for pedestrian detection, if a proper training set, containing *human* and *non-human* image objects, is constructed for SVM. Also, replacing the HOG features with other featuring solutions in this detection process will be considered. We also intend to improve the proposed multiple moving object detection technique [219], so that to become less influenced by the video camera motion. Novel object tracking solutions will be also developed. We consider using Kalman filtering with some point-based features, like SIFT. Introducing the PDE models in our object detection and tracking research represents another future goal. Thus, a PDE-based video motion estimation that would be very useful to the tracking process will be performed. Our estimation approach will compute efficiently the optical flow from the video sequences [244], by using a new PDE variational model. A energy functional to be minimized will be constructed and solving the minimization problem will require 2 Euler-Lagrange equations.

New computer vision subdomains will be considered, as part of our future research. One of them is the *image registration* that involves spatially registering the target image(s) to align with the reference image [245]. Since image similarities are broadly used for image registration, our image similarity metrics can be applied successfully to this domain. Also, some PDE-based registration techniques are planned [246]. Similar to optic flow case, one estimates a realistic displacement (deformation) field mapping corresponding pixels in the template image to the source image, in registration case. So, an effective PDE variational image registration model can be derived from the variational optical flow estimation solutions.

I have also some serious professional and academic career evolvement and development plans. My actual academic position is Senior Researcher I at Institute of Computer Science of the Romanian Academy. Following this abilitation process, I will obtain also the official right of doctoral supervision. So, an important objective of my future professional activity is to form a new generation of well-prepared researchers in my domains of interest. For this purpose I intend to recruit and supervise PhD students that have passion for this research and willingness to work hard in the research collectives coordinated by me.

Building and managing these effective research teams represents another essential objective. Given my high research position, I have a rich experience as a team leader. Since 2004 I have been coordinating a research collective at my institute, whose activity is related to speech, image and video processing and analysis. In the period following my PhD award, our research team has achieved important results in these scientific fields. Thus, 22 of my papers published since 2005 in these domains have some of the members of my research team as co-authors. Also, in this period our research collective has elaborated 20 scientific reports under my supervision, disseminating image processing, biometrics and computer vision results. I intend to strengthen and also enlarge my research team in the future, by co-opting preferably young researchers and PhD students. Since my future doctoral students will follow their PhD program at Institute of Computer Science, they could also participate at our research projects, so I will try to enlarge our team by including them. Besides coordinating this collective at the institute, I am going to organize research teams related to various projects. Since 2005 I have coordinated several research directions, related to biometrics, PDE models and computer vision, in scientific projects (grants) on the basis of contract. In the future I intend to build some strong and larger research teams with whom to win more grant competitions as project director. My future PhD students will also be included in these project-related collectives.

Another objective of my academic career development plan consists of establishing some important collaborative relationships with other institutions and researchers from our country or abroad. In the last years I have established several external collaborations, by performing research and teaching activities at three important foreign universities. So, in May 2012 I activated as visiting academic at Department of Automatic Control and Systems Engineering of the University of Sheffield, United Kingdom, working with a british research team in a video analysis project. In April 2013 I worked for one month as a visiting professor at the University of Bologna, Italy. During that visit I collaborated with professor Angelo Favini, from Department of Mathematics of the university, in the PDE-based image processing domain. The results of our research collaboration were disseminated in a paper published in an ISI journal [16], and included in my most relevant 10 papers. In 2014 I won a DAAD fellowship for university professors and senior researchers with a project in PDE-based image restoration field. My DAAD project, entitled VANDIRES, was conducted at the Department of Mathematics of the Bielefeld University, Germany, in collaboration with a research team led by the professor Michael Roeckner. Last year I also won a GNAMPA fellowship for visiting professors, with another PDE-based computer vision project, which will allow me to work again at Bologna University later this year and to continue the collaboration with its Department of Mathematics. A collaboration with Faculty of Bioengineering of University of Medicine and Pharmacy from Iaşi is also underway. I will continue these collaborations in the future while trying to establish more external cooperations. I believe that all these collaborations will result not only in new published papers and academic exchange visits, but also in strong international research collectives capable to win and conduct bilateral and multinational projects based on contract.

The final main objective is to perform some teaching activity, besides research, in the mentioned areas. Altough my scientific activity has consisted mainly of research, I have also some teaching experience. I activated as visiting professor at Bologna University and Bielefeld University, giving numerous talks at those institutions. Also I have delivered many lectures to the students of the Faculty of Bioengineering of University of Medicine and Pharmacy, Iaşi. So, I would like to continue to transmit my knowledge to young people and I strongly believe that teaching and working with students will be also very helpful to my research career.

(iii) References

[1] F. Guichard, L. Moisan, J. M. Morel, A review of P.D.E. models in image processing and image analysis, *Journal de Physique*, Vol. 4, pp. 137–154, 2001.

[2] A. K. Jain, *Fundamentals of Digital Image Processing*, Prentice Hall, NJ, USA, 1989.

[3] R. Gonzales, R.Woods, *Digital Image Processing*, Prentice Hall, New York, NY, USA, 2nd edition, 2001.

[4] H. E. Ning, L. U. A. Ke, A Non Local Feature-Preserving Strategy for Image Denoising, *Chinese Journal of Electronics*, Vol. 21, No. 4, 2012.

[5] T. Barbu. Novel linear image denoising approach based on a modified Gaussian filter kernel, *Numerical Functional Analysis and Optimization*, 33 (11), pp. 1269-1279, publisher Taylor & Francis Group, LLC, 2012.

[6] V. Barbu, *Partial Diferential Equations and Boundary Value Problems*, Kluwer Academic Publishers, Dordrecht, 1998.

[7] T. Nabi, W. A. Kareem, S. Izawa, Y. Fukumishi, Extraction of coherent vortices from homogeneous turbulence using curvelets and total variation filtering methods, *Computers and Fluids*, Vol. 57, pp. 76-86 2012.

[8] J. Weickert, *Anisotropic Diffusion in Image Processing*, European Consortium for Mathematics in Industry, B. G. Teubner, Stuttgart, Germany, 1998.

[9] P. Perona, J. Malik, Scale-space and edge detection using anisotropic diffusion, *Proceedings of IEEE Computer Society Workshop on Computer Vision*, 16–22, nov. 1987.

[10] S. Esedoglu, An analysis of the Perona-Malik scheme, *Comm. Pure Appl. Math*., 54, pp. 1442-1487, 2001.

[11] T. F. Chan, C. K. Wong, Total variation blind deconvolution, *IEEE Transactions on Image Processing*, 7, pp. 370–375, 1998.

[12] P. Charbonnier, L. Blanc-Feraud, G. Aubert, M. Barlaud, Two deterministic half-quadratic regularization algorithms for computed imaging, *Proc. IEEE International Conf. on Image Processing*, vol. 2, pp. 168–172, Austin, TX, IEEE Comp. Society Press, 1994.

[13] M. Black, G. Shapiro, D. Marimont, D. Heeger, Robust anisotropic diffusion, *IEEE Trans. Image Processing*, 7, 3, pp. 421-432, 1998.

[14] F. Voci, S. Eiho, N. Sugimoto, H. Sekiguchi, Estimating the gradient threshold in the Perona–Malik equation, *IEEE Signal Processing Magazine*, 21 (3), pp. 39-46, 2004.

[15] T. Barbu, Robust anisotropic diffusion scheme for image noise removal, *Procedia Computer Science* (*Proc. of 18th International Conf. in Knowledge Based and Intelligent Information & Engineering Systems, KES 2014*, Sept. 15-17, Gdynia, Poland), published by Elsevier, Vol. 35, pp. 522-530, 2014.

[16] T. Barbu, A. Favini, Rigorous mathematical investigation of a nonlinear anisotropic diffusion-based image restoration model, *Electronic Journal of Differential Equations*, Vol. 2014, No. 129, pp. 1-9, 2014.

[17] S. L. Keeling, R. Stollberger, Nonlinear anisotropic diffusion filtering for multiscale edge enhancement, *Inverse Problems*, vol 18, pp. 175-190, 2002.

[18] T. Barbu, Variational image denoising approach with diffusion porous media flow, *Abstract and Applied Analysis*, Volume 2013, Article ID 856876, 8 pages, Hindawi Publishing Corporation, 2013, DOI: http://dx.doi.org/10.1155/2013/856876.

[19] J. Kačur, K. Mikula, Slow and fast diffusion effects in image processing, *Computing and Visualization in Science*, vol. 13, no. 4, pp. 185–195, 2001.

[20] A. Buades, B. Coll, J-M. Morel, The staircasing effect in neighborhood filters and its solution, *IEEE Transactions on Image Processing* 15, 6, pp. 1499-1505, 2006.

[21] M. Mansourpour, M. A. Rajabi, J. R. Blais, Effects and performance of speckle noise reduction filters on active radars and SAR images, *Proceedings of ISPRS 2006*, Ankara, Turkey, Feb. 14-16, XXXVI-1/W41 2006.

[22] S. Sudha, G. R. Suresh, R. Sukanesh, Speckle Noise Reduction in Ultrasound Images by Wavelet Thresholding based on Weighted Variance, *International Journal of Computer Theory and Engineering*, Vol. 1, No. 1, pp. 1793-8201, April 2009.

[23] N. P. Anil, S. Natarajan, A New Technique for Image Denoising Using Fourth Order PDE and Wiener Filter, *International Journal of Applied Engineering Research*, Volume 5, Issue 3, 2010.

[24] T. Barbu, A PDE based Model for Sonar Image and Video Denoising, *Analele Stiintifice ale Universitatii Ovidius*, Constanta, Seria Matematică, Vol. 19, Fasc. 3, pp. 51-58, 2011.

[25] L. Rudin, S. Osher, E. Fatemi, Nonlinear total variation based noise removal algorithms, *Physica D: Nonlinear Phenomena*, 60.1, pp. 259-268, 1992.

[26] T. Chan, J. Shen, L. Vese, Variational PDE Models in Image Processing, *Notices of the AMS*, Vol. 50, No. 1, 2003.

[27] T. Barbu, A Novel Variational PDE Technique for Image Denoising, *Lecture Notes in Computer Science* (*Proc. of the 20th International Conference on Neural Information Processing, ICONIP 2013*, part III, Daegu, Korea, Nov. 3-7, 2013), Vol. 8228, pp. 501-508, Springer-Verlag Berlin Heidelberg, M. Lee et al. (Eds.), 2013.

[28] T. Barbu, V. Barbu, V. Biga, D. Coca, A PDE variational approach to image denoising and restoration, *Nonlinear Analysis: Real World Applications*, Vol. 10, Issue 3, pp. 1351-1361, June 2009.

[29] K. Popuri, Introduction to Variational Methods in Imaging, *CVR 2010 Tutorial Talk*, May 2010.

[30] C. Fox, *An introduction to the calculus of variations*, Courier Dover Publications, 1987.

[31] T. Barbu, Speech-dependent voice recognition system using a nonlinear metric, *International Journal of Applied Mathematics*, Volume 18, No. 4, pp. 501-514, 2005.

[32] L. Alboaie, T. Barbu, An Automatic User Recognition Approach within a Reputation System Using a Nonlinear Hausdorff Derived Metric, *Numerical Functional Analysis and Optimization*, published by Taylor & Francis, Vol. 29, Issue 11 & 12, pp. 1240 – 1251, Nov. 2008.

[33] T. Barbu, *Modelling Multimedia Information Systems* (in Romanian), edited by Romanian Academy Publishing House, Bucharest, 225 pages, 2006.

[34] J. Henrikson, Completeness and Total Boundedness of the Hausdorff Metric, *The MIT Undergraduate Journal of Mathematics*, Volume 1, pp. 69-80, 1999.

[35] J. von Neumann, Zur Theorie der Gesellschaftsspiele, *Mathematische Annalen*, 100, pp. 295-320, 1928.

[36] T. Barbu, Comparing Various Voice Recognition Techniques, *From Speech Processing to Spoken Language Technology* (*Proc. of 5th International Conference on Speech Technology and Human-Computer Dialogue, SPED'09*), eds. Academy Publishing House, pp. 33-42, Constanta, Romania, June 18-21, 2009.

[37] T. Barbu, Unsupervised SIFT-based Face Recognition Using an Automatic Hierarchical Agglomerative Clustering Solution, *Procedia Computer Science* (*Proceedings of 17th International Conference in Knowledge Based and Intelligent Information and Engineering Systems, KES 2013*, Sept. 9-11, Kitakyushu, Japan), Vol. 22, pp. 385-394, published by Elsevier, 2013.

[38] T. Barbu, Fingerprint Matching Approach Using a Novel Metric, *U.P.B. Scientific Bulletin*, Series A, Issue 2, Vol. 73, pp. 119-128, 2011.

[39] T. Barbu, An Automatic Unsupervised Pattern Recognition Approach, *Proceedings of the Romanian Academy*, Series A: Mathematics, Physics, Technical Sciences, Information Science, Vol. 7, No. 1, pp. 73-78, January-April 2006.

[40] T. Barbu, Automatic Unsupervised Shape Recognition Technique using Moment Invariants, *Proceedings of the 15th International Conference on System Theory, Control and Computing, ICSTCC 2011*, pp. 93-96, Sinaia, Romania, 14-16 Oct. 2011.

[41] T. Barbu, Unsupervised Speaker Recognition Approach using an Automatic Clustering Algorithm, *Proceedings of the 7th Conference on Speech Technology and Human-Computer Dialogue, SpeD 2013*, Cluj-Napoca, Romania, pp. 215-220, 16-19 October 2013.

[42] T. Barbu, Automatic Texture-based Image Segmentation Technique, *Proceedings of The 6th European Conference on Intelligent Systems and Technologies, ECIT'10*, October 7-9, Iaşi, Romania, 2010.

[43] C-T. Chang, J. Z. C. Lai, M-D. Jeng, A Fuzzy K-means Clustering Algorithm Using Cluster Center Displacement, *Journal of Information Science And Engineering*, 27, pp. 995-1009, 2011.

[44] I. Lapidot, H. Guterman, A. Cohen, Unsupervised Speaker Recognition Based on Competition Between Self-Organizing Maps, *IEEE Transactions on Neural Networks*, vol. 13, no. 4, July 2002.

[45] T. Kanungo, D. M. Mount, N. S. Netanyahu, C. D. Piatko, R. Silverman, A. Y. Wu, An Efficient K-Means Clustering Algorithm: Analysis and Implementation, *IEEE Trans. on Pattern Analysis and Machine Intelligence*, Vol. 24, Number 7, pp. 881-892, 2002.

[46] J. Dunn, Well separated clusters and optimal fuzzy partitions, *Journal of Cybernetics*, Vol. 4, pp. 95-104, 1974.

[47] D. L. Davies, D. W. Bouldin, A cluster separation measure, *IEEE Transactions on Pattern Analysis and Machine Intelligence*, Vol. 1 (4), pp. 224-227, 2000.

[48] T. Barbu, M. Costin, A. Ciobanu, An Unsupervised Content-based Image Recognition Technique, *Springer-Verlag - Series: Studies in Computational Intelligence: New Concepts and Applications in Soft Computing*, Vol. 417, pp. 157-164, Berlin, Eds. V. E. Balas, A. V. Koczy, J. Fodor, 2013.

[49] A. K. Jain, P. Flynn, A. Ross, Handbook of Biometrics, Springer, 2007.

[50] H. F. Tipton, M. Krause, *Information Security Management Handbook*, Sixth Edition, published by CRC Press, 3280 pages, May 14, 2007.

[51] M. G. Milone, Biometric surveillance: searching for identity, *Business Lawyer*, Nov. 1, 2001.

[52] A. K. Jain, R. Bolle, S. Pankanti, *Biometrics: Personal Identification in Networked Society*, Kluwer Academic Publications, 1999.

[53] T. Barbu, *Biometric Authentication Techniques* (in Romanian), edited by Romanian Academy Publishing House, Bucharest, 110 pages, 2012.

[54] A. Ciobanu, P. Radu, T. Barbu, M. Costin, S. I. Bejinariu, A Novel Iris Clustering Approach Using LAB Color Features, *Proceedings of the 4th International Symposium on Electrical and Electronics Engineering*, Galati, Romania, Oct. 11-13, 2013.

[55] R. A. Cole, J. Mariani, H. Uszkoreit, A. Zaenen, V. Zue, *Survey of the State of the Art in Human Language Technology*, Cambridge University Press, 1997.

[56] D. A. Reynolds, R. C. Rose, Robust text-independent speaker identification using Gaussian mixture speaker models, *IEEE Trans. Speech Audio Processing*, vol. 3, no. 1, pp. 72-83, 1995.

[57] T. Barbu, A supervised text-independent speaker recognition approach, *International Journal of Computer, Information, Systems and Control Engineering*, Vol. 1, No. 9, 2007.

[58] T. F. Zheng, G. Zhang, Z. Song, Comparison of Different Implementations of MFCC, *Journal of Computer Science and Technology*, 16 (6), pp. 582-589, 2001.

[59] M. Costin, T. Barbu, A. Grichnik, Automatic Speaker Recognition Decision Tools, *Fuzzy Systems and Artificial Intelligence - Reports and Letters*, Vol. 10, No. 3, pp. 167-181, 2004.

[60] T. Barbu, M. Costin, Comparing Various Automatic Speaker Recognition Approaches, *Scientific Bulletin of the Polytechnic University of Timisoara, Romania, Transactions on Electronics and Communications*, Tom (49) 63, Fasc. 1, pp. 291-296, 2004.

[61] Y. Zhang, Z-M. Tang, Y-P. Li, B. Qian, Ensemble Learning and Optimizing KNN Method for Speaker Recognition, *Proc. of 4th International Conference on Fuzzy Systems and Knowledge Discovery, FSKD '07,* Vol. 4, pp. 285-289, 24-27 Aug. 2007.

[62] W.M. Campbell, A SVM/HMM system for speaker recognition, *Proc. ICASSP 2003*, April 2003.

[63] F. Soong et. al., A vector quantization approach to speaker recognition, in *Proc. IEEE ICASSP*, pp. 387-390, 1985.

[64] L. Liu, J. He, On the use of orthogonal GMM in 385 speaker recognition, *IEEE International Conference on 386 Acoustic, Speech, and Signal Processing*, ICASSP'99, vol. 2, pp. 845-849, 1999.

[65] K. R. Farrell, R. J. Mammone, K. T. Assaleh, Speaker recognition using neural networks and conventional classifiers, *IEEE Transaction on Speech and Audio Processing*, 2 (1), pp. 194–205, 1994.

[66] M. Lindasalwa, B. Mumtaj, I. Elamvazuthi, Voice Recognition Algorithms using Mel Frequency Cepstral Coefficient (MFCC) and Dynamic Time Warping (DTW) Techniques, *Journal of Computing*, Volume 2, Issue 3, pp 138-143, March 2010.

[67] T. Barbu, M. Costin, Various Speaker Recognition Techniques Using a Special Nonlinear Metric, *Knowledge-Based Intelligent Information and Engineering Systems*, *Book Series Lecture Notes in Computer Science, Springer Berlin/ Heidelberg,* Volume 5179, pp. 622-629, 2008.

[68] S. Know, S.Narayanan, Unsupervised speaker indexing using generic models, *IEEE Trans. Speech and Audio Processing*, vol.13, no.5, pp. 1004-1013, September 2005.

[69] W. Zhao, R. Chellappa, P. J. Phillips, Face Recognition: A Literature Survey, *ACM Computing Surveys*, Volume 35, Number 4, pp. 399-458, December 2003.

[70] L. Sirovich, M. Kirby , Low-dimensional procedure for the characterization of human faces, *Journal of the Optical Society of America A*, 4 (3), pp. 519–524, 1987.

[71] M. A. Turk, A. Pentland, Face recognition using eigenfaces, In *Proceedings of Computer Vision and Pattern Recognition*, IEEE, pp. 586-591, 1991.

[72] X. Y. Jing, H. S. Wong, D. Zhang, Face recognition based on 2D Fisherface approach, *Pattern Recognition,* Volume 39, Issue 4, pp. 707-710, April 2006.

[73] F. Samaria, S. Young, HMM based architecture for face identification, *Image and Computer Vision*, Vol. 12, pp. 537-583, October 1994.

[74] L. Wiskott, C. Malsburg, *Face Recognition by Dynamic Link Matching*, In J. Sirosh, R. Miikkulainen and Y. Choe editors, *Lateral Interactions in the Cortex: Structure and Function,* UTCS Neural Networks Research Group, Austin, TX, 1996.

[75]T. Barbu, Eigenimage-based face recognition approach using gradient covariance, *Numerical Functional Analysis and Optimization*, published by Taylor & Francis, Vol. 28, pp. 591 – 601, Issue 5 & 6, May 2007.

[76] A.S. Georghiades, P.N. Belhumeur, D.J. Kriegman. From Few to Many: Illumination Cone Models for Face Recognition under Variable Lighting and Pose, *IEEE Trans. Pattern Anal. Mach. Intelligence*, Vol. 23, No. 6, pp. 643-660, 2001.

[77] J. R. Movellan, *Tutorial on Gabor filters*, http://mplab.ucsd.edu/tutorials/gabor.pdf, 2008.

[78] C. Liu, H. Wechsler, Gabor feature classifier for face recognition, In *Proceedings of the ICCV*, Vol. 2, pp. 270-275, 2001.

[79] T. Barbu, Gabor filter-based face recognition technique, *Proceedings of the Romanian Academy*, Series A: Mathematics, Physics, Technical Sciences, Information Science, Volume 11, Number 3, pp. 277 - 283, July-September 2010.

[80] T. Barbu, Two Novel Face Recognition Approaches, Chapter 2 of *Face Analysis, Modelling and Recognition Systems*, published by InTech, edited by Tudor Barbu, pp. 19-32, Oct. 2011.

[81] Q. Chen, K. Kotani, F. Lee, T. Ohmi, *Face Recognition Using Self-Organizing Maps*, Ch. 17 in *Self-Organizing Maps*, published by InTech, April 2010.

[82] B. A. Draper, K. Baek, M. S. Bartlett, J. R. Beveridge, Recognizing Faces with PCA and ICA, *Computer Vision and Image Understanding: special issue on face recognition*, Vol. 91, Issue 1-2, pp. 115-137, 2003.

[83] B. Raytchev, H. Murase, Unsupervised face recognition by associative chaining, *Pattern Recognition* 36, pp. 245-257, 2003.

[84] D. G. Lowe, Object recognition from local scale-invariant features, *Proceedings of the International Conference on Computer Vision*, 2, pp. 1150–1157, 1999.

[85] A. M. Burton et al., Face recognition in poor-quality video: Evidence from security surveillance, *Psychological Science*, 10, 243-248, 1999.

[86] J. K. Singh, *A Clustering and Indexing Technique suitable for Biometric Databases*, MSc Thesis, Indian Institute of Technology Kanpur, Kanpur, India, 2009.

[87] L. C. Jain et al., *Intelligent Biometric Techniques in Fingerprint and Face Recognition*, Boca Raton, FL: CRC Press, 1999.

[88] S. Mazumdar, V. Dhulipala, *Biometric Security Using Finger Print Recognition*, University of California, San Diego, 7 pages, Retrieved 30 August 2010.

[89] J. Ravi, K. B. Raja, K. R. Venugopal, Fingerprint Recognition Using Minutia Score Matching, *International Journal of Engineering Science and Technology*, Vol. 1 (2), pp. 35-42, 2009.

[90] M. U. Munir, M. Y. Javed, Fingerprint Matching using Gabor Filters, *National Conference on Emerging Technologies*, 2004.

[91] H. Costin, I. Ciocoiu, T. Barbu, C. Rotariu, A Complex Biometric System for Person Verification and Identification through Face, Fingerprint and Voice Recognition, *Scientific Studies and Research*, Mathematics Series, Number 16, Supplement, University Bacău, pp. 361-393, September 2006.

[92] D. Maio, D. Maltoni, Direct Gray-Scale Minutiae Detection in Fingerprints, *Journal IEEE Transactions on Pattern Analysis and Machine Intelligence*, Volume 19 Issue 1, January 1997.

[93] E. R. Dougherty, *An Introduction to Morphological Image Processing*, SPIE Optical Engineering Press, 1992.

[94] M. Sonka, V. Hlavac, R. Boyle, *Image Processing, Analysis, and Machine Vision*, 2nd Edition, Pws. Pub. Co, 1998.

[95] *D. Maltoni, D. Maio, A. K. Jain, S. Prabhakar,* Handbook of Fingerprint Recognition (Second Edition), Springer, London, 2009.

[96] J. Park, K. Hanseok, Robust Reference Point Detection Using Gradient of Fingerprint Direction and Feature Extraction Method, *Computational Science – ICCS 2003*, Part 1, 2003.

[97] A. Tudosă, M. Costin, T. Barbu, Fingerprint Recognition using Gabor filters and Wavelet Features, *Scientific Bulletin of the Politehnic University of Timisoara*, Romania, Transactions on Electronics and Communications, Tom (49) 63, Fasc. 1, pp. 328-332, 2004.

[98] T. Barbu, M. Costin, A. Ciobanu, Pattern-based Fingerprint Matching Approach, *Proceedings of International Workshop on Intelligent Information Systems, IIS 2011*, pp. 105-108, 12-14 September 2011, Chisinau, Republic of Moldova.

[99]T. Barbu, Novel Pattern-based Fingerprint Recognition Technique Using 2D Wavelet Decomposition, *Mathematical Methods for Information Science & Economics: Proceedings of the 3rd International Conference for the Applied Mathematics and Informatics (AMATHI '12),* Montreux, Switzerland, pp. 145-149, December 29-31, 2012.

[100] M. P. Dale, M. A. Joshi, Fingerprint matching using transform features, *TENCON 2008, IEEE Region 10 Conference*, 2008.

[101] S. Mallat, *A wavelet tour of signal processing*, Academic Press, San Diego, California, USA, 1998.

[102] M. Tico, P. Kuosmanen, J. Saarinen, Wavelet domain features for fingerprint recognition, *Electronics Letters*, Volume 37, No. 1, 2001.

[103] A. Ross, A. K. Jain, Multimodal Biometrics : An Overview, *Proceedings of 12th European Signal Processing Conference (EUSIPCO),* Vienna, Austria, pp. 1221-1224, September 2004.

[104] H. Korves, L. Nadel, B. Ulery, D. Masi, Multi-biometric Fusion: From Research to Operations, *Sigma, Mitretek Systems*, pp. 39-48, Summer 2005.

[105] A. Ross, A. K. Jain, Information fusion in biometrics, Pattern Recognition Letters, 24 (13), pp. 2115–2125, 2003.

[106] R. Brunelli, D. Falavigna, Person identification using multiple cues, *IEEE Trans. Pattern Anal. Machine Intell.*, vol. 12, pp. 955–966, Oct. 1995.

[107] K. Nandakumar, Y. Chen, S. C. Dass, A. K. Jain, Quality-based Score Level Fusion in Multibiometric Systems, *Proc. of 18th Int'l Conf. Pattern Recognition (ICPR),* Hong Kong, pp. 473-476, 2006.

[108] L. Lam, C.Y. Suen, Optimal combination of pattern classifiers, *Pattern Recognition Letters*, 16, pp. 945–954, 1995.

[109] J. Daugman, *Combining Multiple Biometrics*, Available online at http://www.cl.cam.ac.uk/users/jgd1000/combine/combine.html.

[110]L.Xu, A.Krzyzak, C. Suen, Methods of combining multiple classifiers and their applications to hand writing recognition, *IEEE Trans. on Systems, Man and Cybernetics*, Vol. 22, no. 3, pp. 418–435, 1992.

[111] A. K. Jain, L. Hong, Y. Kulkarni, A multimodal biometric system using fingerprint, face and speech, in *Second International Conference on AVBPA*, Washington D.C., USA, pp. 182–187, 1999.

[112] BioID, www.bioid.com.

[113] H. Costin, T. Barbu, C. Rotariu, C. Costin, A Biometric System for Person Verification and Identification through Fingerprint and Voice Recognition, *Proceedings of The 5th European Conference on Intelligent Systems and Technologies, ECIT'08*, Iaşi, Romania, July 10-12, 2008.

[114] L. Hong, A. Jain, Integrating faces and fingerprint for personal identification, *IEEE Trans. Pattern Analysis and Machine Intelligence* 20 (12), pp. 1295–1307, 1998.

[115] H. Costin, I. Ciocoiu, T. Barbu, C. Rotariu, Through Biometric Card in Romania: Person Identification by Face, Fingerprint and Voice Recognition, *International Journal of Computer, Information, Systems and Control Engineering*, Vol. 2, No. 5, 2008.

[116] T. Barbu, M. Costin. A Human Person Recognition System using Face and Voice Biometrics, *Scientific Bulletin of the Politehnic University of Timisoara, Romania, Transactions on Electronics and Communications,* Tom (53) 67, Fasc. 2, pp. 5-10, 2008.

[117] A. Ciobanu, M. Luca, I. Păvăloi, T. Barbu, Iris Identification based on Optimized LAB Histograms Applied to Iris Partitions, *Bulletin of the Polytechnic Institute of Iasi, Automatic Control and Computer Science Section*, Tom LX (LXIV), Fasc. 3, pp. 37-48, published by "Gheorghe Asachi" Technical University of Iaşi, 2014.

[118] L. G. Shapiro, G. C. Stockman, *Computer Vision*, Prentice Hall, 2001.

[119] R. Ohlander, K. Price, R. Reddy, Picture Segmentation Using a Recursive Region Splitting Method, *Computer Graphics and Image Processing*, 8 (3), pp. 313–333, 1978.

[120] L. Barghout, J. Sheynin, Real-world scene perception and perceptual organization: Lessons from Computer Vision, *Journal of Vision*, 13, 9, pp. 709-709, 2013.

[121] Z. Wu, R. Leahy, An optimal graph theoretic approach to data clustering: Theory and its application to image segmentation, *IEEE Transactions on Pattern Analysis and Machine Intelligence*, Vol. 15, No. 11, pp. 1101–1113, 1993.

[122] T. Lindeberg, M.-X. Li, Segmentation and classification of edges using minimum description length approximation and complementary junction cues, *Computer Vision and Image Understanding*, vol. 67, no. 1, pp. 88-98, 1997.

[123] S. Osher, N. Paragios, *Geometric Level Set Methods in Imaging Vision and Graphics*, Springer Verlag, 2003

[124] M. Kass, A. Witkin, D. Terzopoulos, Snakes: Active contour models, *International Journal of Computer Vision*, 1(4), pp. 321–331, 1987.

[125] T. Barbu, A Pattern Recognition Approach to Image Segmentation, *Proceedings of the Romanian Academy*, Series A, Volume 4, Number 2, pp. 143-148, May-August 2003

[126**]** T. Barbu, Automatic Moment Based Texture Segmentation, *International Journal of Computer, Information Science and Engineering*, Vol. 7, No. 12, pp. 813-818, 2013.

[127] M. Tuceryan, A. K. Jain, *Texture Analysis. Handbook Pattern Recognition and Computer Vision*. Singapore: World Scientific, ch. 2, pp. 235–276, 1993.

[128] V. Levesque, Texture segmentation using Gabor filters, *Center for Intelligent Machines Journal*, 2000.

[129] M. N. Do, M. Vetterli, Wavelet-Based Texture Retrieval Using Generalized Gaussian Density and Kullback-Leibler Distance, *IEEE Transactions on Image Processing*, 11:2, February 2002.

[130] B. Abraham, O. I. Camps, M. Sznaier, Dynamic Texture with Fourier Descriptors, *Proceedings of the 4th International Workshop on Texture Analysis and Synthesis*, pp. 53-58, 2005.

[131] M. Tuceryan, A. K. Jain, Texture Segmentation Using Voronoi Polygons, *IEEE Transactions on Pattern Analysis and Machine Intelligence,* PAMI-12, pp. 211-216, 1990.

[132] R. M. Haralick, K. Shanmugam, I. Dinstein, Textural features for image classification, *IEEE Transactions on Systems, Man, and Cybernetics*, SMC - 3, pp. 610 – 621, 1973.

[133] N. Forcade, C. Le Guyader, C. Gout, Generalized fast marching method: applications to image segmentation, *Numerical Algorithms*, 48 (1-3), pp. 189–211, July 2008.

[134] T. Barbu, Robust contour tracking model using a variational level-set algorithm, *Numerical Functional Analysis and Optimization*, publisher Taylor & Francis Group, LLC, Vol. 35, Issue 3, pp. 263-274, 2014.

[135] S. Osher, J. A. Sethian, Fronts propagating with curvature-dependent speed: Algorithms based on Hamilton-Jacobi formulations, *Journal of Computation Physics*, 79, pp. 12–49, 1988.

[136] T. Chan, L. Vese, Active contours without edges, *IEEE Transactions on Image Processing*, 19 (2), pp. 266-277, 2001.

[137] D. Mumford, J. Shah, Optimal approximation by piecewise smooth functions and associated variational problems, *Comm. Pure Appl. Math.*, 42, pp. 577-685, 1989.

[138] V. Caselles, R. Kimmel, G. Sapiro, On geodesic active contours, *Int. J. Comput. Vis.*, vol. 22, no. 1, pp. 61–79, 1997.

[139] T. Barbu, Novel automatic video cut detection technique using Gabor filtering, *Computers & Electrical Engineering*, Volume 35, Issue 5, pp. 712-721, September 2009.

[140] T. Barbu, An automatic no-threshold video shot identification approach, *Proc. of the 5th European Conference on Intelligent Systems and Technologies, ECIT'08*, Iaşi, Romania, July 10-12, 2008.

[141] Y. Zhuang, Y. Rui, T. S. Huang, S. Mehrotra, Adaptive key frame extraction using unsupervised clustering, *Proceedings of the International Conference on Image Processing* (*ICIP '98*), pp. 866–870, Chicago, Ill, USA, October 1998.

[142] R. Brunelli, O. Mich, C. M. Modena, A survey on the automatic indexing of video data, *Journal of Visual Communication and Image Representation*, vol. 10, pp. 78–112, 1999.

[143] H. J. Zhang, C. Y. Low, S. W. Smoliar, J. H. Wu, Video parsing, retrieval and browsing: An integrated and content-based solution, in *Proc. ACM Multimedia '95*, Nov. 1995.

[144] F. Porikli, A. Yilmaz, Object Detection and Tracking, *Video Analytics for Business Intelligence*, vol. 409, C. Shan, et al., Eds., ed: Springer Berlin Heidelberg, pp. 3-41, 2012.

[145] K. Jin, H.-c. Feng, Q. Feng, C. Zhang, Shot Boundary Detection Algorithm Based on Multi-Feature Fusion, *Proceedings of the 2nd International Conference on Computer Science and Electronics (ICCSEE'13),* January 2013.

[146] O. Robles, P. Toharia, A. Rodriguez, L. Pastor, Automatic video cut detection using adaptive thresholds, *Proc. of the 4th IASTED International Conference on Visualization, Imaging and Image Processing*, pp. 517-522, sept. 2004.

[147] T. Barbu, Content-based Video Recognition Technique using a Nonlinear Metric, *Proceedings of the 47th International Symposium ELMAR-2005, on Multimedia Systems and Applications*, pp. 25-28, Zadar, Croatia, June 2005.

[148] A. Efros, T. Leung, Texture synthesis by non parametric sampling, *Proc. Int. Conf. Computer Vision*, vol. 2, pp. 1033-1038, 1999.

[149] L.-W. Wey, M. Levoy, Fast texture synthesis using tree-structured vector quantization, *Proc. ACM Conf. Comp. Graphics (SIGGRAPH),* 2000.

[150] M. Bertalmío, G. Sapiro, V. Caselles, C. Ballester, Image Inpainting, *Proceedings of SIGGRAPH 2000*, New Orleans, USA, July 2000.

[151] T. F. Chan, J. Shen, *Morphologically invariant PDE inpaintings*, UCLA CAM Report, pp. 01-15, 2001.

[152] P. Getreuer, Total Variation Inpainting using Split Bregman, *Image Processing On Line*, 2, pp. 147–157, 2012.

[153] T. Barbu, V. Barbu, A PDE approach to image restoration problem with observation on a meager domain, *Nonlinear Analysis: Real World Applications*, Vol. 13, Issue 3, pp. 1206-1215, June 2012.

[154] A. Kalaitzis, *Image Inpainting with Gaussian Processes*, Master of Science Thesis, School of Informatics, University of Edinburgh, 2009.

[155] T. Barbu, A novel automatic image recognition technique, *Proc. of the 4th European Conference on Intelligent Systems and Technologies, ECIT'06*, Sept. 2006, eds. H. N. Teodorescu, 2006.

[156] T. Barbu, An Automatic Graphical Recognition System using Area Moments, *WSEAS Transactions on Computers*, Issue 9, Vol. 5, pp. 2142-2147, Sept. 2006.

[156] T. Barbu, An automatic image recognition approach, *Computer Science Journal of Moldova*, Vol. 15, No. 2 (44), pp. 202-211, 2007.

[158] T. Barbu, M. Costin, A. Ciobanu, An Unsupervised Content-based Image Recognition Technique, *Springer-Verlag - Series: Studies in Computational Intelligence: New Concepts and Applications in Soft Computing*, Vol. 417, pp. 157-164, Berlin, Eds. V. E. Balas, A. V. Koczy, J. Fodor, 2013.

[159] T. Barbu, M. Costin, A. Ciobanu, Content-based Image Recognition Technique Using Area Moments, *Proceedings of the 4th International Workshop on Soft Computing and Applications, SOFA 2010*, Arad, Romania, pp. 171-174, 15-17 July 2010.

[160] S. Boughorbel, J.-P. Tarel, N. Boujemaa, Generalized histogram intersection kernel for image recognition, in *Proceedings of ICIP'05*, pp. 161–164, sept. 2005.

[161] O. Chapelle, P. Haffner, V. Vapnik, Svms for histogram based image classification, *IEEE Transactions on Neural Networks. Special issue on Support Vectors*, 1999.

[162] J-H. Zhai, S-F. Zhang, Li-Juan Liu, Image recognition based on wavelet transform and artificial neural networks, *Proc. of International Conference on Machine Learning and Cybernetics*, vol. 2, pp. 789-793, 12-15 July 2008.

[163] T. Barbu, Content-based image retrieval system using Gabor filtering, *Proceedings of the 20th International Workshop on Database and Expert Systems, DEXA '09*, pp. 236-240, 31 August - 4 September, Linz, Austria, 2009.

[164] T. Barbu, A Novel Image Similarity Metric using SIFT-based Characteristics, *Mathematical Models in Engineering and Computer Science: Proceedings of the 2nd International Conference on Computers, Digital Communications and Computing, ICDCC '13*, Brasov, Romania, pp. 15-18, June 1-3, 2013.

[165] T. Barbu, A. Ciobanu, M. Costin, Unsupervised Color-based Image Recognition based on a LAB Feature Extraction Technique, *Bulletin of the Polytechnic Institute of Iasi, Automatic Control and Computer Science Section*, published by "Gheorghe Asachi" Technical University of Iaşi, Tome LVII (LXI), Fasc. 3, pp. 33-41, 2011.

[166] T. Barbu, A. Ciobanu, M. Costin, Automatic Color-based Image Recognition Technique using LAB Features and a Robust Unsupervised Clustering Algorithm, *Latest Advances in Information Science, Circuits & Systems (Proc. of ICAI 2012)*, pp. 140-143, June 2012.

[167] A. Ciobanu, M. Costin, T. Barbu, Image Categorization Based on Computationally Economic Lab Colour Features, *Advances in Intelligent Systems and Computing* 195, pp. 585-593, (*Proc. of 5th Intl. Workshop on Soft Computing and Applications, SOFA'12*, Szeged, Hungary, 22-24 Aug., 2012), V. E. Balas et al. (Eds.): Soft Computing Applications, Springer-Verlag, Berlin Heidelberg, 2013.

[168] T. Barbu, An Automatic Face Detection System for RGB Images, *International Journal of Computers, Communications & Control*, Vol. 6, No.1, pp. 21-32, 2011.

[169] T. Barbu, An Approach to Image Object Recognition and Interpretation, *Proceedings of the Romanian Academy*, Series A, Volume 4, Number 3, pp. 217-223, Sept-Dec. 2003.

[170] T. Barbu, A Computer Vision System for Graphical Object Recognition, *WSEAS Transactions on Circuits and Systems*, Issue 2, Volume 3, pp. 288-294, April 2004.

[171] R. J. Couerjolly, D. Baskurt, *Generalizations of angular radial transform for 2D and 3D shape retrieval*, Technical report, Laboratoire LIRIS, Claude Bernard University, Lyon, 2004.

[172] A. Khotanzad, Y. H. Hong, Invariant Image Recognition by Zernike Moments, *IEEE Transactions on Pattern Analysis and Machine Intelligence*,Volume 12, Issue 5, May 1990.

[173] V. P. Dinesh Kumar, T. Tessamma, Performance Study of an Improved Legendre Moment Descriptor as Region-based Shape Descriptor, *Pattern Recognition and Image Analysis*, Vol. 18, Issue 1, pp. 23-29, Jan. 2008.

[174] E. Persoon, K. Fu, Shape Discrimination Using Fourier Descriptors, *IEEE Trans. On Systems, Man and Cybernetics*, Vol. SMC-7(3), pp. 170-179, 1977.

[175] D. Zhang, G. Lu, A comparative study of curvature scale space and Fourier descriptors for shape-based image retrieval, *Journal of Visual Communication and Image Representation*, Volume 14, Issue 1, pp. 39-57, 2003.

[176] X. Zhang, Complementary Shape Comparison with Additional Properties, *Volume Graphics*, 2006.

[177] V. Natarajanb, H. Doraiswamy, Efficient algorithms for computing Reeb graphs, *Computational Geometry*, no. 42, pp. 606–616, 2009.

[178] S. O. Belkasim, M. Shridhar, M. Ahmadi, Pattern recognition with moment invariants: a comparative study and new results, *Pattern Recognition,* Vol. 24, No. 12, pp. 1117-1138, 1991.

[179] I. Sommer, O. Müller, F. S. Domnigues, O. Sander, J. Weickert, T. Lengauer, Moment invariants as shape recognition technique for comparing protein binding sites, *Oxford Journals, Bioinformatics*, Vol. 23, Issue 23, pp. 3139-3146, 2007.

[180] M. K. Hu, Visual pattern recognition by moment invariants, *IEEE Trans. Inform. Theory*, vol. 8, pp. 179–187, 1962.

[181] JC Nordbotten, Multimedia Information Retrieval Systems, Retrieved 14 October 2011.

[182] A. Guttman, R-trees: a dynamic index structure for spatial searching, *Proceedings of the SIGMOD Conference*, Boston, pp. 47-57, June 1984.

[183] Y. Jia, J. Wang, G. Zeng, H. Zha, X.-S. Hua, Optimizing kd-trees for scalable visual descriptor indexing, *CVPR*, 2010, pp. 3392–3399, 2010.

[184] I. Markov, VP-tree: Content-based image indexing, *Proc. of IJCNN*, 2004.

[185] R. Mao, W. Liu, Q. Iqbal, D. P. Miranker, On Index Methods for an Image Database, *ACM-MMDB*, 2003.

[186] T. Barbu, A. Ciobanu, M. Luca, SAM-based Image Indexing and Retrieval System using LAB Color Characteristics, *Latest Trends in Circuits, Systems, Signal Processing and Automatic Control* (*Proc. of the 5th Intl. Conf. on Circuits, Systems, Control, Signals, CSCS'14*), Salerno, Italy, June 3-5, pp. 266-270, 2014.

[187] M. S. Lew, N. Sebe, C. Djeraba, R. Jain, Content-based multimedia information retrieval: State of the art and challenges, *ACM Trans. Multimedia Comput. Commun. Appl.*, 2(1), pp. 1–19, 2006.

[188] J. Eakins, M. Graham, *Content-based Image Retrieval*, University of Northumbria at Newcastle. Retrieved 2014-03-10.

[189] T. Barbu, M.Costin, A. Ciobanu, Color-based Image Retrieval Approaches Using a Relevance Feedback Scheme, *Springer-Verlag - Series: Studies in Computational Intelligence: New Concepts and Applications in Soft Computing*, Vol. 417, pp. 47-55, Berlin, Eds. V.E. Balas, A. V. Koczy, J. Fodor, 2013.

[190] T. Barbu, A. Ciobanu, Color-based Image Retrieval Technique Using Relevance Feedback, *Proceedings of Third International Conference on Electronics, Computers and Artificial Intelligence, ECAI 2009*, Volume 4, pp. 105-108, Pitesti, Romania, 3-5 July 2009.

[191] T. Barbu, M. Costin, A. Ciobanu, Histogram Intersection based Image Retrieval Technique using Relevance Feedback, *Proceedings of the Third International Workshop on Soft Computing and Applications, SOFA'09*, pp. 65-67, Szeged-Hungary, Arad-Romania, 29 July - 1 August 2009.

[192] A. Yilmaz, O. Javed, M. Shah, Object tracking: A survey, *ACM Computing Surveys*, vol. 38, no. 4, 2006.

[193] H. Moravec, Visual mapping by a robot rover, *Proceedings of the International Joint Conference on Artificial Intelligence* (*IJCAI*), pp. 598–600, 1979.

[194] C. Harris, M. Stephens, A combined corner and edge detector, In *Proc. of 4th Alvey Vision Conference*, pp. 147–151, 1988.

[195] D. Comaniciu, P. Meer, Mean shift analysis and applications, In *IEEE International Conference on Computer Vision (ICCV)*, Vol. 2. pp. 1197–1203, 1999.

[196] P. Viola, M. Jones, Rapid object detection using a boosted cascade of simple features, In *Proceedings of IEEE Conference on Computer Vision and Pattern Recognition*, 2001.

[197] S. Shah, S. H. Srinivasan, S. Sanyal, Fast object detection using local feature-based SVMs, In *Proceedings of MDM'07*, pp. 1-5, 2007.

[198] T. Barbu, Automatic Skin Detection Technique for Color Images, *Proceedings of the International Multidisciplinary Scientific Geo-Conference SGEM'10*, Vol. 1, pp. 1047-1052, Albena, Bulgaria, June 20-25, 2010.

[199] G. Yang, T. S. Huang, Human face detection in a complex background, *Pattern Recognition*, Vol. 27, no. 1, pp. 53-63, 1994.

[200] T. K. Leung, M. C. Burl, P. Perona. Finding Faces in Cluttered Scenes Using Random Labeled Graph Matching, *Proceedings of the 5th International Conference on Computer Vision*, pp. 637-644, Cambridge, Mass., June 1995.

[201] K. C. Yow, R. Cipolla. A probabilistic framework for perceptual grouping of features for human face detection, *Second IEEE International Conference on Automatic Face and Gesture Recognition* (*FG '96*), pp. 16, 1996.

[202] H. A. Rowley, S. Baluja, T. Kanade, Neural Network-Based Face Detection, *IEEE Computer Society Conference on Computer Vision and Pattern Recognition*, pp. 203-208, 1996.

[203] A. V. Nefian, An embedded HMM-based approach for face detection and recognition, *Proceedings of the IEEE International Conference on Acoustics, Speech, and Signal Processing '99*, Vol. 6, pp. 3553-3556, 1999.

[204] T. V. Pham, M. Worring, A. W. M. Smeulders, Face Detection by Aggregated Bayesian Network Classifiers, *Machine Learning and Data Mining in Pattern Recognition*, Book Series *Lecture Notes in Computer Science*, Volume 2123, pp. 249-262, 2001.

[205] M. Nilsson, J. Nordberg, I. Claesson. Face Detection using Local SMQT Features and Split Up SNoW Classifier, *IEEE International Conference on Acoustics, Speech, and Signal Processing* (*ICASSP*), Vol. 2, pp. 589-592, April 2007.

[206] K. Ichikawa, T. Mita, O. Hori, Component-based robust face detection using AdaBoost and decision tree, *Proc. of the 7th Intl. Conference on Automatic Face and Gesture Recognition*, pp. 413 – 420, 2006.

[207] Z. Jin, Z. Lou, J. Yang, Q. Sun, Face detection using template matching and skin-color information, *Advanced Neurocomputing Theory and Methodology*, Vol. 70, Issues 4-6, pp. 794-800, Jan. 2007.

[208] D. A. Forsyth, M. M. Fleck, Identifying nude pictures, IEEE *Workshop on the Applications of Computer Vision '96*, pp. 103-108, 1996.

[209] A. L. Edwards, *An Introduction to Linear Regression and Correlation*, San Francisco, CA: W. H. Freeman, pp. 33-46, 1976.

[210] T. Barbu, SVM-based Human Cell Detection Technique using Histograms of Oriented Gradients, *Mathematical Methods for Information Science & Economics: Proceedings of the 3rd International Conference for the Applied Mathematics and Informatics (AMATHI '12)*, Montreux, Switzerland, pp. 156-160, December 29-31, 2012.

[211] N. Dalal, B. Triggs, Histograms of oriented gradients for human detection, *Computer Vision and Pattern Recognition*, San Diego, CA, June 20–25, 2005.

[212] R. Koprowski, Z. Wrblewski, Automatic segmentation of biological cell structures based on conditional opening and closing, *Machine Graphics and Vision*, 14, pp. 285-307, 2005.

[213] D. H. Ballard, Generalizing the Hough transform to detect arbitrary shapes, *Pattern Recognition*, 13(2), pp. 111–122, 1981.

[214] Y. Liu, A. Haizho, X. Guangyou, Moving object detection and tracking based on background subtraction, *Proceeding of Society of Photo-Optical Instrument Engineers (SPIE)*, Vol. 4554, pp. 62-66, 2001.

[215] R. Jain, H. Nagel, On the analysis of accumulative difference pictures from image sequences of real world scenes, *IEEE Trans. Patt. Analy. Mach. Intell.*, 1, 2, pp. 206–214, 1979.

[217] M. Costin, T. Barbu, M. Zbancioc, G. Constantinescu, Techniques for static visual object detection within a video scene, *Bulletin of the Polytechnic Institute of Iasi, Automatic Control and Computer Science Section*, Tom LI (LV), Fasc.1-4, pp.75-85, Iaşi, 2005.

[218] T. Barbu, Novel Approach for Moving Human Detection and Tracking in Static Camera Video Sequences, *Proceedings of the Romanian Academy*, Series A, Volume 13, Number 3, pp. 269-277, July-September 2012.

[219] T. Barbu, Pedestrian detection and tracking using temporal differencing and HOG features, *Computers & Electrical Engineering*, Volume 40, Issue 4, pp. 1072–1079, May 2014.

[220] T. Barbu, Multiple Object Detection and Tracking in Sonar Movies using an Improved Temporal Differencing Approach and Texture Analysis, *U.P.B. Scientific Bulletin*, Series A, Vol. 74, Issue 2, pp. 27-40, 2012,

[221] J. Serra, P. Soille, Mathematical Morphology and its Applications to Image Processing, *Proceedings of the 2nd International symposium on mathematical morphology* (*ISMM'94*), 1994.

[222] N. A. Ogale, *A survey of techniques for human detection from video*, Dept. of Computer Science, University of Maryland, College Park, www.cs.umd.edu/Grad/scholarlypapers/papers/neetiPaper.pdf

[223] C. Papageorgiou, T. Poggio, A Trainable Pedestrian Detection system, *International Journal of Computer Vision (IJCV)*, pp. 15-33, 2000.

[224] X. Wang, T. X. Ha, S. Yan, An HOG-LBP human detector with partial occlusion handling, *Proceedings of ICCV '09*, 2009.

[225] C. Beleznai, B. Fruhstuck, H. Bischof, Human Tracking by Fast Mean Shift Mode Seeking, *Journal of MultiMedia*, Vol. 1, Issue 1, pp. 1-8, April 2006.

[226] D. Comaniciu, R. Visvanathan, P. Meer, Kernel-Based Object Tracking, *IEEE Trans. Pattern Analysis and Machine Intelligence*, vol. 25, no. 5, pp. 564-575, May 2003.

[227] N. Funk, *A study of the Kalman filter applied to visual tracking*, Tech. Rep., University of Alberta, 2003.

[228] L. Mihaylova, P. Brasnett, N. Canagarajah, D. Bull, Object tracking by particle filtering techniques in video sequences, *Advances and Challenges in Multisensor Data and Information*, pp. 260-268, 2007.

[229] M. Nergui, Y. Yoshida, N. Imamoglu, J. Gonzalez, M. Sekine, W. Yu, Human motion tracking and recognition using HMM by a mobile robot, *International Journal of Intelligent Unmanned Systems*, Vol. 1, Issue 1, pp. 76 – 92, 2013.

[230] L. Xiaowei, K. Qing-Jie, L. Yuncai, A Feature Fusion Algorithm for Human Matching between Non-Overlapping Cameras, *Chinese Conference on Pattern Recognition CCPR'08*, pp. 1-6, 2008.

[231] L. Wixon, Detecting Salient Motion by Accumulating Directionally-Consistent Flow, *IEEE transactions on pattern analysis and machine intelligence*, 22 (8), Aug. 2000.

[232] M. Black, A. Jepson, Eigen-tracking: Robust matching and tracking of articulated objects using a view-based representation, *International Journal of Computer Vision*, 36(2), pp. 101-130,1998.

[233] T. Barbu, Template Matching based Video Tracking System using a Novel N-Step Search Algorithm and HOG Features, *Lecture Notes in Computer Science* (*Proc. of the 19th International Conference on Neural Information Processing, ICONIP 2012,* part V, Doha, Qatar, Nov. 12-15, 2012), Vol. 7667, pp. 328-336, Springer, Heidelberg, T. Huang et al. (Eds.), 2012.

[234] A. Gyaourova, C. Kamath, S.-C. Cheung, *Block matching for object tracking*, Tech. Rep. UCRL-TR-200271, Lawrence Livermore Natl. Lab., Livermore, Calif, USA, 2003.

[235] T. Barbu, Approximations of the filtering problem via fractional steps method, *Communications in Applied Analysis*, Vol. 8, No. 2, Dynamic Publishers, USA, pp. 263-278, April 2004.

[236] T. Barbu, C. Moroşanu, Numerical Approximation of the Riccati Equation via Fractional Steps Method, *Differential Equations and Control Theory*, Series *Lecture Notes in Pure and Applied Mathematics*, vol. 225, pp. 55-62, Marcel Dekker, Inc., New York, 2001.

[237] Y. L. You, M. Kaveh, Fourth-order partial differential equations for noise removal, *IEEE Transactions on Image Processing*, Vol. 9, No.10, pp. 1723–1730, 2000.

[238] T. Barbu, PDE-based Restoration Model using Nonlinear Second and Fourth Order Diffusions, *Proceedings of the Romanian Academy*, Series A: Mathematics, Physics, Technical Sciences, Information Science, Volume 16, Number 1, January-March 2015.

[239] X. Huang, A. Acero, H.-W. Hon, Spoken Language Processing: A Guide to Theory, Algorithm and System Development, Prentice Hall, 2001.

[240] T. Feng, S. Z. Li, H.-Y. Shum, H. Zhang, Local Nonnegative Matrix Factorization as a Visual Representation, *Proc. Second Int'l Conf. Development and Learning (ICDL '02)*, 2002.

[241] W.-H. Tsai, J.-W. Lin, Der-Chang Tseng, Unsupervised Fingerprint Recognition, *IEICE Transactions*, 96-D (9), pp. 2115-2125, 2013.

[242] J. Daugman, How iris recognition works, *IEEE Transactions on Circuits and Systems for Video Technology* 14 (1), pp. 21–30, Jan. 2004.

[243] C. M. Elliott, S. Zheng, On the Cahn–Hilliard equation, *Arch. Rat. Mech. Anal*., 96, 339, 1986.

[244] B. K. P. Horn, B. G. Schunck, Determining optical flow, *Artificial intelligence*, 17(1-3), pp. 185-203, Elsevier, 1981.

[245] L. G. Brown, A survey of image registration techniques, *ACM Computing Surveys* (CSUR) archive, Vol. 24, Issue 4, pp. 325 - 376, dec. 1992.

[246] S. Heldmann, O. Mahnke, D. Potts, J. Modersitzki, B. Fischer, Fast computation of Mutual Information in a variational image registration approach, *Bildverarbeitung fur die Medizin 2004: Algorithmen, Systeme, Anwendungen*, 448, 2004.